CALIBRATION OF FULL-WAVEFORM AIRBORNE LASER SCANNING DATA FOR 3D OBJECT SEGMENTATION

FANAR M. ABED

BSc. Surveying Engineering

MSc. Surveying Engineering

Thesis submitted for the degree of Doctor of philosophy

School of Civil Engineering and Geosciences

Newcastle University

October 2012

ABSTRACT

Airborne Laser Scanning (ALS) is a fully commercial technology, which has seen rapid uptake from the photogrammetry and remote sensing community to classify surface features and enhance automatic object recognition and extraction processes. 3D object segmentation is considered as one of the major research topics in the field of laser scanning for feature recognition and object extraction applications. The demand for automatic segmentation has significantly increased with the emergence of full-waveform (FWF) ALS, which potentially offers an unlimited number of return echoes. FWF has shown potential to improve available segmentation and classification techniques through exploiting the additional physical observables which are provided alongside the standard geometric information. However, use of the FWF additional information is not recommended without prior radiometric calibration, taking into consideration all the parameters affecting the backscattered energy.

The main focus of this research is to calibrate the additional information from FWF to develop the potential of point clouds for segmentation algorithms. Echo amplitude normalisation as a function of local incidence angle was identified as a particularly critical aspect, and a novel echo amplitude normalisation approach, termed the Robust Surface Normal (RSN) method, has been developed. Following the radar equation, a comprehensive radiometric calibration routine is introduced to account for all variables affecting the backscattered laser signal. Thereafter, a segmentation algorithm is developed, which utilises the raw 3D point clouds to estimate the normal for individual echoes based on the RSN method. The segmentation criterion is selected as the normal vector augmented by the calibrated backscatter signals. The developed segmentation routine aims to fully integrate FWF data to improve feature recognition and 3D object segmentation applications. The routine was tested over various feature types from two datasets with different properties to assess its potential. The results are compared to those delivered through utilizing only geometric information, without the additional FWF radiometric information, to assess performance over existing methods. The results approved the potential of the FWF additional observables to improve segmentation algorithms. The new approach was validated against manual segmentation results, revealing a successful automatic implementation and achieving an accuracy of 82%.

ACKNOWLEDGEMENTS

Looking back at the past four years, many wonderful things have happened. I would like to thank everyone who definitively contributed to make those things happen and help me to make my PhD journey enjoyable and unforgettable.

First of all, I would like to thank my supervisors, Jon Mills and Pauline Miller, for their support, advice, and invaluable guidance that make my journey successful.

A big thanks goes to all my friends and colleagues who support me to make my study exciting.

Finally, and importantly, I dedicate my success to my beloved family – my Mum and Dad, and my lovely sisters, for being always with me and smoothen my way although of the thousand miles between us.

Fanar M. Abed

Newcastle upon Tyne

Oct 2012

TABLE OF CONTENTS

CHAPTER THREE: 3D OBJECT SEGMENTATION OF FWF-ALS DATA …75

LIST OF FIGURES

LIST OF TABLES

LIST OF ABBREVIATIONS

ALS	Airborne Laser Scanning
ASD	Analytical Spectral Device
BADC	British Atmospheric Data Centre
CHM	Canopy Height Models
CI	Confidence Interval
COG	Centre of Gravity
CPU	Central Processing Unit
DEM	Digital Elevation Model
DSM	Digital Surface Model
DTM	Digital Terrain Model
FDN	Fixed Distance Neighbours
FOV	Field of View
FWF	Full-Waveform
GNSS	Global Navigation Satellite System
GPF	Gaussian Pulse Fitting
GPS	Global Positioning System
GUI	Graphical User Interface
IMU	Inertial Measurement Unit
INS	Inertial Navigation System
KNN	K-Nearest Neighbours
Lidar	Light Detection and Ranging

LRF	Laser Range Finder
LS	Least Squares
LVIS	Laser Vegetation Imaging Sensor
MLS	Mobile Laser Scanning
MODTRAN	Moderate Resolution Atmospheric Radiance and Transmittance
OPALS	Orientation and Processing of Airborne Laser Scanning
PRF	Pulse Repetition Frequency
PVC	Polyvinyl Chloride
RANSAC	Random Sample Consensus
RGD	Rigorous Gaussian Pulse Detection
RMS	Root Mean Square
RSN	Robust Surface Normal
SLICER	Scanning Lidar Imager of Canopies by Echo Recovery
SLS	Spaceborne Laser Scanning
STD	Standard Deviation
TLS	Terrestrial Laser Scanning

CHAPTER

1

INTRODUCTION

1.1 OVERVIEW

Automatic restoration of 3D objects from geospatial data is the ultimate goal for many different applications such as building extraction and surface modelling (Vosselman and Maas, 2010), reverse engineering (Remondino and El-Hakim, 2006), cultural heritage recording (Miller, 2007), and archaeology (Doneus et al., 2008). This need has rapidly increased in recent years with the vast development in geospatial data acquisition technology, including laser scanning systems (Shan and Toth, 2009). With the dramatic decrease in the cost of computers, the unstructured massive data from laser scanning can be visualised, processed and structured effectively, making the final 3D digital products more accessible to a larger range of users (Vosselman and Maas, 2010).

Once point clouds have been derived, further processing and analysis is required in order to extract information about the topographic surface (Baltsavias, 2004; Wang, 2006). This processing includes visualising, structuring and grouping points for future data handling and processing tasks such as feature extraction (Zizhen et al., 2008). The fundamental process to extract features is by merging nearby points with similar characteristics into sets of similar attributes (Wang and Lu, 2009). This structuring process helps deal with massive geospatial datasets by grouping points to define the surfaces and facets of the required 3D objects (Jiang and Bunke, 1994; Han et al., 2007; Lafarge et al., 2008). In order to deliver the optimal information about object characteristics, a combination of geometric information from laser scanning systems and additional spectral information from other remote sensing techniques such as photogrammetry, is recommended (Habib et al., 2004a; Ronnholm et al., 2008; Zublin et al., 2008; Siqueira et al., 2008; Abdelhafiz, 2009). This is because the geometric information from standard laser scanning systems is not yet sufficient to model land cover features and deliver a comprehensive and optimal representation of Earth's surface details. Although nowadays most laser scanning systems can contribute additional spectral observables, these observables are raw measurements and need careful handling (Akca, 2007).

However, a new type of laser scanning system, specifically full-waveform (FWF) systems, offers the potential to overcome the need to integrate information from different systems. This is achieved through the delivery of additional physical information on land cover alongside the standard geometric information which all systems can provide (Shan and Toth, 2009; Mallet and Bretar, 2009). These FWF systems can save the additional effort and cost needed to synchronise data acquired from separate sensors. However, FWF information is not recommended to be utilised without prior calibration, which is necessary to deliver optimal end products (Wagner, 2010). Therefore, the research reported in this thesis focusses on calibrating the additional information from FWF laser scanning in order to optimise the integration of this information with existing segmentation techniques. This is through fully utilising FWF information in future segmentation, classification and filtering techniques, thus moving towards more accurate 3D object representation and modelling.

1.2 LASER SCANNING

Laser scanning, also referred to as lidar (light detection and ranging) is the digital technique of capturing accurate information about physical objects using laser light (Wagner, 2005). It is a non-contact and non-destructive technology, which scans objects and delivers information about their details remotely through recording free-form shapes by means of physical signals (Wehr and Lohr, 1999). The mechanism starts through the scanning optics system by transmitting a laser beam to illuminate the target, which is supplemented by a lens to focus the beam on the scanned area within certain characteristics. The scan mirror moves the beam forth and back in a rapid manner to create the laser line (Shan and Toth, 2009). This type of mirrors generally have an oscillating mechanism, however other types are also available such as palmer, fiber, and rotating polygon (Wehr and Lohr, 1999; Lin, 2009). Thereafter, the receiver records the signal returned from the target. Following this, the receiver optical system sends the laser light received from the scanned target to the detector to retrieve the signal. The detector will convert the signal into a digital code to be sent to the decoder for processing and interpretation (Shan and Toth, 2009).

Laser scanning is an active data acquisition technique, which provides range measurements between the sensor and the target following the precise measurement of time as described in Eqn. 1.1 (Pfeifer and Briese, 2007; Shan and Toth, 2009).

$$R = (v \cdot t)/2$$ **Eqn. 1.1**

Where:

R is the range between the sensor and the target

v is the velocity of light

t is the elapsed time between the transmitted and the returned signal

The precision of the determined range can be estimated as follows:

$$\Delta R = \Delta v \cdot \frac{t}{2} + v \cdot \frac{\Delta t}{2}$$ **Eqn. 1.2**

Where:

ΔR is the range precision

Δv is the velocity precision

Δt is the time precision

Point clouds can be generated from such measurements to provide the end user with a 3D digital representation of the scanned features (Mallet and Bretar, 2009). To-date there are four main types of laser scanning sensors available for commercial and research purposes; however other sensors are still to come (Pfeifer, 2011). These are aerial (ALS), terrestrial (TLS), mobile (MLS), in addition to spaceborne (SLS) laser scanning systems (Figure 1.1) (Vosselman and Maas, 2010). Because of its early, prosperous and rapid development during the last two decades, ALS is the more investigated and widely utilised system (Pfeifer and Briese, 2007).

Figure 1.1. Existing laser scanning systems (Ullrich, 2009; Wagner, 2009).

Due to its capability for direct acquisition, laser scanning is often favoured for the collection of accurate information about objects in 3D space (Habib and Rens, 2008). Laser scanning systems consist of two main components, the laser range finder unit (LRF), and the positioning and orientation unit (GNSS/INS). The LRF unit delivers range information between the sensor and the target, whereas the GNSS/INS unit supplies the user with the positional and the orientation of the platform through GNSS (primarily GPS) and IMU sensors respectively (Wehr and Lohr, 1999). Figure 1.2

shows the main components of laser scanning systems and demonstrates the mounting layout of these components in an aerial platform.

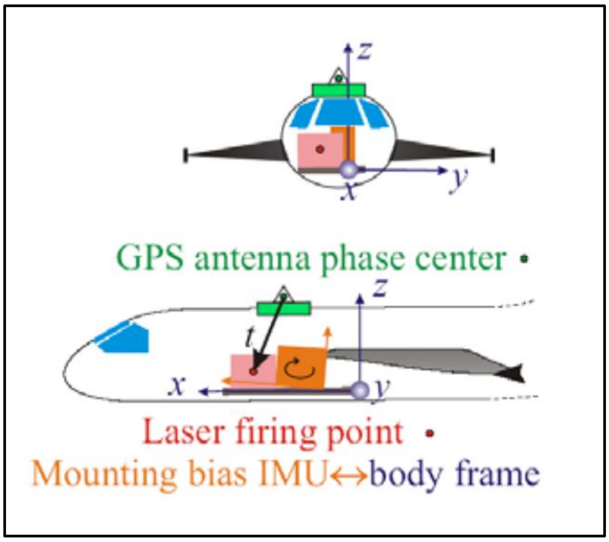

Figure 1.2. The typical components of laser scanning systems demonstrated by aerial platform (Pfeifer, 2009).

Following the Lidar equation (Eqn. 1.3), which includes range, positional, and orientation measurements in addition to other system parameters that define the relationship between the three combined components, the ground coordinates of the point cloud can derived (Figure 1.3) (Pfeifer et al., 2005; Habib et al., 2008). After post-processing analysis the derived data can be used to extract 3D information for various applications, such as surface modelling, environmental monitoring, shoreline management, and many other applications (Shan and Toth, 2009).

$$\vec{X}_G = \vec{X}_o + R_{yaw,pitch,roll}\ \vec{P}_G + R_{yaw,pitch,roll}\ R_{\Delta\omega,\Delta\emptyset,\Delta k}\ R_{\alpha,\beta}\begin{bmatrix}0\\0\\-\rho\end{bmatrix} \qquad \textbf{Eqn. 1.3}$$

Where:

$\vec{X}_G$: represents the ground x-coordinate of the point cloud.

$\vec{X}_o$: represents the vector between the ground and the IMU origins.

$R_{yaw,pitch,roll}$: represent the rotation matrix between the ground and the IMU coordinate systems.

$\vec{P}_G$: represent the offset between the laser and the IMU coordinate systems.

$R_{\Delta\omega,\Delta\emptyset,\Delta k}$: represent the rotation matrix between the laser and the IMU coordinate systems.

$R_{\alpha,\beta}$: represents the rotation matrix between the laser unit and the laser beam coordinate systems.

ρ : represents the laser range vector between the exposure and the object points.

Similar equations would be formed for the $\overrightarrow{Y_G}$ and $\vec{Z}_G$.

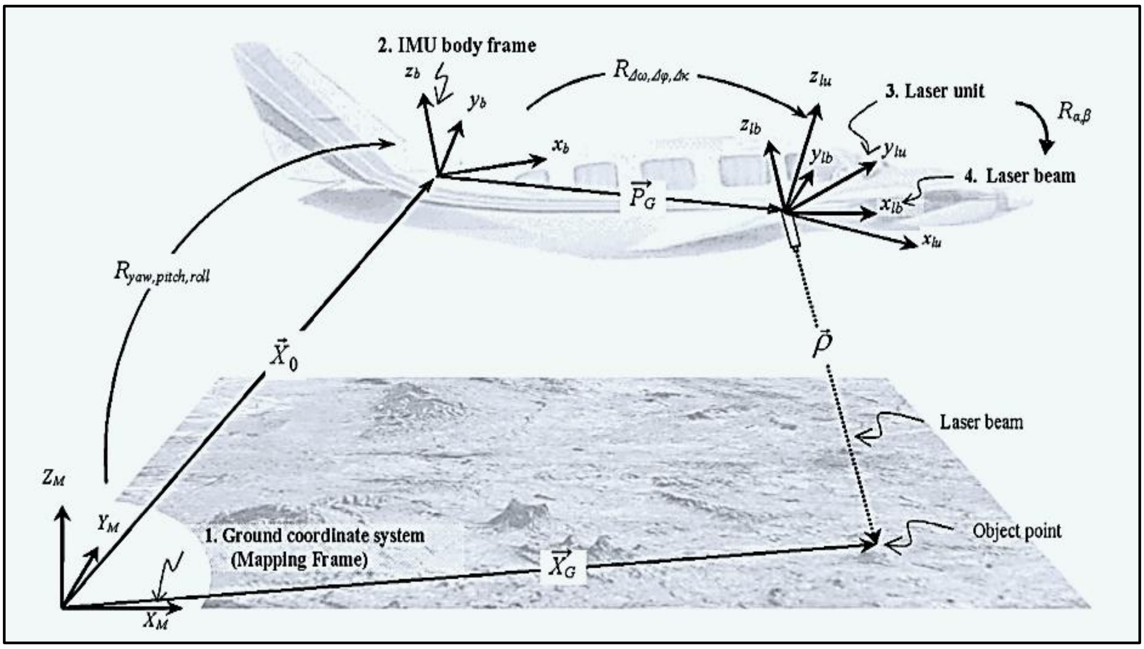

Figure 1.3. Coordinate systems and parameters involved in the Lidar equation (Habib et al., 2010).

1.2.1 Aerial Laser Scanning (ALS)

Topographic ALS is a laser scanning system mounted on an airborne platform and provides range measurements to the Earth's surface. It delivers a vertical accuracy of 5-10cm and decimetre-level planimetric accuracy, depending on the terrain type and flying height (Ackermann, 1999; Mallet and Bretar, 2009). Land cover features are scanned either from a fixed wing or a helicopter platform in order to collect the necessary information to model the topographic surface (Vosselman and Maas, 2010). A digital camera is usually flown alongside the ALS systems for orthophoto generation and data integration. This can be achieved by processing the photogrammetric information alongside the laser information to support laser range data for subsequent optimal interpretation. This can play a significant role in identifying land cover features in cases where the objects are found to be difficult to interpret from the blind range data only. However, this requires some extra effort to register and georeference the sensors after data collection and through post-processing analysis (Vosselman and Maas, 2010).

Commercial ALS systems typically operate at wavelengths between 800 and 1550 nm. This wavelength range is utilised to acquire data for different applications as the type and the amount of the received physical signal from an object primarily depends on the laser wavelength. Therefore, it is essential to select the system of the appropriate wavelength to meet with the project objectives (Wehr and Lohr, 1999). With regard to modelling usage and application, ALS systems are utilised either for topographic or bathymetric measurement (Shan and Toth, 2009). The first system works within a certain wavelength (infrared) and comprises of one LRF unit, which emits high-frequency pulses in order to estimate the range to the ground targets. The bathymetric system combines two LRF unit which emit simultaneous pulses at two different wavelengths (infrared and green) in order to estimate water depth based on time differences between the received pulses in both wavelengths (Axelsson, 2010). Figure 1.4 and Figure 1.5 illustrate the technical design of the topographic and the bathymetric aerial systems respectively. The airborne topographic system is the focus in this research.

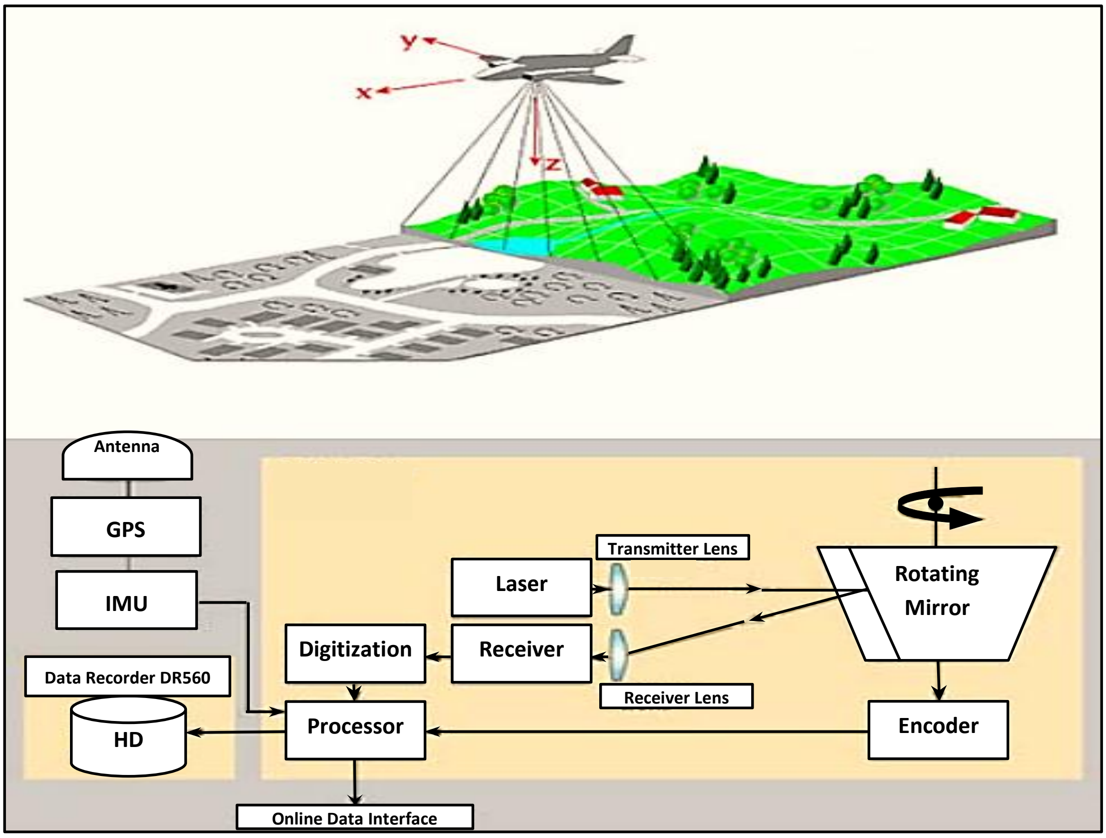

Figure 1.4. Technical concepts of an airborne topographic laser scanning system (Petrie, 2009).

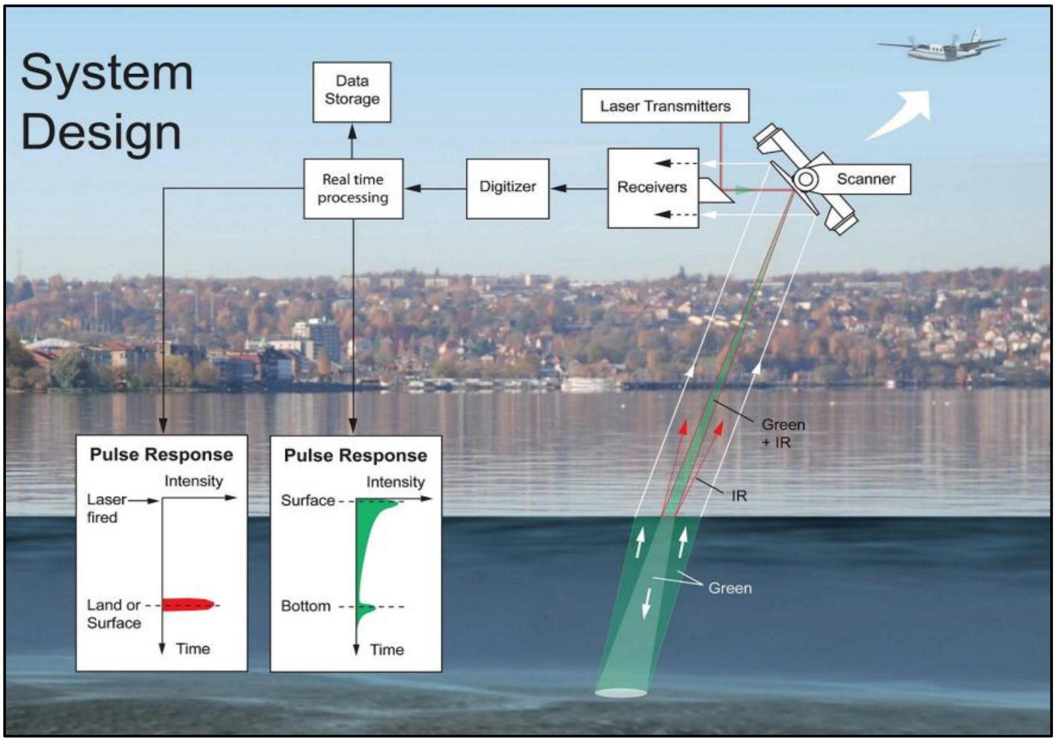

Figure 1.5. Technical concepts of an airborne bathymetric laser scanning system (Axelsson, 2010).

Topographic ALS systems are now fully operational to meet the needs of specific applications such as surface modelling (Mallet and Bretar, 2009). In contrast to photogrammetry, ALS is an active system, which can operate during day and night. Both ALS and photogrammetry are able to produce a digital terrain model (DTM). In photogrammetry, the ground point measurements are usually performed by user operator, however these points are localised automatically following a certain control structure, which depends on the image specifications. In contrast, ALS can automatically delivers ground points in a certain pattern, as priory determined by the system design (Ackermann, 1999). The laser beam from an ALS system can penetrate vegetation to the ground through gaps available in the canopy. This capability demonstrates potential to model the ground surface beneath, and deliver accurate DTMs where photogrammetry may fail (Kraus and Pfeifer, 1998). Furthermore, ALS outperforms photogrammetry by overcoming the shadow problem, because of being an active and sun-independent system. Figure 1.6 shows the difference between photogrammetry and laser scanning with respect to terrain measurements and the effects of shadowing on the determined ground points. Figure 1.6-a demonstrates the data acquisition situation in photogrammetry where point number 4 was the only visible ground point from both trajectories and therefore represents the terrain in this extended area. On the other hand, Figure 1.6-b illustrates the scan situation with ALS where both flightlines are independent and therefore all of the detected ground points from both flightlines are determined.

With regard to the technical physical principles, ALS can be grouped into two main systems, discrete-return and FWF (Shan and Toth, 2009; Mallet and Bretar, 2009). Both systems are designed to estimate range measurements using the physical concept of the pulsed laser mechanism. When the receiver only provides the start and the end of a signal at a certain rise time of the echo, then the system is called discrete-return. However, if the complete digital signal is digitised with extra information about the echo shape, then the system is called full-waveform. Further details about both systems are introduced in the following sections.

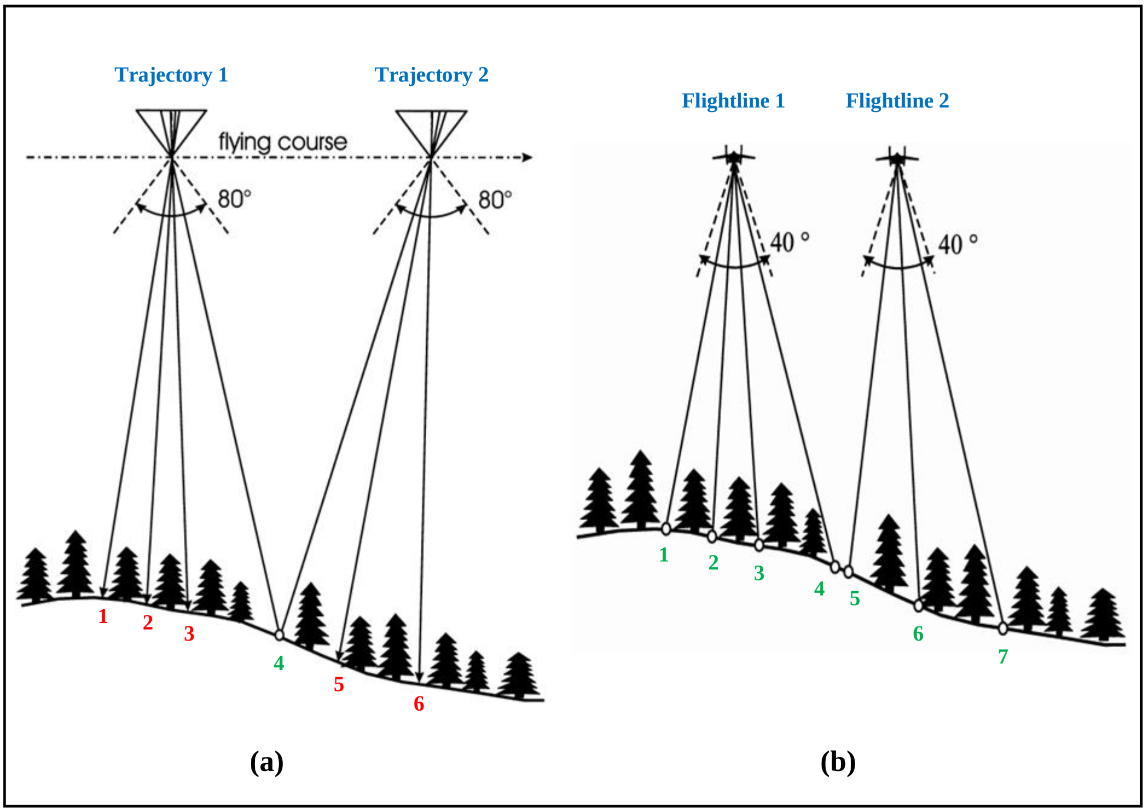

Figure 1.6. Principles of terrain measurements: **(a)** photogrammetry **(b)** ALS (Kraus and Pfeifer, 1998).

1.2.1.1 Discrete Systems

Discrete-return ALS systems can often capture up to four echoes per emitted pulse while some other systems are capable of detecting up to six individual echoes (Mallet and Bretar, 2009). Any object will be detected as a separate echo if the distance between successive returns is larger than the length of the laser pulse. However, the system will only record defined echoes of interest (e.g. first, last, and limited intermediate). This means that information about objects between the recorded echoes are lost within discrete ALS systems (Lin et al., 2010). The first commercial discrete ALS systems provided one echo per emitted pulse, but this system is only sufficient when one target is detected within the footprint of the laser beam. For example in a vegetated area, accurate modelling applications using this kind of system is restricted even for a small laser footprint (0.2-2 m diameter), because all objects (e.g. tree branches) between the first recorded echo, which represents the top of the tree, and the ground are being neglected. Moreover, in the presence of gaps between tree branches, the laser light can penetrate to reach the ground beneath, which provides information to model the ground surface for DTM generation applications. Therefore, multi-echo discrete systems have been introduced to overcome single echo system limitations (Mallet and Bretar, 2009).

The majority of the multi-echo discrete systems are designed to record only the first and the last echoes, although some other systems can also record intermediate echoes (Doneus et al., 2008). From a physical point of view, the first two detected echoes typically comprise about 90% of the received signal (Wagner et al., 2004). Based on this concept, there is a large chance of considering the rest of the detected echoes to be noise unless robust pulse detection methods are utilised, especially in vegetated areas. This is not applicable in this type of system as the pulse detection process is a “black-box” and not provided for end users. As the majority of the received signal is being discarded with the discrete-return systems, these systems are considered to be “lossy” with respect to the amount of the energy being lost by the detectors (Doneus et al., 2008). Therefore, for accurate surface modelling applications it is recommended to switch to FWF systems, which are able to record the complete received signal, which provides the opportunity to extract extra information and thus deliver more accurate range observables.

1.2.1.2 Full-Waveform Systems

FWF-ALS is unlike the discrete-return systems in that it records the entire backscattered signal of the laser pulse and stores it in the system recorder for post-processing (Jutzi and Stilla, 2006; Bretar et al., 2009). Capturing the complete waveform of the backscatter signal enables distinguishing between neighbourhood echoes of a range smaller than the pulse length (Jutzi and Stilla, 2006). Furthermore, complex and weak laser echoes can be detected towards improving modelling products such as DTMs (Lin et al., 2010). Figure 1.7 illustrates data recording and post-processing techniques of FWF-ALS signals from the Riegl LMS-Q560 system. This demonstrates the waveform signal digitising as a function of time, and the range derivation and analysis within the post-processing phase. In contrast with the discrete-return systems, which provides end users with a single range measure to the ground target, FWF stores the entire time history of the backscatter signal with a high sampling resolution as shown in Figure 1.8

(Vosselman and Maas, 2010). This gives the user the opportunity to model the received signal, applying a function that better fits with the physical trend towards robust range estimations and accurate data modelling (Mallet et al., 2011).

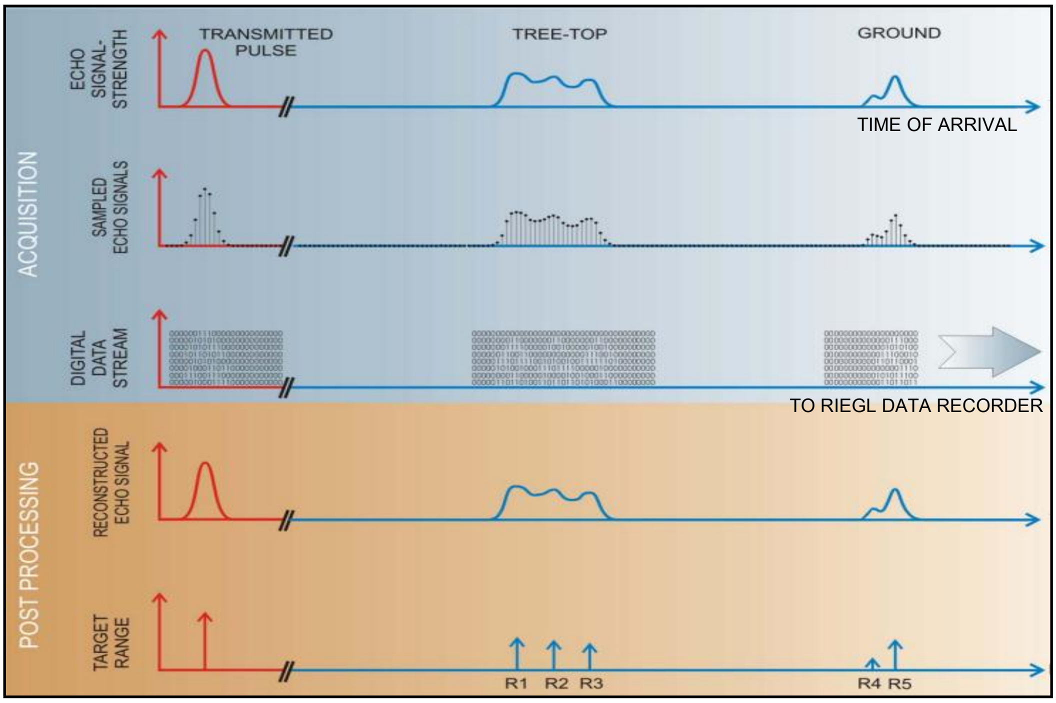

Figure 1.7. FWF data digitising and post-processing from Riegl LMS-Q560 system (Rieger et al., 2006).

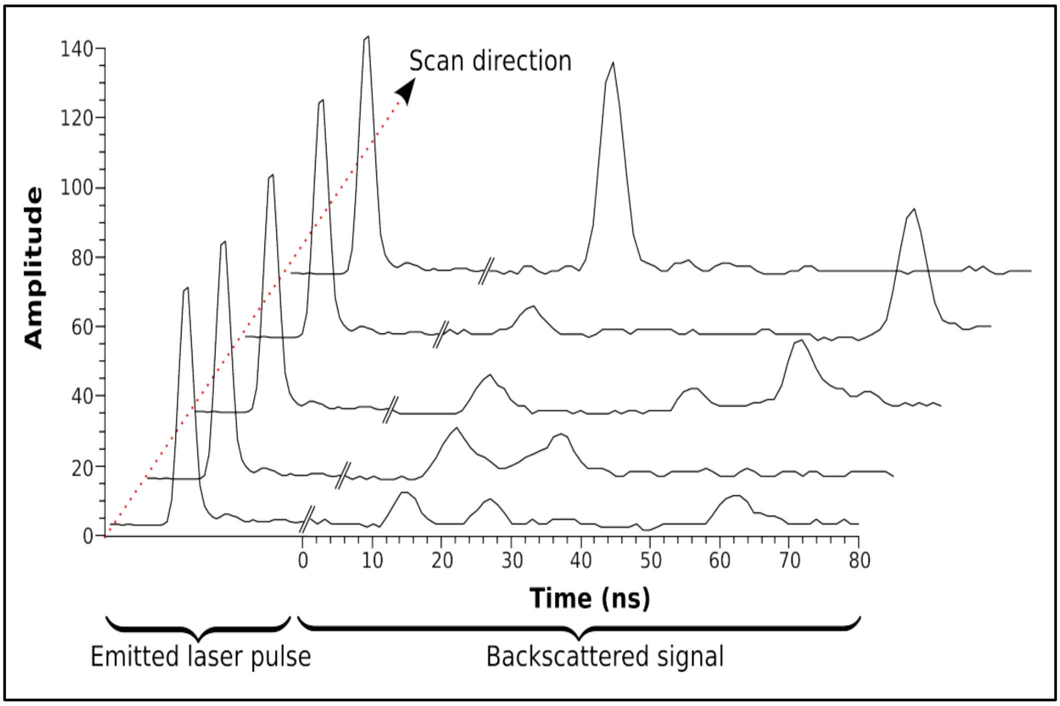

Figure 1.8. Simulation of raw FWF data show five emitted signals alongside their received backscatter digitised signal (Bretar et al., 2009).

The technical potential of FWF was firstly demonstrated during the 1990s by NASA through a large-footprint ALS system (10-70 m diameter), namely the Scanning Lidar Imager of Canopies by Echo Recovery (SLICER) and the Laser Vegetation Imaging Sensor (LVIS) (Wagner, 2005). Multiple experiments were conducted to study the system potential over various land cover types with multiple feature surfaces. The first commercial small-footprint FWF system, the Riegl LMS-Q560, was available on the market in 2004 and was followed by systems from Optech and Topeye (Wagner et al., 2006; Mallet and Bretar, 2009). These systems provide high point density and a more detailed description of the illuminated surfaces than large-footprint systems which are majorly influenced by the flying height and the beam divergence of the laser emitter (Vosselman and Maas, 2010).

FWF analysis and post processing may increase the accuracy and the resolution of the range measurements by providing end users with the chance to interpret the physical backscatter signals of the individual pulses (Doneus et al., 2008). This is achievable through pulse detection methods which give the user a significant opportunity to select the function which best fits the signal. In contrast with the discrete systems, FWF is applicable to determine the errors acquired from the limitations in the standard pulse detection methods that lead to inaccurate range measurements (Lin et al., 2010). Following waveform post-processing, denser point cloud data are generated than those delivered from the discrete systems. This deliver a great potential for the most land cover applications towards optimal data modelling (Bretar et al., 2009). FWF analysis also provides additional information about the physical backscattering properties of the illuminated targets (Lin et al., 2008; Mucke, 2008). The pulse width of the echo delivers information about surface roughness, slope, scan angle, or the depth of the volumetric object, while echo strength (amplitude) delivers information about target backscatter properties (Wagner et al., 2006). This provides a promising source of information to better identify surface features, as shown in Figure 1.9.

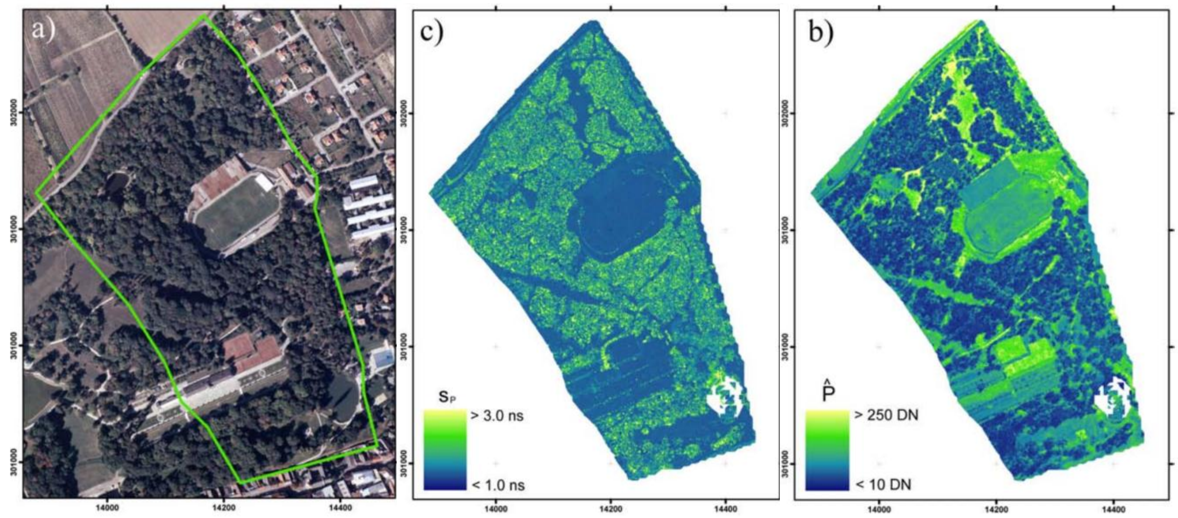

Figure 1.9. Visualisation of FWF signal parameters: **(a)** orthophoto **(b)** echo width **(c)** echo amplitude (Mucke, 2008).

1.2.2 Processing of Laser Scanner Data

1.2.2.1 Data Calibration

ALS is a multi-sensor system that is affected by many error sources during data capture (Shan and Toth, 2009). Modelling these errors through the data quality assurance process is essential for accurate end products (Schaer et al., 2007; Aguilar and Mills, 2008). The data quality process, including registration and calibration tasks, should be performed prior to point cloud applications (Vosselman and Maas, 2010). The registration process is concerned with establishing the coordinate system of the point cloud and the transformation functions used to deliver these coordinates from multi-sensor systems (Eqn. 1.3) (Habib et al., 2004a). The calibration process is more concerned with identifying, modelling, and estimating the errors inherent in these data (Skaloud and Lichti, 2006; Skaloud and Schaer 2007). Because calibration and modelling is a crucial aspect of the research presented here, data calibration and error compensation is further discussed.

As explained earlier, FWF provides geometric and physical information to the end user, which therefore requires some form of calibration. Geometric calibration aims to remove systematic errors from the ALS point cloud, which exist due to bias in the system parameters (Habib et al., 2011). This bias can be effectively eliminated either through applying system-driven or data-driven approaches (Shan and Toth, 2009). Data driven approaches such as strip adjustment are more preferable in this respect as information about system measurements (e.g. rotation angles between system components) are usually restricted to the system manufacturer (Habib and Rens, 2008). Strip adjustment is reliant on the mathematical model used to relate the point cloud from overlapping flightlines to the scanning system, which involves the transformation function for registration purposes (Vosselman, 2004). These transformation functions are mainly based on a selected primitive type (point, line, or areal regions) which are used to relate points from overlapping flightlines (Habib et al., 2004a). This aims to determine the discrepancies in the 3D offsets between overlapping flightlines, (e.g. Figure 1.10), towards minimising these differences.

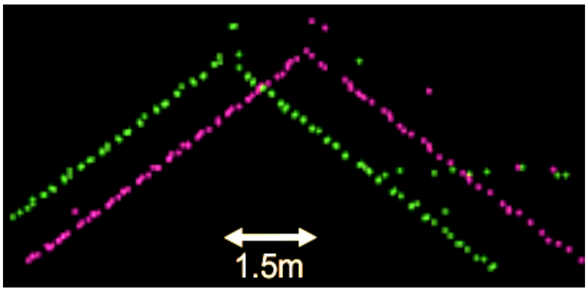

Figure 1.10. Cross-section visualisation of strip discrepancies observed over a house roof (Pfeifer, 2009).

The additional physical information from FWF also requires calibration towards optimal feature identification. However, this research area is still at a relatively early stage, and requires further investigations, which will be the focus of this research. The backscatter energy of the individual echoes can be re-constructed after post-processing from the echo width and the amplitude values, however these measurements require proper radiometric calibration (Wagner, 2010). These waveform attributes have demonstrated potential after calibration for segmentation and classification techniques (Höfle et al., 2012; Alexander et al., 2010), which is promising to be integrated with the geometric information to improve feature modelling.

The aim of radiometric calibration is to calibrate the received laser energy from all variables affecting the signal as it travels between the sensor and the target. This enables delivery of a calibrated signal which is proportional to the target scattering characteristics (Wagner, 2010; Kaasalainen et al., 2011). These processes are dependent on the theoretical model selected to describe all the physical phenomena affecting the laser energy towards a calibrated laser signal within a desired accuracy (Wagner et al., 2008). The radiometric calibration is also reliant on the practical process applied to correct the signal. When the backscatter signal is corrected according to different altitudes, incidence angles, and temporal (atmospheric) effects for a single sensor case, radiometric calibration is considered to be relative (Kaasalainen et al., 2011). This kind of calibration is more applicable when comparing signals delivered from the same system. However, when the signal is corrected to enable comparison to data from other systems, which is necessary for integration purposes, then the calibration is considered absolute (Kaasalainen et al., 2011). Because in this case, the signal is corrected to be independent by compensating for all error sources affecting the received signal, thus referring to the target physical characteristics only. Therefore, the absolute radiometric calibration is more desirable for a wide range of applications. Figure 1.11 demonstrates the visual differences in the backscatter physical signal received from two overlapping flightlines over an urban area. This can be realised over all the interest area and particularly over the house roofs where the recorded backscatter signals are clearly different between both flightlines and therefore requires calibration for further processing.

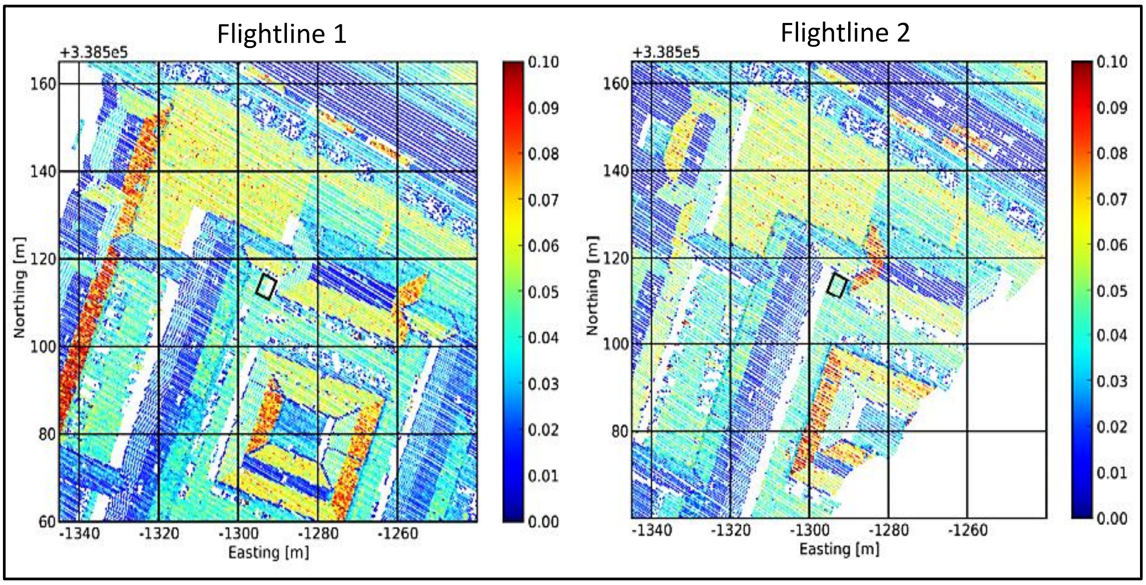

Figure 1.11. Backscatter signal visualisation from two overlapping flightlines (Briese and Lehner, 2009).

1.2.2.1 Data Structuring

Segmentation is a well-known point cloud handling and structuring process which is often recognised as the first step to extract information for advanced processing in various applications (Vosselman and Maas, 2010). Automatic segmentation is a valuable process to group points with similar characteristics into regions automatically (Figure 1.12). These regions could be planes, cylinders, or smooth surfaces following the selected segmentation algorithm and the features of interest (Mallet et al., 2011). As this processing is fully automated, this supports future use of the data for advanced processing, such as data modelling and feature extraction strategies (Schiewe, 2002). However, if the surface is divided into more than one segment, this results in an over-segmentation problem. In contrast, under-segmentation occurs when more than one surface is combined in one segment (Han et al., 2007; Wang and Lu, 2009; Appia et al., 2010). Although it is recommended to be very careful in selecting thresholds within the segmentation algorithm to avoid these problems, over-segmentation is usually more preferable. This is because with over-segmentation it is possible to apply extra manual editing to the segmentation results towards the optimal solution, whereas with under-segmentation it is harder and more challenging to optimise the results (Rabbani et al., 2006).

Figure 1.12. Automatic segmentation of ALS data into planar segments (Vosselman and Maas, 2010).

Automatic point cloud segmentation emerged from 2D image segmentation techniques for pattern recognition and computer vision applications. It aims to cluster image pixels into salient regions to emphasis individual surfaces or objects from the background (Atkinson, 1996). Thereafter, the process was modified for 3D applications by utilising methods those tailored for 2.5 D data and later extended to handle 3D unstructured point cloud (Sithole, 2005). Point cloud segmentation can be classified into four main approaches (Rabbani, 2006), although other algorithms can also be developed as classification is subjective to different variables:

1. Scanline-based segmentation.
2. Edge-based segmentation.
3. Surface-based segmentation.
4. Hybrid algorithms.

Scanline-based segmentation is designed to group points on a scanline basis (Sithole, 2005). Thus, each row (scan line) is treated individually based on 3D line detection followed by establishing similarity measures between adjacent scan lines to group points into meaningful segments. However Sithole and Vosselman (2003) further developed this concept by defining profiles in different directions rather than in the scan direction only which is more relevant to ALS data. Consequently, edge-based segmentation is designed to detect breaklines prior to the segmentation process (Shan and Toth, 2009). It detects feature edges and outlines their borders as a first step in segmentation. Thereafter, the process group points within these borders into regions to identify the final segments (Tovari, 2006). This algorithm is very sensitive to the presence of noise in the dataset, therefore it is more relevant to image processing than to lidar point clouds. In contrast, surface-based segmentation is relatively less sensitive to the noise in lidar data and therefore it is preferable. It aims to group local points into segments with similar properties using a similarity measure function (Shan and Toth, 2009). The points should be close enough to each other and within a certain distance from the selected seed point in order to achieve optimal results. This distance should be pre-defined to meet with the study objectives and the dataset specifications. The similarity measure should be selected precisely to maintain the final goal, and is usually optimised based on the region type properties (i.e. surface characteristics) (Rabbani, 2006). As for the final type, hybrid algorithms, as implied by the name, these combine more than one of the previously mentioned algorithms to deliver the final segments. It usually combines edge-based and surface-based techniques for better results (Rabbani, 2006).

1.3 RESEARCH MOTIVATION

The integration of multiple geospatial datasets (such as ALS and photogrammetry) can produce more accurate results and more reliable information than that which can be obtained from a single source (Habib et al., 2004b). This is due to the fact that each data source can provide information about features which the other system cannot deliver. Therefore combining multiple information from different systems can compensate the limitations in the information provided by a single system. This leads to better feature identification and more accurate data modelling results. However, FWF-ALS systems provide the end user with a powerful combination of geometric and physical information about land cover features in a single system. This information has been found to be promising and encouraging to be exploited together towards improving end products. Therefore, this research is motivated by the concept of fully-exploiting FWF-ALS data to increase the performance of automatic 3D object segmentation routines.

1.4 RESEARCH OBJECTIVES

The overall aim of this research is to fully investigate and optimise FWF-ALS data in order to enhance automatic segmentation techniques, which are able to decompose 3D objects into coherent point clusters based on reliable estimation of the surface properties.

To meet this aim, the following objectives were established:

1. Investigate the potential of the additional information from FWF to improve existing 3D object segmentation techniques through reviewing available segmentation algorithms and addressing the weaknesses in the identified standard methods.

2. Develop an effective automatic routine to manage and process FWF-ALS datasets in a manner which requires less human effort and reduces the time needed to process large laser scanning datasets efficiently.
3. Calibrate the FWF backscatter signal from all error sources that affected the signal during its path between the target and the sensor to provide the backscatter energy estimate following a comprehensive calibration workflow.
4. Assess the developed calibration technique to assure reliability for integration in the developed segmentation algorithm.
5. Develop an automatic segmentation routine that fully integrates the calibrated FWF additional information alongside the standard geometric information to deliver highly accurate and more detailed segmentation outputs.
6. Assess and validate the developed segmentation method on real datasets with different specifications to establish potential.

1.5 RESEARCH METHODOLOGY

To achieve the overall aim of this research, a literature critique, including evaluation of available segmentation techniques and all related processing strategies, necessary to accomplish the final goal, is presented. This is adopted to diagnose the weaknesses in existing methods which can be fulfilled with the FWF data exploitation. Thereafter, the methodology is established, based on the findings delivered from the literature review phase, and classified into four main stages. The first stage deals with the processing of FWF-ALS data and the strategies required to manage such a large dataset and deliver the outputs within a reasonable period of time. The second stage addresses the signal normalisation approach needed to implement and compensate the received laser signal for incidence angle effects. The third stage comprises the calibration workflow of the backscatter signal to normalise the physical signal for all relevant influencing effects. Finally, the fourth stage concentrates on the development of an automatic segmentation routine through the integration of the calibrated additional information from FWF with the standard geometric information. Finally, the developed methodology is tested, assessed and validated through visual and statistical analysis to check potential.

1.6 THESIS STRUCTURE

The thesis is composed of six chapters, as explained in the following flowchart:

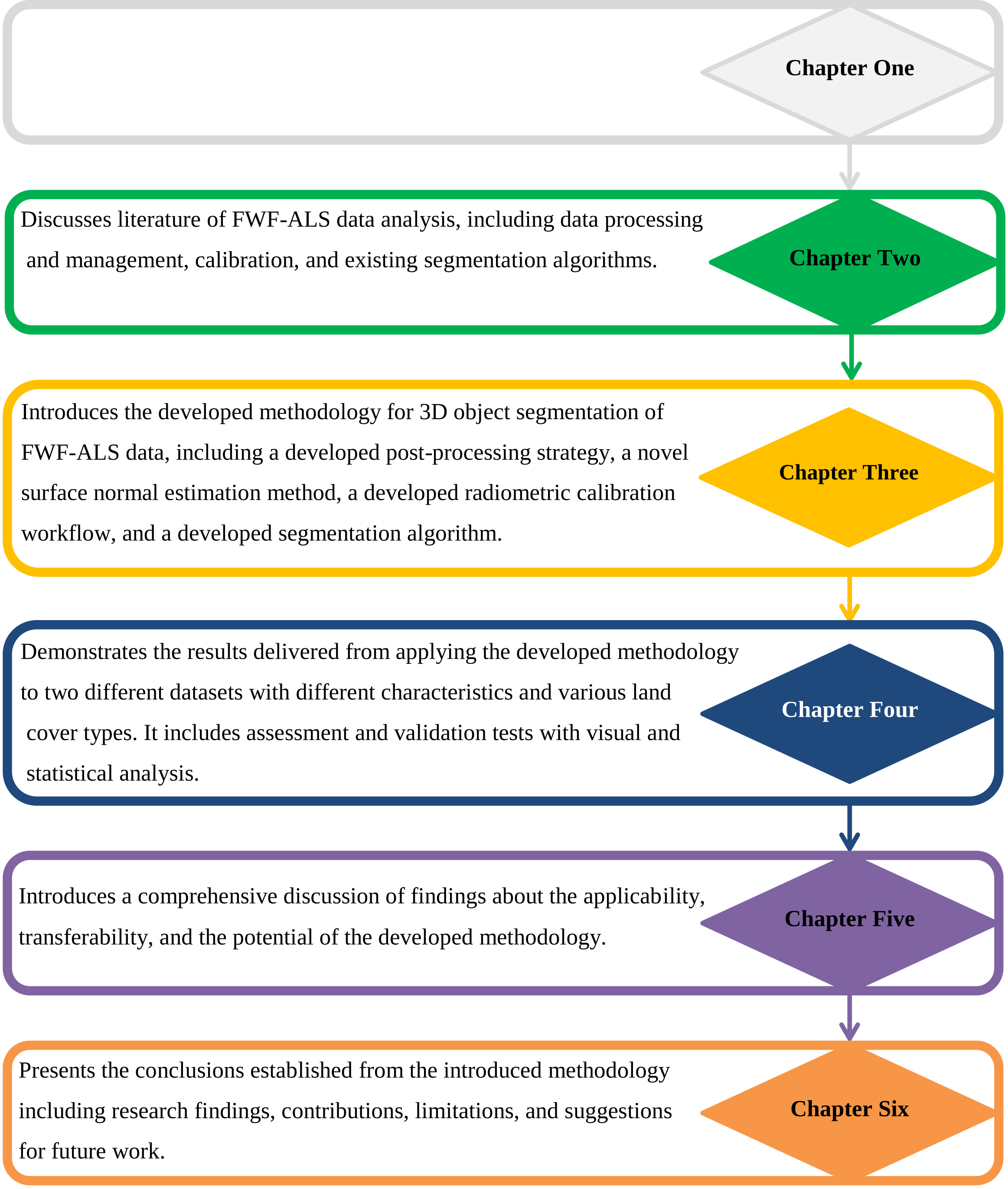

Chapter One

Chapter Two

Discusses literature of FWF-ALS data analysis, including data processing and management, calibration, and existing segmentation algorithms.

Chapter Three

Introduces the developed methodology for 3D object segmentation of FWF-ALS data, including a developed post-processing strategy, a novel surface normal estimation method, a developed radiometric calibration workflow, and a developed segmentation algorithm.

Chapter Four

Demonstrates the results delivered from applying the developed methodology to two different datasets with different characteristics and various land cover types. It includes assessment and validation tests with visual and statistical analysis.

Chapter Five

Introduces a comprehensive discussion of findings about the applicability, transferability, and the potential of the developed methodology.

Chapter Six

Presents the conclusions established from the introduced methodology including research findings, contributions, limitations, and suggestions for future work.

CHAPTER

2

LASER SCANNING DATA PROCESSING AND ANALYSIS

2.1 INTRODUCTION

Laser Scanning is a fully commercial technology, which has developed rapidly in photogrammetry and remote sensing community to remotely determine the geometry of the Earth’s surface in a rapid and accurate manner. (Shan and Toth, 2009). It has become an increasingly important data acquisition technique to produce quantitative 3D digital representation of the land cover features for different applications (Vosselman and Maas, 2010). Any application generally necessitates automatic processing, such as segmentation and clustering, of the massive data delivered from these systems for better object recognition and optimal end products (Lin, 2009; Shan and Toth, 2009). Segmentation is an essential process to identify surfaces (Awwad et al., 2010). Since surfaces are the basic units to define features, segmentation is required for many feature extraction applications (Sithole, 2005).

Laser scanning systems can capture geometric information of Earth surface features (Mallet et al., 2008; Vosselman and Maas, 2010). Filin (2002) found that geometric information such as the spatial point distribution and the point density cannot be considered as fixed for segmentation and clustering purposes. In order to overcome the unstructured nature of the point cloud to deliver accurate segmentation scenarios, most segmentation approaches are geometric-based (Filin and Pfeifer, 2006). However, laser scanning systems can also provide additional physical information about these features alongside their geometric information with FWF sensors.

FWF systems first emerged around twenty years ago and have become popular in the last five years (Mallet et al., 2011). FWF systems can be characterized from the well-known discrete-return systems by their capability to record the entire backscatter laser energy from the surface targets and also by providing additional physical information about these targets (e.g. echo width and amplitude, unlimited number of returns, etc.) (Lin and Mills, 2009b; Guo et al., 2011). Figure 2.1 shows the principles of both FWF and discrete ALS systems. The physical observables from FWF can provide additional information to segmentation and classification techniques (Mandlburger et al., 2010; Mucke et al., 2010a; Niemeyer et al., 2011). Nowadays the majority of the discrete systems can deliver intensity measurements for land features alongside the standard geometric information (Jutzi and Gross, 2010). However, both physical information from FWF and intensity records from discrete systems are not recommended to be directly exploited for accurate end products without pre-calibration (Lehner et al., 2011; Kaasalainen et al., 2011b). This is because the backscatter signal is affected by many variables during the travel between the sensor and the target that therefore need to be eliminated (Wagner, 2010; Jutzi and Gross, 2010; Roncat et al., 2011).

This chapter will discuss FWF-ALS analysis for 3D object segmentation applications. Firstly, the chapter will overview FWF post-processing techniques and available frameworks to process and handle the massive data volumes produced. Additionally, it will highlight approaches available to calibrate the physical information from FWF and their potential to enhance segmentation algorithms. This has reviewed through discussing variables affecting the received backscatter signal and available scenarios to overcome the effects of these variables such as the essential incidence angle effect. The chapter also provides a comprehensive review of the available geometric-based segmentation approaches, including a critical discussion of the merits and demerits of individual techniques.

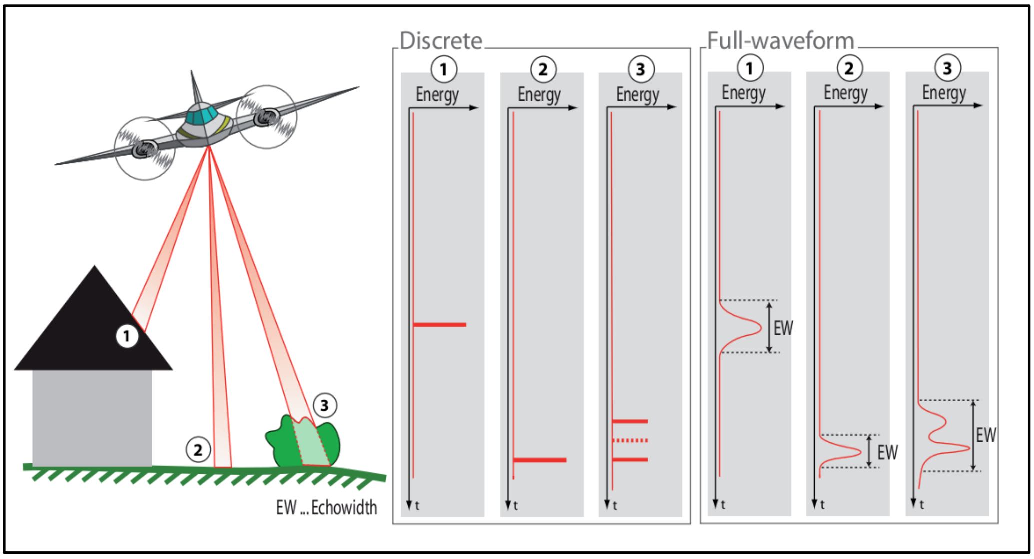

Figure 2.1. Principles of discrete and FWF ALS systems (Mandlburger et al., 2010).

2.2 FWF VS DISCRETE-RETURN ALS SYSTEMS

Latest generation commercial discrete ALS systems can deliver geospatial 3D point clouds to the end user usually with additional intensity values for individual echoes (Wagner et al., 2004). Despite the delivery of data with high point density and accuracy, the limitation of these systems is that it is not always possible to interpret these measurements for all targets (Mallet et al., 2008; Lin, 2009). This is particularly the case when multiple echoes are detected and the detection method implemented by the lidar operator is unknown, thus the accuracy of the generated echoes may be questionable (Wagner et al., 2007). Therefore the end user cannot estimate the errors resulting from the limitations in the pulse detection method adopted (Mallet and Bretar, 2009). Using inaccurate range determination measurements provided directly from discrete pulse operators can effectively reduce the accuracy of the end products and limit opportunity for further analysis (Ducic et al., 2006).

In contrast, FWF-ALS systems record the entire waveforms of the received pulses which provides the possibility to derive a more detailed description of the features' structure and provide more accurate range measurements (Briese et al., 2002; Nordin, 2006; Mallet and Bretar, 2009; Heinzel and Koch, 2010). The potential of FWF-ALS systems can be summarised as follows (Rieger et al., 2006):

- Can deliver high multi-target accuracy;
- Can deliver unlimited number of returns per emitted signal;
- Delivers information about surface roughness and slope;
- Records information about the received laser backscatter signal.

Using robust fitting functions to model FWF data, accurate range measurements can be delivered and more targets can be detected than those detected by discrete systems (Wagner et al., 2007; Chauve et al., 2007; Höfle and Hollaus, 2010). In a comparison with discrete systems, FWF can provide not only five returns per signal, but rather an almost unlimited number of returns which is likely to be the case with vegetation (Neuenschwander et al., 2009). Furthermore, the additional physical observables which FWF provides can deliver extra information of land cover features which the geometric information cannot deliver (Ullrich et al., 2008). For example, Doneus and Briese (2006) and later Lin and Mills (2009a) followed by Hollaus and Höfle (2010) found that FWF echo width is particularly sensitive to surface roughness and slope and thus can be used to deliver information on these aspects. In addition, both echo width and amplitude can deliver comprehensive information about the backscatter energy of the individual echoes (Briese et al., 2008; Abed et al., 2010; Lehner and Briese, 2010). Moreover, several studies have shown that using the additional physical information from FWF alongside the existing geometric information can effectively increase the reliability of the final products (Höfle et al., 2007; Lin and Mills, 2009b; Alexander et al., 2010; Mallet et al., 2011). However, all such information cannot be generated directly from FWF raw data as this is provided to the user in waveform profiles. Thus emerges a necessity for pulse detection analysis for better range accuracy (Jutzi and Stilla, 2005a; Wagner et al., 2007).

2.3 POST-PROCESSING OF SMALL-FOOTPRINT FWF-ALS DATA

To process laser scanner data for segmentation applications, several stages must be followed. These include pulse detection adoption, data calibration such as target orientation consideration, and segmentation algorithms implementation. This section is particularly discussing post-processing techniques and available pulse detection methods for FWF-ALS data.

Small-footprint topographic FWF-ALS systems firstly became commercially available in 2004 (Mallet and Bretar, 2009). These provide users with the advantage of using the small-footprint to assess the topographic surface in more detail using a small ground footprint size (Lin, 2009; Chehata et al., 2009). The associated waveforms need to be post-processed through signal analysis techniques in order to deliver detailed information about the geometric and physical properties of the backscattering objects (Jutzi and Stilla, 2006; Mallet et al., 2010).

It is evident from the signal analysis literature that pulse detection is considered to be a challenging task with respect to retrieving information in a geometric form (e.g. 3D point clouds) (Jutzi and Stilla, 2005a; Nordin, 2006; Mucke, 2008; Lin, 2009). Several methods have been developed to detect echoes from FWF signals. This includes threshold, constant fraction, peak, and centre of gravity (COG) detection methods (Lin, 2009). However, each method has its own weaknesses when applied to small-footprint FWF-ALS data, and may limit the final range accuracy (Jutzi and Stilla, 2005b; Lin, 2009). Therefore, for high accuracy range resolution, it is necessary to adopt more sophisticated pulse detection methods.

Gaussian decomposition is a popular pulse detection technique to model laser waveforms of approximate Gaussian distribution (Wagner et al., 2006; Jutzi and Stilla, 2006). It was found that the Gaussian function (Eqn. 2.1) can best describe, and therefore effectively model, the small-footprint FWF-ALS data from the Riegl LMS-Q560 system (Wagner et al., 2006; Jutzi and Stilla, 2006; Reitberger et al., 2008). Therefore, the Gaussian decomposition technique can be used fit the Gaussian function to the Riegl LMS-Q560 signals in order to detect all possible echoes within individual waveforms.

$$y = N_{level} + \sum_{i=1}^{n} A_i \, exp\left[-\left(\frac{x-x_i}{width_i}\right)^2\right] \qquad \textbf{Eqn. 2-1}$$

Where:

y is the quantized amplitude values

N_{level} is the noise level in the waveform signal

n is the number of Gaussians

A_i is the amplitude of the i^{th} Gaussian

x is the samples time values

x_i is the i^{th} Gaussian peak

$width_i$ is the pulse width of i^{th} Gaussian = $\sqrt{2} * 6_i$

6_i is the standard deviation of the i^{th} Gaussian

The Gaussian pulse detection approach presumes that the laser pulses are transmitted with a Gaussian-like distribution and thus the received signal can be treated as a sum of multiple Gaussian pulses (Wagner et al., 2006). It aims to detect multiple echoes from individual waveforms as an amplitude-against-time measure. As a result of fitting the waveforms to the Gaussian function, multiple echoes can be detected and geometric and physical information can be extracted for individual echoes (Figure 2.2). This method can deliver accurate range resolution and provide a reliable solution as compared with other available methods. Consequently, accurate geo-referenced 3D point clouds alongside echo width and amplitude measurements can be provided to end users for individual echoes in addition to the total number of detected returns (Wagner et al., 2007). However, the Gaussian decomposition method is considered to be problematic in the case of complex and weak waveform signals (Wagner et al., 2006; Lin et al., 2008).

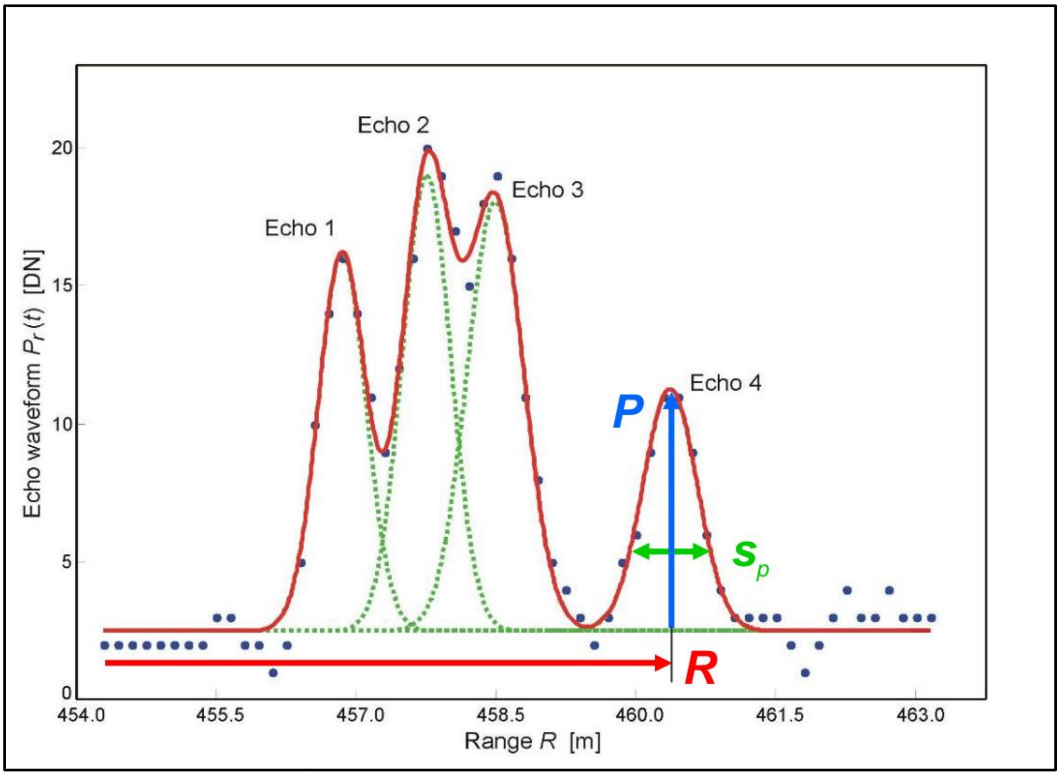

Figure 2.2. Fitting Gaussian function to detected FWF signal from the Riegl LMS-Q560: (Blue dots) recorded waveform signal; (Green dotted lines) fitted Gaussians per echo; (Red lines) sum of all Gaussian functions; (R) is the range to the sensor; (P) is the echo amplitude; (S_p) is the echo width (Mandlburger et al., 2007).

Motivated by overcoming the weaknesses in the available pulse detection methods, a Rigorous Gaussian pulse Detection (RGD) method was developed by Lin et al. (2010). This was motivated by the need to develop a sophisticated and reliable method, which could decompose complicated waveform signals. RGD was originally designed to improve range resolution and accuracy and overcome information loss due to limitations in range estimations from standard approaches (Lin et al., 2010). The RGD approach also provides a solution to tackle complex overlapping waveforms and difficulties in detecting weak signals (Lin, 2009). These two limitations are considered to be the main challenges faced by the standard pulse detection methods. RGD is an iterative technique based on Gaussian decomposition definition. It is implemented with rigorous initial values and applies a sophisticated iteration procedure (Lin, 2009). The method can detect overlapping signals in complex waveforms by analysing the second derivative of the Gaussian function. Figure 2.3 demonstrate the detection of visible and overlapping peaks with RGD from complex waveforms. However weak pulses are detected based on analysis of residuals derived from the least squares fitting procedure and the pulse width value delivered from individual echoes (Lin et al., 2010).

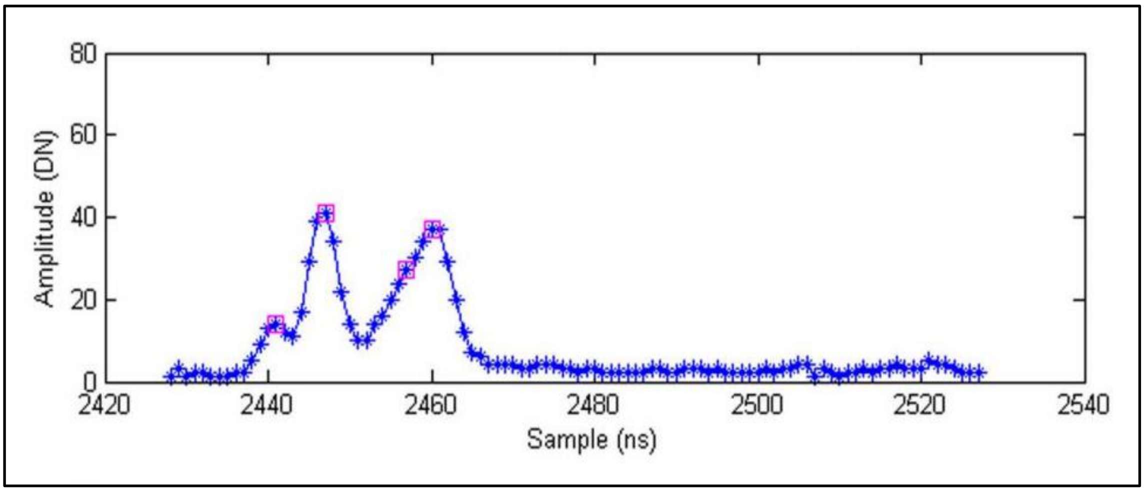

Figure 2.3. RGD method detecting overlapping peaks in a complex waveform from the Riegl LMS-Q560 system (Lin, 2009).

The method has proven to be capable of extracting a greater number of valid echoes from individual laser pulses than those extracted through standard available approaches (Lin et al., 2010). Figure 2.4 demonstrates the performance of the RGD method against two popular algorithms available from leading commercial software. It shows that RGD outperforms the comparator algorithms by delivering extra valid echoes for DTM and canopy modelling applications as highlighted by red dots. Both complex and weak waveform pulses can be resolved with the RGD approach, which was validated through comparison to ground truth data. Refer to Lin et al. (2010) for further details. Adding to this, the improved range resolution results from the RGD method shows particular potential when the vertical separation between targets is small (less than one pulse length). This can reduce the chance of overestimating and underestimating classification procedures and deliver more robust products such as DTM or canopy height models (CHM) (Lin and Mills, 2009b).

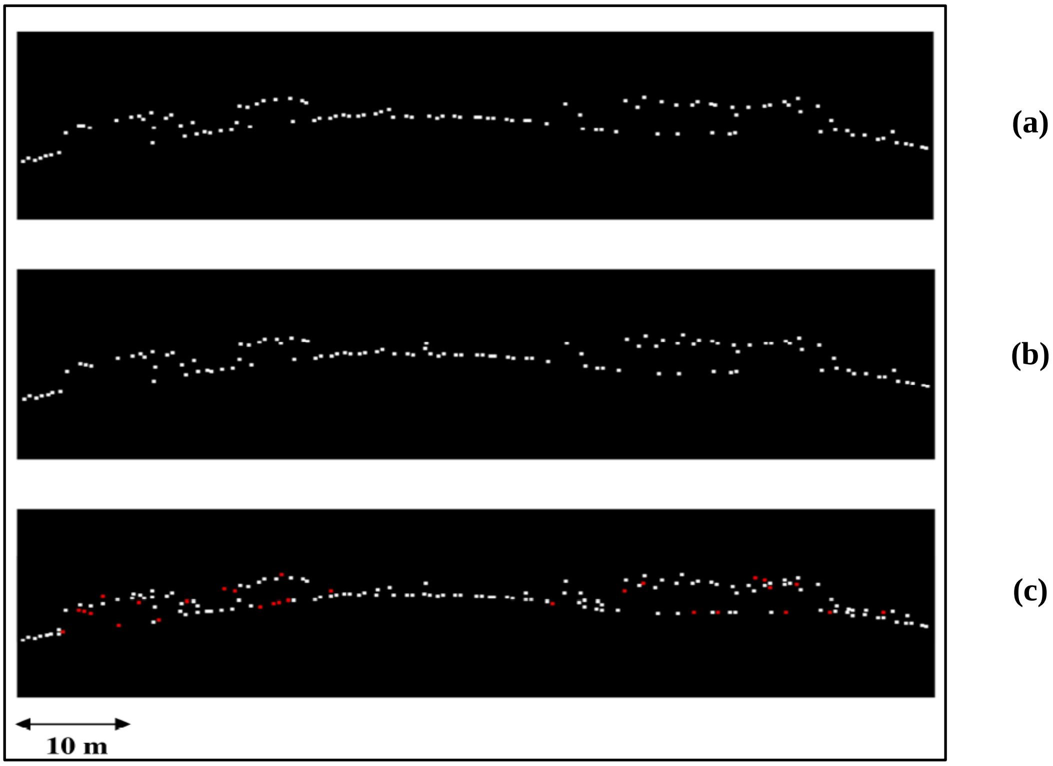

Figure 2.4. RGD pulse detection method vs. algorithms from commercial software assessing an 80m profile section in a vegetated area: **(a)** centre of gravity (COG) method **(b)** Gaussian pulse fitting (GPF) method **(c)** RGD method (Lin, 2009).

In addition to the 3D object location of multiple laser echoes, output from the RGD software, which was developed in-house at Newcastle University, delivers backscatter properties, including echo amplitude and width parameters. These parameters have demonstrated a capability to enhance available classification/filtering algorithms (Doneus and Briese, 2006; Lin and Mills, 2009a). However, managing and processing dense FWF datasets is a challenging task (Chauve et al., 2009; Guan and Wu, 2010). This is because of the dramatic increase in the data volume due to unlimited return echoes and delivers a serious problem in computing processing and storage capacity. However, organised management of computing resources can effectively improve computing usage, but more human effort is required (McGough et al., 2010). Therefore, there is a high demand for an effective processing tool or strategy to reduce processing time for laser scanning data.

2.4 HANDLING LASER SCANNING DATA

The efficient handling of laser scanning data has been an issue since FWF systems first emerged. The stored waveform profiles delivered from a FWF sensor after a flight campaign of 1.6 hours with a mean pulse repetition frequency (PRF) of 50 kHz can occupy about 140 GB (Chauve et al., 2009). Therefore, managing this huge amount of information for further processing is considered to be a challenging task in the context of large flight campaigns.

For efficient data management, effective resources should be utilised, where resources here refer to processor, memory, and disk space. There are three main types of resources available for processing approaches: single processor, symmetric multi-processor, and distributed processor. With the single processor, only one central processing unit (CPU) is used, with centralised memory and disk space. The symmetric processor (e.g. quad-core, dual-core) is efficient to use in some cases when the dataset is relatively large as the user can take advantage of the multi-core system design. The limitation of the symmetric processor is that all CPUs share the same memory, which can significantly slow the processing. However, the distributed processor system is considered to be the most efficient solution to run massive datasets, as all processors have their own dedicated memory but have to communicate with each other to access the centralised memory resource (e.g. network) (McGough, 2011). Figure 2.5 shows the three mentioned resource types used in data managing and processing.

Mandlburger et al. (2009) developed the software package, OPALS, as a complete set of processing tools for ALS datasets. This software included multiple modules to process and visualise ALS data, including FWF for various applications. It is provided in Shell script for Linux users, patch for Windows, and also in Python code (Mandlburger et al., 2010). As the software modules are originally designed to run under a Linux environment, no graphical user interface (GUI) is available. The software can be downloaded from OPALS (2009). However, the software is originally designed for use with both single and symmetric processor types.

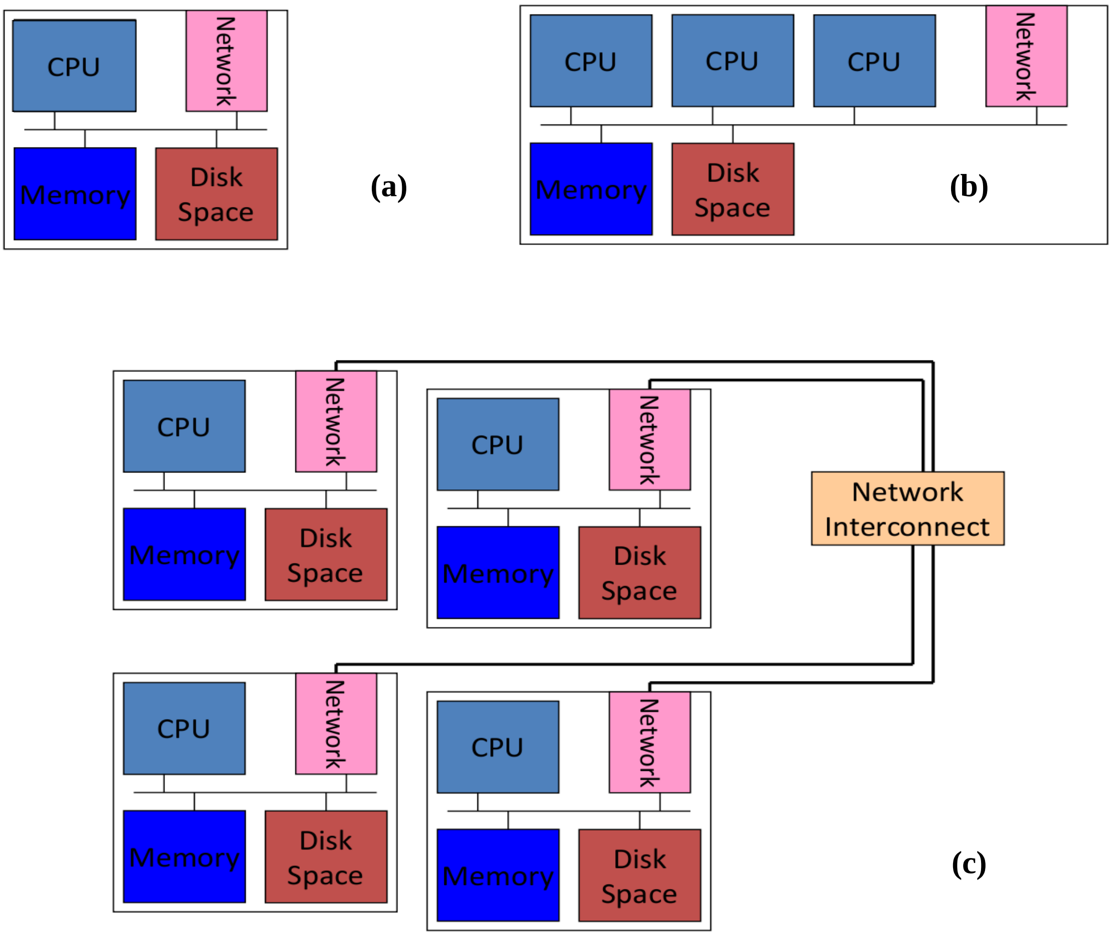

Figure 2.5. Resource types used in data management and processing: **(a)** single processor **(b)** symmetric multi-processor **(c)** distributed processor (McGough, 2011).

Chauve et al. (2009) introduced a toolkit called FullAnalyze to visualise and process laser scanning datasets, including FWF, as a 1D signal or in 3D point cloud format. This software is also applicable for either single or symmetric processor types and it was released in October 2009 as an open source software (FullAnalyze, 2009). The software runs under a Linux environment, and requires a virtual Linux environment to be installed on the machine if the user decides to operate under Windows (FullAnalyze, 2009). Further, all available commercial software designed for laser scanning data management and processing, such as TerraScan from Terrasolid (Terrasolid, 2008) or RiAnalyze from Riegl (Riegl, 2008), are designed to run under high specification single or symmetric processors.

On the other hand, Guan and Wu (2010) demonstrate the potential of using a symmetrical (multi-core) processor to manage laser scanning datasets and improve performance against the single processor scenario. They processed raw laser scanning data by partitioning these data into multiple blocks, which have been interpolated individually and finally merged into one integrated Digital Elevation Model (DEM). Their approach achieved a powerful increase in speed of performance, and effective reduction in the overall processing time. However, the proposed technique is not the optimal solution for massive datasets.

The most efficient processor system which is extremely powerful for handling massive datasets is the distributed system (Raman et al., 1998). The key leveraging in the distributive resources is its compatibility to run independent parallel jobs on different physical computers and later integrate these jobs to deliver one combined solution. It is best suited to manage multiple independent processing operations where individual tasks are highly independent and do not require input from other operations. In this context, this mechanism can therefore efficiently meet the requirements for laser scanning data processing. The most powerful processing technique which can efficiently manage the distributed processor system of large-scale resource sharing, is grid computing mechanism (Dai et al., 2002; McGough et al., 2010). Grid computing is a technique of combining multi-computer resources to achieve one single goal (Raman et al., 1998). It provides consistent, independent and flexible access to intensive computational capabilities in the presence of network connection to maintain the necessary resources (Dong and Akl, 2006). The ideal solution to manage, process, visualises, and also monitor powerful distributed jobs of massive datasets is through Condor. Condor is a well-known computing project which provides resource optimisation and support for high- throughput computing techniques including grid computing on large-scale distributed computing resources (Condor, 1988). It can run a large number of jobs concurrently and provide high quality service with a high network usage (Litzkow et al., 1988). Submitting jobs through Condor can be designed as illustrated in Figure 2.6. The process starts by designing a robust code that solves the current problem and ensures that the code is well designed to run in the Condor environment before submission. In certain cases, a compilation is needed against middleware on the Condor server, which can be managed through a third-party tool. Following a well-structured submission plan, Condor can deploy the independent jobs to the computing resources within the network. So far Condor has proven to be extremely effective in improving the productivity of massive datasets (Dean and Ghemawat, 2008; Thain et al., 2005) and significantly reducing the time needed to generate the results (Abed and McGough, 2010), which is an important factor in the case of laser scanning datasets.

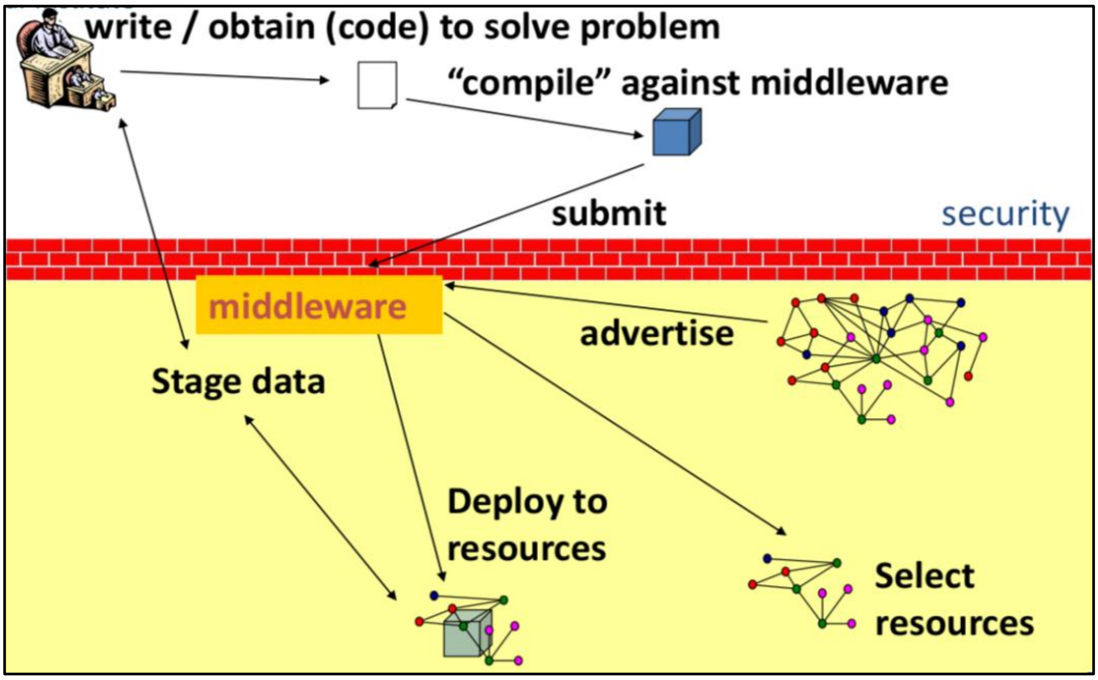

Figure 2.6. Principles of the Condor project (McGough, 2011).

2.5 CALIBRATION OF LASER SCANNING DATA

FWF laser scanning systems can better define land cover features by delivering both geometric and the physical characteristics of the backscattered energy by means of 3D point cloud and physical information for individual echoes. For further analysis it is necessary to calibrate this information whether from FWF or from traditional discrete systems to increase the benefits of the collected positional and physical information (Wang and Lu, 2009; Habib et al., 2011; Anttila et al., 2011). Considering scanning geometry and terrain properties is essential for improving the quality of ALS geometric data (Maas, 2002; Kager, 2004; Filin, 2005; Pfeifer et al., 2005; Schaer et al., 2007; Lee et al., 2007; Habib et al., 2008; Ressl et al., 2008). However, the geometric calibration of ALS data is beyond the focus of this research as it has been widely addressed in the literature. Consequently, calibrating the backscatter physical energy to enable the full utilisation of the FWF information is the overarching focus in this research.

The physical information that laser scanning data provides is affected by many variables during the travel between the sensor and the target. These include sensor properties, atmospheric conditions, incidence angle and other target characteristics effects (Luzum et al., 2004; Höfle and Pfeifer, 2007; Abed et al., 2012; Shaker et al., 2011). A robust radiometric calibration strategy must be capable of eliminating all aforementioned effects and delivering more reliable physical information for land cover features (Wagner et al., 2008b; Qin et al., 2010). Only a limited numbers of studies that deal with this important topic have contributed to the literature so far. However, more studies can be expected in near future that fully utilise these information in developing end products, especially as FWF systems mature.

2.5.1 Theoretical Background

The measurement principles of ALS systems were first expressed through the principles of radar systems (Wagner, 2005). Due to the similarity between ALS and radar systems, scientists tend to use the radar equation (Eqn. 2-2) to describe all the parameters affecting the received laser power P_r (Steinvall, 2000; Briese et al., 2008; Wagner, 2010).

$$P_r = \frac{P_t D_r^2}{4\pi R^4 \beta_t^2} \cdot \sigma \cdot \eta_{sys} \cdot \eta_{atm} \qquad \textbf{Eqn. 2-2}$$

Where:

P_t is the transmitted power

Dr is the diameter of the receiver aperture

R is the range between the sensor and the target

β_t is the laser beam divergence

σ is the backscatter cross-section

η_{sys} is the system transmission factor

η_{atm} is the atmospheric transmission factor

The laser backscatter cross-section σ is a measure of the directional scattering power which encompasses all target characteristics (Eqn. 2-3) including scattering direction, reflectivity and area of illumination (Jelalian, 1992; Steinvall, 2000; Pfeifer et al., 2008; Wagner, 2010).

$$\sigma = \frac{4\pi}{\Omega} \rho A_i \qquad \textbf{Eqn. 2-3}$$

Where:

Ω is the scattering solid angle

ρ is the surface reflectivity

A_i is the size of the area illuminated by the laser beam

Note that A_i is defined in literature as the target area highlighted in green in Figure 2.7, which was first defined by Jelalian (1992). For fast derivation of the backscatter cross-section parameter, A_i can be replaced by A_{lf} (highlighted in yellow in Figure 2.7) to avoid the additional efforts of estimating the local incidence angle (α), as it has been assumed in some literature (Wagner, 2010), however this is not the case herein.

The reflection direction is generated from the angle between the laser beam and the area enclosing the target by means of the so-called incidence reflection angle. The incidence angle is defined as the angle between the surface normal and the illumination direction, which alternatively defines the target orientation. However, the reflectance of individual echoes is just a portion of the entire reflected incidence radiation from the total target area enclosed within the footprint which could be termed in FWF as the convoluted backscatter signal (Wang et al., 2009). Therefore the magnitude and the nature of the backscattered signal is dependent on the target properties (Wagner et al., 2004).

In FWF-ALS systems, and when using the Gaussian function to retrieve the laser signal, P_r can be represented as a the product of echo amplitude $\hat{P}_i$ and echo width $s_{p,i}$ and thus can be replaced by $\hat{P}_i s_{p,i}$ for simplification (Wagner et al., 2006; Höfle et al., 2008). Further, the target is considered to be extended within the footprint area, having a solid angle Ω of π steradians with Lambertian scattering characteristics.

To simplify Eqn. 2-2, all unknown parameters assumed to be constant in one scan campaign can be combined to one single constant called the calibration constant, C_{cal} (Wagner et al., 2006; Briese et al., 2008; Lehner and Briese, 2010; Wagner, 2010). As a result the calibration equation which can deliver the σ value for individual echoes in ALS systems can be extracted as follows:

$$\sigma = \frac{C_{cal} 4\pi R^4 \hat{P}_i s_{p,i}}{\eta_{atm}} \qquad \textbf{Eqn. 2-4}$$

Consequently, the calibration constant will be:

$$C_{cal} = \frac{\beta_t^2}{P_t D_r^2 \eta_{sys}} \qquad \textbf{Eqn. 2-5}$$

The atmospheric transmittance η_{atm} in Eqn. 2-4 can be delivered by modelling the metrological data on the day of the scan using a suitable atmospheric data modeller, such as MODTRAN (Chen et al., 2007; Asmat et al., 2008). However, to estimate the calibration constant for a certain ALS campaign, it is necessary to have a reference target with a known reflectivity value to deliver σ (Eqn. 2-3). A_i should also be estimated, where A_i represents the area of the target illuminated by the laser beam. This area can be estimated from the range *R*, the beam divergence $\beta_{t,}$ and angle of incidence α, refer to Figure 2.7. For simplification, and to avoid additional efforts to estimate the incidence angle for certain applications, the laser footprint area at the scattering object (A_{lf}) can replace the value of A_i as follows (Lutz et al., 2003):

$$A_i = \frac{R^2 \beta_t^2 \pi}{4 cos\alpha_i} \qquad \textbf{Eqn. 2-6}$$

$$A_{lf} = \frac{\pi R^2 \beta_t^2}{4} \qquad \textbf{Eqn. 2-7}$$

Thus, $A_i = \frac{A_{lf}}{cos\alpha_i}$ **Eqn. 2-8**

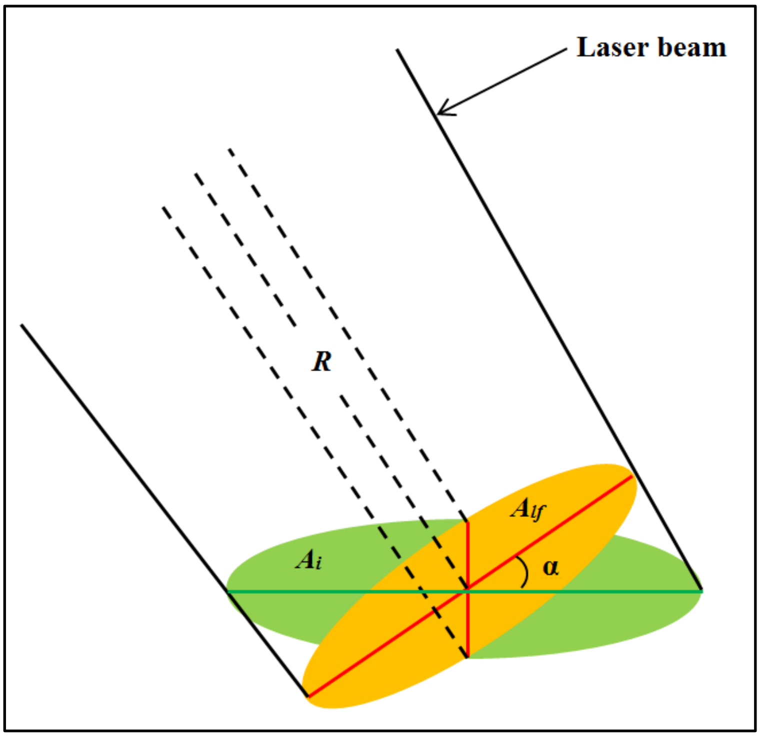

Figure 2.7. Principles of laser footprint area in an ALS system (Lehner and Briese, 2010).

Once the calibration constant has been delivered, the backscatter cross-section parameter can be estimated for individual laser echoes for the entire dataset (Lehner et al., 2011). However, Wagner et al. (2008a) introduced another backscatter parameter, the backscatter coefficient (γ), which is more stable than σ as the latter tends to vary significantly with different system and target characteristics. When the incidence angle of the laser beam is changed, then the illumination area is also changed and therefore γ can be called the normalised backscatter cross-section with respect to the area of the incoming beam and can be derived as follows:

$$\gamma = \frac{\sigma}{A_i cos\alpha} \qquad \textbf{Eqn. 2-9}$$

However, neither σ nor γ are free from the incidence angle effect (Mandlburger et al., 2010; Wagner, 2010). Therefore, both parameters should be normalised with respect to the incidence angle by dividing each parameter by the cosine of the incidence angle within the Lambertian scatterer assumption as detailed in Eqn. 2-10 and 2-11 respectively (Lehner and Briese, 2010). This will deliver two more backscatter parameters for individual echoes of the entire dataset in addition to σ and γ.

$$\sigma_\alpha = \frac{\sigma}{cos\alpha} \qquad \textbf{Eqn. 2-10}$$

$$\gamma_\alpha = \frac{\gamma}{cos\alpha} \qquad \textbf{Eqn. 2-11}$$

The quantity sought from the radiometric calibration process in FWF systems is the calibration constant. All the available mathematical models propose the estimation of one constant for the entire scan campaign in this respect. However, Roncat et al. (2011) introduced a study to quantify the uncertainty of the calibration constant which can be acquired due to the variations in the emitted energy. In the derivation process of C_{cal}, the parameters of the transmitted energy, which are considered as unknowns, are assumed to be constant during one scan campaign. However, Bretar et al. (2009) claimed that the transmitted laser energy cannot be assumed to be “constant enough” for proper radiometric calibration purposes. Therefore, it is essential to check the behaviour of the transmitted energy in individual flightlines to quantify the energy variations through the adoption of a calibration constant per flightline instead of considering one constant for the entire campaign.

2.5.2 Incidence Angle Estimation

2.5.2.1 Overview

In order to calibrate the physical information of FWF-ALS data, the incidence angle effect of individual echoes needs to be firstly considered (Briese et al., 2008; Jutzi and Gross, 2010; Lehner et al., 2011; Roncat et al., 2011). The incidence angle of the laser beam plays a crucial role in object recognition (Phong, 1975), as it varies over differing land cover targets according to the different flying directions and positions of multiple flightlines (Lutz et al., 2003; Kukko et al., 2008). The Earth's surface comprises various land cover types including natural and man-made features, and the reflected energy from these surfaces is highly influenced by the incidence angle of the laser beam (Ruiz-Cortes, 2002). Figure 2.8 shows principles of the incidence angle and highlights the difference between incidence and scan angles in ALS. In the case of flat surfaces, the scan angle and the incidence angle are coincident.

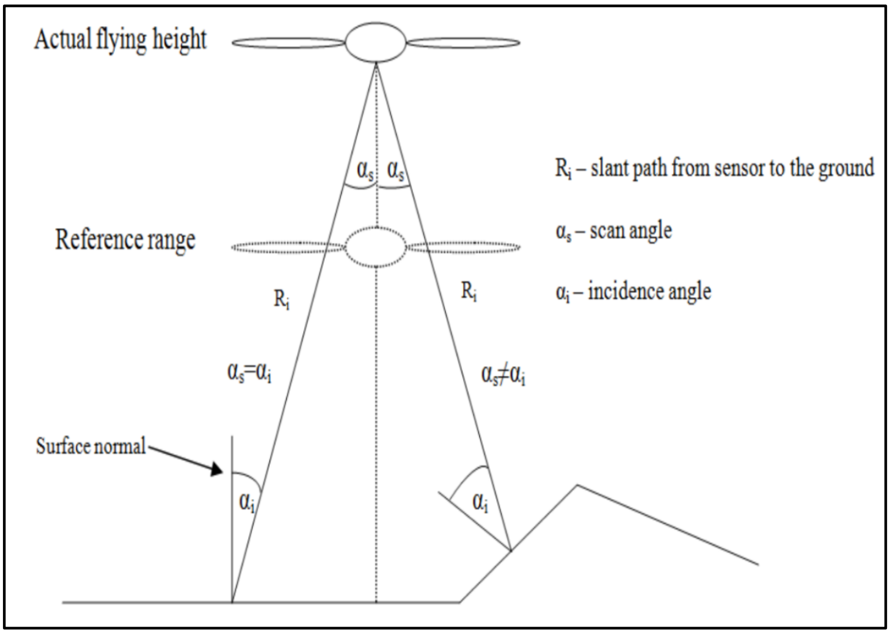

Figure 2.8. Differences between incidence and scan angles (Vain et al., 2009).

The incidence angle is defined as the angle between the surface normal and the illumination direction, which can be estimated for individual echoes from the 3D laser point coordinates and the scanner position. This effect can significantly increase the reflected echo amplitude values at higher incidence angles over different target materials and from multiple flightlines (Jutzi and Gross, 2010; Shaker et al., 2011). This is mainly because the variation in the incidence angle (object orientation) affects the size of the laser footprint which can significantly influence the amount of the reflected energy (Wagner, 2010). However, if object position and orientation within a certain surface can be determined, it should be possible to eliminate this effect and thus deliver more reliable normalised signals (Jutzi and Gross, 2010; Kukko et al., 2008; Jutzi et al., 2002).

Kukko et al. (2008) investigated the dependency of the laser intensity signal on the incidence angle by means of target brightness on TLS data and later compared the results with ALS data. The study was implemented over artificial and natural targets using different incidence angle settings. The incidence angle effect was found to be evident on all targets and significant for incidence angles >20°. Kaasalainen et al. (2011a) further analyse this effect on TLS intensity data and deliver similar outcomes from multiple TLS instruments. Jutzi et al. (2009) and later Jutzi and Gross (2010) introduced a study that demonstrated the role of the incidence angle effect on the received ALS intensity signals. This is illustrated through Figure 2.9 which shows the intensity image of a selected region delivered from four different flightlines. Although the highlighted area represents planes from the same materials, the scan direction effectively impacts the amount of the reflected energy, causing clear signal discrepancies between overlapping flightlines. This highlights the importance of intensity data normalisation with respect to incidence angle for a comprehensive radiometric correction.

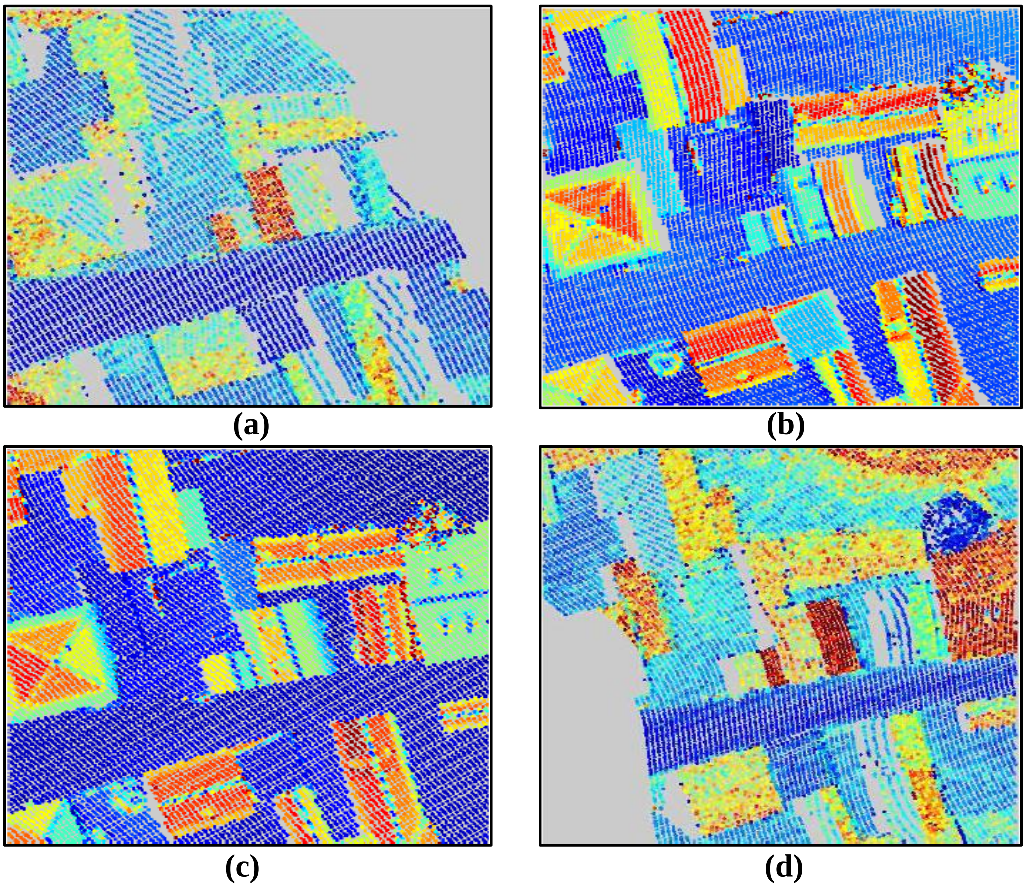
(a) (b)
(c) (d)

Figure 2.9. Influence of the incidence angle on ALS intensity signals: **(a)**, **(b)**, **(c)**, and **(d)** represent the intensity image of a selected region from four different overlapping flightlines (Jutzi et al., 2009).

Further, investigations by Kaasalainen et al. (2009c) showed that Lambert’s Cosine Law (Swinehart, 1962) works reasonably well in normalising laser scanning intensity data for most targets across a broad range of incidence angles. This was demonstrated to be valid even in cases when the scattering surface was not considered to have Lambertian characteristics. Moreover, Chelle (2006) showed that Lambert’s Cosine Law can deliver a satisfactory estimation of light absorption modelling for rough surfaces such as dense crop canopies in both active and near infrared spectral domains. This was also confirmed by Jutzi and Gross (2010) in demonstrating that echo amplitude variations caused by incidence angle and range effects can be eliminated by using the standard Lambertian reflection model. It was shown that considerable improvements in the normalized intensity signals can be delivered by adopting this model. This conclusion was based on an extended study by Jutzi and Gross (2010) to investigate the optimal surface reflection model which should be used to model laser backscatter characteristics and overcome variables affecting echo amplitude signals including the angle of incidence effect. Three different diffuse models were tested, including Lambertian, the extended Lambertian, and the Phong reflection model (refer to Jutzi and Gross (2010) for further details).

2.5.2.2 Normal Vector Estimations

Recent studies have shown that the laser echo amplitude of a target is strongly correlated to the incidence angle of the laser beam (Kukko et al., 2008; Jutzi and Gross, 2010; Kaasalainen et al., 2009c; Kaasalainen et al., 2009b; Abed et al., 2012). Other studies have discussed the incidence angle impact on the radiometric calibration techniques and the laser backscatter signal (Kaasalainen et al., 2007; Kaasalainen et al., 2008; Vain et al., 2009; Lehner and Briese, 2010; Abed et al., 2011; Shaker et al., 2011). Because the incidence angle is a function of the surface normal vector associated with the point, robust normal vector estimation is needed towards an optimal radiometric calibration.

In order to deliver the normal vector for individual points, surfaces enclosing these points should firstly be defined. Any local surface geometry cannot be generated from irregular 3D points without considering the distribution of these points following a certain neighbourhood assumption. Several neighbourhood assumptions which can deliver normal vector estimations and represent feature surfaces have been previously presented. Filin and Pfeifer (2005) have fully described and discussed available neighbourhood systems applied to ALS data point clouds such as triangulation (Filin, 2002; Hofmann, 2004), rasterisation (Wehr and Lohr, 1999), and rectangular cells adaption (Kraus and Pfeifer, 1998). All these approaches are traces of 2D concepts, which have been adapted to 3D. Laser scanning data is a 3D representation of a variety of surface features which could be massively complicated and cannot be handled with 2D concepts (Vosselman and Maas, 2010). Moreover, the irregular distribution of the laser scanning data makes feature extraction highly challenging due to the huge amount of information which the data comprise (Shan and Toth, 2009; Yokoyama et al., 2011). Adding to this, data density can vary substantially among different datasets and is not accounted for within these neighbourhood definitions (Filin and Pfeifer, 2005; Abed et al., 2012; Demantke et al., 2011). For these reasons, the previously mentioned approaches fail to deliver adequate neighbourhood definitions as necessary to represent the variety of the surface features. Note that these approaches are based purely on geometric relationships amongst points in 3D space.

One of the fundamental requirements for a large variety of geomatic applications in discrete 3D space data systems is to find the optimal neighbourhood relationships. The neighbourhood retrieval of the 3D laser points is usually defined by the *k*-nearest means inside a small environment centred on the point of interest (Vosselman and Maas, 2010). There are two primarily neighbourhood environments which better define the unstructured characteristics of the 3D laser point clouds. These are the spherical and the cylinder neighbourhood definitions (Lee and Schenk, 2001; Kim et al., 2007; Demantke et al., 2011). Figure 2.10 illustrates these two definition concepts.

Lee and Schenk (2002) developed a robust perceptual organisation approach for irregular 3D point clouds. This is based on the adoption of a spherical 3D volumetric concept to define the relationship among the unstructured 3D points. This defines a neighbourhood system within a certain radial distance from each point in question (refer to Figure 2.10-a). All points within the system are considered to determine the orientation estimation of the defined volumetric system. The spherical definition was used to structure the irregular point clouds into perceptual surfaces and then clustering these surfaces points into meaningful classes (Lee and Schenk, 2002). The method was visually inspected using a real ALS data to test the quality of the structured output points, which can serve as a valuable source for subsequent object recognition processes.

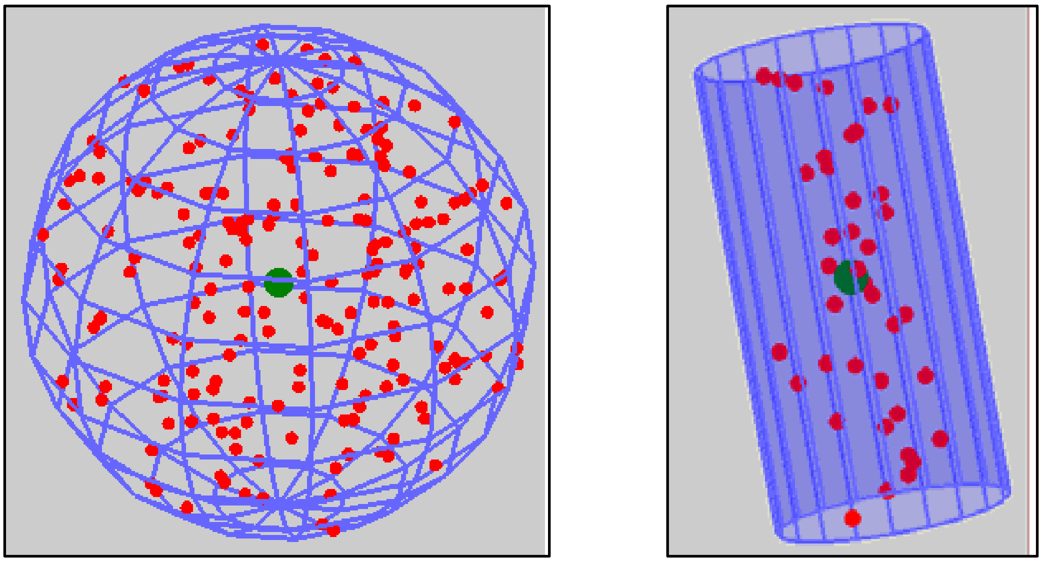

(a) (b)

Figure 2.10. Volumetric definition of neighbourhood approaches: **(a)** spherical definition **(b)** cylindrical definition (Gross and Thoennessen, 2006).

Subsequently, Filin and Pfeifer (2005) introduced a cylindrical-based neighbourhood definition, termed the slope adaptive method. The method is based on defining a cylinder volume for an individual point of interest from the *k*-nearest neighbours' points, defined by a certain radius and height (Figure 2.10-b). As already discussed, variable data density due to survey characteristics is a crucial aspect. Therefore, the parameters of the defined volume are specified based on data characteristics. This method was able to deliver more reliable normal vector estimations over planar surfaces than the commonly applied triangulation method. However, the cylinder approach was originally designed for simple structure features rather than natural or complicated surface structures with minor details. Furthermore, the investigations of Filin and Pfeifer (2005) revealed that a spherical-based neighbourhood may be more feasible for dense datasets. Although the cylindrical method is adaptive and suited particularly for urban environments, the method ignores the assumption of including non-homogeneous points in individual neighbourhood definitions which is likely to happen in dense datasets.

The spherical-based neighbourhood definition is more generic and appropriate to adopt in case of dense discrete data. However, the question which still arises is how to make sure that the points within individual volumetric neighbourhood definitions belong to the same surface. This concept was discussed by West et al. (2004) and addressed by developing a solution using the geometric aspects of the problem without integrating any other information such as intensity. The algorithm relies on the eigenvalues delivered from the covariance matrix generated from the 3D spherical volumetric definition of individual points using a constant radius value. These eigenvalues have been used to define the structure tensor features for each defined spherical definition to facilitate classification analysis and target detection in 3D space. Although the method can effectively differentiate between different features structures, it is hard to deliver accurate orientation estimations for individual features. Following this, Demantke et al. (2011) introduced a multi-scale neighbourhood definition based on the spherical assumption. This approach estimated the 3D geometry of the ground features (linear, planar, or volumetric) from ALS, TLS, and MLS data points to deliver knowledge about the optimal neighbourhood radius to adopt in the spherical definition. The method relies on the matrix of covariance delivered for each point from West et al. (2004) assumption. However, the method considers purely the geometric location of these points and discards the noisy functionality of laser scanning data which can effectively bias the dimensionality labelling.

Following definition of the neighbourhood, there are three types of representation methods which can be adopted to deliver information about surfaces such as the normal vector. The first method is to characterise a mathematical formula that accurately represents data properties and feature characteristics (Filin and Pfeifer, 2005; Kim et al., 2007; Abed et al., 2012). Although it is challenging to deliver a generic model that fits with all surface features, it is possible to identify common properties that meet with the endeavour goal of the study. The second option is to interpolate the data to deliver the required information about the extracted surface (Habib et al., 2011; Yan et al., 2011). The third option is to approximate the surface in a least squares sense by fitting the discrete points to an assumed standard surface (Meek and Walton, 2000; Ou Yang and Feng, 2005; Duan et al., 2011). Although the second and the third methods are appropriate to use with noisy data such as laser scanning, they approximate the data to define the required surface, which may not necessarily reflect the actual object properties.

The majority of the existing normal vector estimation methods are based upon the spherical approach (Weingarten et al., 2004; Gross and Thoennessen, 2006; Vosselman and Maas, 2010; Gross and Thoennessen, 2006Jutzi and Gross, 2010;; Demantke et al., 2011; El-Halawany et al., 2011). Hoppe et al. (1992) described an algorithm to reconstruct 3D objects from irregular laser point clouds by trying to fit these points to an unknown surface and minimise differences between both in a least squares sense. The spherical definition was used to define the neighbourhood for individual points by means of Euclidean distances and the normal vector presents a surface criterion for each point. The introduced method associates an oriented plane (tangent plane) to individual points and attempts to minimise the difference in the distance between the associated surface point with the tangent plane, and the centroid point from the defined neighbourhood volume. Later Ou Yang and Feng (2005) developed a new method to estimate the normal vector by fitting a directional tangent vector to the data using a Voronoi mesh. The normal vector is delivered by minimising the variance between the normal vector and the associated directional tangent vector by means of the vector dot product. Castillo and Zhao (2009) developed the method originally introduced by Hoppe et al. (1992) to deliver robust results on surfaces edges by weighting the solution with the orthogonality mismatch residuals. Noise in laser scanning point clouds is a significant source of error when determining the approximate normal vector. Therefore, Castillo and Zhao (2009) incorporate data denoising constraints to the normal estimation to make the solution more appropriate for noisy data. The segmentation-based normal vector process using the developed approach delivered improved results.

The normal vector can be established from a 3D spherical volume for individual point cloud according to the Euclidian distance between points in 3D space following a 3D moment invariant method described by Hu (1962), developed later by Teague (1980) in 2D, and later by Reeves et al. (1988) in 3D. The spherical volume is defined for each point cloud with a radius R and all of the points within this volume are assigned to the volume and analysed through the 3D moments as described by Maas and Vosselman (1999) and improved later by Gross and Thoennessen (2006). This definition can deliver the centre of gravity and the matrix of covariance, which defines the dispersion between points in the system. This leads to Eigenvalue analysis of the point clouds within the defined system and thus delivers a normal vector estimation which allows for optimal object recognition (Kawashima et al., 2001). The moments (m_{ijk}) are defined as in Eqn. 2.12 which describes the assumption in the discrete case (e.g. laser point clouds).

$$m_{ijk} = \int_{v=v_1}^{v_n} x_v^i \; y_v^j \; z_v^k \quad f(x,y,z)\, dv \qquad \ldots\ldots\ldots$$

$$= \sum_{v=1}^{v=n} x_v^i \; y_v^j \; z_v^k \quad f(x,y,z)\, dv \qquad \textbf{Eqn. 2-12}$$

Where:

$i, j, k \in n$ and n is the number of neighbourhood points

$i + j + k$ is the order of the moment

v is the individual point

$f(x,y,z)$ is the weighting function

There are no restrictions regarding the moment order to select, as the moment invariant is theoretically possible to be derived for any order (Mangin et al., 2003). On the other hand, the weighting function can be considered as constant for all points assigned to the system. However, where non-homogeneous materials are included within the defined system, it is recommended to assign a certain measure to individual points to express the non-homogeneity such as the intensity signal (Gross and Thoennessen, 2006). In this aspect, Jutzi et al. (2005) presented a scheme to extract man-made features from laser scanning data by considering the intensity value for individual echoes. Their investigations showed accuracy improvements of a factor of at least ten when identifying feature edges using a sub-pixel edge localisation algorithm. These outcomes can lead to more stable segmentation results, refer to Jutzi et al. (2005) for further details. Motivated by these findings, Gross and Thoennessen (2006), Gross et al. (2008), Jutzi et al. (2009), Jutzi and Gross (2010), and Abed et al. (2012) showed improvements in the results of the final products with the adoption of intensity values as a weighting function in the moment definition.

Following the moment definition, the centre of gravity of the estimated volumetric definition can be estimated as follows:

$$\bar{x} = \frac{m_{100}}{m_{000}}, \qquad \bar{y} = \frac{m_{010}}{m_{000}}, \qquad \bar{z} = \frac{m_{001}}{m_{000}} \qquad \textbf{Eqn. 2-13}$$

Thus, the centralised moments are defined as in Eqn. 2-14 with the dependency on all points enclosed within the spherical volume and selected within the defined radius *R*.

$$\bar{m}_{ijk}\left(x_a, y_{a,} z_a\right) = \sum_{v=1}^{v=n} (x_v - \bar{x})^i (y_v - \bar{y})^j (z_v - \bar{z})^k \quad f(x_v, y_v, z_v)\Delta v \qquad \textbf{Eqn. 2-14}$$

Where *a* is the point of interest.

Due to the moments' dependency on all points inside the sphere with a selected radius *R*, the normalised moments will be as follows:

$$\tilde{m}_{ijk} = \frac{\bar{m}_{ijk}}{R^{i+j+k}\bar{m}_{000}} = \frac{\sum_{v=1}^{v=n} (x_v - \bar{x})^i (y_v - \bar{y})^j (z_v - \bar{z})^k f(x_v, y_v, z_v)}{R^{i+j+k} \sum_{v=1}^{v=n} f(x_v, y_v, z_v)} \qquad \textbf{Eqn. 2-15}$$

For each point of the dataset, the covariance matrix (*M*) can be delivered as illustrated in Eqn. 2-16. The Eigenvector of the smallest Eigenvalue represents the normal vector of the centroid point and can be considered to be the normal of the point of interest (*a*).

$$M = \begin{pmatrix} \tilde{m}_{200} & \tilde{m}_{110} & \tilde{m}_{101} \\ \tilde{m}_{110} & \tilde{m}_{020} & \tilde{m}_{011} \\ \tilde{m}_{101} & \tilde{m}_{011} & \tilde{m}_{002} \end{pmatrix} \qquad \textbf{Eqn. 2-16}$$

Thus, it is more preferable to adopt the spherical neighbourhood definition in dense dataset for optimal normal vector estimation to avoid discarding target details. This is a non-linear least squares case, which can be solved by adopting the moment invariant definition as stated above. However, data characteristics (e.g. density and accuracy) should be considered for reliable outcomes over different land cover features.

2.5.2.3 Point Cloud Data Management

Selecting the optimal neighbourhood definition is a crucial and challenging mission for several applications in 3D space such as for delivering the local surface normal which is essential for angle of incidence estimations (Demantke et al., 2011). The 3D neighbourhood allocation of lidar point clouds is usually defined by the *k*-nearest neighbours algorithm (Hoppe et al., 1992; Hastie and Tibshirani, 1996). Based on this algorithm either the vertical or the Euclidean distance is estimated between the point of interest and its *k*-neighbourhood points in order to define the 3D volume environment for normal vector estimation. However, direct use of the unstructured point clouds is not recommended as it cannot provide an explicit representation of the data distribution (Vosselman and Maas, 2010; Lari et al., 2011). Moreover, using the data without prior organisation such as spatial indexing can render the computational aspects inefficient and time consuming (Shen et al., 2011). Therefore, it is important to structure the irregular data to define the relationship between neighbourhood points in the 3D space for further computation.

The *K*-d tree technique proposed by Friedman et al. (1977), is a popular and effective data structure which is compatible with irregular and dense datasets such as lidar point clouds (Vosselman and Maas, 2010). This algorithm is designed to partition a certain file with *n* data records into dimensional nodes and afterward using a *k*-dimensional binary search to sort the data effectively. This facilitates searching the location of the nearest neighbours of individual point cloud. It can be done by spatially indexing each point based on *k* value to reduce computation time upon calling for the required point. For further details see Friedman et al. (1977) and Vosselman and Maas (2010). Figure 2.11 shows an example for the *K*-d tree binary search.

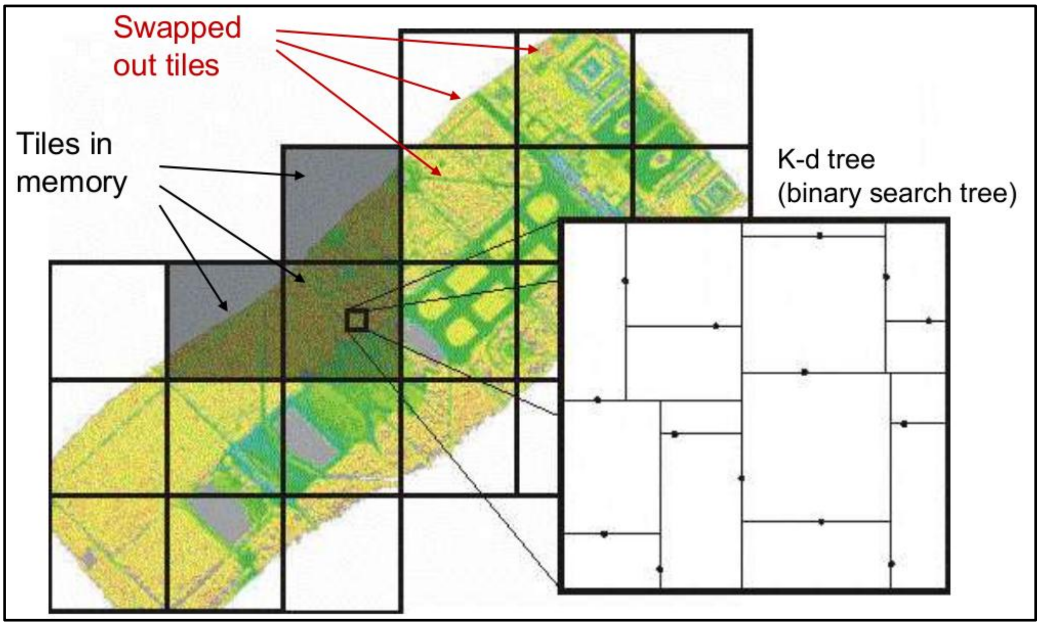

Figure 2.11. Sample ALS data shows *K*-d tree binary search technique (Mandlburger, 2011).

2.5.3 Available Radiometric Calibration Approaches

There are different approaches, which have been already introduced regarding the radiometric calibration of ALS data in literature. Multiple studies concentrate on the potential of the calibrated intensity values from discrete systems in improving the quality of the final products (Noel et al., 2002; Höfle et al., 2007; Hopkinson, 2007; Höfle et al., 2009). Luzum et al. (2004) presented an algorithm for correcting the inconsistencies in the intensity signals caused by variations in range, such as flying height and differences in ground topography. Although the model introduced is simple to be utilised for various applications, it does not consider sensor properties and target characteristics. Attempting to consider all variables affecting the received backscatter signal, Höfle and Pfeifer (2007) present two methods for intensity correction: data-driven and model-driven approaches. The data-driven approach is based on estimating a calibration parameter for the whole flight campaign by using the laser echo measurements delivered from multiple flying heights over a homogeneous extended area. The second approach is derived from the radar equation and is based on physical target properties of individual echoes and atmospheric conditions estimated from a single flying height. Both methods were found to successfully correct intensity values and are well-suited for implementation on large datasets. However, the second approach is more preferable as measurements are not required from multiple flying heights.

Later Yoon et al. (2008) discussed the potential of ALS intensity data in distinguishing land cover types and its capability to replace spectral information delivered from the near-infrared band of optical images after calibration. They examined the effects of reflectance and range on the ALS intensity behaviour using small-footprint data and investigating its radiometric properties as a pre-processing procedure. They found that intensity fails to effectively distinguish land cover types as vegetation cannot be well- differentiated from other objects. On the other hand, the range was found to be the major factor affecting intensity measurements except over vegetation. This is primarily because vegetation intensity signals were found to be low and similar to the intensity of other targets thus, no clear relationship with range could be determined over vegetation. As a result, Yoon et al. (2008) recommend a radiometric calibration with respect to range over all land cover types except vegetation, because signals can be overcorrected in case of vegetation as range effect is not well manifested over vegetation. Aiming to improve the quality of the derived products from ALS data, Habib et al. (2011) and later Yan et al. (2011) present a combined radiometric and geometric calibration approach for ALS data. They investigate the potential of the calibrated intensity values on the accuracy of the land cover classification results. A physical model based on the radar equation for the radiometric calibration of the intensity data was applied by taking sensor properties, topographic effects and atmospheric attenuation into consideration. After the implementation of this radiometric calibration, improvements in the classification results of up to 11.6% were delivered. However, their proposed angle of incidence correction approach is not robust enough for accurate applications. This is because the incidence angle estimation delivered from interpolated Surface (DSM) and not from the original point cloud, which incorporates more error source to the solution.

Some of the developed calibration approaches assume absolute workflow by using reference targets to calibrate the entire dataset using physical models that take into account effects on individual point clouds (Höfle et al., 2008). Kaasalainen et al. (2005) introduced a new calibration approach of using portable artificial brightness targets to calibrate ALS intensity data. These targets are made from polyester fabric and coated with polyvinyl chloride (PVC) of nominal reflectance from 5% to 70% for validation purposes. A goniometer and ASD FieldSpec Pro spectrometer have been utilised to measure the targets' reflectivity from multiple incidence angle settings in the lab. Thereafter the laser intensity behaviour was examined at different wavelengths and incidence angle settings by calibrating the reference targets reflectivity measures with a Spectralon reference panel. This showed that surface brightness has a major effect on the backscattering energy at 1064 and 632.8 nm wavelengths. Kaasalainen et al. (2005) claimed that following this calibration routine the calibrated intensity data would facilitate separation between vegetation and other surface types supported improved classification and segmentation results. Following these findings and by using the same reference targets utilised by Kaasalainen et al. (2005), Ahokas et al. (2006) calibrated ALS intensity data from different flying heights relying on the radar equation. Their findings highlighted the necessity for correcting ALS intensity values with respect to transmitted power differences, in addition to range, incidence angle, and atmospheric conditions. These effects should be considered before integrating intensity observables in further data analysis where intensity will refer to target reflectance after calibration (Wagner et al., 2006; Korpela et al., 2010).

A similar approach was later presented by Coren and Sterzai (2006), but this time by using homogeneous asphalt sections as natural reference targets for the calibration process. The results proved the potential of using natural targets as reference and also introduced the calibration procedure as an effective tool to correctly image land cover features through the calibrated intensity image. Following this, Kaasalainen et al. (2007) showed the feasibility of using natural reference targets as an alternative to fabric targets in a practical radiometric calibration approach. This was further investigated and later discussed in several studies where the potential of using natural reference targets to calibrate ALS intensity data (Kaasalainen et al., 2008; Kaasalainen et al., 2009a), and TLS data (Pfeifer et al., 2007; Pfeifer et al., 2008; Kaasalainen et al., 2011a) was approved. However, particular attention should be given when selecting a suitable reference target and sampling its reflectivity measures (Vain et al., 2009).

Since ALS systems first became available, a number of researchers have concentrated on assessing and evaluating the potential of exploiting intensity for further analysis. However, the intensity measurements are not representative of all the parameters that affected the received backscattered energy, in contrast to the physical observables which FWF systems can deliver. Based on these physical parameters, various approaches to the calibration of FWF data have been developed and exploited in several studies, demonstrating significant improvements in the relevancy of the final products for various applications (Höfle et al., 2008; Reitberger et al., 2009b; Bretar et al., 2009; Reitberger et al., 2009a; Mallet et al., 2011). FWF radiometric calibration routines were firstly undertaken shortly after small-footprint FWF systems first emerged. There was a particular interest in this topic as small-footprint systems can deal with the received laser power more precisely than the large-footprint systems. This is because the convoluted backscatter signal in small-footprint systems can comprise a limited number of targets as compared with the case of large-footprint systems. Wagner et al. (2008b) introduced a novel usage of backscatter parameters which defined all target properties, and discussed the potential of these parameters for calibrating the FWF backscattered signal. This is applicable by using the additional physical information from FWF data (echo width and amplitude) in a comprehensive physical mathematical model that takes all parameters affecting the recorded backscatter power into consideration. This was approved later by Briese et al. (2008) through a practical absolute radiometric calibration workflow. They investigated the backscatter parameter introduced by Wagner et al. (2008b) which defines a measure of the electromagnetic energy intercepted and radiated by land cover features and consider it as the required parameter to calibrate the backscatter energy. The proposed approach utilises a natural reference target with known backscatter information to derive the calibration constant for the entire campaign. This facilitated the calibration process, which relies on the radar equation to create the relationship among all variables affecting the laser energy. In contrast with all previously proposed radiometric calibration approaches, the presented routine proposes to measure the backscatter information of the reference target by means of reflectivity in the field. This can be achieved through utilising a portable reflectometer to maintain the same scan conditions. However, the introduced workflow ignores the incidence angle effect on individual laser echoes in the calibration process.

Following the previous findings, Wagner et al. (2008a) and later Alexander et al. (2010) investigated the potential of using the backscatter parameter to improve 3D point cloud classification results. This could be generated from FWF systems through the adoption of the radar equation as a calibration mathematical model. Wagner et al. (2008a) demonstrated the successful separation between broad tree canopy and terrain echoes by applying the backscatter cross-section parameter introduced earlier (Wagner et al., 2008b). Following this, the 3D point cloud was classified into vegetation and non-vegetation echoes with more than 90% overall mean accuracy. Following this, Alexander et al. (2010) detected improvements in classification performance through the backscatter cross-section parameter as compared with results delivered from utilising the original echo amplitude signals. A further backscatter parameter, so called the backscatter coefficient, introduced by Wagner et al. (2008b) and later reviewed in more details by Wagner (2010) was also investigated. This parameter considers the change in the laser illumination area with respect to the incidence angle. They show the potential of using this parameter to classify 3D point clouds in preference to the backscatter cross-section parameter in FWF systems. However, the main weaknesses in the proposed routine of Alexander et al. (2010) is ignoring the consideration of the incidence angle effect firstly when estimating the calibration constant for the whole campaign and later when estimating the backscatter parameters for individual echoes.

By aiming to overcome the weaknesses in the previously introduced radiometric calibration approaches, Lehner and Briese (2010) incorporated the incidence angle effect in the radiometric calibration workflow proposed by Briese et al. (2008). Consequently, and by building on the findings of Alexander et al. (2010), they used the derived incidence angle estimations from their approach to deliver the normalised backscatter coefficient parameter with respect to incidence angle for individual echoes. Later, they investigated various backscatter parameters to compare differences in the backscatter signals between overlapping flightlines and accessing the calibration accuracy. Figure 2.12 shows these outcomes before and after calibration over a selected interest area. However, although, the presented routine is highly valid over planar features, their findings concluded that results are uncertain over natural features with challenging surface trends.

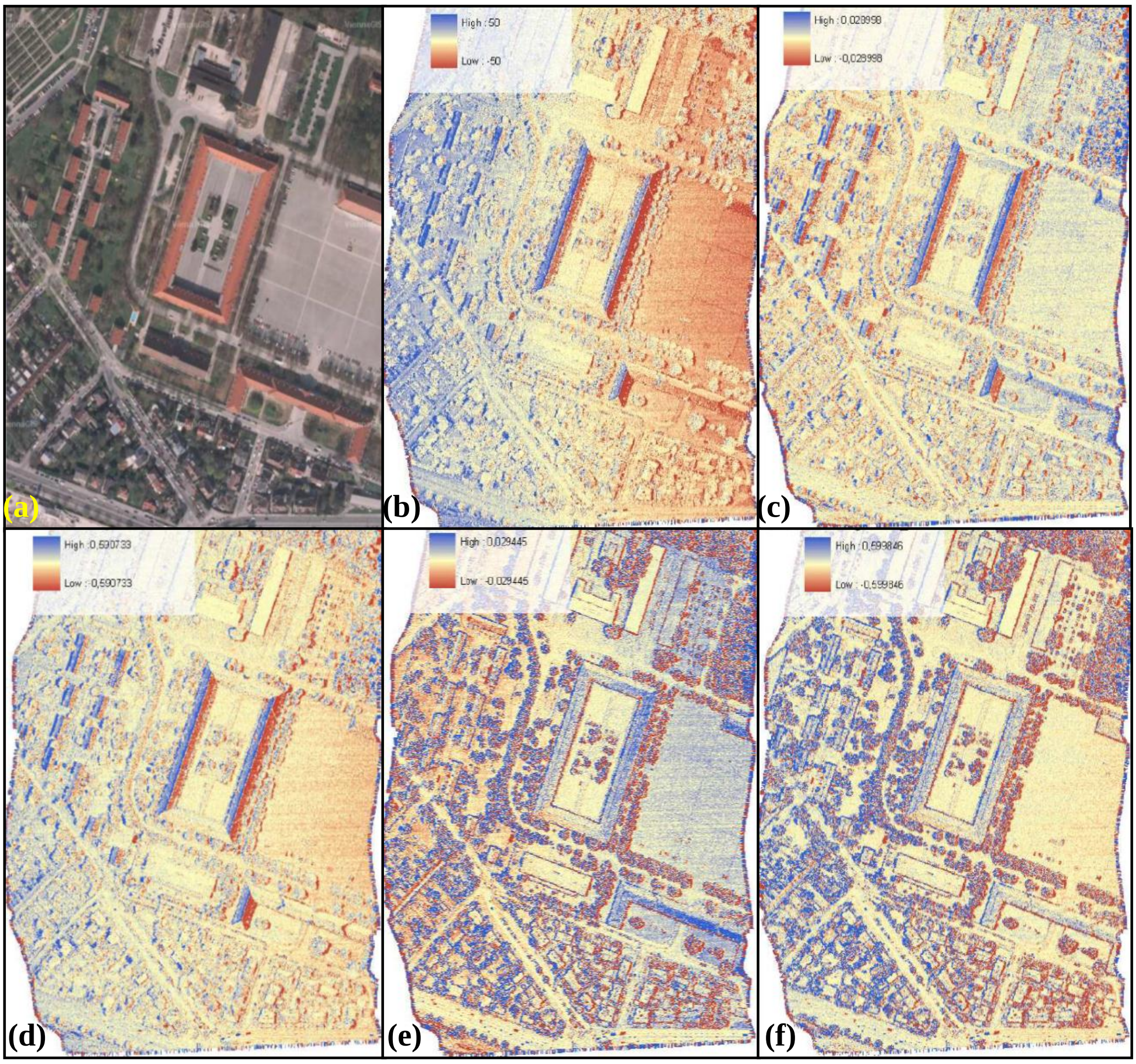

Figure 2.12. Difference maps of the backscatter signals from two overlapping flightlines before and after radiometric calibration: **(a)** Orthophoto **(b)** original amplitude **(c)** backscatter cross-section **(d)** backscatter coefficient **(e)** normalised backscatter cross-section with respect to incidence angle **(f)** normalised backscatter coefficient with respect to incidence angle (Lehner and Briese, 2010).

2.6 SEGMENTATION OF LASER SCANNING DATA

Segmentation is the process of partitioning a given data set into meaningful subset segments (Schiewe, 2002; Hofmann et al., 2002; Melzer, 2007). These segments should be geospatially connected and related to objects with similar attributes, such as planes, cylinders, or spherical surfaces, defining features of interest (Rabbani, 2006; Mucke, 2008). The majority of feature extraction methods are often initialised through a segmentation or clustering process (Vosselman and Maas, 2010).

The term segmentation is often mixed with clustering in computer vision and image analysis. Clustering primarily operates in feature space by grouping points with similar characteristics but not necessary belonging to same object. In contrast, segmentation works in object space where the segmented points are constrained to represent individual objects (Sithole, 2005). Because of similarity between both techniques, many segmentation approaches adapt ideas from clustering methods and vice versa. Numerous segmentation approaches have been developed for laser scanning data for a diversity of applications, such as feature extraction and modelling. These methods differ in terms of the selected segmentation criterion (the similarity measure between points), the segmentation function, and the algorithm developed to group points (Vanco, 2002; Rutzinger et al., 2008a; Vosselman and Maas, 2010). Hough transform and random sample consensus (RANSAC) are the most widely-applied segmentation algorithms, whereas surface growing and scanline segmentation are particularly the popular segmentation strategies in computer vision (Vosselman and Maas, 2010). These approaches will be discussed in detail in the following sections for various applications. These techniques are either based purely on geometric information or additionally integrate laser intensity data. However, there are some recent studies that investigated the potential of FWF additional information and have shown potential when integrating this information into the available solutions.

2.6.1 Segmentation Algorithms

2.6.1.1 Hough Transform

The Hough transform is a popular fitting technique to identify points of similar properties in order to describe shapes or surfaces with certain characteristics (Hough, 1962). It is commonly used for feature detection and extraction applications by segmenting similar points following a voting scheme procedure. This enables the identification of meaningful clusters from the unstructured point cloud, such as segmenting a house roof data into multiple facets (Liu et al., 2009). The Hough transform was originally invented to detect lines in 2D space and later extended to detect complex features in 3D space mainly for segmentation and clustering analysis (Vosselman and Maas, 2010).

The technique in 2D space is based on defining the candidate points with a constant distance and declination parameters from the defined origin (Figure 2.13), by trying to fit lines passing through these points to represent these parameters (Eqn. 2.17). In order to detect a line passing through points in object space, the method maps all points to the lines in a parameter space and then determine line function parameters based on the high number of lines passed through the defined point (Hough, 1962). Points those defined the same line will deliver the same parameters within a pre-defined threshold value. These points are identified as points of similar attributes in order to be grouped later into individual segments. To deliver accurate line parameters in object space, least squares fitting is usually applied to improve the final results. However, the size of the defined neighbourhood system is correlated to the accuracy of the final results which are severely affected by data noise in the case of laser point clouds (Vosselman and Maas, 2010).

$$\rho = x\cos\theta + y\ \sin\theta \qquad \textbf{Eqn. 2-17}$$

Where:

ρ is the orthogonal distance between the line and the origin

θ is the line orientation with respect to the origin coordinate system

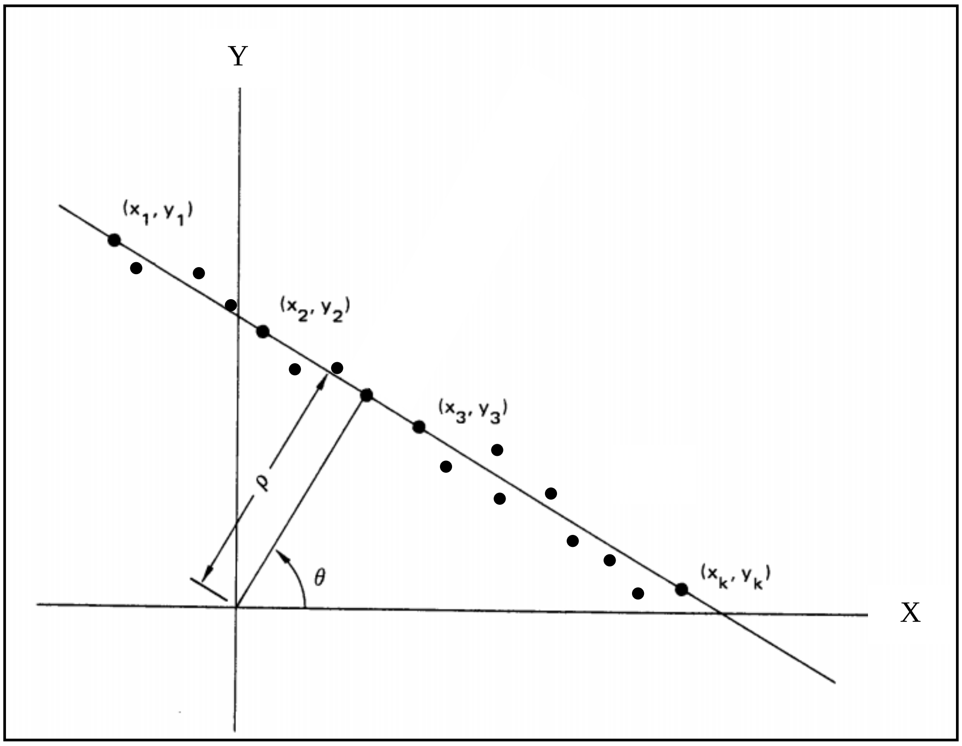

Figure 2.13. The Hough transform algorithm in 2D space.

This concept was extended to detect planes in 3D space by aiming to deliver plane parameters instead of line parameters (Eqn. 2.18). These concepts are described in further detail by Vosselman (1999) and Maas and Vosselman (1999) using real point cloud datasets.

$$\rho = x\cos\alpha\cos\beta + y\sin\alpha\cos\beta + z\sin\beta \qquad \textbf{Eqn. 2-18}$$

Where $\rho, \alpha,$ and β are the plane parameters.

Using the extended version of the Hough transform in 3D space, Vosselman and Dijkman (2001) present an automatic technique to detect planar features for building model reconstruction applications. They described two strategies to improve the parameters of the detected objects. The first strategy is reliant on detecting intersection lines and height differences between segmented planar surfaces. The second approach enables detection of a larger number of building details through the adoption of a coarse initial neighbourhood system in first place, thus delivering more useful results. The parameters delivered from both models are refined through least squares adjustment. Vosselman and Dijkman (2001) claim that using a dense dataset can improve the results and allow detection of minor features. However, in some cases, the latter method demonstrated the extraction of incorrect and non-existent details.

Later, Lee et al. (2005) presented a Hough-based algorithm to extract linear features from ALS data in order to detect discrepancies between overlapping flightlines. To extract these features they segmented the point clouds into planar segments based on the similarity in the normal distance between the defined plane and each tested point. Subsequently, Tovari and Pfeifer (2005) introduced a segmentation based classification method to separate ground from non-ground points for DTM derivations. The method relies on normal vector estimation following Hough definition. It presumes that points from *n* nearest neighbours should show similarity in the normal vector within a pre-defined threshold. However, distance between the candidate point and the current point in the neighbourhood definition in addition to the distance between the adjusted plane and the candidate point should also be below a certain value. Points which fulfil these three conditions are grouped and the region is grown until no more points can be found to meet these criterion. The definition is affected by the three mentioned parameters in addition to the number of neighbours used to define individual systems. The eigenvalues from moment invariant approach was utilised to deliver plane parameters in Tovari and Pfeifer (2005) approach. Although the presented method proposed many parameters to be fulfilled to deliver the final solution, the results show promising outcomes for various feature details. However, the introduced method works partially in 2.5D as the ground segments were interpolated to generate a reference surface to act as the adjusted plane.

A similar approach was implemented by Rutzinger et al. (2008a) which demonstrates convincing results with planar features. However, Sampath and Shan (2008) utilise the eigenvalue analysis to detect breaklines in planar surfaces and was later extended by Wang and Shan (2009) for building extraction applications. Dorninger and Nothegger (2007) present a surface fitting Hough-based algorithm within an iterative re-weighted least squares workflow. Although re-weighting data measurements enables improved handling of noisy data than the standard least squares workflow, it still sensitive to data density and distribution. A comprehensive data-driven automatic building extraction approach was later presented by Dorninger and Pfeifer (2008) for ALS data. The method is based on the assumption that each planar object can be modelled from a set of planar surfaces. They utilised the normal vector delivered from LS fitting using a spherical assumption to define individual planar surfaces by taking local roughness of the defined system in consideration. The planar surfaces delivered from the fitting function are compared with the initial segments and the merging process is adopted upon similarity. The procedure continues to iterate until no more segments can be merged. Although the method shows successful results to segmenting building facets efficiently, it showed shortcomings in modelling small structures on house roofs such as chimneys.

Although the Hough transform can reliably detect planes in point clouds, it is not necessary that all points in the parameter space represent one planar surface in the object space (Vosselman and Maas, 2010). Figure 2.14 shows an example of this assumption over a house roof target and highlights the differences between the parameter space and object space. In this particular example, the Hough transform considers all the points within the parameter space (the grey region) as having the same geometric attributes and belonging to the same surface. This is practically incorrect as points from multiple facets of the house roof were grouped in one single segment. Therefore, this assumption should not be accepted unless adjacency among points is well considered. To overcome the limitation of this assumption, cylindrical detection in Hough space has emerged.

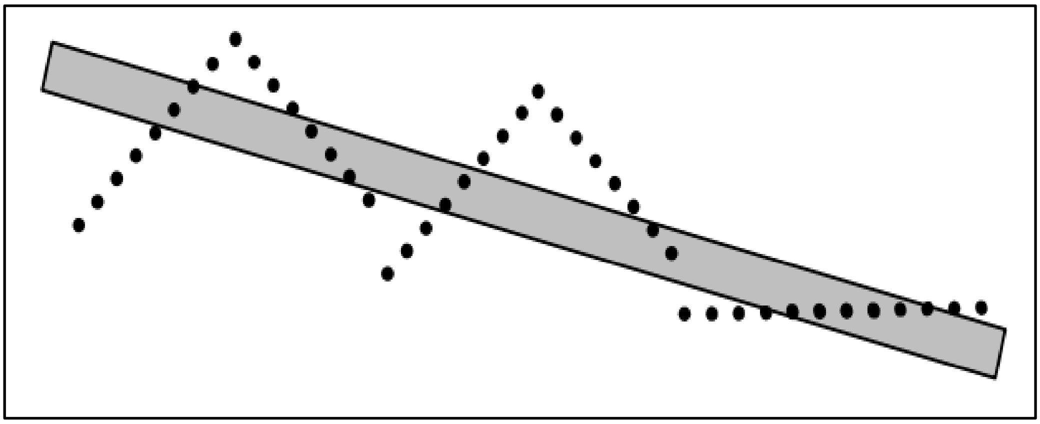

Figure 2.14. Incorrect planar surface detection with the Hough transform algorithm (Vosselman and Dijkman, 2001).

Cylinders are commonplace in industrial scenes, therefore the cylindrical assumption as described in 2.5.2.2 is more compatible for Hough space within these kinds of objects. The parameter space of the cylindrical definition is defined by the cylinder radius and height (Rabbani and Heuvel, 2005) thus the normal vector from such systems is able to deliver better results in industrial scenes. Rabbani et al. (2006) applied this assumption to a TLS dataset of an industrial landscape to segment the unstructured point clouds into smooth surfaces. They used the surface normal as the only segmentation criterion to group the points, as this can be reliably delivered even with noise presence, which is the case in laser scanning data. The algorithm includes two main steps, normal vector estimation, and region growing strategy (Rabbani, 2006). The normal vector is delivered by adopting the cylindrical assumption in the Hough space where the neighbourhood relation among points is either defined from adopting the *k*-nearest neighbours (KNN) or fixed distance neighbours (FDN) definitions. They adopted the non-linear Least squares solution to solve the plane fitting problem in the parameter space and later used plane fitting residuals to detect surfaces of high curvature. The potential of using the residuals as an indicator to detect curvature was investigated. This was implemented by estimating the normal vectors to a sample of dataset from different radius cylinders and plotted against $1/r^2$ where r represent the residuals from the plane fitting solution. It was found that in the absence of noise the residuals are quite similar to $1/r^2$ however there is a shift related to the amount of noise in case of noise presence (Rabbani, 2006). The results of the cylindrical-based segmentation approach show effectiveness with these kinds of feature objects. However, in case of ALS data, the cylindrical definition might not be the optimal solution for the multiple land coverage types with various surface details.

Exploring similar aspects in the Hough space, Filin and Pfeifer (2006) presented a segmentation-based clustering approach using the cylindrical definition. Point density, horizontal and vertical distribution, and data accuracy were taken into consideration when defining the neighbourhood system. Following this, surface parameters were delivered, represented by the normal vectors, which were utilised subsequently as the main segmentation criterion. In comparison with the Rabbani and Heuvel (2005) approach, the Filin and Pfeifer (2006) method applied the segmentation procedure in reverse order as the points are firstly partitioned in the feature space, and then discriminated in the object space. Filin and Pfeifer's (2006) approach was compared to the standard triangulation method and found to successfully detect more structures, such as vertical walls, and overcome the influence of outliers to a greater extent. This method was extended by Nizar et al. (2006) to overcome misclassified building points and present an automatic approach to reconstruct buildings from ALS data. Further, the adaptive cylindrical definition was utilised by Lari et al. (2011) to represent an efficient point cloud segmentation approach for planar surfaces. However, this time the coordinates of the projection origin of the best fitting plane of individual points are used as the only segmentation criterion to prevent ambiguity.

2.6.1.2 The Random Sample consensus (RANSAC) Algorithm

RANSAC is a general approach for robust model fitting in computer vision (Schnabel et al., 2007). It has been applied for various applications to model datasets with large numbers of gross outliers where it proves its efficiency. Figure 2.15 shows an example of noisy point clouds in a TLS scan of a church and highlights the performance of the RANSAC algorithm in tackling the presence of numerous outliers near the top of the towers, ultimately delivering a robust model.

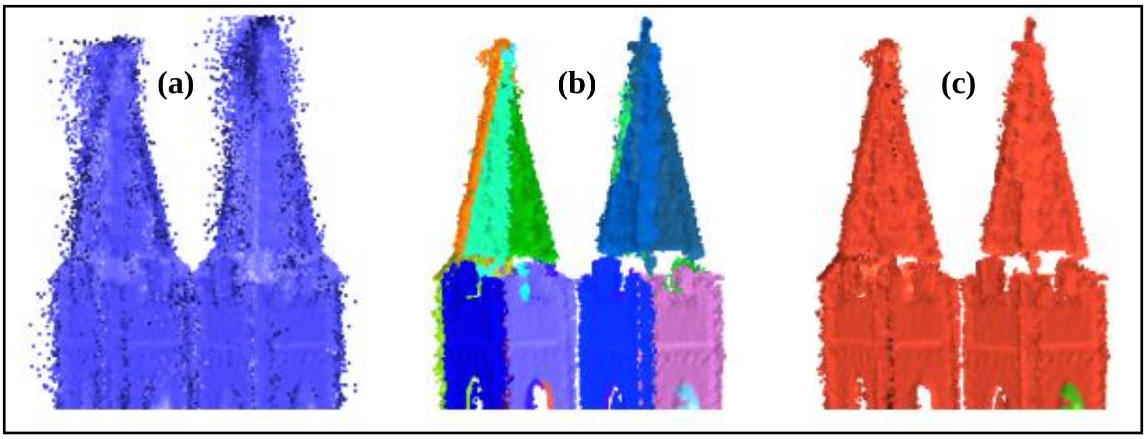

Figure 2.15. Fitting planes to noisy data containing 20% outliers with RANSAC: **(a)** original point cloud **(b)** the generated model with random colours **(c)** the generated model coloured by shape type (Schnabel et al., 2007).

The method is based on adopting a minimum set of sample data required to define the model (e.g. three points for a plane and four points for a sphere). It delivers the model parameters based on a certain selected error tolerance value which should be defined from empirical estimates (Neidhart and Sester, 2008). The model parameters are delivered from a unique solution in case of the availability of the minimum number of points required to define the shape type (Boulaassal et al., 2007).

However further refinements have been adopted to enhance the RANSAC model using least squares (Vosselman and Maas, 2010). As the data may have a high level of noise, in addition to the presence of outliers, the selection of the error tolerance value has a significant impact on the final fitted model (Boulaassal et al., 2007). A modified version that partially tackles this problem was presented by Torr and Zisserman (1998). However, the probability to differentiate between different surface types (e.g. walls, doors, windows, etc.) from one scene is still questionable for some extents. Vosselman and Maas (2010) used RANSAC to detect planes from ALS data for segmentation applications in an urban area and found that planes are reliably detected, in this case roofs and streets. However, these were mixed with erroneously detected planes in vegetation regions. To overcome this problem, Awwad et al. (2010) utilised the normal vector as an additional check with the original RANSAC algorithm to detect planes in an urban scene from TLS scan data. The segmentation results showed improvements over the original approach by successfully discriminating between parallel-graded planar surfaces such as stairs. However, the method still encountered problems and the results show failure in extracting surface edges. The main shortcomings in the standard RANSAC algorithm are its relative inadequacy in detecting surfaces from different data sources and the spurious results in some of the extracted segments which is not useful for users (Awwad et al., 2010). Furthermore, RANSAC was found to deliver many meaningless segments because of the over-segmentation behaviour, which necessitated further manual editing.

2.6.1.3 Other Approaches

In addition to the standard segmentation approaches discussed in the previous sections, other approaches have been introduced through the literature and are worthy of mention here. One of these approaches is the mean shift based segmentation proposed by Melzer (2007) to segment power lines and vegetation in ALS data. Mean shift is a non-parametric approach which works on the original (non-gridded) data. This algorithm was introduced originally by Fukunaga and Hostetler (1975) and is known to be an effective tool for filtering, classification, and segmentation of unstructured ALS data. Although the method has the advantage of being non-parametric and works without any probability distribution assumptions, it is restricted to certain applications as it is based on the assumption of "letting the data speak for themselves" which is not always reliable and, further, not practical. Later, Zou and Ye (2007) introduced a direct multi-resolution segmentation technique based on a pre-approximation of the point cloud's boundary volume using a hierarchical space partitioning data structuring approach. The method can tackle the limitations in the mesh-based segmentation algorithms by using the original point cloud data as an input rather than relying on the topology information delivered from the mesh surface. Furthermore, the approach can directly process large-scale datasets into distinct features within a reasonable period of time. However, shortcomings have been delivered at the edges of the segmented patches, which demonstrated non-smoothness between the adjacent segments.

On the other hand, integrating additional information from other remote sensing systems such as photogrammetry to be exploited alongside the laser scanning geometric attributes has seen some investigation in segmentation applications. In this regard, Zhao et al. (2011) integrated spectral information from photogrammetry with the geospatial information from ALS data in order to enhance automatic building segmentation. The method delivered improved results by detecting elevation-error points during the region growing process by taking into account elevation, gradient, spectral, and entropy information from photogrammetry to identify building from non-building points. These findings are promising for various applications as much of this additional information can provide additional knowledge about surface features, which could not be extracted from the standard laser scanning systems. However, this method is lacking in accuracy, as the method adopts a triangular network which works in 2.5D rather than 3D.

2.6.2 Similarity Measures

In order to identify surface features from unstructured 3D point clouds efficiently, the points should be modelled into functional structured shapes (Bornaz et al., 2003). These shapes can be delivered from segmentation process following a proper similarity measure to group points into distinct clusters. Using standard functions, shapes can be identified as lines, planes, spheres, cylinders, etc. (Barnea and Filin, 2008). Based on the area of study and data characteristics, the most suitable approach should be selected to highlight objects of interest in each dataset. In a least squares sense, to fit any surface to a group of given points it is required to estimate the parameters that minimise the sum of squares of the distances between the points and the estimated surface. These distances are usually defined in the orthogonal direction and aimed to be minimised as much as possible to deliver the optimal solution. In terms of complexity this is a non-linear least squares solution; however the problem could be simplified to be solved as an eigenvalue operation in 3D vector space. In theory and in cases of dense datasets, planes can efficiently define most types of complex objects, even spheres and cylinders which could be represented by the normal vector, as shown in Figure 2.16. However, robust selection of the neighbourhood definition in 3D space should be implemented and data noise should be considered (Filin and Pfeifer, 2006).

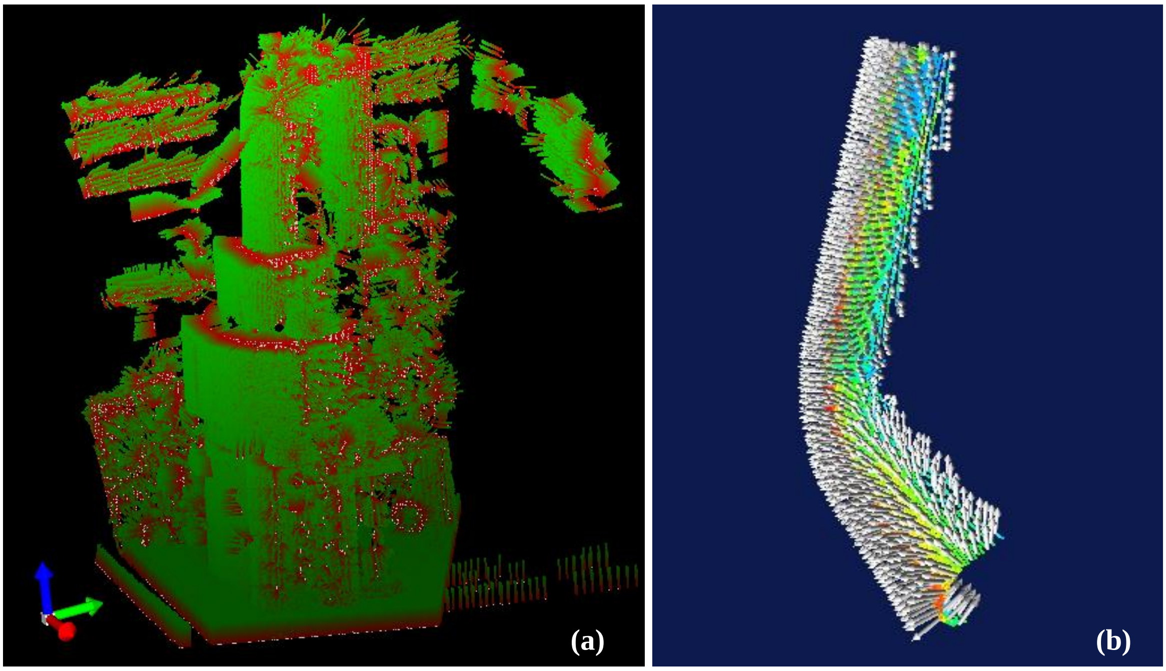

Figure 2.16. Fitting planes to 3D point cloud data using the normal vector: **(a)** sphere, cylinders, and planes **(b)** L-junction in industrial landscape (Rabbani, 2006).

The normal vector is the most trustworthy parameter which can be reliably generated as a proper segmentation criterion from 3D point cloud data even in the presence of noise (Rabbani, 2006; Filin and Pfeifer, 2006). This is true only when the neighbourhood definition is selected properly. It delivers the fitting function solution by estimating the orthogonal distances between the points and the fitted surface which can truthfully define the strength of the suggested solution (Filin, 2002; Kim et al., 2007). The segmentation-based normal vector techniques can detect sharp edges, as well as flat or highly curved surfaces as shown in Figure 2.17 (Vanco, 2002; Sithole, 2005).

Figure 2.17. Visualised normal vectors of three house roofs (OPALS, 2009)

The majority of the reliable segmentation approaches for feature extraction applications adopt the normal vector as the main criterion to detect planarity (Rabbani et al., 2006; Filin and Pfeifer, 2006; Rutzinger et al., 2008a; Dorninger and Pfeifer, 2008). However, some authors have incorporated other attributes to emphasise certain behaviours and avoid mis-clustering results. These include height difference and surface slopes (Filin, 2002; Zhao et al., 2011), however these two parameters are highly sensitive to the noise level in the data. The majority of these methods are segmentation based classification approaches to improve the separation procedures between surfaces of similar characteristics. They are particularly useful to separate high vegetation from low vegetation and smooth surfaces from rough surfaces.

2.6.3 Segmentation Strategies

2.6.3.1 Surface Growing

Surface growing is the popular segmentation strategy of grouping points in the proximity neighbourhood system into homogeneous attribute clusters (Tovari and Pfeifer, 2005). This is based on similarity in the segmentation criterion earlier defined in object space. The method is considered as the 3D version of the well-known region growing technique in image processing (Vosselman and Maas, 2010; Awwad et al., 2010). It is often utilised as a strategy to group adjacent points of similar attributes into small segments (Zhan et al., 2008). These segments are grown gradually by adding new nearby points to the seed surface in order to represent meaningful surfaces in the object space (Jochem et al., 2012). The method assumes that in the object space a part of the dataset which is defined within a specific distance are related to the same surface (Vosselman et al., 2004).

The method commences by selecting seed points based on either certain conditions or random selection (Pu and Vosselman, 2006; Pu, 2008). Then similarity between points is assessed through checking the attributes of the surrounding neighbour points (Roggero, 2002). Later, seed points are grown to be seed surfaces and the similarity checking is performed then with the new estimated attributes of the seed surface such as the normal vector. When a point is added to the seed surface the plane parameters are re-estimated by delivering a new normal vector to improve the accuracy of the implemented technique. The growing of the surfaces is based on fulfilling one or more of the following conditions which could be delivered from the normal vector (Awwad et al., 2010):

1. Proximity of points.
2. Surface planarity.
3. Surface roughness.

Using normal vector similarity to group points into segments is quite interesting as this criteria does not necessary search for only planarity (Tovari and Pfeifer, 2005). However, the robustness of the generated segments is related to several considerations such as data noise and density as discussed in 2.6.2. The surface growing technique suffers from sensitivity to noise, which is particularly the case where seed points are wrongly selected. Thus, the error could significantly grow with erroneous seed points selection in the presence of noisy data. However, this can be overcome by adopting a reliable selection of seed points based on robust criterion such as normal vectors and their residuals (Rabbani et al., 2006). The technique is considered to be reliable and truthful if the noise is considered carefully and adequately during the process. Otherwise, alternative approaches such as the clustering features based model or the fitting model could be adopted as a segmentation strategy instead. However, both approaches have serious shortcomings in dealing with noise which is recognised as a common problem in the available segmentation strategies (Awwad et al., 2010).

2.6.3.2 Scanline

Scanline segmentation is an aggregation technique to segment the 3D point cloud on scan row basis into multiple entities each of similar attribute contents (Han et al., 2007; Vosselman and Maas, 2010). The method is known as range image segmentation in computer vision literature (Jiang and Bunke, 1994) which has been extended to work in 3D. Each scan line (row of 3D points) is split into small parallel segments of similar attributes and then merged to the adjacent linear segments to define a certain object (Sithole and Vosselman, 2003). However, Sithole and Vosselman (2005) introduce a new definition to the scan line technique by segmenting scan line segments with multiple orientations (i.e. not parallel). Specifically, the method slices points in different directions in order to deliver multiple profiles. A weighted minimum spanning tree is then generated for individual profiles to facilitate the workflow (Sithole and Vosselman, 2005). Following this, all edges with a weight exceeding a pre-defined threshold value should be withdrawn from the overlaying profile solution. Later, these profiles are segmented together to deliver line segments followed by a surface growing procedure. Figure 2.18 shows an example of the developed scanline segmentation definition by segmenting the point clouds of a cube object and the background beneath into continuous segments in different directions. These procedures are based on similarity criteria and follow the surface growing technique (Vosselman et al., 2004). The later definition of scanline technique can ensure better results than those from the standard scanline definition; however, both techniques are better designed to deal with structured data, which is not always the case with ALS data.

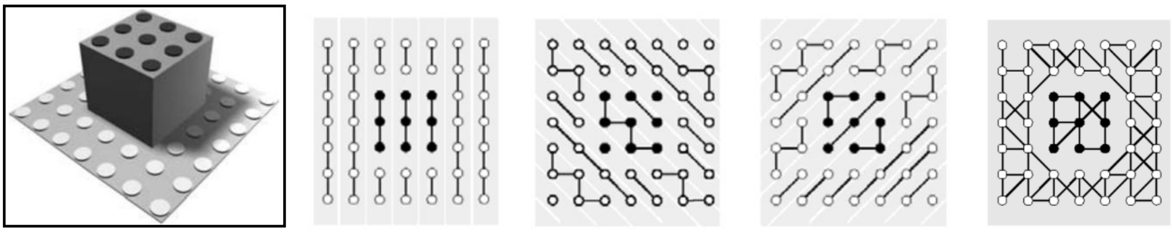

(a) (b) (c) (d) (e)

Figure 2.18. Scanline segmentation technique: **(a)** 3D model **(b)-(d)** line segments in parallel, left diagonal, and right diagonal directions **(e)** overlaying segments from all directions (Sithole and Vosselman, 2005).

2.6.4 Segmentation Challenges

The key for successful and effective point cloud segmentation can be described as follows (Kim et al., 2007):

1. Adoption of a meaningful neighbourhood definition to extract the volumetric system in 3D space.
2. Definition of reliable segmentation algorithm and criteria to detect similarity among the point cloud.
3. Definition of a proper aggregation strategy, which better defines data characteristics and fits with the study aims.

However weaknesses of the available approaches can be summarised as follows (Rabbani, 2006):

1. The majority of available approaches are designed to work only with simple planar features and face shortcomings to define complex features.
2. Most of these approaches fail to detect minor features and handling curved objects is unsatisfactory.
3. Most of these approaches work in 2.5D and are not compatible with 3D data.
4. Many of these approaches implement solutions which are dependent on a large number of parameters.

Further, most of the available approaches discard noise presence and do not account for variation in data density. Additionally, existing approaches are targeted at man-made objects and are not adaptable to natural features. However, the common of all available approaches can be described as a failure to distinguish between different features of similar geometric attributes such as asphalt and bricks ground or bare ground and mown grass.

2.6.5 Fusion of the Additional Information from ALS Systems

The physical information from FWF-ALS offers tremendous potential to better identify surface features by delivering information about surface roughness and reflectivity (Doneus and Briese, 2006; Höfle et al., 2009; Heinzel and Koch, 2010; Mucke et al., 2010b). Therefore integrating this information in segmentation and classification routines alongside standard geometric information can enhance the results and provide a stronger solution than relying on the geometric information alone (Reitberger et al., 2009b; Song et al., 2002; Höfle and Hollaus, 2010; Mallet et al., 2011).

Before discussing the potential of FWF, it is important to review some of the available segmentation techniques, which integrate ALS, intensity signals to enhance final results. In this respect, Höfle (2007) evaluated the integration of intensity values to improve results for specific applications. Particularly, a developed 3D object segmentation workflow was presented to segment glacier surfaces using the geometric and intensity information of the ALS point cloud. It was demonstrated that exploiting the intensity signals jointly with the geometry of ALS data is more sufficient for segmenting and classifying features than using individual information source alone. Later, Xudong et al. (2008) presented a building segmentation workflow based on a filtering algorithm which uses range and intensity information from ALS points. The approach is based on data fusion theory by integrating spectral and geometric information from laser scanning data to improve feature extraction and modelling techniques. The results proved the feasibility of the presented approach in urban areas. On the other hand, it was demonstrated by Höfle et al. (2009) that accurate water surface modelling can be achieved from ALS data when combining intensity with standard geometric information. A novel automatic technique, combining a segmentation and classification model to define water areas and boundaries is presented. The technique relies on the corrected intensity signals to establish a basis for a successful water area identification (Höfle et al., 2009).

In the same respect, FWF has also been discussed in the literature and assessed to investigate the potential of the additional information (e.g. echo width and amplitude) to improve segmentation algorithms. The majority of the literature which utilises FWF for segmentation were developed to segment and extract tree regions (Rutzinger et al., 2008b, Neuenschwander et al., 2009; Reitberger et al., 2009b). One of the pioneer studies in this instance is the approach presented by Gross et al. (2007). In this study, the eigenvalues delivered from the covariance matrix (refer to Section 2.5.2.2) for a spherical neighbourhood volumetric system were considered to describe features of interest. ALS intensity values have integrated as a weighting function in the moment definition to deliver the eigenvalues, demonstrating potential by improving segmentation results. Only data with low point density was included in their investigations, and therefore a large radius was utilised to define the neighbourhood environment for optimal feature representation. This leads to loss in the representation of walls and false detection of trees. As an alternative, this approach was extended to include the cylindrical neighbourhood definition to overcome these shortcomings. This showed that the values of detection of the surface features are influenced by the modifications of the parameters of the sigmoid function (a function defines surface planarity, intensity, and variance), refer to Gross et al. (2007) for further details. However, it was claimed that FWF post-processing can deliver further information which was expected to lead for better object identification and more precise segmentation outcomes. Gross et al. (2007) also demonstrated that the spherical definition can better define planes, edges, and corners than the cylindrical definition. In contrast, Rutzinger et al. (2008b) relied on the echo width from FWF to define the roughness criterion in the surface growing algorithm to segment vegetation. Significant improvements in separating tall vegetation from non-vegetation echoes which have high echo width values have been delivered in urban areas. However, it was found that echo amplitude is of major significance in identifying surface features in addition to the echo width. Similar findings have been presented by Neuenschwander et al. (2009) to highlight the potential of the physical information from FWF to define the structural differences in land cover features. On the other hand, Reitberger et al. (2009b) present a novel routine to segment single trees using a FWF-ALS dataset. The normalised cut segmentation approach (presented earlier by Shi and Malik (2000) for image segmentation) was adopted to define single trees and tackle shortcomings in the stem detection approaches. The introduced method exploited FWF intensity and echo width parameters alongside the coordinates of the detected voxels to identify trees. It was concluded that the modified approach can significantly improve the tree detection rate results.

FWF additional information was also integrated alongside the geometric information to improve classification results in urban areas. This was demonstrated by Alexander, et al (2010) by making use of the backscatter coefficient as an attribute to separate classes following a decision tree classifier. The study has demonstrated the advantages of the FWF laser data over the discrete return data to improve classification methodologies.

2.7 SUMMARY

Chapter Two has disscussed the workflow of the FWF-ALS data processing and analysis to enhance automatic segmentation routines. The first phase of the chapter considered data processing and management by revewing post processing techniques and highlighted available strategies to handle massive laser scanning datasets. The second part of the chapter reviewed the available radiometric calibration strategies to correct the additional information from FWF. This was acheived through reference to the shortcomings in the standard routines to provide comprehensive results. Thereafter, a review was presented regarding the available 3D object segmentation techniques of ALS data where the strengths and weaknesses of these methods were addressed. This included the current geometric-based approaches as well as discussing the potential of integrating the physical observables from FWF. The following outcomes can be highlighted as a result of the literature reviewed in this chapter:

- It was shown that in order to achieve optimal improvements in range resolution and accuracy of the FWF-ALS data, it is necessary to account for the overlapping and weak echoes in the complex convoluted waveforms. Therefore, it is required to adopt a robust post-processing technique to compensate information loss delivered from standard algorithms which is capable to deliver more potential representation of land cover features.
- It is required to calibrate the backscattered signal from FWF to increase the benefits of the collected information for further analysis. It was shown that the weaknesses of existing approaches relate to their failure to include all the variables affecting the received energy, and shortcomings in the methods utilised to derive individual

variables. It was shown from the literature that the radar equation is the optimal radiometric calibration model for ALS because it describes all the parameters that affect the received laser power.

- With respect to 3D object segmentation, it was shown from the literature that the normal vector is the most trustworthy parameter for reliable segmentation of the 3D point cloud. However, a reliable definition of the neighbourhood volumetric environment should be implemented to achieve optimal results. Surface growing was found to be a worthy reliable segmentation strategy provided noise is adequately considered during the process.
- Potential was shown to utilise the physical information from FWF to better identify features and thus improve segmentation and classification techniques.

CHAPTER

3

3D OBJECT SEGMENTATION OF FWF-ALS DATA

3.1 INTRODUCTION

FWF-ALS data has shown potential for enhancing segmentation and classification approaches through the additional information it can provide (Rutzinger et al., 2008; Reitberger J. et al., 2009). Investigation of individual FWF echoes can significantly enhance the identification of ground features based on the geometric and physical information generated through post processing (Mallet et al., 2008; Coren and Sterzai, 2006). However, this additional information is unable to directly provide a valid physical representation of surface features due to many variables affecting the backscattered energy during travel between the sensor and the target (Vain et al., 2010). These include sensor properties, flying height and target characteristics (Coren and Sterzai, 2006; Hopkinson, 2007). Effectively, this delivers a mis-match between signals from overlapping flightlines. Therefore direct use of this information is not recommended without the adoption of a comprehensive radiometric calibration strategy that accounts for all these effects.

Dealing with FWF raw data is more challenging than the standard 3D point clouds, and post processing of FWF data is a time consuming procedure. Although commercial software can effectively speed up the process, the pulse detection methods and their accuracy is considered to be “black-box” for end users. Therefore the development of an effective processing strategy with high accuracy considerations is highly desirable for a range of downstream applications. A new processing strategy using grid computing has been proposed and implemented in this research and has shown to be effective in managing dense datasets (Abed and McGough, 2010). The output delivers geometric information, echo amplitude and width for individual echoes, as well as the total number of echoes for each pulse and the echo number (Lin et al., 2008). However, converting echo amplitude and width into reflectivity measures for subsequent integration in a segmentation technique, needs more advanced consideration of factors such as surface orientation. Therefore, echo amplitude normalisation as a function of the incidence angle effect has been applied initially. This is implemented based on the development of a novel approach for rigorous estimation of the surface normal vector for individual echoes (Abed et al., 2010). The new approach, termed the Robust Surface Normal (RSN) method, has proved to be effective in normalising FWF amplitude values and providing more comprehensive physical information for further calibration applications. In order to fully utilise FWF additional information and to better describe land cover features, a more comprehensive parameter that defines all target characteristics is required. This research utilises the normalised backscatter parameters, as proposed by Wagner (2010), where these parameters are normalised with respect to the incidence angle (Abed et al., 2011). Following this, the calibrated additional information has been integrated with the standard geometric information to develop a new segmentation routine for various applications.

The first part of this chapter (Section 3.2) describes the study sites and datasets used in this research. The second part discusses the segmentation workflow following the simplified outline presented in Figure 3.1. The developed FWF-ALS data processing strategy is discussed in Section 3.3. Next, the development of the RSN method for echo amplitude normalisation is presented in 3.4. Section 3.5 discusses the practical radiometric calibration approach using portable reference targets. Finally, the developed 3D object segmentation technique, utilising FWF information, is introduced in Section 3.6. The last part of the chapter (Section 3.7) focuses on the implementation and testing of the methodology followed by a summary of the main outcomes.

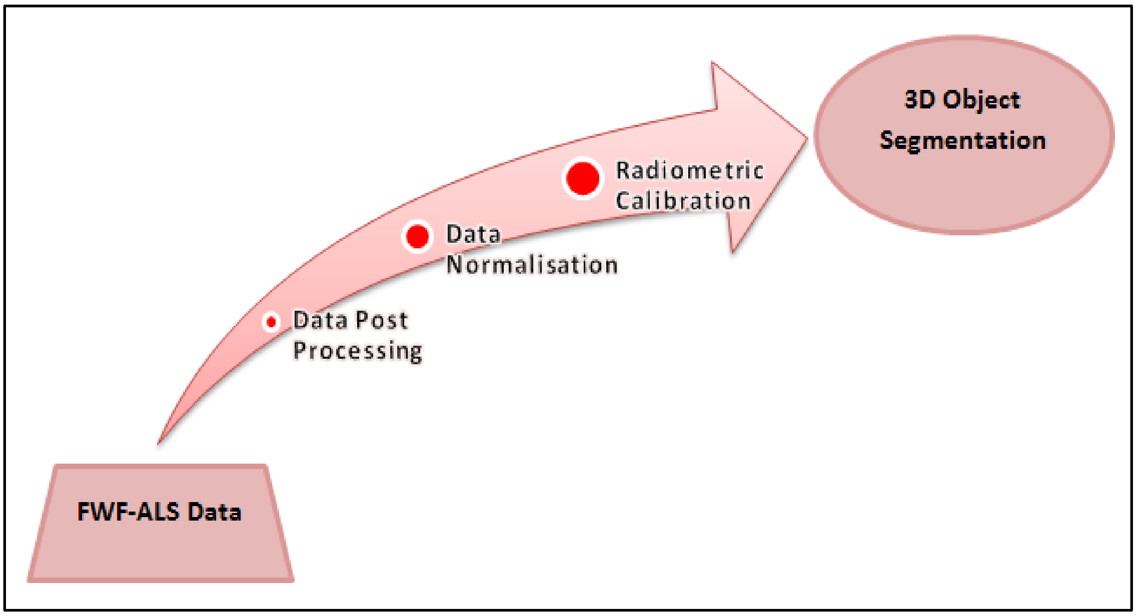

Figure 3.1. The developed 3D object segmentation workflow for FWF-ALS data.

3.2 STUDY SITES AND DATASETS

Two study sites were investigated and utilised to develop the methodology in this research. The first site, located on the south coast of England, includes an urban area over Bournemouth city centre, with additional data acquired at a rural site (Hurn) located to the north-east of the city and composed of natural terrain cover with various landforms. The second site is located in the south-west of England, within the city of Bristol. The site comprises urban areas to the north-west of Bristol city centre and alongside the River Avon. Figures 3.2 and 3.3 show the extents (red lines) of the Bournemouth and Bristol study sites respectively, together with their flight lines marked in grey lines.

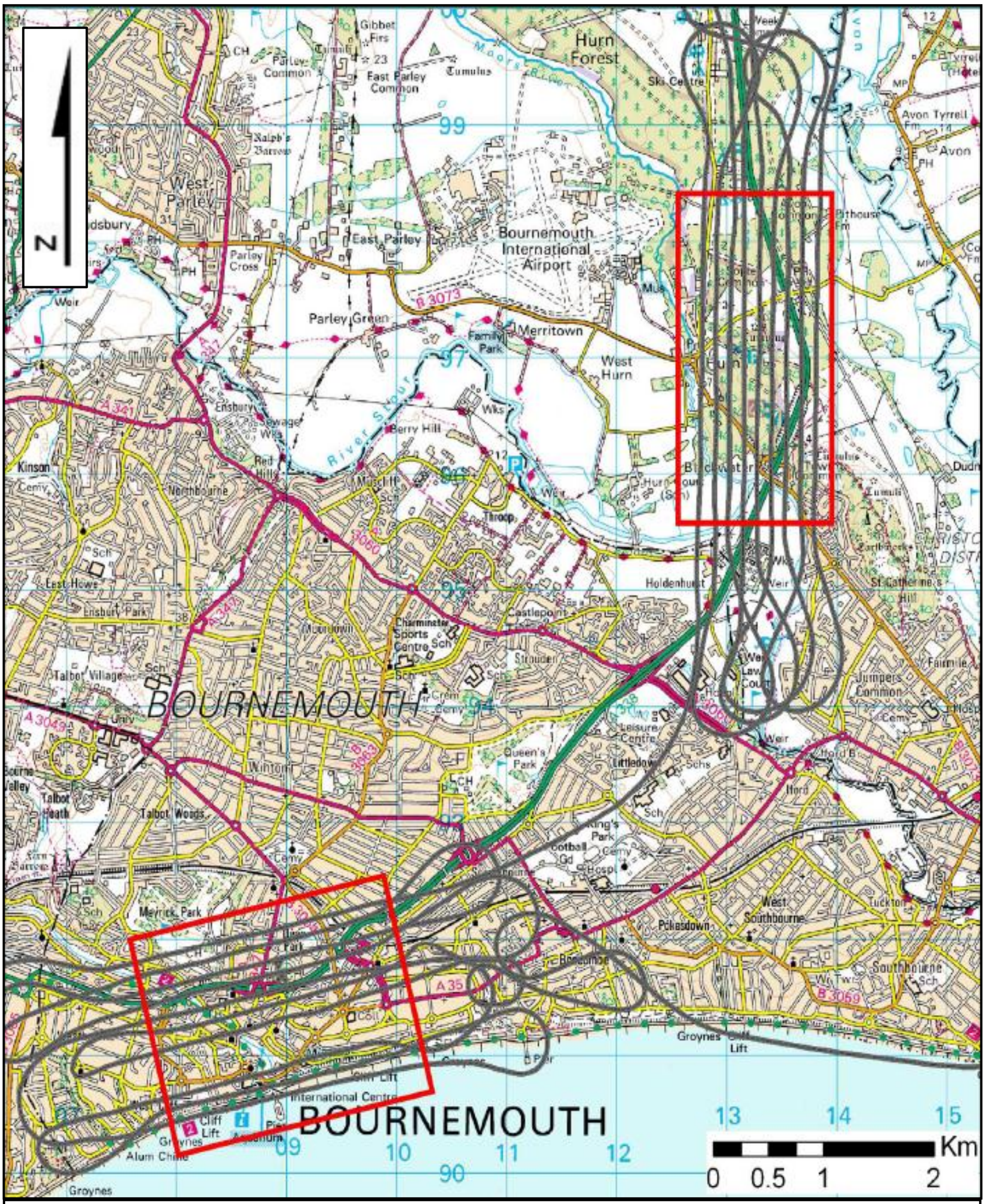

Figure 3.2. Bournemouth study site, with red blocks representing the ground coverage. Urban area to the south-west and rural area to the north-east.

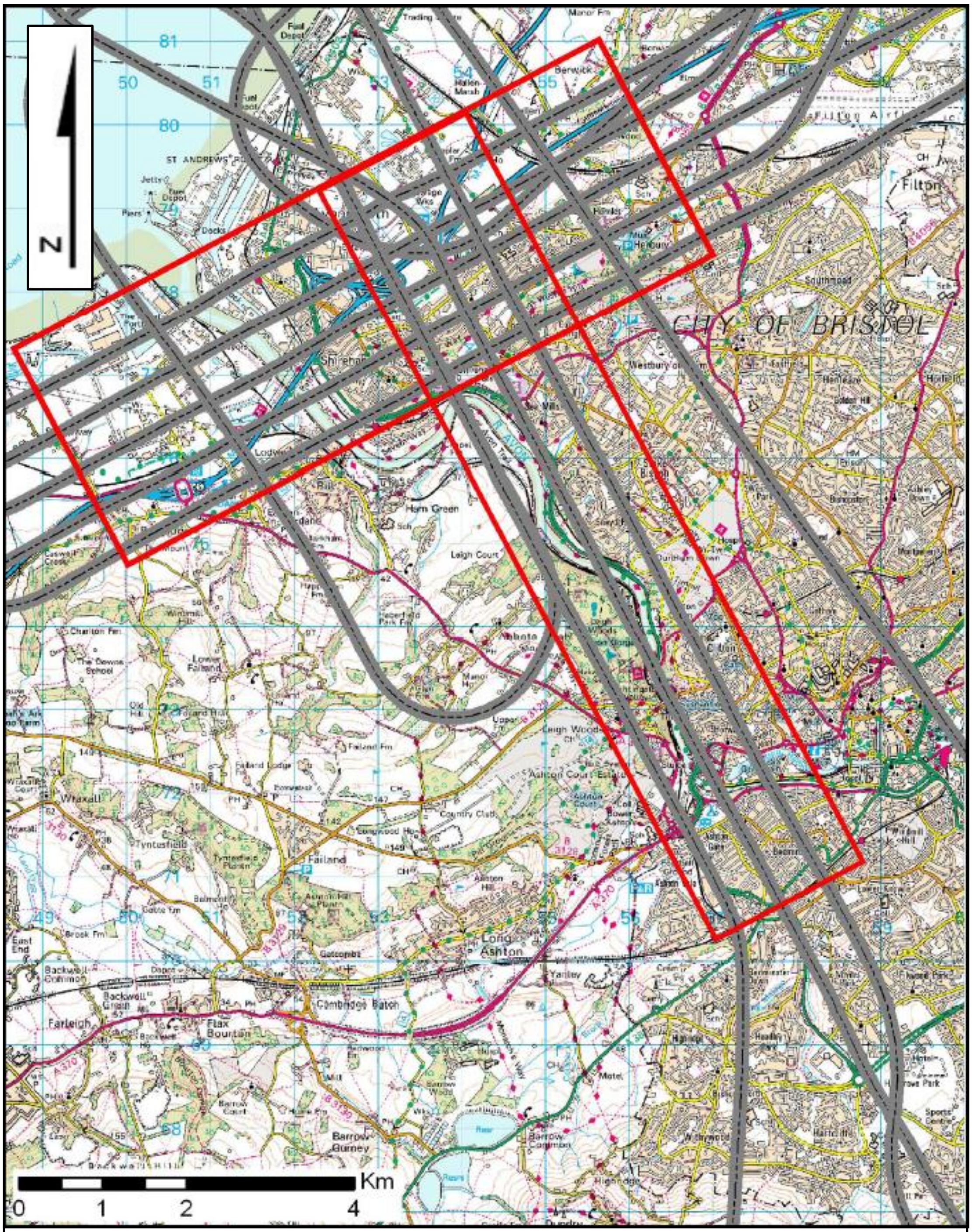

© Crown Copyright/database right 2011. An Ordnance Survey/EDINA supplied service. FOR EDUCATION USE ONLY.

Figure 3.3. Bristol study site, with red block representing the ground coverage.

Small-footprint FWF-ALS datasets for both sites were captured with a 1550 nm wavelength Riegl LMS-Q560 scanner. The technical specifications of this system are described in the Table 3.1.

Laser wavelength	1.5 µm
Laser beam divergence	≤ 0.5 mrad
Scanning mechanism	rotating polygon mirror
Scan pattern	parallel scan lines
Scan angle range	± 22.5° = 45° total (± 30° = 60° total)
Scan speed	10-160 lines/sec
Angle measurement resolution	0.001°
Laser pulse repetition rate	up to 120 kHz @ 45° scan angle
Footprint size	0.5 m @ 1 km
Pulse width at half maximum	4 ns
Minimum range	30 m
Intensity measurements	16 bit intensity information is provided for each echo signals

Table 3.1. Technical specifications of Riegl LMS-Q560 FWF-ALS system (Riegl, 2009).

The Bournemouth dataset is composed of nineteen flightlines with an average flying height of 350 m and was collected from a helicopter platform in May 2008. The Bristol dataset was captured during August 2006 from 1000 m flying height using a fixed wing aircraft and is composed of nine flightlines. The Bournemouth dataset offers a higher point density than the Bristol dataset, with more than 15 points/m^2 and a 0.18 m footprint diameter size compared to 0.5-0.8 points/m^2 and 0.47 m nominal footprint in the case of Bristol. The swath width and scan angle of the Bournemouth dataset is ~430 m and ±30° respectively. In contrast, the Bristol dataset has a wider swath width of ~780 m and narrower scan angle of ±22.5°. Both datasets were directly geo-referenced through an on-board GNSS-IMU system. The Bournemouth dataset has been assessed as having an average RMS accuracy of 0.09 m in the urban area and 0.12 m in the rural area, whilst the RMS of the Bristol dataset is averaged to 0.08 m (refer to Lin, 2009). The datasets, together with the trajectory information and orthophoto coverage, were provided by Ordnance Survey, Great Britain’s national mapping agency.

In the case of Bournemouth, nine flightlines (1-9) were captured for the rural site at Hurn while ten flightlines (10-19) cover the urban site. Figure 3.4 shows the flightline coverage, with each flightline illustrated through a different colour. This highlights the loss of data over the urban site, particularly in flightlines 16 and 17 where poor quality data and problematic raw files (which failed to be read during the processing stage) were delivered. This was due to inclement weather conditions at the time of the survey, with rain and cloud adversely affecting data quality. Consequently, only 15 flightlines (1-15) have been processed to test and validate the research methodology. The last two flightlines (18 and 19) were excluded as they primarily covered the sea and shorelines and this was beyond the main focus of this research.

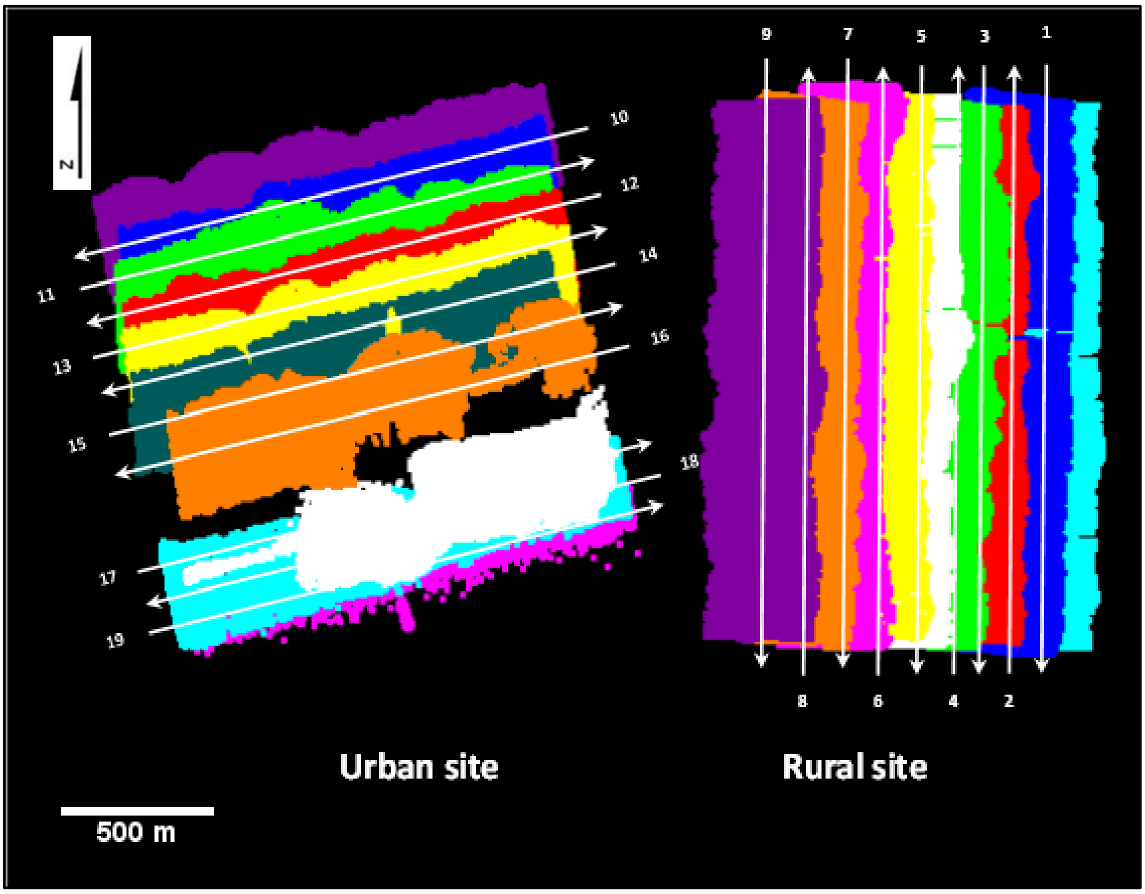

Figure 3.4. Bournemouth flightlines coverage.

As for the Bristol campaign, the dataset was collected from eight flightlines (1-5 are in the same direction and 6-8 are cross strips), as shown in Figure 3.5. All flightlines were processed successfully and no data quality problems where encountered.

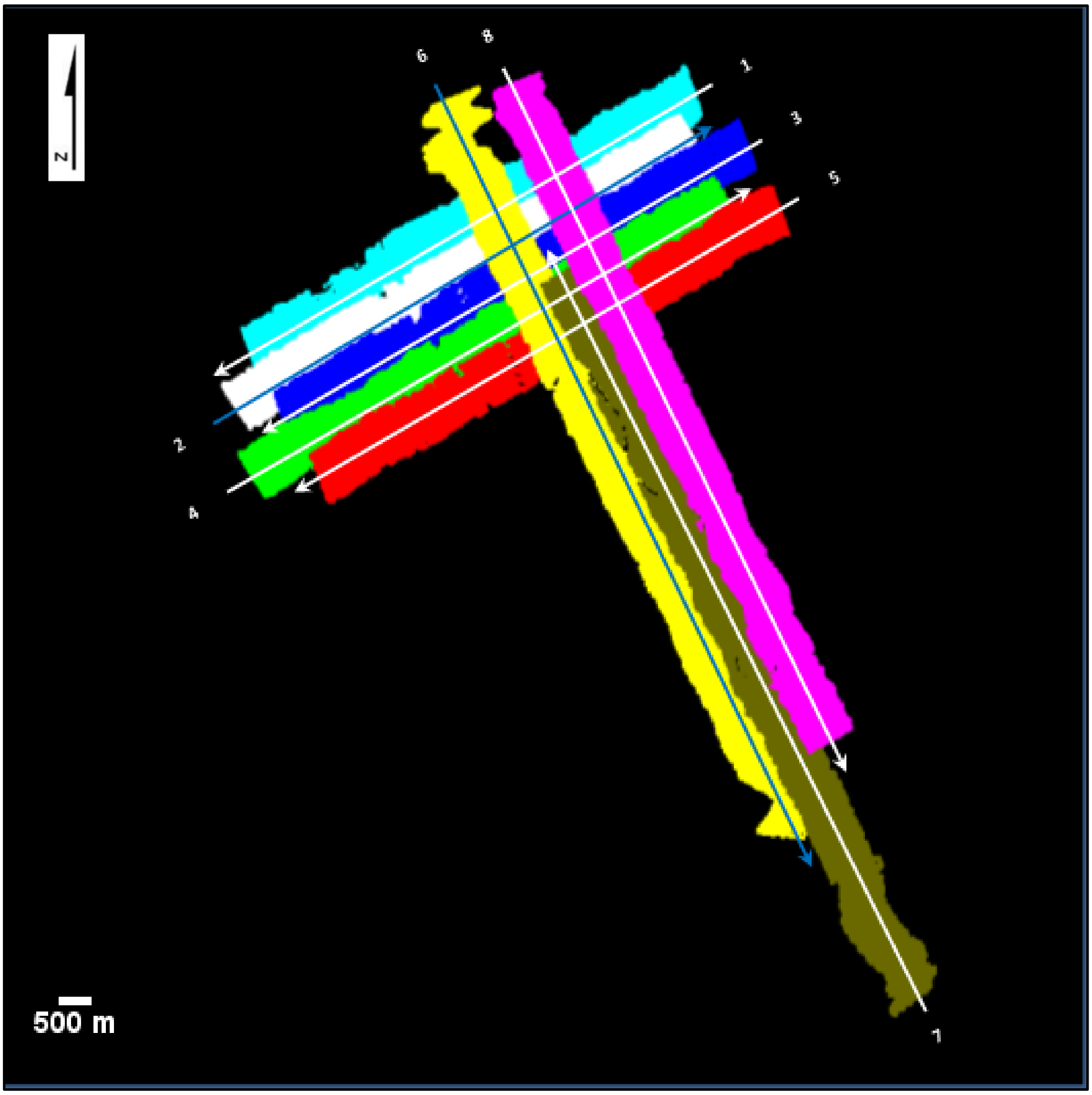

Figure 3.5. Bristol flightlines coverage.

3.3 FWF DATA POST PROCESSING USING GRID COMPUTING

Motivated by overcoming limitations in available post processing techniques, RGD method was selected as the optimal pulse detection algorithm to post process FWF-ALS data in this research (refer to Section 2.3). For detailed information about the implemented routine in terms of assumptions, parameters, and thresholds adopted for the Bournemouth and the Bristol datasets, refer to Lin (2009).

Due to processing complexity, which stems from large datasets and the substantial number of echoes that the Rigorous Gaussian pulse Detection (RGD) method can detect (refer to Section 2.3 for details), an effective processing strategy was developed using a grid computing technique. The new routine relies on high-throughput computing utilizing the Newcastle University PC network and taking advantage of Matlab functionality provided through the Matlab Distributed Computing Server (Abed and McGough, 2010). Grid computing provides the opportunity to run large numbers of independent jobs concurrently (McGough et al., 2010; Guan and Wu, 2010). This technique can be implemented through utilising the intelligent processing Condor project (Condor, 1988; Litzkow et al., 1988).

Condor provides a powerful job invocation environment which is capable of successfully executing large sets of parameter sweep jobs. Parameter sweep operations relate to the execution of many similar jobs, which are run by changing only the input parameters. Therefore, adopting a Condor-based approach was essential in order to feasibly process the datasets in this research. Condor provides the ability to perform checkpointing and migration of executions on remote computers where inputs and outputs from a user program are staged back to the submitting computer. Checkpointing is an intelligent application which is often used in grid computing to save intermediate data on a reliable storage for a period of time during long term processing. This technique is basically used to recover the run in case of job failure rather than restart the application from the beginning (Blythe et al., 2003). This can effectively save computing time and provide more elastic processing workflow in cases of complicating computation and large datasets. However, this requires the user to compile his/her own code alongside the Condor libraries which run under a UNIX based operating system. This is something which is not always possible - such as when using a commercial package like Matlab. Therefore, it would be desirable to provide some equivalent functionality to checkpointing, to help reduce failed execution time in Condor.

For effective run time reduction, the execution routine implemented within Condor in this research is based on two main aspects. Firstly, the data can be used many times as soon as it is staged to the Condor computer, where data staging is a managing process between the submitting and the remote computers for efficient grid deployment (Elwasif et al., 2001). Secondly, data generated on the Condor computer can be staged back to the submitting computer as soon as possible. That means the routine has separated the data staging part of the Condor job submission from the job deployment phase and provides a mechanism for returning data to the user while the code is still running on the remote computer. The user is required to provide new logic in the form of how to process the returned data and how to deal with incomplete returns when the job is evicted before complete execution.

The application that is used within the Condor system to run the data is packaged into a compressed archive to facilitate transfer files and reduce time needed for submission. The Condor cluster at Newcastle is composed predominantly of ~1100 Windows computers (~3000 CPUs in total), thus the scripts are written as Windows Batch files. Therefore, these files are converted to UNIX shell scripts to be compatible with the Condor library's operating system. The 7zip archive format (see Condor, 1988 for details) is used for data compression as this was already deployed across the Newcastle Windows clusters. As the clusters work under the Windows operating system, the server then starts to submit Condor jobs containing archive and Java client to the cluster, as Java Script code is written into an HTML page and can be read with any browser regardless the computer operating system (Lindholm and Yellin, 1999). To prevent excessive load on the server, the number of jobs that can be launched at any one time and the frequency at which these are launched is limited. As each job starts to request sub-jobs from the server, the server can deploy new jobs into Condor until the pre-defined limit is reached.

Following this, the Java client can request the next piece of work from the server side. As the link between data transfer and execution has now broken, and the data has already been staged to the server, requesting sub-jobs can be as small as possible with the client asking for further tasks without having to re-request data from the submitted computer or re-downloading the original dataset. The execution of the original application is invoked by Java which is able to send back the results of these sub-jobs to the server immediately on completion. The client is now able to contact the server for further sub-jobs and will terminate only when being instructed by the server or due to eviction of a Condor job from the host computer. Figure 3.6 illustrates the overall architecture of the developed routine.

The Matlab code has been compiled into a binary executable using the Matlab compiler. This code requires a number of configuration arguments. The data file, the index file which defines a unique index number for individual FWF echoes, the data point within this file to process, the path where to write the output and index data for this output file. All of these parameters will remain the same except for the data point to process. The shell script is passed through this index before invoking the Matlab executable. The code written for the client takes the output file and the index entry for this output file and returns them after successful execution.

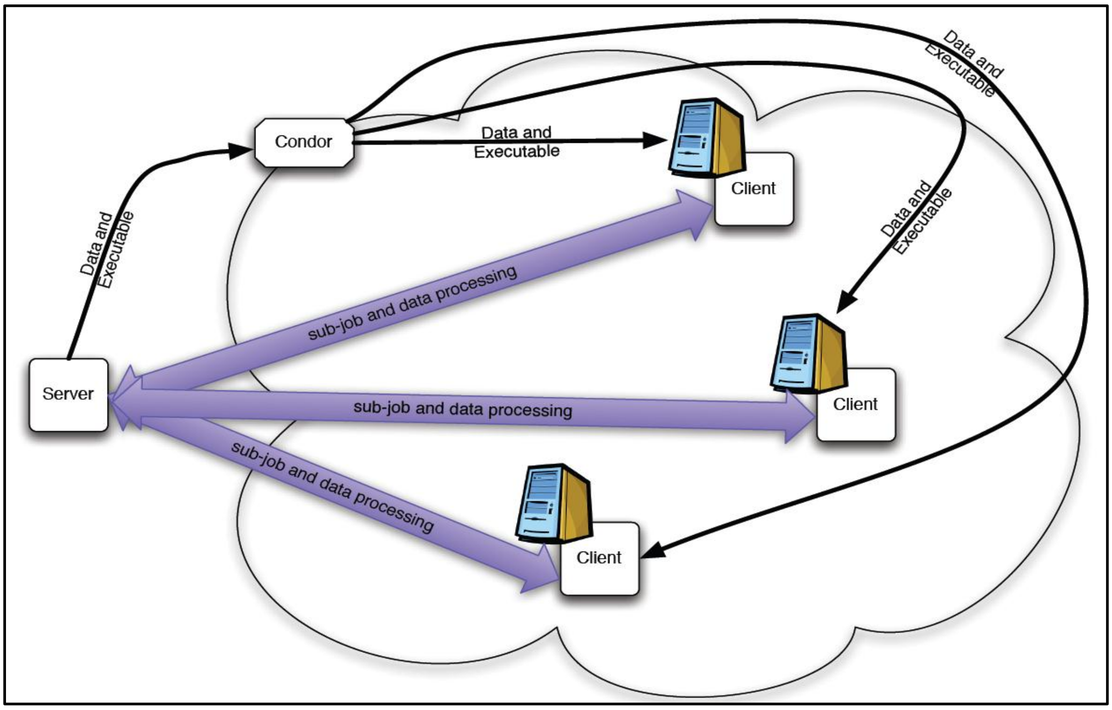

Figure 3.6. The general architecture of the developed Condor-based FWF-ALS data post processing.

The presented technique essentially reverses the normal Condor push job model (sending successive jobs without any interaction with the client after submission) into a client based pull model (an efficient interaction between the client and the server computers controlled by the client). This is particularly useful in situations where the user has large datasets which require significant time to distribute to worker nodes, allowing nodes which already have the data to keep on requesting sub-jobs until either evicted or all sub-jobs are completed. The developed approach was used to process both FWF-ALS datasets (Bournemouth 2008 and Bristol 2006). In the Bournemouth dataset, only 15 flightlines out of 19 were processed due to the reasons explained in Section 3.2. In contrast, all eight flightlines from the Bristol dataset were successfully processed by the developed routine.

The introduced technique was capable of reducing run time by 100-300 % depending on dataset density and submission configurations, as it lends itself best to programs where a large data set is used repeatedly, which means that a large number of jobs can run concurrently on Condor.

3.4 FWF DATA NORMALISATION USING ROBUST SURFACE NORMAL ESTIMATION

Incidence angle is a function of illumination direction from the sensor to the target and the surface normal vector associated with the point. Figure 3.7 illustrates the perfect case when the terrain surface is completely flat, where *N* is the normal vector, *R* is the range between the sensor and the target, α is the incidence angle, and A_i is the area illuminated by the laser beam (refer to Section 2.5.2 for details). In this research, the FWF echo amplitude signals have been normalised as a function of the incidence angle effect. The standard Lambertian reflection model has been adopted to normalise the signals.

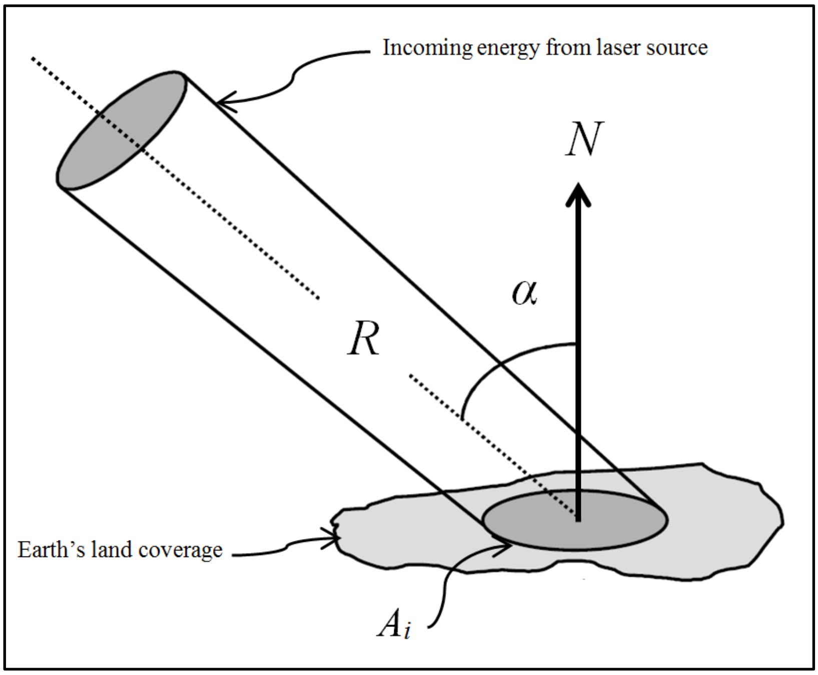

Figure 3.7. Incidence angle definition as a function of illumination direction between the sensor and target, and the normal vector (*N*).

3.4.1 Normal Vector Estimation using the RSN Method

Since a minimal size of neighbourhood should be maintained to accurately estimate surface normal (Filin and Pfeifer, 2005), a novel method that uses a limited number of points to define the normal vector of individual echoes has been developed. This new approach, termed the Robust Surface Normal (RSN) estimation method, is based on the *k*-nearest neighbours algorithm. It defines the 3D spherical volume by including only the three nearest Euclidian neighbouring points to the point in question. The well-known theory of 3D moment invariants has been adopted to estimate the normal vector (refer to Section 2.5.2.2). For the sake of simplicity, the moment order is restricted to $i+j+k <= 2$ in this research. The method works on a flightline basis, so the three nearest neighbours are acquired from a single flightline, and then the procedure is repeated separately for additional flightlines. As it cannot be assumed that natural terrain targets are composed of homogeneous material coverage, signal echo amplitude has been applied as a weighting function to individual echoes in the 3D moments definition, motivated by the findings of Jutzi et al. (2005).

With the output symmetric covariance matrix generated for each echo (refer to Section 2.5.2.2), the eigenvector will be determined based on the smallest eigenvalue computed in the defined 3D volume. This eigenvector represents the required normal for each point in question if, and only if, the defined spherical volume is comprised of those points belonging to the same plane. In reality, this assumption may not always be valid due to the varying distribution of neighbourhood points. It is therefore necessary to validate the computed normal. Although a planarity check (e.g. West et al., 2004) could discard points from other planes and deliver more reliable normal vector estimations, localised roughness trends are still hard to overcome and may be erroneously considered as forming a single plane. Therefore, a simple assumption based on the vector dot product in 3D space is adopted.

The dot product between two perpendicular vectors is equal to zero in Euclidian geometry. In each defined 3D spherical volume it is necessary to prove the vector ***V*** between the point in question (P) and the centre of gravity (C) which was estimated from the three neighbourhood points plus P itself, is perpendicular to the normal vector ***N*** (Figure 3.8).

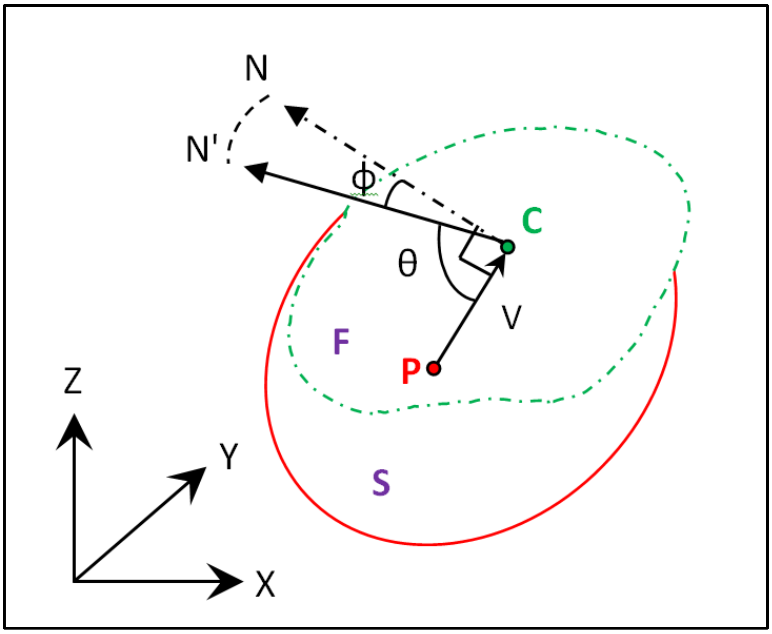

Figure 3.8. The geometric relationship between point P and C (COG) in Euclidean geometry.

In Figure 3.8, S represents the 3D neighbourhood domain of point P, F represents the generated plane from point C and the true normal vector N. N’ represents the estimated normal vector, V is the vector between C and P, θ describes the angle between vectors V and N’, and ϕ defines the uncertainty in the normal vector estimation due to noise effects in the ALS points, as explained below in relation to Figure 3.9.

In perfect conditions and when both points are belonging to the same plane, θ should be equal to 90° and ϕ equal to 0°. Therefore for validation purposes, a check is performed to determine how θ deviates from the perpendicular condition (by means of ϕ = abs [90°- θ]), with the definition rejected where ϕ exceeds a predefined threshold.

Figure 3.9 describes the threshold determination of ϕ based on the theoretical vertical accuracy (m_Z) of point C and the horizontal distance (D) between point C and the theoretical point of interest P in the neighbourhood system. The angle ϕ represents the uncertainty level in the estimated normal and is dependent on the values of D and m_Z. In this case, the distance, D, is derived from the spatial resolution of the dataset. It is therefore essential to check the point density after FWF post processing and consider the accuracy in the laser data for optimal estimation of D and m_Z respectively. This enables the determination of a reasonable threshold value which is then used to determine whether to accept or reject the definition of the 3D volume, following Eqn. 3.1.

$$\phi = tan^{-1}\left(\frac{m\_Z}{D}\right)$$ **Eqn. 3-1**

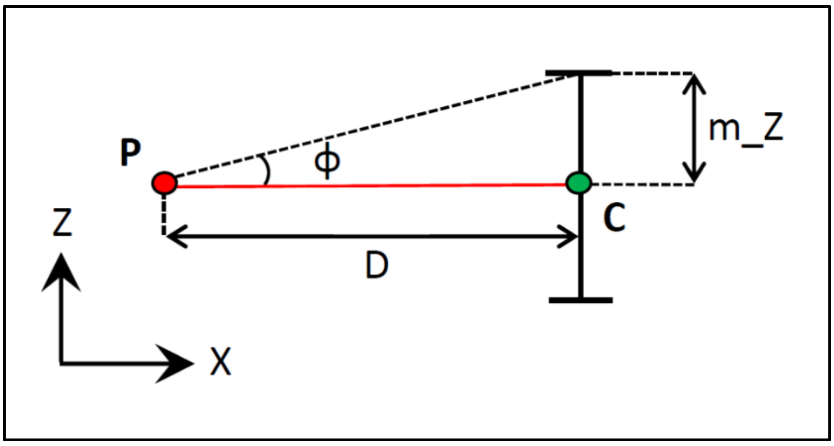

Figure 3.9. Threshold determination of ϕ.

Heuristic investigations based on *K*-d tree search results (refer to Section 2.5.2.3) were made following FWF post processing. This determined that the mean Euclidian distance from the third farthest neighbouring point to point P approximates to 0.3 m and 1.5 m for the Bournemouth and Bristol datasets respectively. As point C would lie somewhere between P and the third farthest neighbouring point, these distances will be considered as upper limits for D in Eqn. 3.1, as specified for each dataset respectively.

The vertical accuracy of each individual point cloud is a function of both range and scan angle accuracies (Figure 3.10), where β is the scan angle. Refer to Section 2.5.2.1 to avoid confusion between the scan angle and the incidence angle. The laser range accuracy and scan angle resolution for the Riegl LMS-Q560 system are quoted as 20 mm at 1Ϭ (60 mm at 3 Ϭ), and 0.001° respectively (Riegl, 2009). Therefore, error propagation theory is applied (Eqn. 3-2 and 3-3) using these values, delivering a value of 60 mm (3Ϭ) for the vertical accuracy (m_o) of a single point in the system which was found, coincidentally, to be identical to the range precision. Note that the super script (Ϭ) has been used throughout the thesis to denote sigma (standard deviation) to avoid confusion with the backscatter cross-section parameter which denoted by (σ).

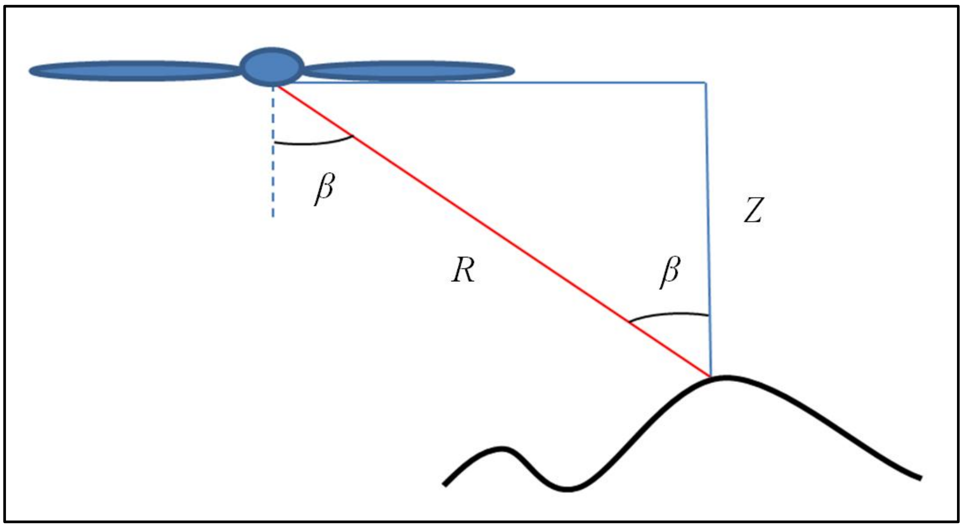

Figure 3.10. The Derivation of the vertical accuracy (m_o) of a single laser point as a function of both range (R) and scan angle (β) accuracies.

$$Z = R\cos\beta \qquad \textbf{Eqn. 3-2}$$

$$m_o = \sqrt{\left(\frac{\partial Z}{\partial R}\right)^2 \cdot 6_R^2 + \left(\frac{\partial Z}{\partial \beta}\right)^2 \cdot 6_\beta^2} \qquad \textbf{Eqn. 3-3}$$

As point C is estimated from the three neighbourhood points plus point P itself, the combined accuracy of these points should be considered in order to estimate the level of uncertainty in the geometric position of point C. A mathematical derivation of the relationship between the estimated surface height due to this positional uncertainty effect and the number of laser points used to generate the surface is presented by Filin and Pfeifer (2005) and described in Eqn. 3.4.

$$m\_Z = \pm \frac{m_o}{\sqrt{n}}$$ **Eqn. 3-4**

Where m_o is the accuracy of laser points, and n the number of points used to define the system.

This formula assumes the explicit plane model *z* = *f(x,y)* to estimate the local plane parameters (see Filin and Pfeifer (2005) for derivation). However, in this research the implicit form *f(x,y,z) = 0* was performed to estimate plane parameters for individual points by the 3D moment definition, as points could be inverted from vertical and near vertical features if the form *z* = *f(x,y)* is utilised.

Following this, Eqn. 3-4 delivers a value of ± 30 mm for m_Z, which equates to the upper level of uncertainty in point C due to noise effects as illustrated in Figure 3.9. Consequently, following Eqn. 3-1, approximate values of ± 6° and ± 2° can be adopted for ϕ in the Bournemouth and Bristol datasets respectively. These values define sensible thresholds for accepting the 3D volume definition and applying the normal estimation for further processing.

Thereafter, the angle θ between the two vectors V and N' is computed based on the dot product following Eqn. 3.5 (Fraleigh and Beauregard, 1995), and an estimation of the deviation from the perpendicular condition (by means of ϕ) is performed for the individual 3D volume system.

$$\theta = cos^{-1}\frac{V \cdot N'}{|V||N'|}$$ **Eqn. 3-5**

If ϕ (i.e. 90°- θ) exceeds the predefined threshold, a further check will be performed to compute the distance between P and C for the current definition in order to assess the possibility of both P and C belonging to the same XY plane but having different elevations. If this distance happens to be equal to zero then the system will be accepted, otherwise the current neighbourhood system will be rejected and a new definition will commence. Any one or more of the included points used to define the neighbourhood system could be the cause of the rejection. Therefore, vectors are computed from each of the three candidate points to point C and ϕ is computed. The point that most exceeds the allowable predefined threshold is rejected from the system and the next nearest point is used as replacement to define the new neighbourhood system. Thereafter, a new normal estimation will commence, followed by planarity checking as previously stated.

If the threshold is met, the normal will be verified and adopted, otherwise the procedure will iterate until the optimal normal value is delivered with the condition that D should not exceed the predefined value. If no optimal value is detected, a new assumption will be considered by adopting the neighbourhood system that delivers the smallest value for ϕ amongst all tested systems and accepting this as the best possible normal estimation for the point of interest.

3.4.2 Incidence Angle Estimation and Echo Amplitude Normalisation

Trajectory information was available for both datasets from the data provider. As stated earlier, the incidence angle is a function of the illumination direction from the sensor to the target and the normal vector associated with the point (Figure 3-7). Therefore, linear interpolation which defines the concatenation of the linear interpolated points between each successive trajectory records was performed. This enabled the computation of illumination direction between the sensor and individual ALS echoes. Thereafter, incidence angle estimation was undertaken between the normal estimated from the RSN method and the illumination direction of each individual echo following Eqn. 3-5. However, in this case V is defining the illumination direction between the sensor and individual echoes while θ delivers the incidence angle.

Thereafter, the echo amplitude signals of the individual ALS points were normalised using Lambert’s Cosine Law for all selected targets in both datasets, following Eqn. 3-6.

$$A_N = \frac{A_O}{\cos(\alpha)} \qquad \textbf{Eqn. 3-6}$$

Where A_N is the normalised echo amplitude signal as function of the incidence angle effect, A_O is the original echo amplitude signal, and α is the incidence angle.

3.5 RADIOMETRIC CALIBRATION ROUTINE

The variables which affect the physical characteristics of the FWF during travel from the sensor to the surface target and back can effectively cause a mis-match between the backscatter signals delivered from overlapping flightlines. A comprehensive radiometric calibration strategy must be capable of robustly eliminating the effects of all these variables and delivering more reliable radiometric information relating to ground features for further downstream applications. Eliminating the discrepancies of FWF backscatter signals between overlapping flightlines is the primary focus of the radiometric calibration routine presented in this research.

A practical and reliable radiometric calibration routine accounting for all the variables affecting the backscattered energy, including the essential factor of angle of incidence is presented herein. The routine is based on the radar equation (refer to Section 2.5.1) and relies on the robust incidence angle estimation using the developed RSN method introduced in the previous section. This includes the estimation of four different backscatter parameters (σ, γ, σ_α, γ_α) for individual laser echoes. The backscatter cross-section parameter (σ) and backscatter coefficient (γ) were firstly proposed by Wagner et al. (2006) and Wagner (2010) respectively. The normalised version of those two parameters with respect to incidence angle (σ_α and γ_α) has been discussed by Lehner and Briese (2010). However, no comprehensive studies focusing on these parameters over specific land cover types has been presented in the scientific literature so far. The complete workflow of the developed radiometric calibration routine considering all these factors is illustrated in Figure 3.11. As the incidence angle estimation workflow (red part) has been discussed in detail in the previous sections, the next few sections will only discuss the remaining parts of the flowchart illustrated in Figure 3.11.

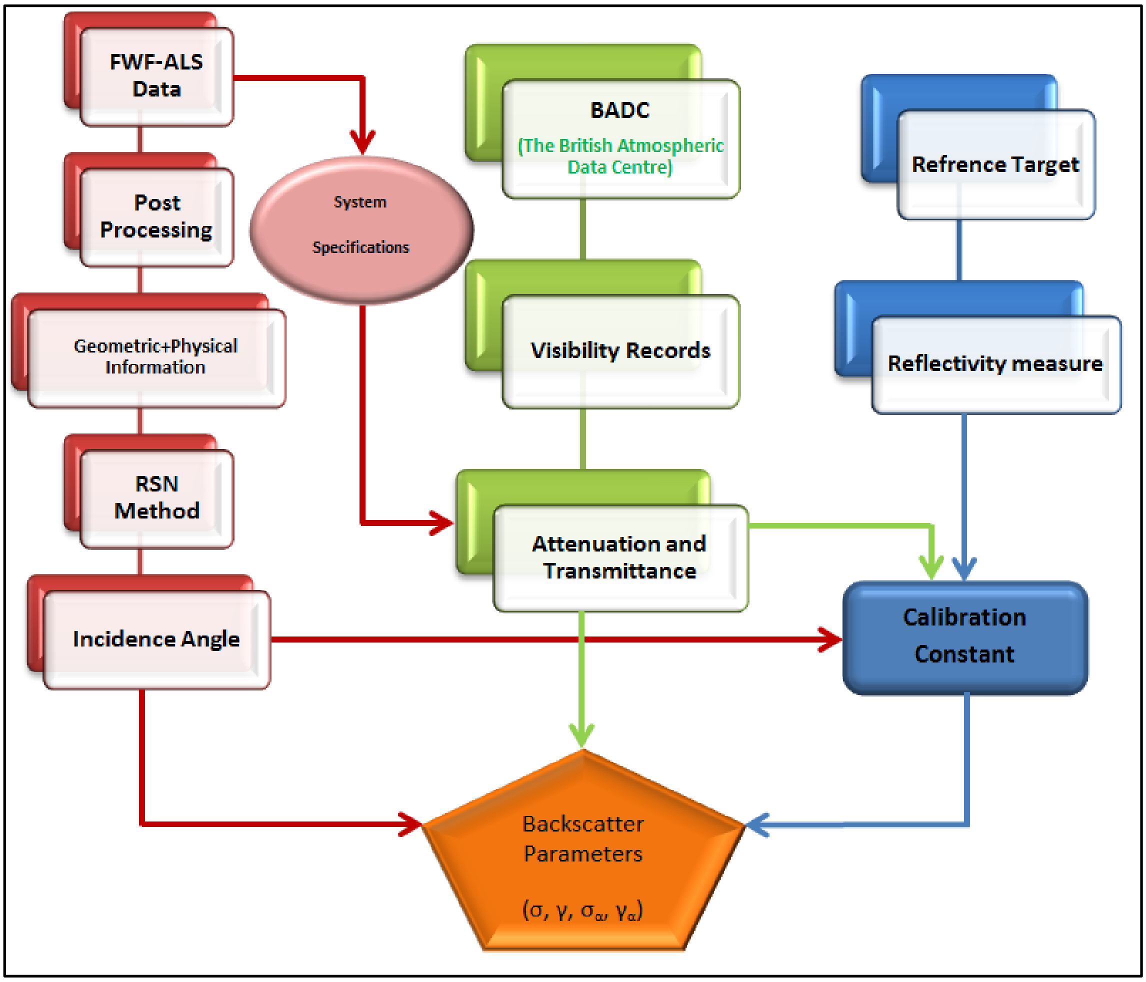

Figure. 3.11. The flowchart of the developed radiometric calibration routine.

3.5.1 Modelling Atmospheric Scattering

In order to deliver a comprehensive calibrated backscatter signal, the energy loss due to atmospheric scattering and absorption effects during time of flight of the laser pulse should be considered in the calibration model (Vain et al, 2010; Briese et al, 2008; Höfle and Pfeifer, 2007). The calibration constant derived from the lidar adapted formulation of the radar equation comprises all unknown parameters in one ALS campaign, including atmospheric conditions alongside other variables affecting laser energy in the travel between the senser and the target. An absolute calibration routine aims to independently account for these effects to provide a calibrated backscatter signal which is free from such error sources. It is therefore required to deliver estimations of these effects including atmospheric scattering towards a reliable calibration constant value. Even if we presume the atmospheric scattering effect to be constant within a certain ALS campaign, the range strongly influnces this extinction (Höfle and Pfeifer, 2007). Therefore, it is highly recommended to model the atmospheric conditions and consider flying height dependency of η_{atm} on the day of scan for optimal calibration outcomes, especially with high flying heights and in bad weather conditions.

In this research the atmospheric transmittance has been estimated based on the model described by Höfle and Pfeifer, (2007) and presented in Eqn. 3.7.

$$\eta_{atm} = 10^{-2Ha/10000} \qquad \textbf{Eqn. 3-7}$$

Where η_{atm} is the atmospheric transmittance, H is the flying height in meters, and a is the atmospheric attenuation in dB/Km.

In order to estimate the atmospheric transmittance, which typically increases with higher flying heights (Jelalian, 1992), it is necessary to first estimate the attenuation coefficient. As the atmospheric attenuation coefficient of the laser power is strongly affected by laser wavelength and visibility, attenuation modelling was undertaken using the model described by Kim et al. (2000) as follows:

$$a = \frac{3.91}{V}\left(\frac{\lambda}{550}\right)^{-q} \qquad \textbf{Eqn. 3-8}$$

Where V is the visibility measured in km, λ is the wavelength in nm, and q is the size distribution of the scattering particles.

The British Atmospheric Data Centre (BADC) provided the visibility records from the nearest metrological stations to both investigated study sites. The climate station details and the delivered visibility records on the day of the surveys are listed in Table 3.1 for both the Bournemouth and Bristol study sites.

Study Site	**Climate Station**	**Station's Latitude (°)**	**Station's Longitude (°)**	**Station's Elevation (m)**	**Visibility (km)**
Bournemouth	Kings Park station	50.734	-1.822	27	2
Bristol	LULSGate	51.383	-2.713	189	25

Table 3.2. Atmospheric visibility records of both investigated datasets.

As for the size distribution of the scattering particles, the following assumption has been utilised based on experimental results presented by Middleton (1952) and described in Eqn. 3.9.

$$q = \left\langle \begin{array}{ll} 1.6 & \text{if } \mathrm{V} > 50\ km \\ 1.3 & \text{if } 6\ \mathrm{km} < V < 50\ km \\ 0.585\ V^{\frac{1}{3}} & \text{if } \mathrm{V} < 6\ km \end{array} \right\rangle \qquad \textbf{Eqn. 3-9}$$

Once the atmospheric transmittance is delivered for individual datasets, it used to deliver the calibration constants to account for this effect for all laser echoes in subsequent datasets.

3.5.2 Measurement of Reference Target Reflectivity

In order to estimate the backscatter parameters for all echoes in both datasets, it was necessary to use reference targets with known reflectivity values in order to estimate the calibration constants (refer to Section 2.5.1 for details). These targets should be deployed before scanning and successive reflectivity measures should be undertaken throughout the scanning mission to deliver the best reflectivity estimation for these reference targets under the conditions experienced at the time of survey.

In the case of Bournemouth, 24 1 m-radius circular "photogrammetric" PVC fabric targets (see Figure 3.12) were distributed across the urban and rural sites as shown in Figure 3.13 and 3.14 respectively. The targets were set-up in the field as control targets for strip adjustment calibration and not particularly for radiometric calibration purposes. These targets were subsequently then utilized as reference targets for radiometric calibration in this research.

Figure. 3.12. Reference target in Bournemouth study sites.

Although successive reflectivity measures should be undertaken for the reference targets during data capture to guarantee the same surface conditions such as wetness, dirt, etc., this condition was not met in this dataset since radiometric calibration was not the intended function. Therefore, post-survey indoor reflectivity measurements using an Analytical Spectral Device (ASD) with two different fore-optics (1° and 8° FOV) and in two different modes (white reference and raw mode) were undertaken.

ASD is a FieldSpec Pro spectroradiometers which is widely used in remote sensing applications to deliver spectral measurements such as reflectivity to the targets in the field. It works with a high resolution of a 350 - 2500 nm spectral range and has two lenses used as a fore-optic attachment to the fibre-optic cable. This helps to apply the measurements with different incidence angle settings using lenses of different field of views for better comprehensive reflectivity measurements. It delivers reliable spectral measurements as it offers a superior signal enhancing components, refer to NERC (2009) for details. Different incidence angle measurements, between 0° and 90°, were performed, in order to deliver the optimal reflectivity estimations for the reference targets.

The measurements were conducted in a dark room using a portable lamp mounted on a fixed tripod for illumination purposes. The height of the tripod was 0.54 m and the lens height was 0.44 m. This set-up was configured to avoid generating shadows during the measurements process. The measurements were undertaken successively using 1° and 8° optics over multiple regions of the reference target to assure homogeneity. For each lens, five different sets of incidence angle measurements were undertaken at 0°, 10°, 20°, 30°, and 40° of successive 25 measurements per angle using white reference and raw modes, refer to MacArthur (2007a; 2007b) for further details about measurements modes.

The ASD delivers spectral data files in a binary format. Therefore, these files have been converted into ASCII files using the View Spec Pro program available for free download from ASD (2009). Thereafter, post processing of the recorded spectral data was undertaken using Excel Post Processing Template files provided by NERC (2009). This included comparing the recorded data with the ASD white-reference reflectivity (Spectralon® panel), followed by mean value computations for individual lenses to deliver the best absolute reflectivity estimation for the reference target from different incidence angle settings. Figure 3.15 shows a sample of nadir measurements with a 1° fore-optic.

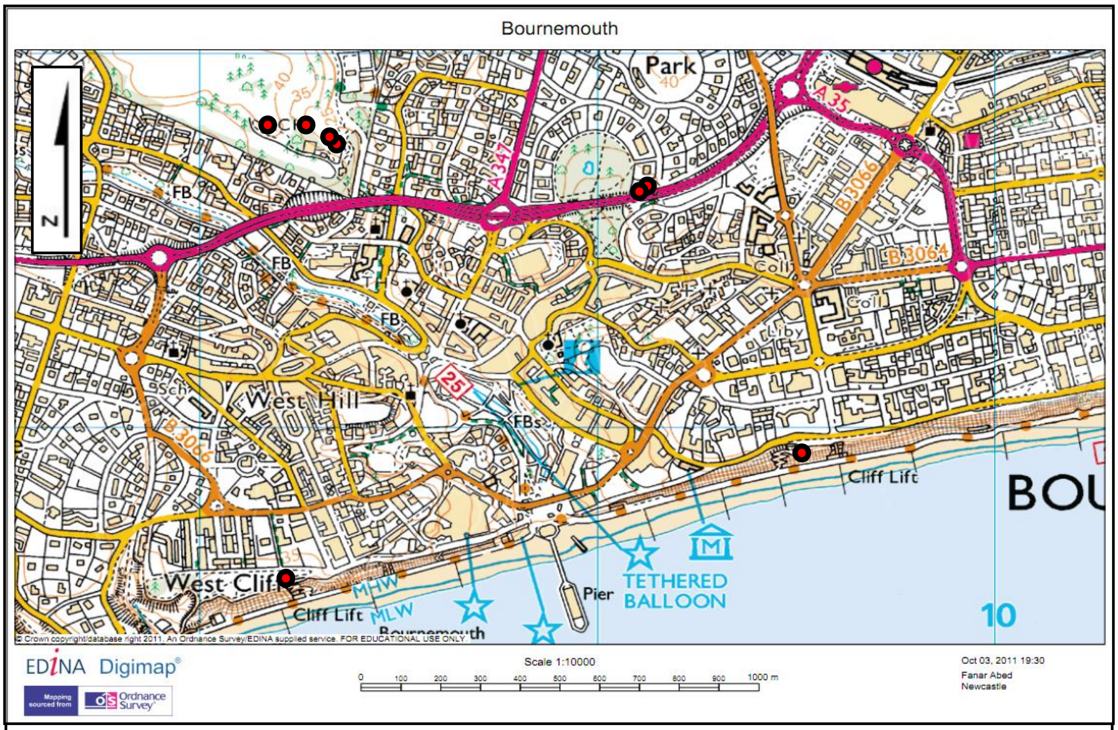

Figure. 3.13. Reference target distribution in Bournemouth urban sites.

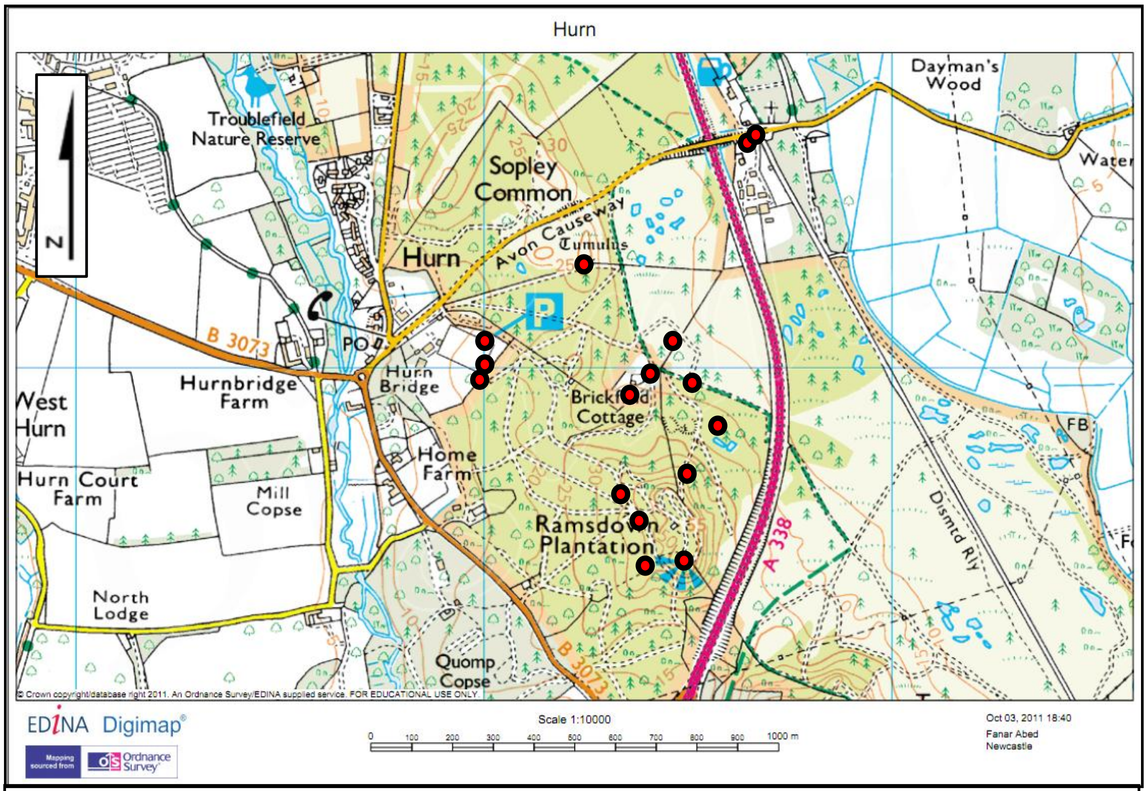

Figure. 3.14. Reference target distribution in Bournemouth rural sites.

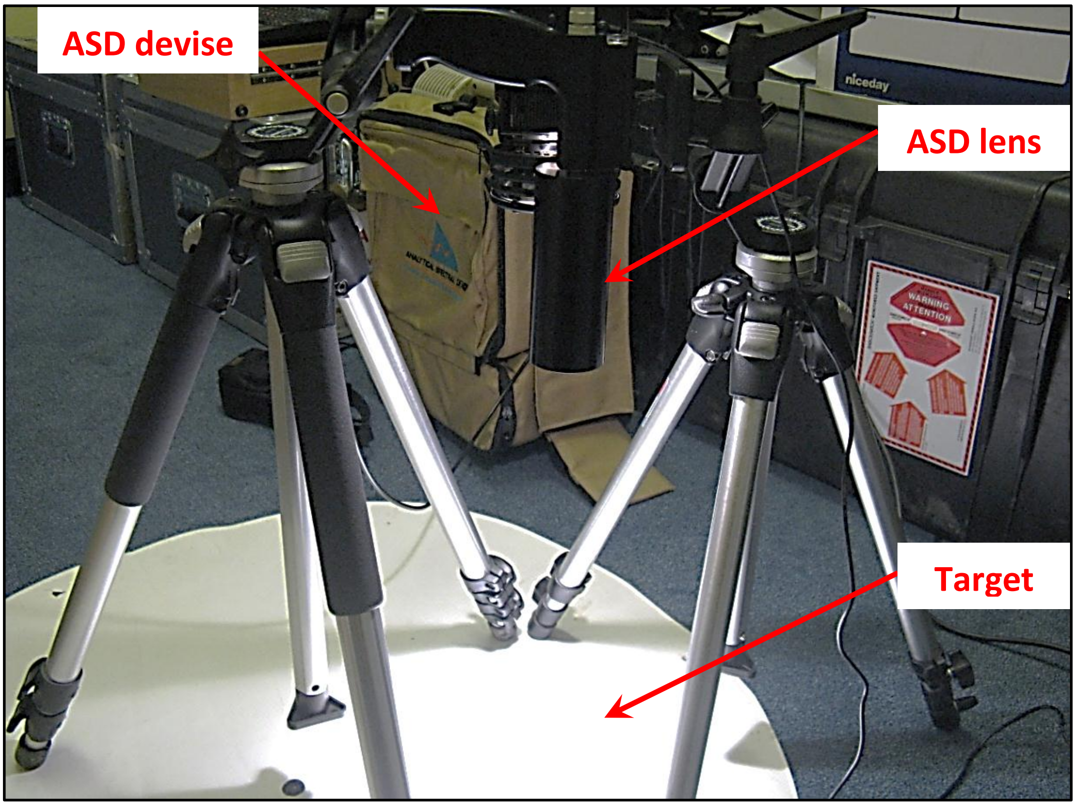

Figure. 3.15. Reflectivity measurements using the Analytical Spectral Device.

A total of 754 points were delivered from 22 of the 24 reference targets (as 2 of the reference targets had been set out above shorelines where data was not processed (refer to Section 3.2). These echoes have been used to estimate the calibration constant for the Bournemouth dataset.

In the case of Bristol dataset, no reference targets were deployed prior to the ALS campaign. Therefore, natural reference targets had to be utilised for radiometric calibration purposes. Eight asphalt road sections were selected from different flightlines, comprising a total of 966 laser points. These were then used to deliver the calibration constant for the Bristol dataset. A value of 0.25 was adopted for asphalt reflectivity in this research for the Bristol dataset, based on previous experiments presented by Briese et al. (2008). Figure 3.16 shows the distribution of the selected asphalt sections across the Bristol site. It was necessary to ensure that the point selection was very precise in order to avoid including white road markings, road edges, or any distracting minor features other than asphalt. As the reference targets used at both sites were not guaranteed to be perfectly flat, incidence angle has been estimated across all reference target echoes to account for this effect in both datasets, and was consequently considered in the calibration process.

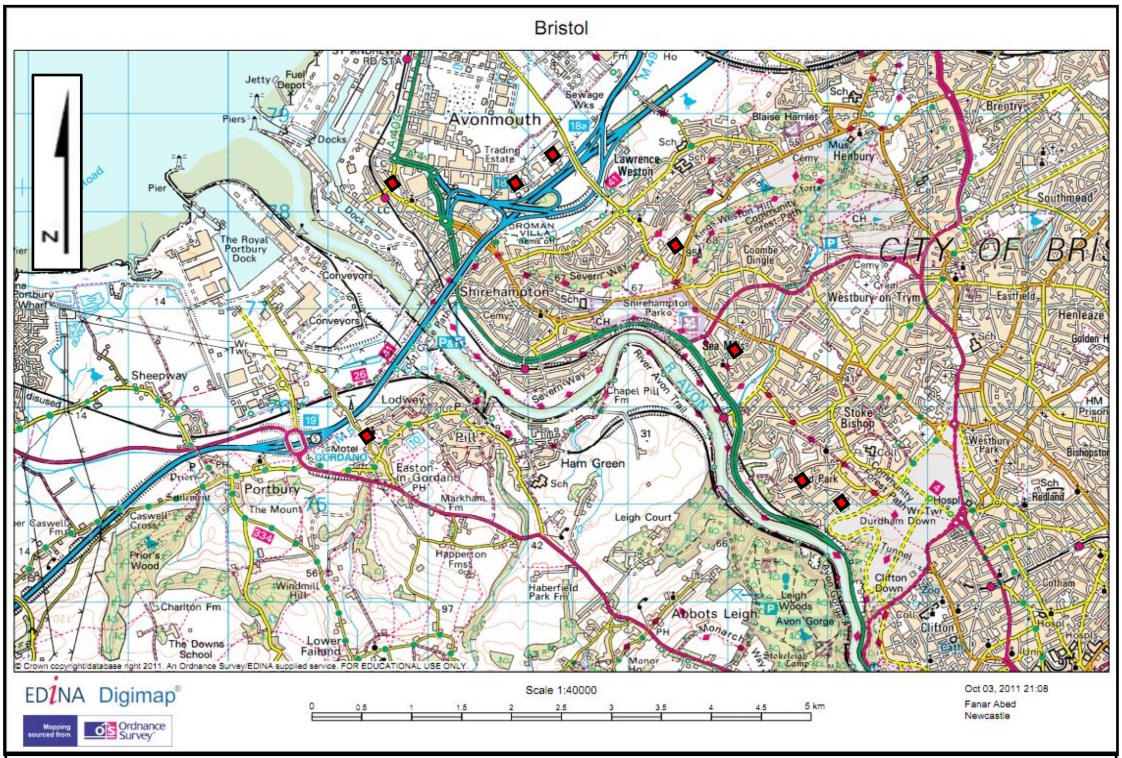

© Crown Copyright/database right 2011. An Ordnance Survey/EDINA supplied service. FOR EDUCATION USE ONLY.

Figure. 3.16. Reference target distribution at the Bristol site.

3.5.3 Estimation of the Calibration Constant

As the backscatter coefficient has a close relationship with bi-conical reflectance (refer to Section 2.5.1), it has been considered as the parameter of choice to estimate the calibration constants of both investigated datasets in this research. The backscatter cross-section was firstly estimated for all individual echoes from the reference extended targets in both datasets following Eqn. 3.10 (Jelalian, 1992).

$$\sigma = \pi\rho R^2\beta^2$$ **Eqn. 3-10**

This includes 754 echoes from the PVC targets in Bournemouth and 966 echoes from the natural targets in Bristol. An ideal Lambertian scatter has been assumed in the case of reference targets, with the incidence angle effect considered in the reflectivity computations following Eqn. 3.11.

$$\rho = \rho_o \cos(\alpha) \qquad \textbf{Eqn. 3-11}$$

Where ρ is the reflectivity when assuming an ideal Lambertian scatterer, ρ_o is the reflectivity at incidence angle zero, and α is the incidence angle.

As the emitted laser energy is not guaranteed to remain constant throughout the scanning process, it is necessary to consider whether more than one calibration constant should be adopted for the flight campaign. Therefore, the possibility of adopting multiple calibration constants, on a flightline by flightline, basis has been investigated.

As the backscatter energy is described as the product of FWF echo amplitude and width, it is affected by the strength of both aspects. Therefore, both pulse amplitude and width should be analysed within individual flightlines. This has been implemented by estimating simple statistics such as minimum, maximum, mean, standard deviation, and coefficient of variation for these parameters for all echoes per flightline. This can help to reveal the shape and the distribution of the echo amplitude and width signals in both datasets before calibration.

The analysis of echo amplitude and width from both datasets shows that the backscatter signals were relatively stable, with no serious variations in the emitted pulse that could adversely affect the backscatter signal in particular flightlines. Based on this evidence, a decision was made to adopt a single calibration constant for each campaign.

Calibration constants were then delivered for all reference target echoes in the Bournemouth and the Bristol datasets as illustrated in Eqn. 3.12, refer to Section 2.5.1 for details.

$$C_{cal} = \frac{\gamma\, \eta_{atm}}{4\pi R^4 \hat{P}_i s_{p,i}}$$ **Eqn. 3-12**

This means that both the incidence angle and atmospheric effects have been considered over reference targets echoes. To avoid noise effects, a mean calibration constant was determined after excluding all outlier points. The calibration constants for the two datasets were subsequently utilised for the determination of the four backscatter parameters (σ, γ, σ_α, γ_α) for individual echoes of the entire datasets following Equations 2.4, 2.9, 2.10, and 2.11 respectively.

3.5.4 Estimation of Backscatter Parameters

The methodology proposed to calibrate FWF backscatter signals aims to eliminate the discrepancies in the signals delivered from overlapping flightlines. This can be considered as a radiometric strip adjustment procedure, aiming to improve the relative accuracy of the overall backscatter signal.

To achieve this goal, it was proposed to find the backscatter parameter that delivers the best match between signals from overlapping flightlines after calibration. In order to achieve this, it was necessary to undertake a detailed study over different land cover types and analyse the individual results.

In order to carry out this study, it was necessary to consider all factors affecting the backscatter signal. Therefore, four different backscatter parameters (σ, γ, σ_α, γ_α) were estimated for individual echoes within the selected target regions tested in this research. The σ_α and γ_α parameters demonstrate the influence of the incidence angle effect on the reflected backscatter signal. Additionally, these parameters also reflect the performance of the developed incidence angle estimation using RSN method.

These backscatter parameters were then adopted to develop an improved segmentation technique, which is better able discriminate between surface features with similar geometric characteristics but differing surface characteristics, following a reliable and automatic routine.

3.6 DEVELOPMENT OF AN ENHANCED SEGMENTATION TECHNIQUE

Segmentation approaches presented in scientific literature are highly reliant on geometric information alone to group laser points into classes which exhibit similar characteristics. However, the calibrated backscatter signals delivered from FWF systems can enhance the identification of surface features, by offering improved discrimination between different targets with otherwise similar geometric attributes such as mowed grass and asphalt. The developed segmentation routine presented herein aims to integrate the calibrated backscatter signals in order to overcome the weaknesses in the available approaches.

Regarding the optimal backscatter parameter to use in the developed segmentation routine, and considering the four presented parameters, radiometric calibration analysis shows that no general assumption can be applied to all surface feature types. However, two main classes do appear to be clearly distinguishable based on their surface roughness specifically vegetation and non-vegetation. However, it is not possible to differentiate between the two on the basis of an exact roughness value. However, experimental studies should help to deliver a better understanding of roughness, and ultimately lead to the determination of threshold settings for specific datasets.

It has been shown that pulse width is the optimal parameter in terms of defining roughness (Lin and Mills, 2009; Doneus and Briese, 2006). Consequently, in this research, analysis was performed in order to assess the behaviour of pulse width over different land cover types in both investigated datasets. The goal of these analyses was to discriminate between land cover classes in order to facilitate the selection of the optimal backscatter parameter to use in the segmentation routine. The developed segmentation strategy includes two main stages: segmentation criteria computations, and segmentation strategy to group points into meaningful segments. Both stages are described and discussed in detail in the following sections.

3.6.1 Characterising the Developed Method

The segmentation routine presented in this research adopted the following considerations:

1. The raw unstructured 3D point clouds were used as input to the developed routine. This included all FWF echoes delivered from data post processing stage. No interpolation or thinning of the original data was performed prior to segmentation.
2. The method is reliant on integrating the calibrated backscatter parameters with the geometric information from FWF.
3. As the normal vector is considered as the optimal criterion to define similarity between laser echoes (refer to Section 2.6.2) it was used herein as the only segmentation criterion.
4. The calibrated backscatter parameters were used as a weighting function in the normal vector definition to improve detecting homogeneous points that have similar criterion such as planarity, smoothness and physical characteristics.
5. The method used pulse width and the number of returns to discriminate vegetation.
6. Due to its reliability and flexibility, surface growing was the selected strategy to segment points, refer to Section 2.6.3.1.

3.6.2 Normal Vector for the Developed Segmentation Routine

The normal vector is a well-known geometric criterion which can well define the orientation of 3D objects and works efficiently in unstructured 3D point clouds. It can define the measure of similarity between 3D points by identifying points that belonging to same surface based on smoothness constraints (refer to Section 2.6.2). However, the possibility of discriminating points with similar geometric characteristics with otherwise different physical attributes such as artificial and natural bare ground cannot be reliantly offered from only geometric information. The backscatter parameters, which can only be delivered from FWF, are capable of defining the physical properties of the surface features. Therefore, a developed normal vector was estimated from integrating backscatter parameters with the standard geometric information and then selected to be the criterion of choice to segment FWF echoes in this research.

The normal for individual points has been estimated using the RSN method described in Section 3.4.1. However, this time the weighting function in the moment invariant definition used for individual echoes was the backscatter parameter delivered from FWF calibration instead of the original amplitude value. As four different backscatter parameters were produced for individual echoes from the calibration process, a condition was set based on the surface roughness and number of echo returns to select the optimal backscatter parameter for individual surface targets.

The estimated normal vectors from the RSN method deliver ϕ for individual points as an indicator of the uncertainty in the normal vector estimation due to noise effects. These values are subsequently used in the surface growing algorithm as a residual to select seed points. Therefore these values are saved in the memory for each point, and are called on later as a vector defined by point index number.

3.6.3 Surface Growing

After defining the segmentation criterion to be used, it is required to define the strategy to be implemented to group these points into meaningful segments. In this research, this was achieved through the adoption of a surface growing technique using robust normal vectors and their residuals. The technique was originally proposed by Rabbani (2006) (refer to Section 2.6.1.1), and has been further developed here using specific configurations which meet the aims of this research.

The inputs for the proposed algorithm are as follows:

- Point clouds (P_i) and their 3D coordinates, where i represents the point number.
- Normal vector for individual points (N_i). This is delivered from applying the RSN method as explained in Section 3.6.2.
- Normal vector residuals (ϕ_i) defined by ϕ from the RSN method.
- Residual threshold (ϕ_{th}). This constant defines the threshold of the maximum allowable limit required to upgrade the current point to be a seed point. It has been set to define the noise presence in the dataset. Therefore, values of 6° and 2° have been used for the Bournemouth and the Bristol datasets respectively.
- Nearest neighbour definition function (Ω_i) delivered from K-d tree search results.

- Difference angle threshold (δ). This constant defines the difference in ϕ between the normal of the seed region and the normal of neighbourhood points. This value is defined through experimental results where it was determined that a value of less than 5° may deliver meaningless segments. Therefore a 5° threshold value has been used in this research. However, this primarily depends on the application and features of interest.

Additionally, the conditions which should be maintained throughout the workflow are as follows:

- The points in a segment should be geometrically connected and the distances between them should be as close as possible. Following experimental investigations in both datasets using the K-d tree search function, it was found that using K=20 can meet the requirements in this research.
- The algorithm is searching for homogeneous and relatively smooth surfaces. Therefore, each segment should meet the following condition:
  $|N_p \cdot N_s| > \cos(\delta)$ Where N_p is the normal vector of the current point, N_s is the normal vector of the seed region, and <·> is the dot product.

The presented algorithm is described in Figure 3.17.

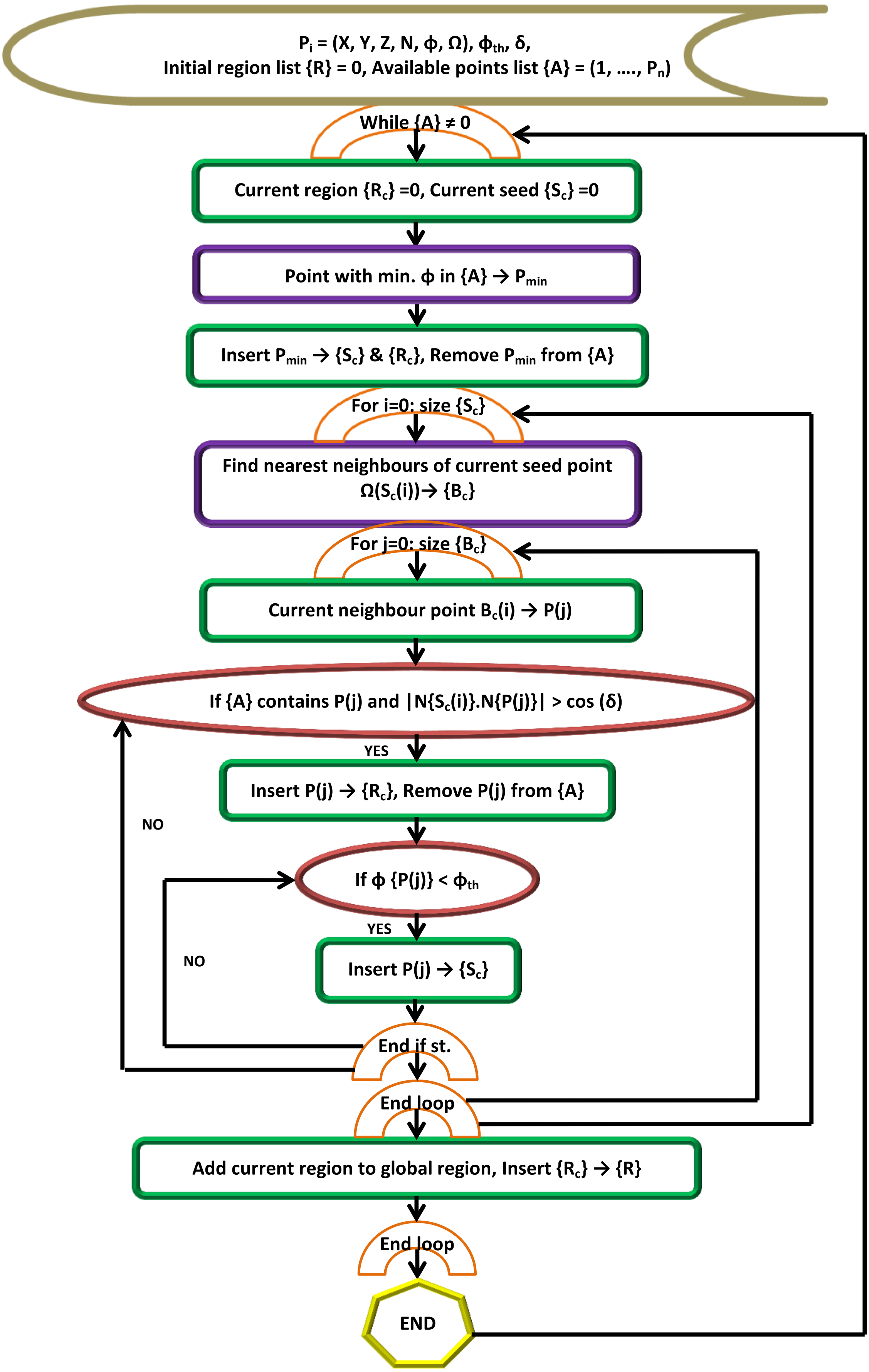

Figure. 3.17. Developed segmentation routine.

3.7 TESTING AND VALIDATING THE DEVELOPED METHODOLOGY

The developed methodology was implemented over different land cover types, including simple and challenging surface trends. The investigated features and interest areas have been selected from multiple flightlines and particularly from overlapping regions, to assess the accuracy and reliability of the proposed technique from different flying directions and positions. Both the new RSN method and the practical radiometric calibration routine were tested and compared to existing approaches. The developed segmentation algorithm was validated against a human-based manual workflow. This section deals with the main three parts of the methodology, discussing the testing and the validation approaches.

3.7.1 RSN Method and the Normalised Amplitude Signals

In order to overcome the signal amplitude discrepancies in adjacent overlapping flightlines over any land cover type, a more rigorous approach than currently existing methods was developed to estimate the normal for individual points. The overarching focus of the developed RSN method was to improve normalisation of the all-important echo amplitude parameter as a function of the incidence angle effect.

To check the validity of the developed approach, the method presented by Maas and Vosselman (1999) and improved by Gross and Thoennessen (2006), hereafter referred to as the spherical method, was implemented for comparison purposes. This method is based on defining the neighbourhood system within a fixed radial distance from the point in question (refer to Section 2.5.2.2). A 1 m and 2.5 m radius distance for the Bournemouth and Bristol datasets respectively was utilised. These optimised radial distances were selected based on testing data density over various land cover types in both datasets. Investigation of lower radial distances was shown to fail in the case of the selected targets. This was because the use of a lower radial distance resulted in the detection of a lower number of points than the minimum number required when applying the moment invariant theory (less than 3 points) over some features. This is mainly due to varying point density and point distribution over different land cover types.

Following normal vector computations, the incidence angle was estimated for each investigated target and values were delivered from the developed approach and the comparative spherical method. Thereafter, the echo amplitude signals of the individual ALS points for each selected target in both datasets were normalised using Lambert's Cosine Law.

The overlapping flightlines was used as a measure of the performance of the respective methods. The normalised signals for each target were then acquired from overlapping flightlines from both methods. The standard deviation of the echo amplitude for each target type was then acquired for each flightline, and the differences in standard deviation between overlapping flightlines was used as a criteria to compare the performance of the relative methods. This approach was undertaken to validate the RSN method after compensation for the angle of incidence effect over different land cover types as illustrated in Figure 3.18. Although the spherical method was originally designed primarily for planar surfaces, it was chosen for comparison here as the RSN method is also based on a spherical assumption. However, the main validation criterion is to compare the amplitude signals before and after normalisation from multiple flightlines.

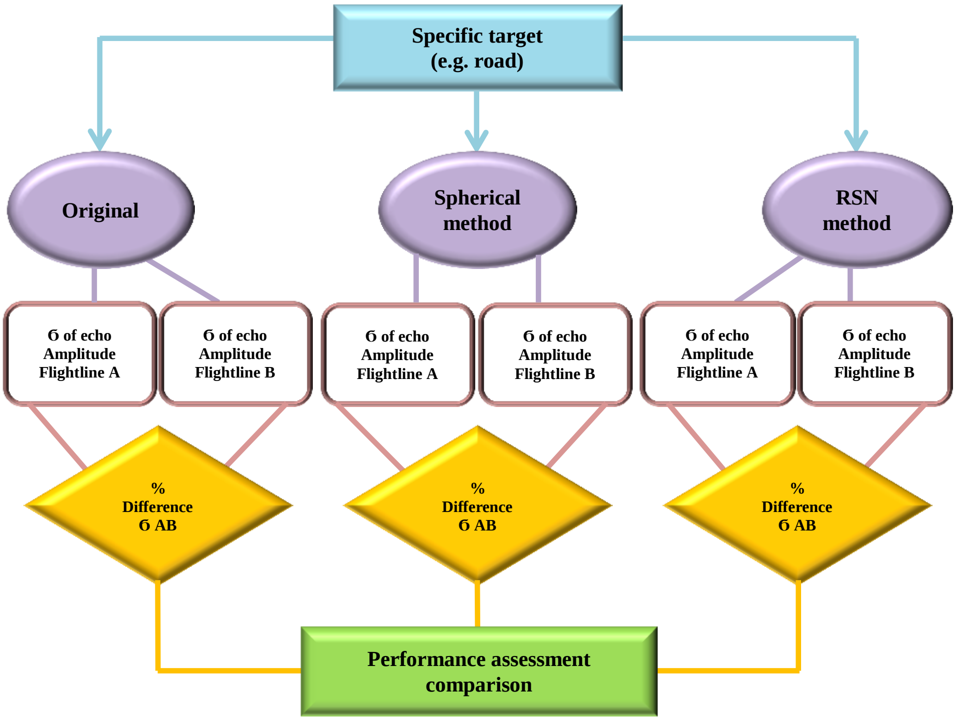

Figure. 3.18. RSN method validation workflow.

3.7.2 Radiometric Calibration Routine

In this research, a practical radiometric calibration routine for FWF data is presented and validated over different land cover types, including man-made and natural, with the aim of eliminating FWF backscattered signal discrepancies between overlapping flightlines. In contrast to other approaches, the developed routine utilises the backscatter coefficient instead of the backscatter cross-section parameter to deliver the calibration constant for the whole campaign. Moreover, the incidence angle effect has been considered in estimating the backscatter parameter of the reference target and the atmospheric transmittance was also accounted for when delivering the calibration constant.

The implemented method uses the radar equation and delivers calibrated backscattered signals by means of four different backscatter parameters (σ, γ, σ_α, γ_α). It was tested over several targets with different surface trends and properties. The results were analysed both visually and statistically and a comparison between the backscattered signals delivered from the overlapping flightlines presented for each target.

In order to assess the influence of accounting for the incidence angle effect on the calibration constant estimation, the developed method was compared with the method presented by Alexander et al. (2010) where the incidence angle effect over natural reference target echoes has been neglected. Furthermore, in order to assess the reliability of using the PVC targets to deliver the calibration constant for the Bournemouth dataset, a sample study was carried out, by comparing backscatter signals using the PVC reference targets with those delivered from adopting a natural reference target.

3.7.3 Segmentation Technique

With the aim of integrating the calibrated backscatter signals into a more comprehensive and reliable 3D object segmentation technique, a segmentation routine is developed and validated in this research. The new technique is dependent on the reliability of the presented radiometric calibration routine and particularly on the robustness of the incidence angle estimation delivered from the RSN method.

The calibrated backscatter parameters have been utilised in the segmentation routine to differentiate between different surface targets, including those with similar geometric characteristics. This was accomplished by integrating these parameters to weight the geometric information in order to exploit the full potential of waveform parameters for automated point cloud segmentation.

The developed technique was tested over selected surface features from both datasets. However, an interest area from the high density (Bournemouth) dataset was utilised for validation purposes through comparison to a manual segmentation process in order to assess the accuracy and the performance of the implemented strategy. To better demonstrate the improvement acquired with the adoption of FWF physical observables, results are presented comparing the segmentation performance with the use of FWF additional information to results delivered without FWF information following the same routine.

3.8 SUMMARY

Chapter Three has presented a methodology which aims to delivered reliable FWF backscatter laser signals for exploitation alongside the geometric information in a developed segmentation technique. This aims to address weakness in existing 3D object segmentation approaches.

The novel outcomes of the presented methodology can be summarized as follows:

- A new effective processing strategy for FWF-ALS data has been developed using a grid computing Condor-based technique. The presented technique shows potential in situations where large datasets such as lidar data are utilised. This is achieved by reversing the normal Condor push job model into a client based pull model which helped to reduce processing time by 100-300 % in the case of the datasets investigated in this research.

- A novel echo amplitude normalisation approach based on Robust Surface Normal (RSN) estimation has been developed. This is based on determination of the incidence angle of individual echoes, from the illumination direction and local surface orientation. The local surface orientation estimation method computes the normal to an individual point using the minimum number of neighbourhood points. 3D moment invariants are used to deliver the normal vector using a weighting function. Thereafter a vector dot product in 3D space is adopted to check planarity, ensuring robustness.

- A practical radiometric calibration routine for FWF datasets is presented where the backscatter coefficient (γ) has been utilised to deliver the calibration constant. This aims to eliminate the discrepancies of FWF backscattered signals between overlapping flightlines. This routine is based on applying the RSN method, to deliver robust incident angle estimation for reference target echoes and thereafter for individual point clouds in both investigated datasets. These angles are used to deliver the normalised backscatter coefficient and backscatter cross-section parameters for individual echoes for further analysis and applications.

- An automatic 3D object segmentation technique has been developed and presented. The method aims to fully utilise FWF information to overcome the weaknesses in the available approaches. The motivation is to prove that integrating FWF physical observables can potentially improve segmentation scenarios by distinguishing between surface features with similar geometric information. The method uses the calibrated backscatter signals as a weighting function to estimate the segmentation algorithm criteria. Thereafter, a region growing technique is utilised to segment the 3D point clouds into meaningful groups.

CHAPTER

4

RESEARCH OUTCOMES

4.1 INTRODUCTION

A new methodology to integrate FWF backscatter signals in an existing segmentation technique was introduced and developed in Chapter Three. The method aims to fully utilise FWF information to improve the identification of Earth surface features following a comprehensive segmentation routine for downstream applications. The method relies on a developed technique to estimate the orientation direction of individual ALS echoes. These estimations are used afterward to enhance the calibration of the FWF backscatter signals for integration in a 3D object segmentation algorithm.

This chapter will focus on assessing the developed methodology by separately testing and validating each distinct part of the workflow. The method was applied over different land cover types using two different datasets and the results were analysed both visually and statistically to assess performance of the introduced routine. The investigated targets were selected in order to provide different surface characteristics such as orientation, material, and roughness. In order to evaluate the method over a greater variety of land cover types, and to deliver more comprehensive outcomes for use in future analysis, several interest areas were investigated over both urban and rural sites. The targets and the investigated interest areas were selected from multiple flightlines with different positions and orientations, covering both the Bournemouth and Bristol study sites.

The chapter is divided into three main parts following the methodology introduced in the previous chapter. Firstly, the novel RSN method and the normalised amplitude signals were assessed and compared against the reference spherical method. Then the comprehensive radiometric calibration routine is tested and validated over a variety of land features from multiple flightlines and also compared with a recognised existing technique. A justification of the use of one calibration constant for each individual campaign is presented based on FWF backscatter signal analysis. Finally, the developed segmentation algorithm is tested and later validated against manual processing in order to assess the absolute accuracy of the automatic routine. To demonstrate the potential of exploiting FWF information in the automatic segmentation routine, the results from the developed approach were compared with the results obtained from applying the same approach on the same interest area but without integrating the physical observables of FWF.

The Bournemouth dataset produces more detailed representation of surface targets than the Bristol dataset due to the higher point density. Thus the Bournemouth dataset was given priority to demonstrate the performance of the methodology. This is because the introduced methodology is relying on the RSN method which is optimised for application to denser datasets.

4.2 ASSESSING THE RSN METHOD AND THE NORMALISED FWF AMPLITUDE SIGNALS

Data from the high point density Bournemouth site and the lower density Bristol site were tested to validate the performance of the RSN method against the reference spherical method over both natural and urban surfaces. This validation incorporates more than 750,000 points comprising 56 land cover types from Bournemouth and 21 types from Bristol. A lower number of targets were selected from Bristol because the lower point density of this dataset limited the variety of land cover types. Selected areas included a total of 34 natural targets with non-planar surface trends (such as rough terrain, steep terrain, undulating terrain, low vegetation, grass, shrubs, etc.) and 43 man-made targets with planar trends (including roads, slanting roofs, complex roofs, walls, cars, semi-flat ground, highway barriers, etc.). These targets were used to visualise the improvements in the normalised amplitude signals using the RSN method and later to assess the accuracy of these results following standard statistical tests.

4.2.1 Visual Analysis

In the case of Bournemouth, the RSN method was firstly tested over man-made features to validate its performance over high planarity surfaces. The normal vector results obtained from the Bournemouth dataset demonstrated that the RSN method is capable of detecting small disturbing objects on slanted roofs and delivering an accurate estimation of the normal for relatively minor features such as small windows and chimneys. In contrast, the reference method completely failed to detect their presence by delivering normal vectors with approximate similar directions, as shown in Figure 4.1 for the extent highlighted area.

These results arise because through the spherical method the normal value was approximated to fit the plane enclosing all the points which are defined by a fixed radius from the outset, thus ignoring minor details. In contrast, the RSN method applies a smaller local neighbourhood system, comprising a limited number of points which are used to estimate reliable normal values for minor detail features. This is preferable to the unreliable normal delivered from fitting a plane to a group of points with different orientations, which is commonly acquired over natural land coverage and surfaces with complex and rough trends. This is basically because the normal delivered from the spherical method and other similar approaches could be reliable to some of the points used to define the system but not necessarily for the point of interest itself, which translates later to the wrong normalised echo amplitude values.

The RSN approach is therefore better able to consider the distribution of the included points and describe the localised complex trends of the surface. Moreover, the robust planarity checking procedure makes the definition more reliable by including only the points that belong to one plane within each small 3D system. Figure 4.2 demonstrates another example of the robustness of the RSN method by detecting chimneys over a complex roof target. Due to a mis-match between photos during orthophoto production, the right chimney in Figure 4.2-a is not visible. However, the point cloud image in Figure 4.2-b shows its presence.

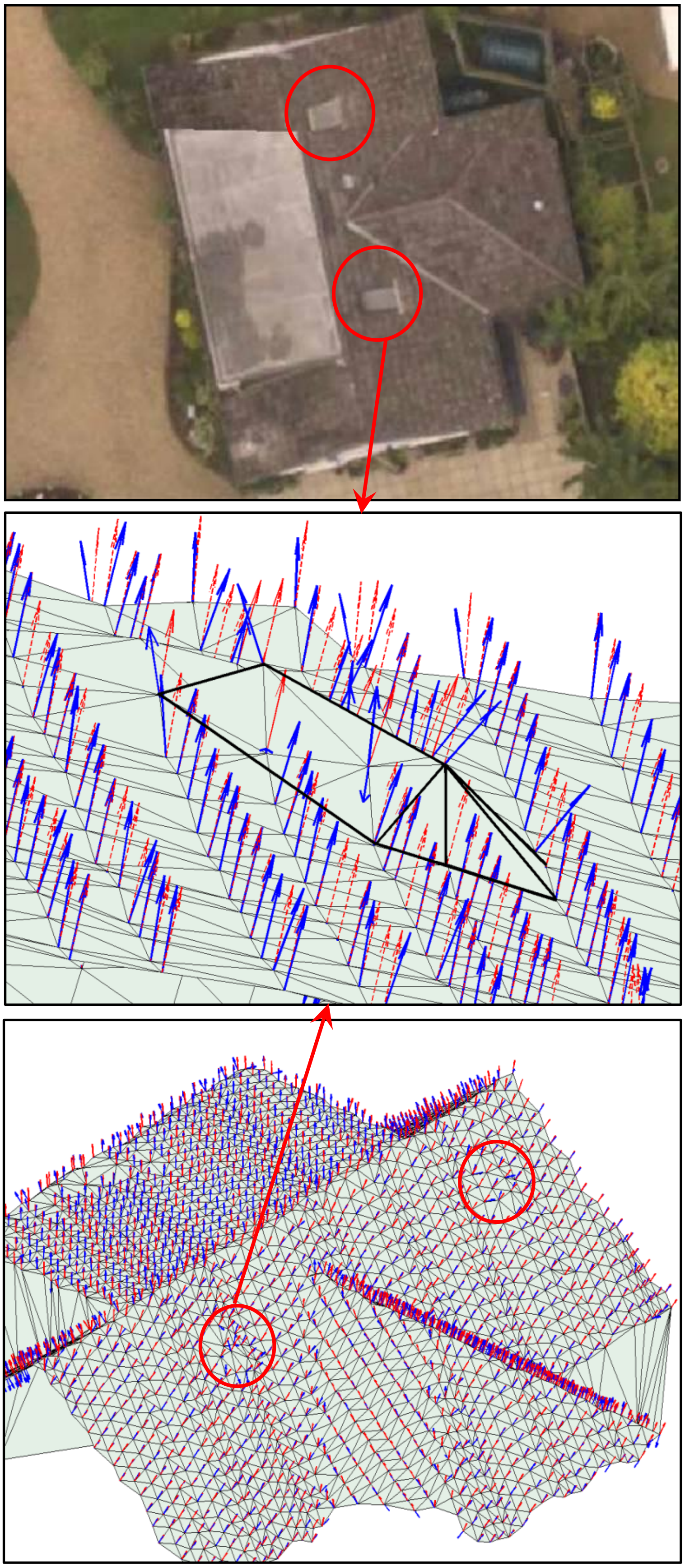

(a) Orthophoto of roof target showing the small window highlighted in the red circle.

(b) Detailed view of the highlighted window (extent outlined in black, bold) showing the normal vectors obtained from the RSN method (solid blue arrows) against the spherical reference method (dashed red arrows).

(c) Visualised normals delivered from both methods for the roof target.

Figure 4.1. Normal vector estimation over a simple roof target in the Bournemouth dataset.

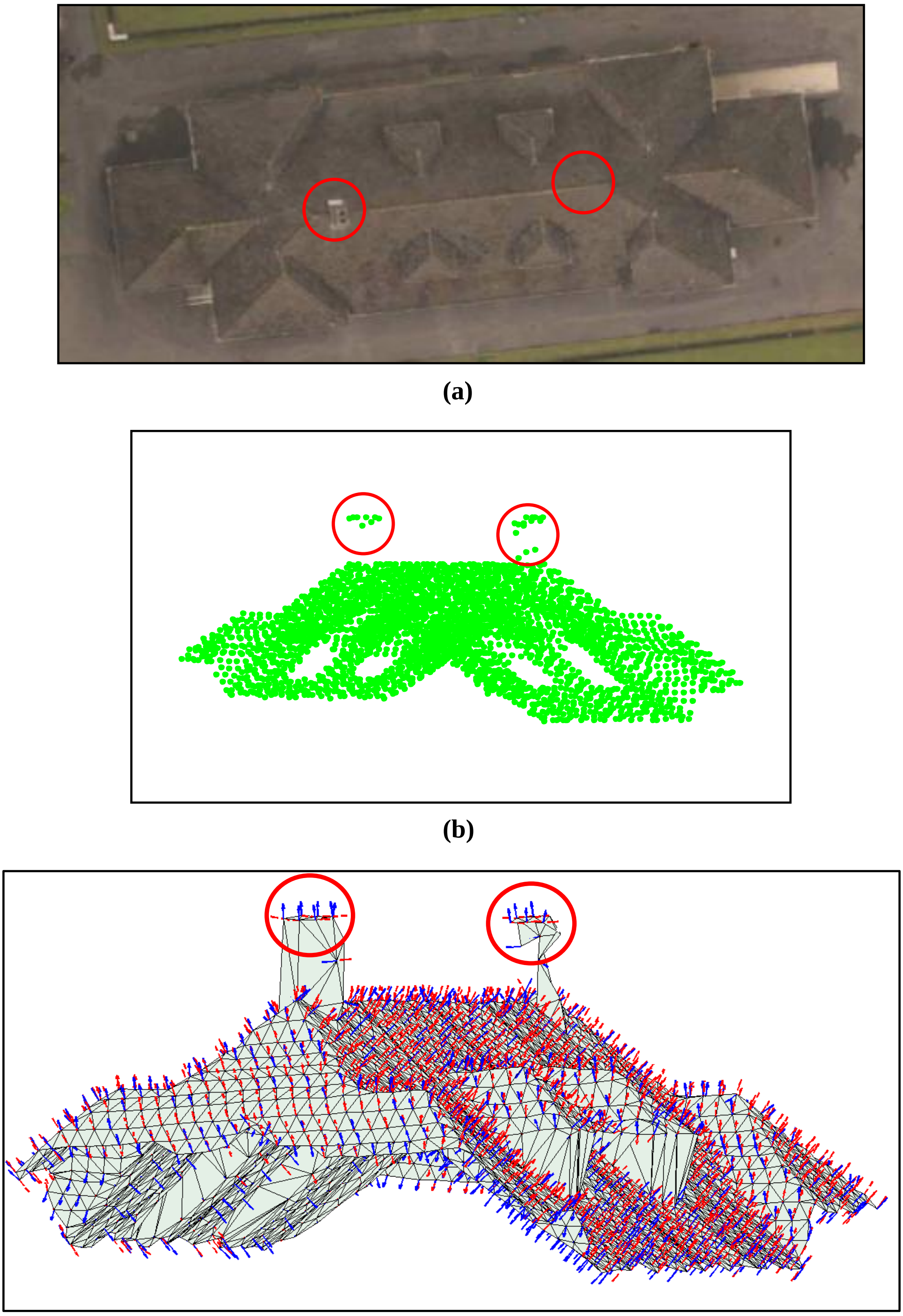

(a)

(b)

(c)

Figure 4.2. Normal vector estimation over a complex roof target in Bournemouth dataset (the chimneys are highlighted in red circles): **(a)** orthophoto image **(b)** point cloud image **(c)** visualised normals delivered from RSN (solid blue arrows) and spherical (red arrows) methods.

It was also found that the RSN method is better able to distinguish between features at sharp-edged corners and those with challenging planar trends such as the example shown from the Bristol dataset in Figure 4.3.

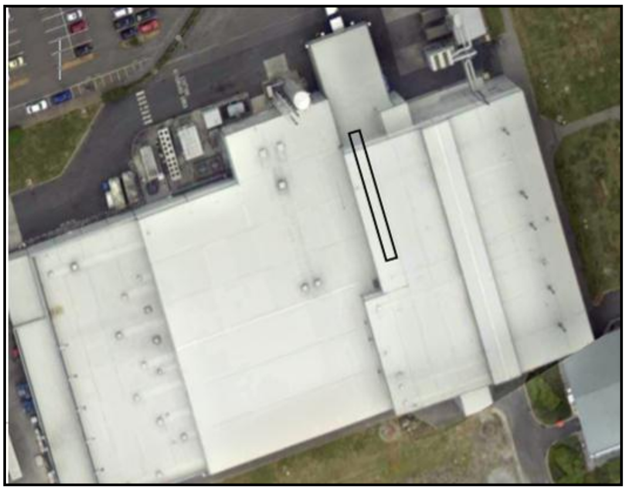

(a)

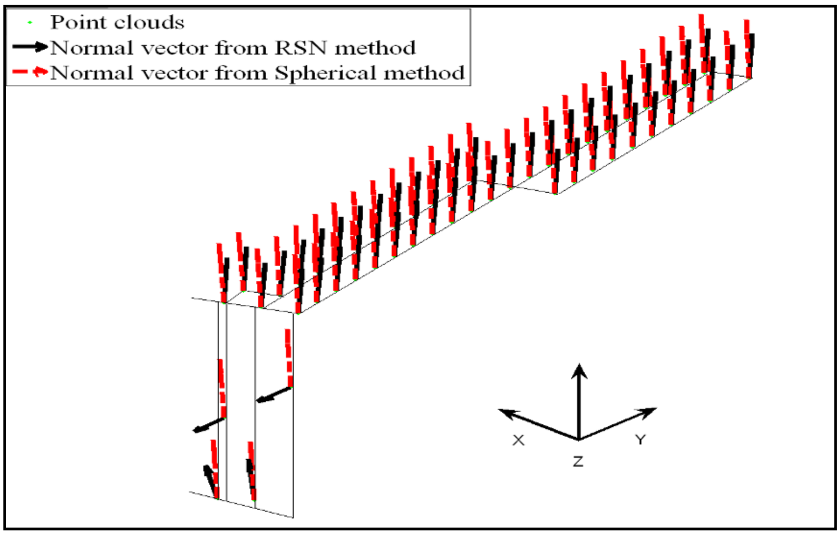

(b)

Figure 4.3. Normal vector estimation over a flat roof and wall surfaces in Bristol dataset: **(a)** orthophoto of the target highlighting the selected section **(b)** normal vectors obtained from the RSN method (black arrows) against the spherical reference method (dashed red arrows) for the selected profile section.

Specifically, this approach successfully managed to differentiate walls from roofs and clearly delivers appropriate normal values for the vertical wall, where the spherical approach fails. In these instances, the normal estimates for a point near a corner on one plane are not degraded by the influence of points on an adjacent plane which is oriented differently. However due to unavoidable opposite normal direction in the developed technique, the normal vectors of other neighbourhood points on the highlighted wall are not visible in Figure 4.3. This finding is highly promising for segmentation scenarios and urban feature extraction. Although the method still has weaknesses in estimating the correct normal for corner points where the adjacent surfaces are of differing material types (e.g. where a concrete wall meets a grass-cover ground surface), further improvements could be achieved through the inclusion of accurate radiometric information such as the backscatter parameters, which more fully consider all influences on the reflected signal. This is investigated in the following sections after application of the developed radiometric calibration routine.

To assess the performance of the developed RSN method over non-planar surfaces, the method was tested over challenging surface trends such as natural land coverage. It was applied over natural terrain of a discontinuous nature (e.g. bare undulating ground, bare sloping terrain, rough terrain with grassy patches, rough sloping terrain and rough ground with severe gradient changes, etc.) and its performance compared with that of the reference method, initially through visualisation of differences between the results. The normal vector results showed that the RSN method successfully followed the trend of the challenging natural surfaces and was able to faithfully reflect minor rough details where the spherical method failed. For such surfaces the RSN method more effectively defined the discontinuities, and as a result delivered more robust normalised echo amplitude signals.

To demonstrate these improvements, an interest area of discontinuous natural terrain which comprises some vegetated patches was selected from the Bournemouth study site, as highlighted in Figure 4.4. For this interest area, Figure 4.5 presents a series of plots which indicate flightline differences for the RSN and reference methods. For both flightlines, the plots indicate that the RSN method is able to deliver details which better describe the discontinuous surface trend as shown in Figure 4.5-d and Figure 4.5-e for the overlapping flightlines. In comparison, the spherical method shows smoothing of such details, discarding the localised roughness trends as shown in Figure 4.5-g and

4.5-h respectively. Furthermore, in the case of the RSN approach, Figure 4.5-c, and Figure 4.5-f demonstrate a reduction in the difference of the echo amplitude signals between overlapping flightlines in comparison to the original signals. In contrast, the spherical method shows relatively poor performance due to the non-robust spherical assumption.

(a)

(b)

Figure 4.4. A selected interest area of natural terrain from the Bournemouth dataset: **(a)** orthophoto showing the selected region with the cross-section in the middle **(b)** the visualisation of the selected cross-section showing the discontinuous surface trends.

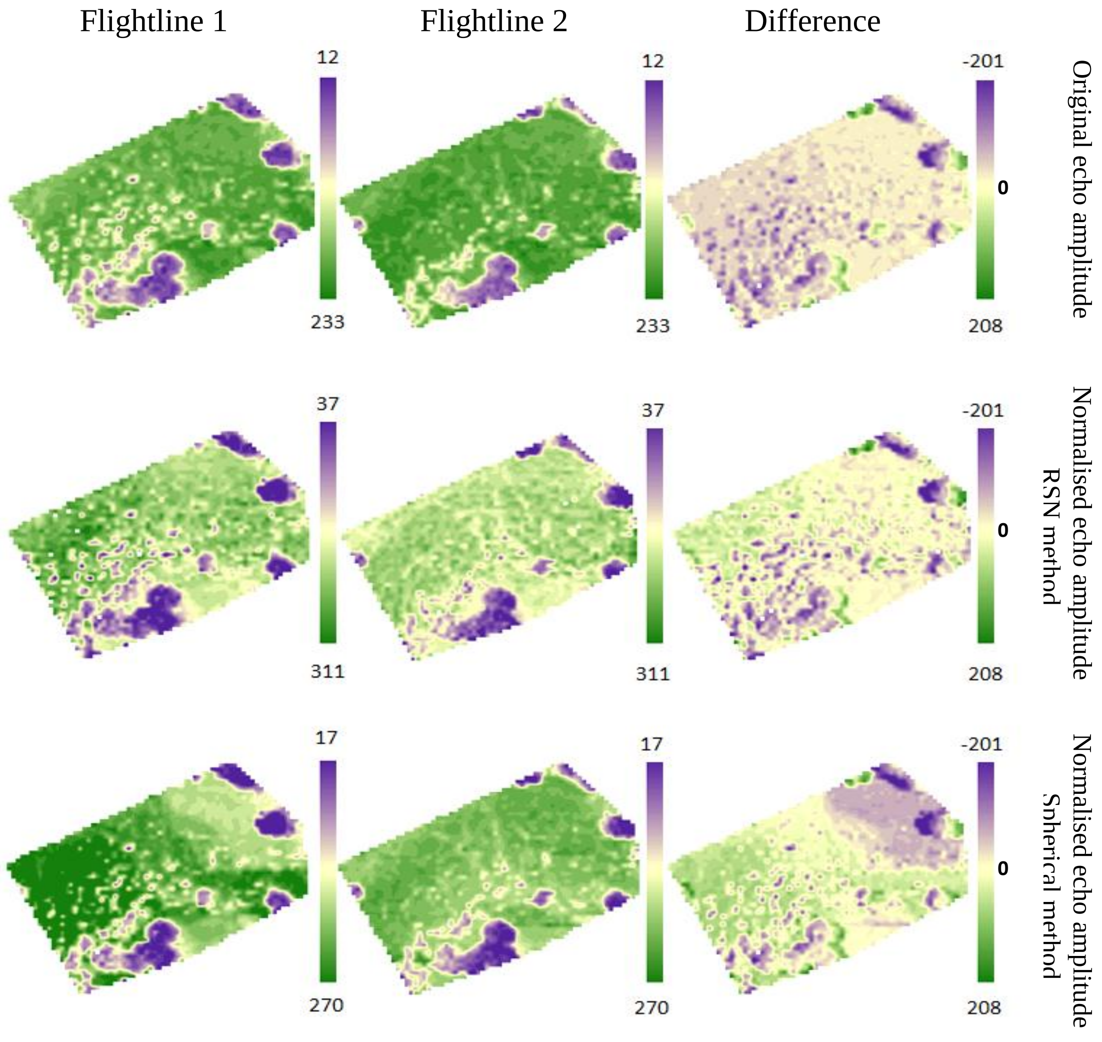

(g) (h) (i)

Figure 4.5. Colour-coded map of two overlapping flightlines for the selected region in figure 4.4: **(a)** and **(b)** show the original echo amplitude signals **(d)** and **(e)** show the normalised echo amplitude signals using the RSN method **(g)** and **(h)** show the normalised echo amplitude signals using the reference method **(c)**, **(f)** and **(i)** portray the flightline differences between the original signals, the RSN and the spherical methods respectively.

Moreover, the method also revealed promising results over low vegetation regions such as grass and hedges. However, this will be better realised after accounting for all other effects influencing the backscatter signal in the radiometric calibration and later in the segmentation results.

4.2.2 Statistical Analysis

In order to assess the accuracy of the developed method, normalised echo amplitude signals delivered from the RSN and the reference method over 77 distinct targets from both datasets were tested and validated statistically. The analysis investigates the deviation of the mean values and demonstrates the differences in the standard deviation between overlapping flightlines delivered from both methods individually. This allows for inspection of discrepancies for individual targets between overlapping flightlines before and after normalisation.

For demonstration purposes, results for both datasets from natural and man-made targets, as highlighted in Figure 4.6 are presented in Figure 4.7 and Figure 4.8 respectively. These figures show the histograms and the normal distribution curves for the echo amplitude signals from the two overlapping flightlines before and after normalisation through both approaches. Results from a natural, undulating terrain surface, are highlighted in Figure 4.7. Figure 4.8 demonstrates the performance over a complex roof target selected from the lower resolution Bristol dataset. Both Figure 4.7 and Figure 4.8 demonstrate improvements in the signal amplitude discrepancies between overlapping flightlines after normalisation using the RSN method. The increased standard deviation values derived from the RSN method for the individual flightlines arise due to the sensitivity of this method in detecting discontinuities. However, the key outcome is the decreased difference between the standard deviation values for the overlapping flightlines achieved through the RSN method, indicating improved normalisation. Figure 4.8 highlights the impact of a lower density dataset on the RSN method’s performance, delivering a less marked improvement in comparison to the results from the Bournemouth dataset, although still out-performing the spherical method (Figure 4.8-b and Figure 4.8-c).

In order to generalize the outcomes from both methods, all tested targets from both datasets were grouped into two different sets according to their surface trends. The first set contains targets with planar trends while the second set relates to non-planar targets. The standard deviation difference (as a percentage) between overlapping flightlines was computed before and after normalisation. This is based on the mean standard deviation of all selected targets in each single flightline and is presented in Table 4.1 and 4.2 for the Bournemouth and Bristol datasets respectively. It can be seen from both tables that the discrepancies between overlapping flightlines were markedly reduced with the RSN method over both target sets in both datasets. However, less improvement was generally realised from the Bristol dataset because of the lower data density which essentially means that due to different point distributions between the flightlines, certain surface details are included in one flightline, but not in the other. Although small improvements can be seen in the normalised signals delivered from the spherical method over the planar target set, poor results were delivered for non-planar targets, thus demonstrating the shortcomings of the spherical method over natural land cover types.

(a) Orthophoto showing the undulating terrain surface target from the Bournemouth dataset.

(b) Orthophoto showing the complex roof target from the Bristol dataset.

Figure 4.6. Selected targets from both datasets to assess the performance of the RSN method**.**

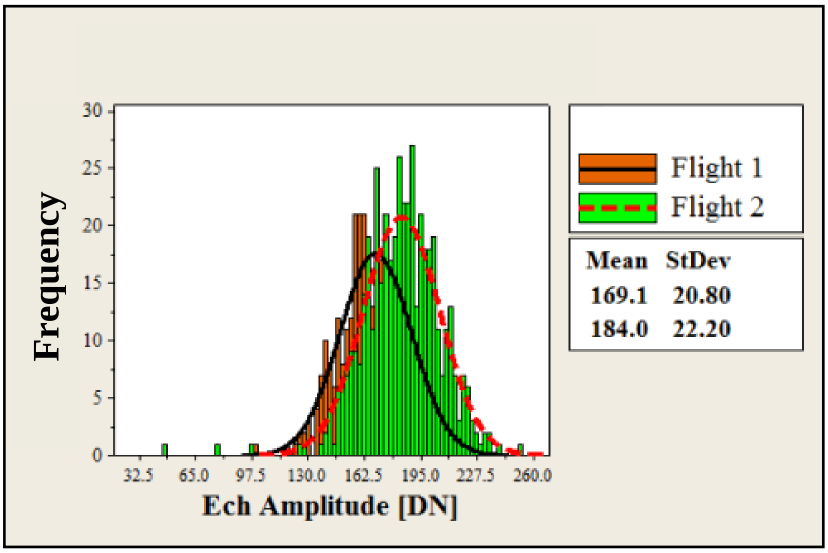

(a) The original echo amplitude signals.

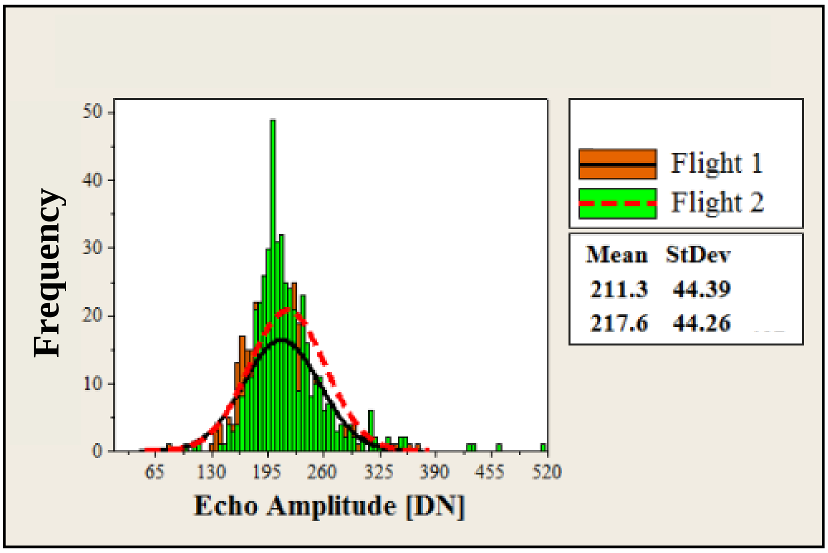

(b) The normalised echo amplitude signals using the RSN method.

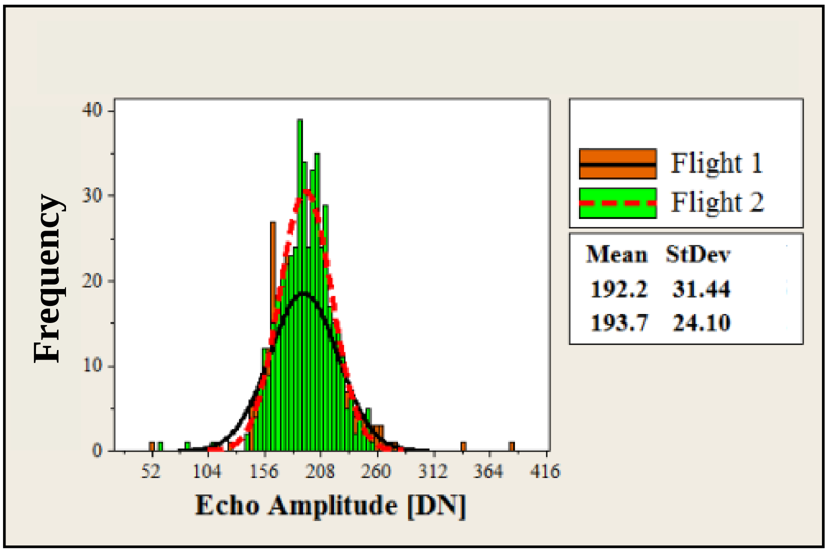

(c) The normalised echo amplitude signals using the reference method.

Figure 4.7. Echo amplitude normalisation of two overlapping flightlines over undulating terrain surface from the Bournemouth dataset.

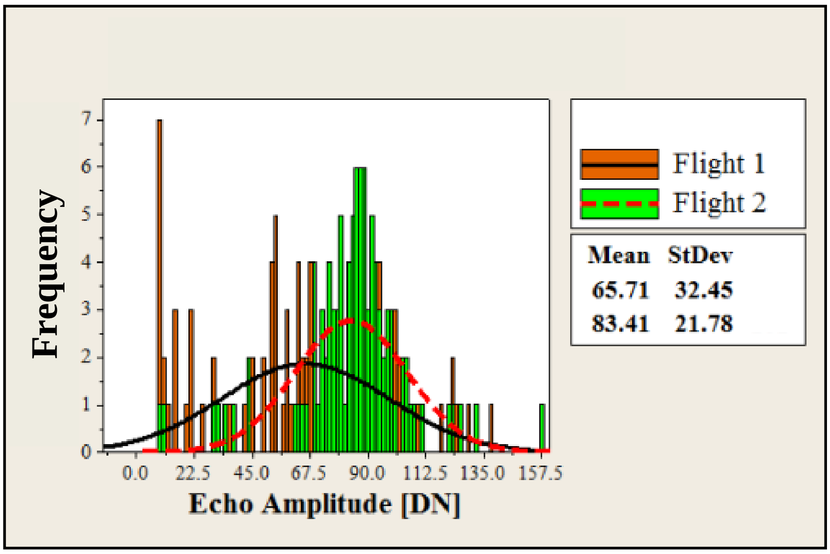

(a) The original echo amplitude signals.

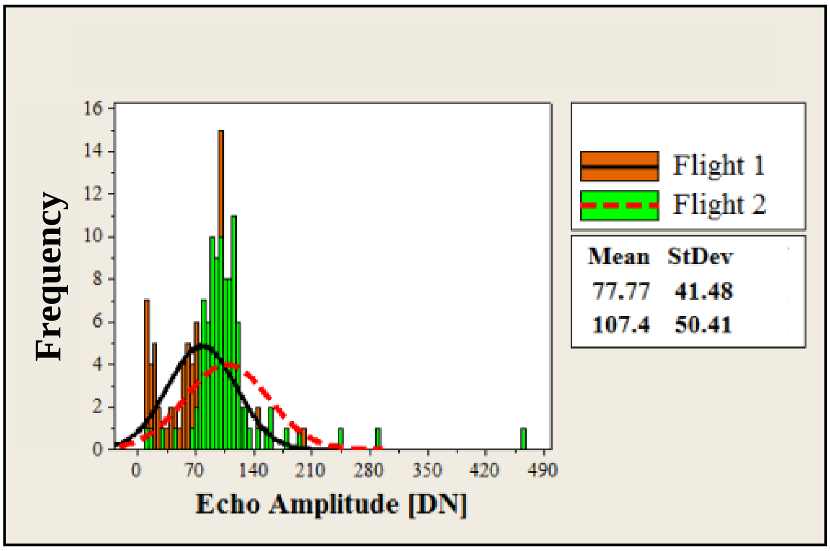

(b) The normalised echo amplitude signals using the RSN method.

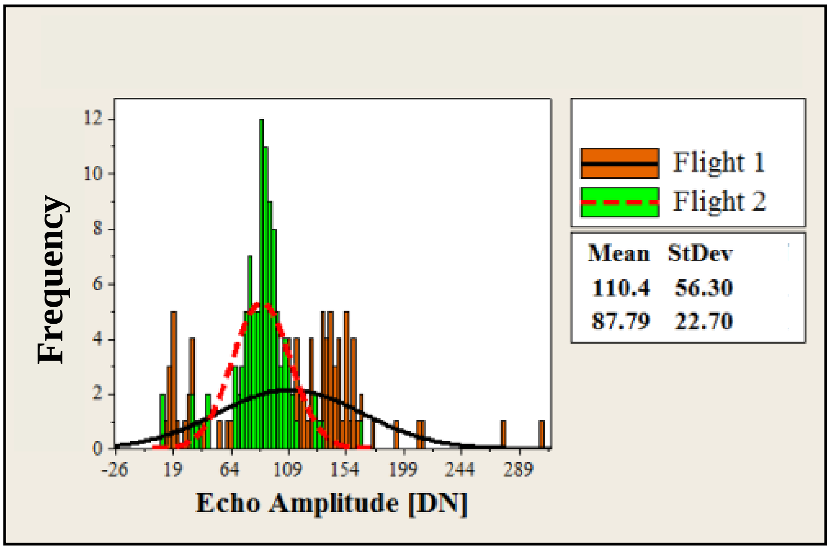

(c) The normalised echo amplitude signals using the reference method.

Figure 4.8. Echo amplitude normalisation of two overlapping flightlines over a complex roof target from the Bristol dataset.

Targets Groups	No. of targets	No. of points	Mean Ϭ of the original echo amplitude signals		Mean Ϭ of the normalised echo amplitude signals				% Ϭ Differences in the echo amplitude signals before and after normalisation		
			Flightline 1	Flightline 2	RSN Method		Spherical Method		Original	Normalised RSN Method	Normalised Spherical Method
					Flightline 1	Flightline 2	Flightline 1	Flightline 2			
Planar Surfaces	32	190,655	24.611	26.982	29.298	28.832	30.400	28.499	8.787	1.616	6.670
Non-Planar Surfaces	24	335,480	29.01	26.267	34.596	33.830	36.809	32.561	10.442	2.264	13.046

Table 4.1. Mean standard deviations (Ϭ) and differences in percentage between overlapping flightlines before and after normalisation in the Bournemouth dataset using RSN and spherical methods.

			Mean Ϭ of the original echo amplitude signals		Mean Ϭ of the normalised echo amplitude signals				% Ϭ Differences in the echo amplitude signals before and after normalisation		
Targets Groups	**No. of targets**	**No. of points**	**Flightline 1**	**Flightline 2**	**RSN Method**		**Spherical Method**		**Original**	**Normalised RSN Method**	**Normalised Spherical Method**
					Flightline 1	**Flightline 2**	**Flightline 1**	**Flightline 2**			
Planar Surfaces	11	123,327	24.815	22.205	29.102	27.044	24.024	26.512	11.754	7.609	9.384
Non-Planar Surfaces	10	120,354	21.177	23.230	21.851	21.006	28.971	26.178	8.837	3.726	10.669

Table 4.2. Mean standard deviations (Ϭ) and differences in percentage between overlapping flightlines before and after normalisation in the Bristol dataset using RSN and spherical methods.

4.3 ASSESSING THE DEVELOPED RADIOMETRIC CALIBRATION ROUTINE

After delivering robust incidence angle estimations for individual FWF-ALS echoes using the RSN method, the incidence angle needs to be integrated alongside other parameters, which affect the backscatter signal. This enables calibration of the received power and delivers more comprehensive physical observables for use in further analysis. This was achieved by adopting the developed radiometric calibration routine introduced in Chapter Three.

This section introduces the results delivered from applying the developed calibration technique over different land cover types, including man-made and natural, with the aim of eliminating FWF backscattered signal discrepancies between overlapping flightlines. The routine is tested, analysed, and validated over different targets with various surface trends and properties. Later, a comparison is made between backscatter signals delivered from overlapping flightlines for each investigated target and area of interest. In order to assess which configuration is able to best eliminate flightline discrepancies, the four backscatter parameters introduced in Chapter Three are investigated.

Firstly, the reflectivity measures of the reference target used in the absolute radiometric calibration in the Bournemouth dataset are introduced and analysed. Then, a justification for adopting one single calibration constant for the individual campaigns rather than per flightline is presented. A statistical comparison between the use of artificial and natural reference targets was undertaken for the Bournemouth dataset. Then, a statistical study which compares the adopted routine with an existing approach that uses a natural reference target for the calibration process, neglecting incidence angle effects was undertaken. Finally, all the results obtained from applying the developed routine over various targets and interest areas are presented visually and analysed statistically using standard statistical tests.

4.3.1 Reference Target Reflectivity Measures Analysis

As stated in Chapter Three, polyvinyl chloride (PVC) targets and asphalt natural sections were utilised as reference targets in the radiometric calibration workflow for the Bournemouth and the Bristol datasets respectively. Based on the literature, a reflectance of 0.25 at 1550 nm wavelength was used for asphalt to estimate the calibration constant for the Bristol dataset, (refer to Section 3.5.3). However, a practical reflectivity measure was required for the PVC targets in the Bournemouth dataset to deliver the optimal reflectivity value for these targets.

Although successive reflectivity measures should be taken for the reference targets during data capture in order to ensure consistency in terms of the day of scan and atmospheric conditions, this condition could not be met for this dataset as already explained (refer to Section 3.5.2). As an alternative, indoor reflectivity measurements were performed for the 1 m-radius PVC targets using an Analytical Spectral Device (ASD), refer to 3.5.2 for more details.

Figure 4.9 shows a sample of spectral reflectivity measurements recorded by 1° fore-optic and 0° incidence angle over the PVC reference target. The X-axis represents wavelength spectral range while the Y-axis shows the absolute reflectivity values after post processing. The graph shows the distribution of the successive 25 series measurements, with the first series always eliminated in order to assure high measurement precision. This is because the first measurement could deliver an unstable value due to effects with the previous measurement. As the atmosphere strongly absorbs radiation between 1350 and 1460 nm wavelengths, and also between 1790 and 1960 nm, these bands were removed as it can be realised from the data gaps in Figure 4.9. This is because these spectral regions are very sensitive to the atmosphere and thus very noisy data is delivered in these two regions.

It can be realised from the graph that at the 1550 nm wavelength which defines the wavelength of the Riegl LMS-Q560 system, the absolute reflectivity for the PVC target is shown to be approximately 70% at nadir. This was delivered from all measurements after accounting for the multiple incidence angle settings effect. Therefore, a 0.7 reflectivity value for the reference target was adopted for further processing in the Bournemouth dataset.

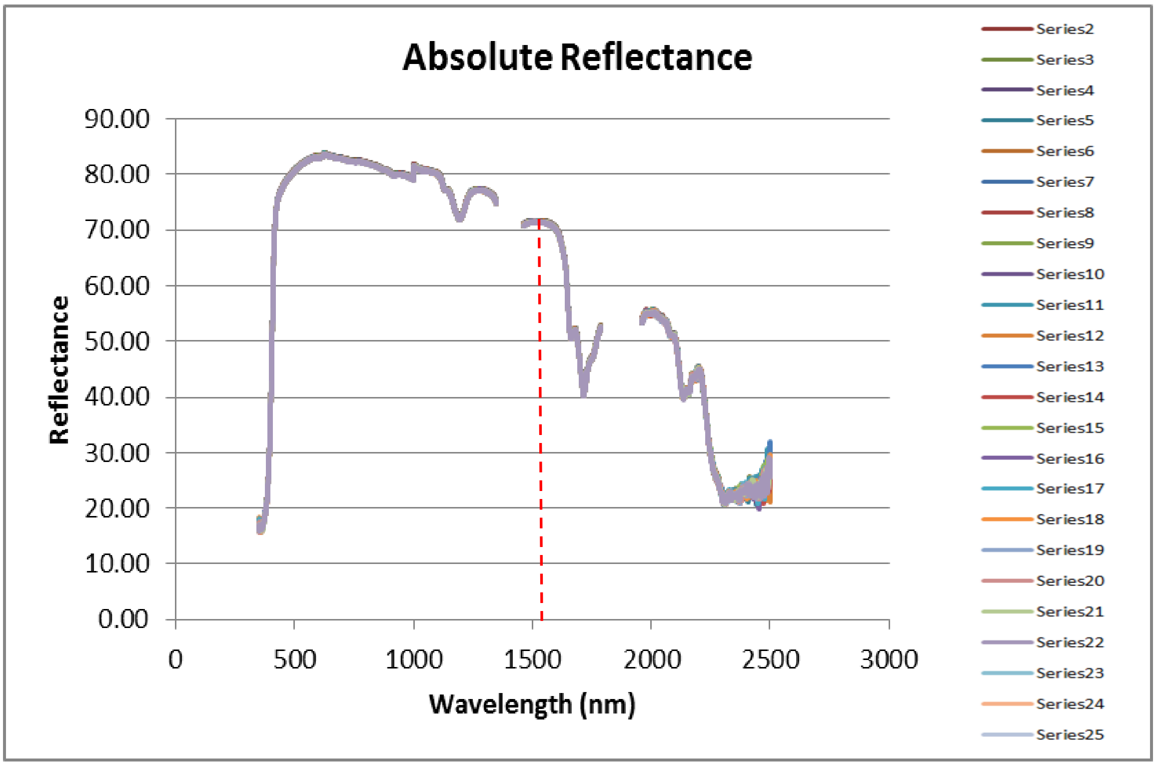

Figure 4.9. Absolute reflectivity measurements of a sample series records over PVC target using 1° fore-optic and 0° incidence angle.

4.3.2 Empirical Analysis of FWF Echo Amplitude and Width

The variations of emitted laser energy (echo amplitude and width) were investigated on behalf of the Bournemouth and the Bristol flight campaigns in this research. This includes analysis to detect any major faults in the emitted signal, which might deliver from particular flightlines, and could affect the calibration constant determination. This is based on the findings of Roncat et al. (2011) who studied the relationship between the calibration constant and FWF echo amplitude and width parameters, assuming how this can best deliver a consistent representation of the behaviour of the emitted energy. This follows the empirical evidence presented by Bretar et al. (2009) who claimed that the emitted energy cannot be considered as “constant enough” throughout the ALS campaign for radiometric calibration purposes.

In FWF-ALS the received signal can be represented as the product of echo amplitude and width. Both variables are affected by the final amount of the received energy and therefore need to be analysed. This is based on individual analysis of echo amplitude and width signals of all flightlines delivered from post processing. To study the shape and the behaviour of individual values, normal distribution curves and standard statistical computations were produced. Minimum and maximum values in addition to mean, standard deviation (Ϭ), and coefficient of variation (CoefVar) per flightline per FWF parameter were computed for the Bournemouth and Bristol datasets.

Table 4.3 and Figure 4.10 demonstrate the similar distribution of echo width signals in the Bristol dataset for the different flightlines. This illustrates that they exhibit approximate mean values and only slightly different standard deviation and coefficient of variation values to those delivered from multiple flightlines. Although the distribution curve in Figure 4.10 is shifted to the left due to the presence of outliers, the data from all flightlines seems to be normally distributed and the signals are approximately coincident with each other. Similarly, Figure 4.11 shows nearly perfect normal distribution of the echo amplitude data signals of the same dataset with no evidence for skewness or kurtosis following statistical tests. Although, some slight difference in the mean values can be realised from Table 4.4, particularly in flightlines 1 and 5, the data still exhibits the same distribution. For a comprehensive output, two types of histograms were utilised to represent frequency distribution behaviour of the various data types. These include frequency and density histograms, refer to Mladen (1996) for further details.

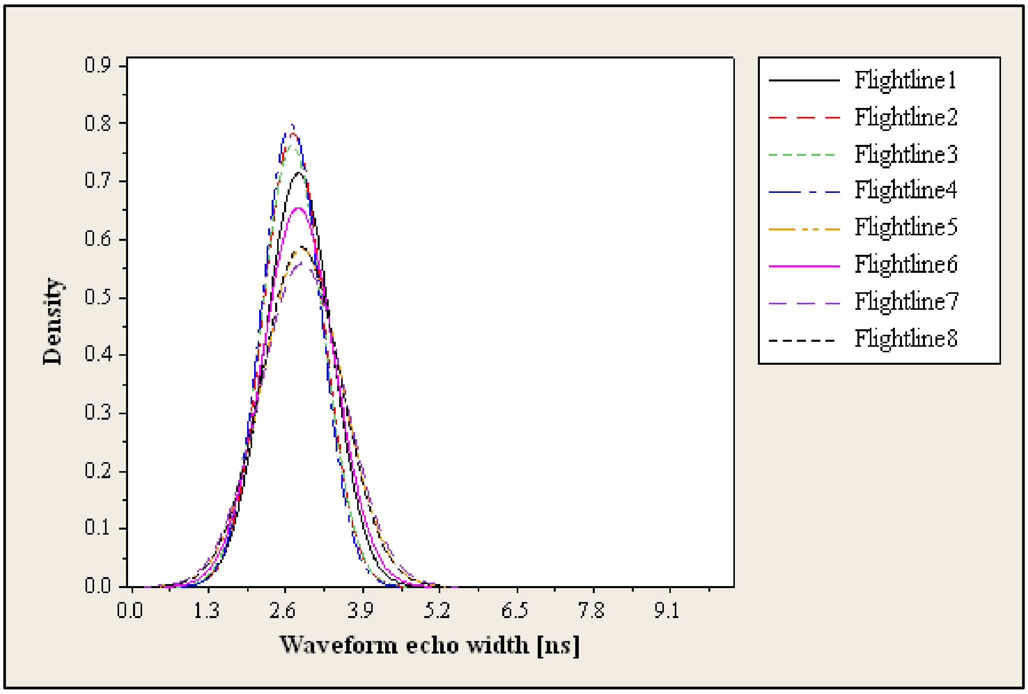

Figure 4.10. Normal distribution curves of FWF echo width signals in Bristol dataset.

	Mean	σ	CoefVar	Minimum	Maximum
Flightline1	2.817	0.557	0.198	1.000	9.982
Flightline2	2.721	0.509	0.187	1.000	9.930
Flightline3	2.705	0.522	0.193	0.118	9.902
Flightline4	2.690	0.499	0.186	0.111	9.964
Flightline5	2.871	0.682	0.238	0.119	9.981
Flightline6	2.813	0.608	0.216	0.114	9.950
Flightline7	2.880	0.713	0.248	1.000	9.946
Flightline8	2.859	0.679	0.237	0.115	9.966

Table 4.3. Statistics of the FWF echo width signals in Bristol dataset in [ns].

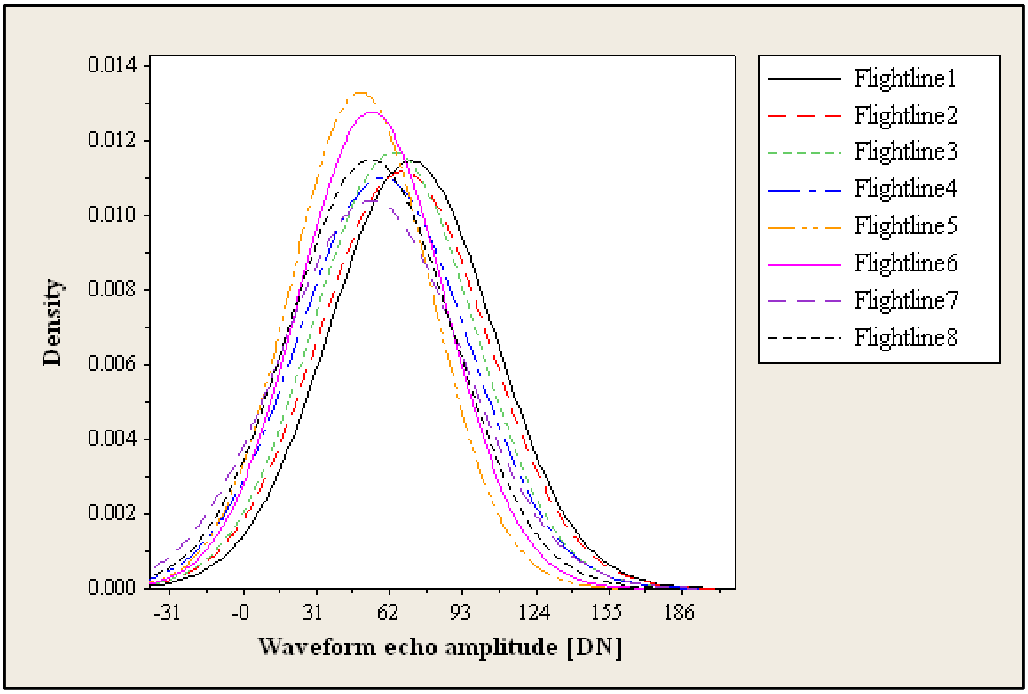

Figure 4.11. Normal distribution curves of FWF echo amplitude signals in Bristol dataset.

	Mean	Ϭ	CoefVar	Minimum	Maximum
Flightline1	71.330	34.866	0.489	4.087	201.343
Flightline2	67.771	35.753	0.528	4.240	202.035
Flightline3	63.848	34.193	0.536	4.064	203.480
Flightline4	59.187	36.267	0.613	4.013	202.761
Flightline5	49.831	30.032	0.603	4.006	203.567
Flightline6	54.518	31.276	0.574	4.201	202.345
Flightline7	54.414	38.407	0.706	4.500	201.041
Flightline8	54.034	34.741	0.643	4.162	201.263

Table 4.4. Statistics of the FWF echo amplitude signals in Bristol dataset in [DN].

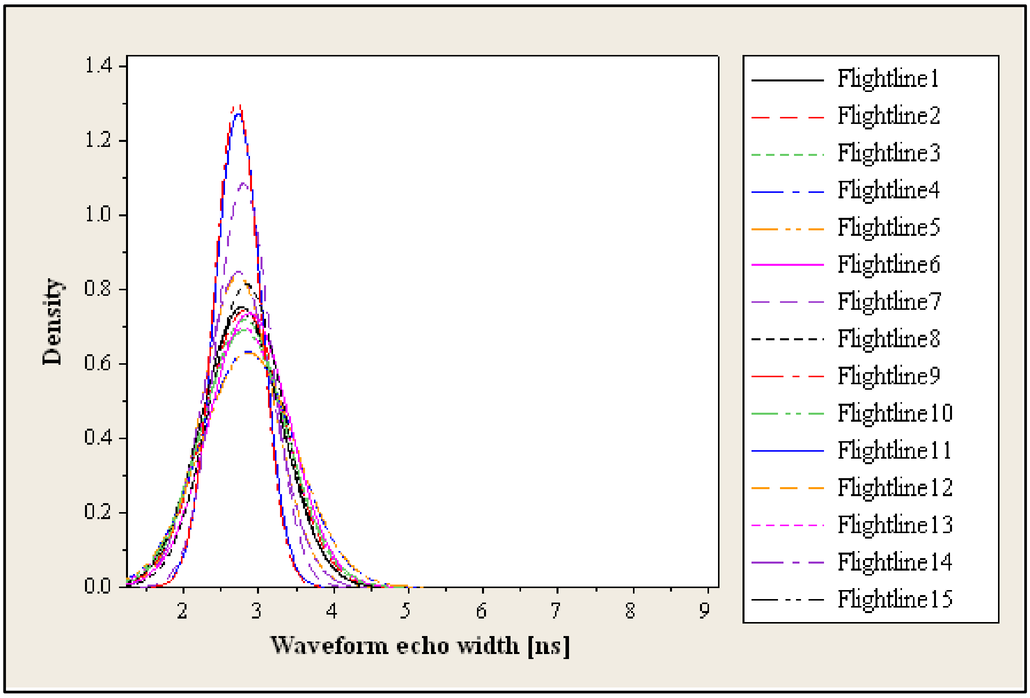

Figure 4.12. Normal distribution curves of FWF echo width signals in Bournemouth dataset.

	Mean	ϭ	CoefVar	Minimum	Maximum
Flightline1	2.765	0.531	0.192	1.700	8.999
Flightline2	2.803	0.538	0.192	1.700	8.997
Flightline3	2.799	0.557	0.199	1.700	8.997
Flightline4	2.847	0.631	0.222	1.700	8.999
Flightline5	2.856	0.634	0.222	1.700	8.999
Flightline6	2.869	0.543	0.189	1.701	8.998
Flightline7	2.787	0.369	0.132	1.700	8.996
Flightline8	2.826	0.491	0.174	1.700	8.984
Flightline9	2.702	0.307	0.114	1.701	8.979
Flightline10	2.793	0.580	0.208	1.700	8.999
Flightline11	2.715	0.314	0.116	1.701	8.991
Flightline12	2.717	0.478	0.176	1.700	8.999
Flightline13	2.789	0.573	0.205	1.700	8.994
Flightline14	2.720	0.471	0.173	1.700	8.994
Flightline15	2.758	0.542	0.196	1.700	8.998

Table 4.5. Statistics of the FWF echo width signals in Bournemouth dataset in [ns].

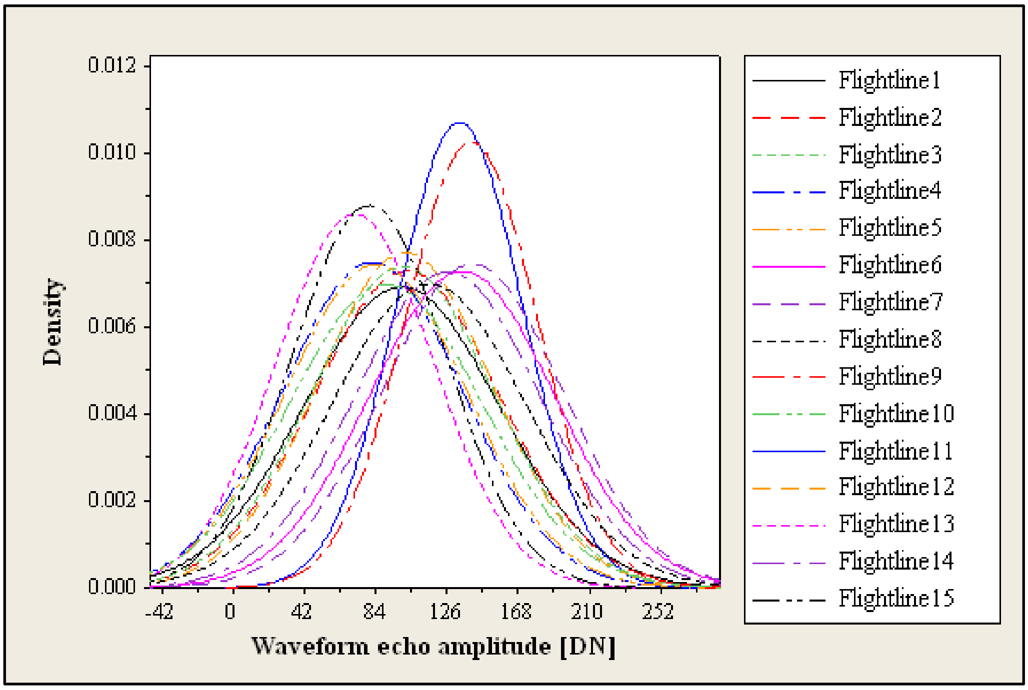

Figure 4.13. Normal distribution curves of FWF echo amplitude signals in Bournemouth dataset.

	Mean	**б**	**CoefVar**	**Minimum**	**Maximum**
Flightline1	99.282	57.579	0.580	4.501	257.841
Flightline2	102.581	54.664	0.533	4.500	252.380
Flightline3	99.986	53.946	0.540	4.501	256.883
Flightline4	82.189	53.238	0.648	4.500	252.419
Flightline5	84.512	53.539	0.634	4.501	255.420
Flightline6	135.08 4	54.766	0.406	4.500	256.610
Flightline7	141.12 2	53.482	0.379	4.500	255.970
Flightline8	115.36 6	56.948	0.494	4.500	280.540
Flightline9	140.42 2	38.857	0.277	4.510	246.770
Flightline10	90.098	57.050	0.633	4.501	252.273
Flightline11	133.48 9	37.232	0.279	4.100	246.300
Flightline12	101.411	51.680	0.510	4.500	256.210
Flightline13	71.762	46.396	0.647	4.500	256.240
Flightline14	126.37 1	54.847	0.434	4.230	257.900
Flightline15	80.260	45.310	0.565	4.315	255.944

Table 4.6. Statistics of the FWF echo amplitude signals in Bournemouth dataset in [DN].

In contrast, the Bournemouth dataset shows more challenging results. This is particularly obvious from the distribution of the echo amplitude signals in Figure 4.13. However, the echo width and amplitude signals in Figure 4.12 and Figure 4.13 deliver curves which follow the normal distribution and no skewness or kurtosis behaviour can be detected. Further, the mean values in Table 4.5 show greater similarity than the echo amplitude mean values in Table 4.6. Although the mean values from Table 4.6 show significant variations among flightlines, the standard deviation delivers more consistent results except in the case of flightline 9 and 11. As a result, the coefficient of variation for echo amplitude and width (Table 4.5 and 4.6) are similar for all flightlines, and no odd behaviour can be detected.

Within the concept of radiometric calibration, the current state of the art is to consider one calibration constant per flight campaign (Briese et al., 2008; Lehner and Briese, 2010; Roncat et al., 2011). However, high laser pulse variations (amplitude and width) within individual flightlines can influence the determination of the calibration constant (Roncat et al., 2011). Following this statistical analysis, the output energy was found to be delivered without any major faults over all flightlines as no serious variations in the emitted signals have been detected which could influence the determination of the calibration constant. However, both datasets showed evidence of noisy signals, visible from the minimum values of echo amplitude and width (Tables 4.3 to 4.6). This was therefore considered in the estimation of the calibration constants for both datasets afterwards.

4.3.3 Artificial vs. Natural Reference Target for the Bournemouth Dataset

To check the potential of using the PVC target as reference in the calibration process for the Bournemouth dataset, a statistical comparison between two approaches of different reference targets was adopted. This was undertaken by estimating the backscatter parameters (σ, γ, σ_α, γ_α) for an arbitrarily selected simple house roof target with the geometry depicted in Figure 4.14 and highlighted in red, using the PVC as reference. Consequently, the four backscatter parameters were re-estimated for the same target but this time by adopting a natural reference target. Thereafter, a comparison between the signals delivered from overlapping flightlines through both approaches was undertaken.

The two calibration constants from both approaches were estimated following the radiometric calibration routine introduced in Section 3.5.

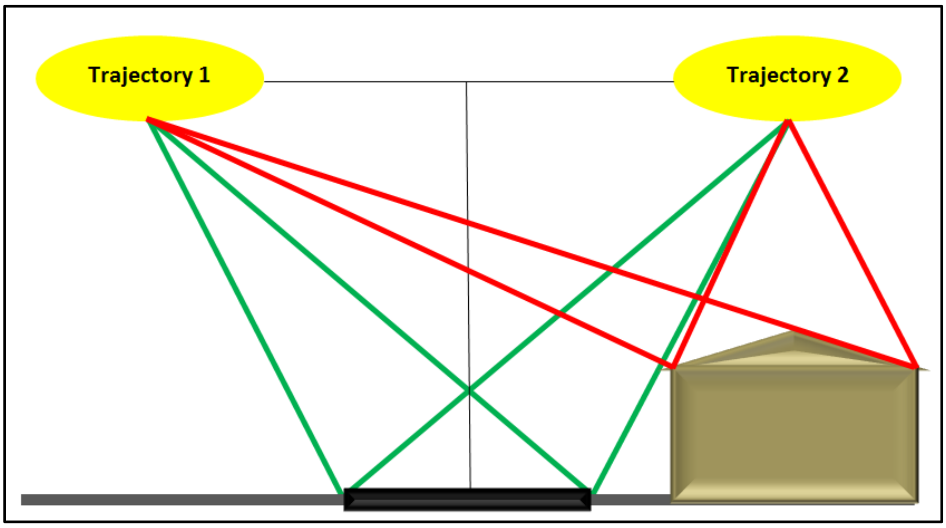

Figure 4.14. The geometry of the house roof and the road target selected to check the potential of using PVC as a reference target and used later to assess the calibration constant for the Bournemouth dataset.

Using 754 echoes over the PVC reference targets and 920 echoes collected from five different asphalt road sections in Bournemouth, two empirical calibration constants were estimated. Thereafter, the four backscatter parameters (σ, γ, σ_α, γ_α) for individual house roof echoes were estimated from both approaches and compared with the signals delivered from the overlapping flightlines.

The statistical analysis for the four backscatter parameters of the selected roof target shows that the backscatter coefficient normalised according to the incidence angle effect (γ_α) delivers the best performance (agreement) between overlapping flightlines in both approaches. This was demonstrated through the standard deviation differences in percentage between overlapping flightlines which delivered the lowest value in the case of γ_α as illustrated in Table 4.7. This is an evidence of the importance of considering the incidence angle effect throughout the radiometric calibration process; therefore γ_α was selected for the comparison purposes in this test.

However, the purpose of this comparison test was not to find the optimal backscatter parameter which delivers the optimal match between flightlines. This test was aimed to investigate the potential of using the PVC target to deliver the calibration constant for the Bournemouth dataset. This can be obtained by comparing the signals from overlapping flightlines between those delivered from utilising a PVC reference target with signals delivered from adopting a natural reference target. The relationship between both approaches should be the same for each backscatter parameter over the selected target, except for the differences in the calibration constants. Thus, the differences in the standard deviation differences between backscatter parameters in the corresponding approaches should be the same as well. Therefore it is not important for which parameter to select to apply the comparison in this particular test as long as the comparison is performed using the same parameter in both approaches. However, finding the optimal backscatter parameter which delivers best agreement between overlapping signals amongst the rest of the backscatter parameters, was investigated in the following sections.

Parameter	**% Ϭ Differences**	
	PVC reference target	**Asphalt reference target**
Echo amplitude	34.301	34.301
σ	26.320	30.620
γ	24.549	28.849
σ_α	24.943	29.243
γ_α	20.340	24.640

Table 4.7. The standard deviation difference in percentage of the backscatter parameters and the original amplitude signals delivered from overlapping flightlines of a house roof target using PVC and asphalt reference targets.

The results from adopting a PVC reference target perform better than those delivered from the asphalt reference target, as realised from Table 4.7 and shown through the box plot analysis of the γ_α parameter in Figure 4.15. It can be realised from this plot that the match between flightlines is better achieved between signals delivered by adopting artificial reference targets than those delivered by adopting natural reference targets. In particular, this can be noticed from the gradient of the red line connect between median values from the overlapping flightline signals in individual approaches which is reported to be greater in the case of the asphalt reference target. This is also visible from normal distribution analysis of the γ_α parameter in Figure 4.16, and evidenced from the lower means and standard deviation differences between flightlines in Figure 4.16-a as compared to Figure 4.16-b. Although the differences between overlapping flightline signals shown in Figure 4.16 are small, the results demonstrated the potential of using the PVC target as a reference in the calibration routine. As both the incidence angle effect and atmospheric transmittance were considered in estimating the calibration constants in both approaches, it seems that the main parameter affecting the outcome was the reflectivity value of the reference target. However, the next section will introduce more comprehensive results delivered from comparing the developed routine with an existing technique by adopting further statistical testing.

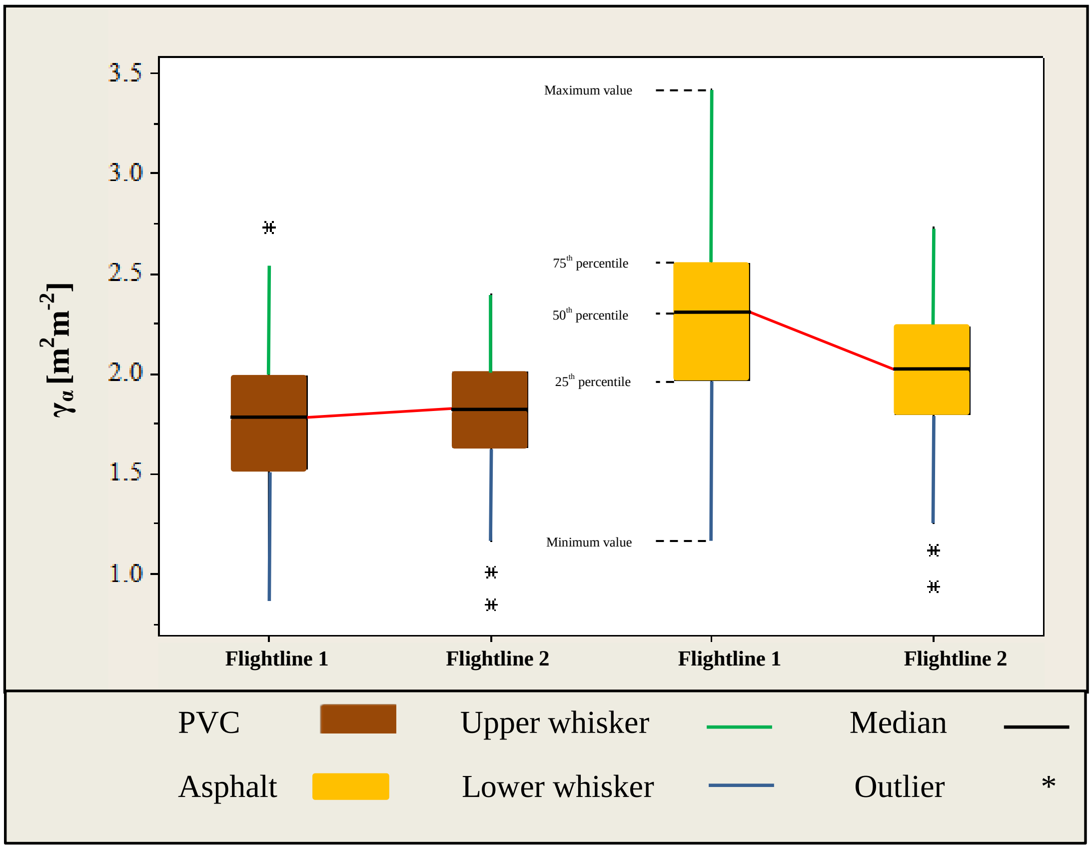

Figure 4.15. Box plot analysis of house roof target from overlapping flightlines in the Bournemouth dataset, showing the performance of the γ_α parameter and comparing the two calibration constants, from artificial and natural reference targets.

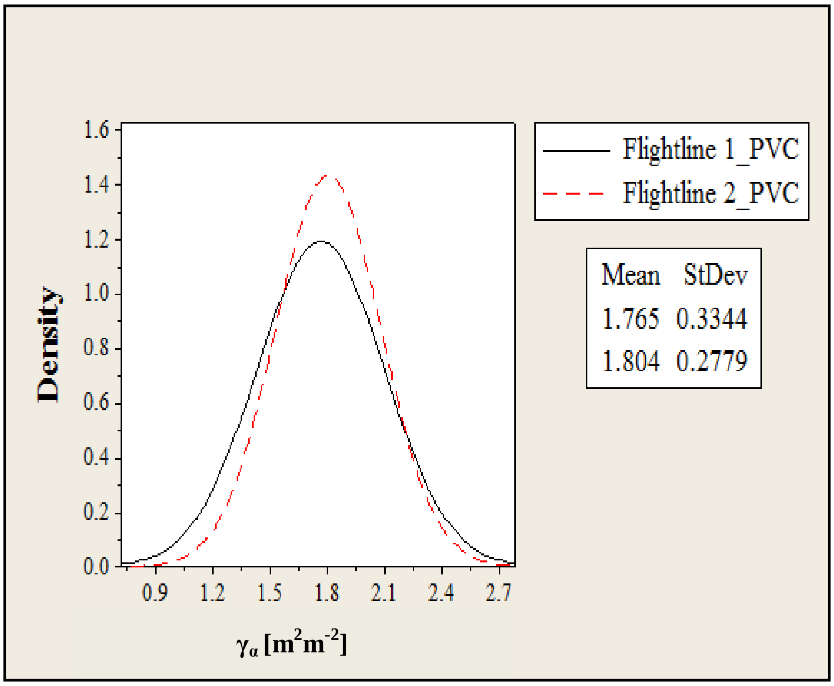

(a) Results from using PVC reference target.

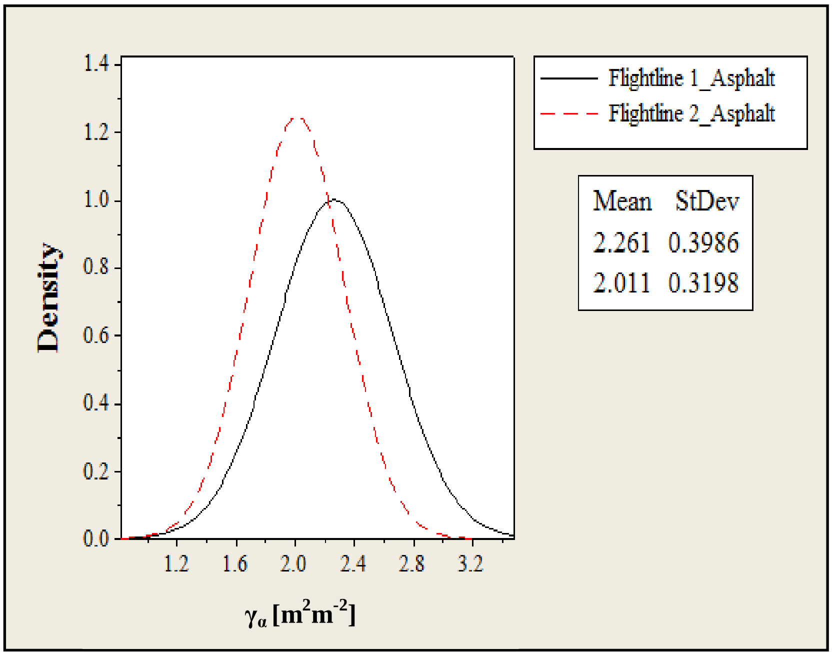

(b) Results from using asphalt reference target.

Figure 4.16. Distribution analysis of house roof target from overlapping flightlines in Bournemouth dataset, showing the performance of the γ_α parameter delivered from adopting two calibration constants from artificial and natural reference targets.

4.3.4 Assessing the Calibration Constant for the Bournemouth Dataset

In this research, after approving the potential of using the PVC artificial reference target to estimate the calibration constant for the Bournemouth dataset, it is important to assess this constant by comparing it to constants from other approaches. An alternative technique to estimate the calibration constant for the same dataset is presented by Alexander et al. (2010). They estimate the calibration constant for the Bournemouth dataset by using asphalt road sections as a reference target to calibrate the whole dataset. The incidence angle effect was neglected for the reference target signals and instead only near-nadir echoes were used. They utilised a literature reflectance value of 0.25 for the asphalt, and no reflectivity measurements were undertaken in order to calibrate this dataset. Following this configuration the backscatter cross-section of the reference target was estimated and used to deliver the calibration constant for the whole dataset. This is in contrast with the approach developed here, which uses the backscatter coefficient parameter (γ) as a measure of the backscatter energy for the PVC reference target.

To assess the calibration constant adopted in this research, the developed routine is compared with that presented by Alexander et al. (2010) over a road target which appears in overlapping flightlines in the Bournemouth dataset. This target was selected in order to minimise the incidence angle effect as much as possible in order to allow more direct comparison to the Alexander et al. (2010) method. To assure approximately similar conditions (e.g. range and scan angle) from both flightlines, the road target was selected to meet the geometry proposed in Figure 4.14 (highlighted in green). Thus in perfect conditions, the received backscatter signals from overlapping flightlines are assumed to be the same over this particular target. These particular settings were chosen in order to test the potential of using the backscatter coefficient parameter (γ) in estimating the calibration constant in comparison to the backscatter cross-section (σ) as adopted by Alexander et al. (2010). It should be highlighted that Alexander et al. (2010) stated the calibration constant value of their approach and it is thus used for direct comparison without pre-estimation here.

Firstly, the developed technique was applied on the individual selected road target echoes and the signals compared from both overlapping flightlines. The histogram of the γ parameter in Figure 4.17-b shows a significant improvement over the original amplitude signals in Figure 4.17-a whereas the results from the σ parameter (Figure

4.17-c) shows a significant reduction. This was approved by the standard deviation (Ϭ) and mean differences in percentage between signals from overlapping flightlines as illustrated in Table 4.8. The reduction in the σ results as compared with original signals was not expected, which might be acquired by overcorrecting. However, the γ parameter shows encouraging results as the differences were reduced significantly in a comparison with the original signals as demonstrated by Figure 4.17 and Table 4.8.

However, the results of the normalised version of the backscatter coefficient with respect to incidence angle effect (γ_α) deliver a nearly perfect match between the overlapping flightlines signals which are highlighted in Figure 4.17-d and demonstrated through small mean and Ϭ differences in Table 4.8. Although the investigated target was selected to be as flat as possible, it seems that it is not a perfectly flat surface and the incidence angle is still affecting the received signals, as demonstrated in Figure 4.17-d. The results of the γ_α parameter agreed with the assumption made when selecting this target in the first place, which assures similar conditions (e.g. range and scan angle) from both flightlines.

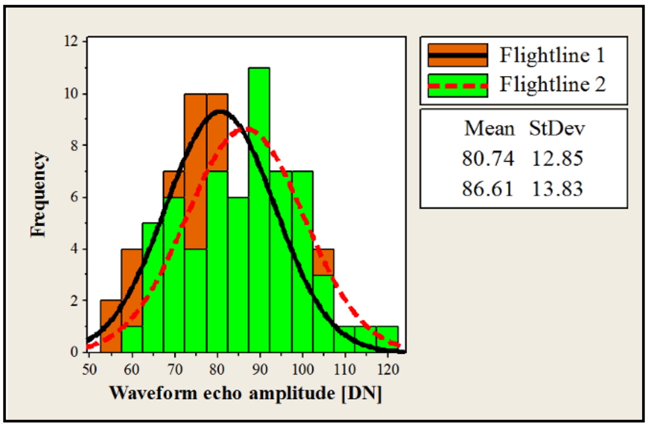

(a) The original amplitude signals.

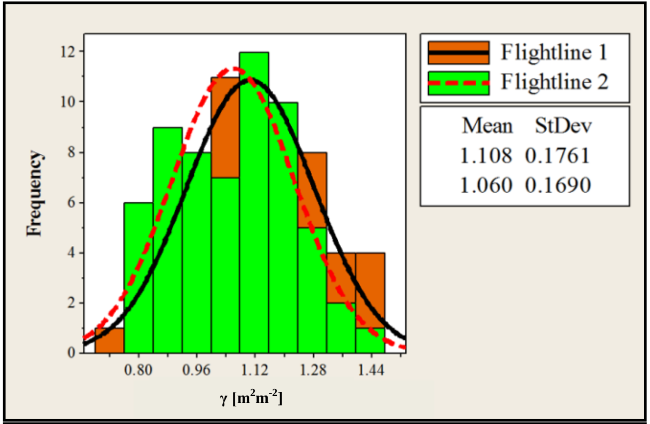

(b) The backscatter coefficient signals.

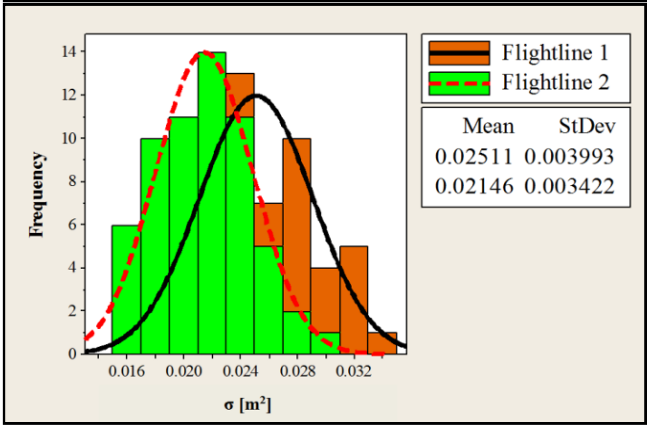

(c) The backscatter cross-section signals.

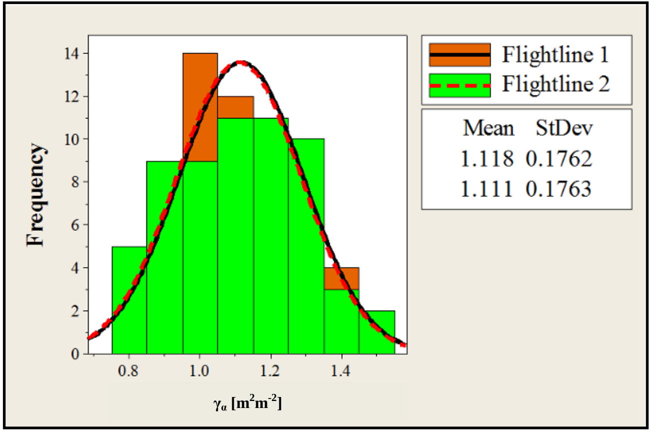

(d) The normalised backscatter coefficient signals with respect to incidence angle.

Figure 4.17. The histogram of the original amplitude signals and the backscatter parameters after calibration following the developed radiometric calibration routine of a selected road target from overlapping flightlines in the Bournemouth dataset.

Parameter	% Differences	
	Mean	**б**
Echo amplitude	7.270	7.630
γ	4.530	4.210
σ	17.250	17.540
γ_α	0.630	0.060

Table 4.8. The mean and the standard deviation differences in percentage of the signals delivered from overlapping flightlines of a road target before and after calibration using the developed approach.

Thereafter, new γ signals were estimated for individual echoes enclosed within the selected target from overlapping flightlines using the calibration constant estimated by Alexander et al. (2010). The histogram results of the γ signals of the selected target following Alexander et al. (2010) routine are demonstrated in Figure 4.18. As the approach of Alexander et al. (2010) neglects the incidence angle effect throughout the calibration workflow, no incidence angle is available to use for comparison. Therefore the comparison between the presented and Alexander et al. (2010) routines are based on the backscatter coefficient parameter (γ) of the road target as both routines delivered improvements with this parameter after calibration, as shown in Figure 4.17-b and Figure 4.18 respectively.

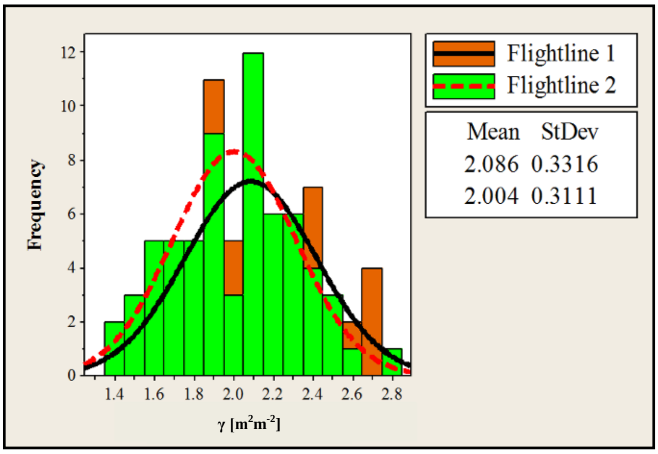

Figure 4.18. The histogram of backscatter coefficient signals after calibration using Alexander et al. (2011) radiometric calibration routine of a selected road target from overlapping flightlines in the Bournemouth dataset.

It can be realised from Figure 4.18 that the Alexander et al. (2010) routine proves to deliver significant improvements after calibration as compared with the original signals in Figure 4.17-a. This can be justified by delivering low mean and Ϭ differences between overlapping flightlines of 4.1% and 6.6% respectively, in a comparison with the original signals from Table 4.8. However, the potential of the results improvements delivered from applying the Alexander et al. (2010) approach against those delivered from applying the developed approach is still in need for further investigations. To achieve this, a statistical 2-sample T-test is used to compare the backscatter coefficient (γ) results delivered from both approaches, (refer to Montgomery (2005) for further details). This statistical test is designed to compare the means of two sample datasets based on variance check analysis, by delivering an index value known as the P-value that better describes the probability that both datasets are significantly different to each other or not. In this case, the datasets used in this comparison are representing the signals from overlapping flightlines obtained through the two approaches. The test was applied using the 95% confidence level. Thus, a P-value of less than 5% means that the datasets are significantly different. However, this test cannot be applied without checking the variance of both datasets. This was undertaken using the F-test, which compares the variances and checks whether the datasets have similar variances or not, in order to use the outcome as an input to the subsequent T-test. It is worth noting that comparing the variances of the two datasets delivers P-values from two distinct hypotheses, the F-test and Levene's test. Levene's test assumes the normality of the comparative datasets is questionable. However, the F-test assumes the comparative datasets are normally distributed. As our datasets conform to a normal distribution, as evidenced through the histograms in Figure 4.17, the F-test results were adopted in this particular study. For more details about these statistical tests and their analysis refer to Montgomery (2005).

Figure 4.19 demonstrates the results delivered from comparing the variances of backscatter coefficient signals delivered from overlapping flightlines through both approaches. As can be seen, the P-value delivered from the F-test shows that the comparative datasets have similar variances in both approaches, as described by the high P-value (> 0.05). Thereafter, the T-test was applied for final decision of this statistical assessment.

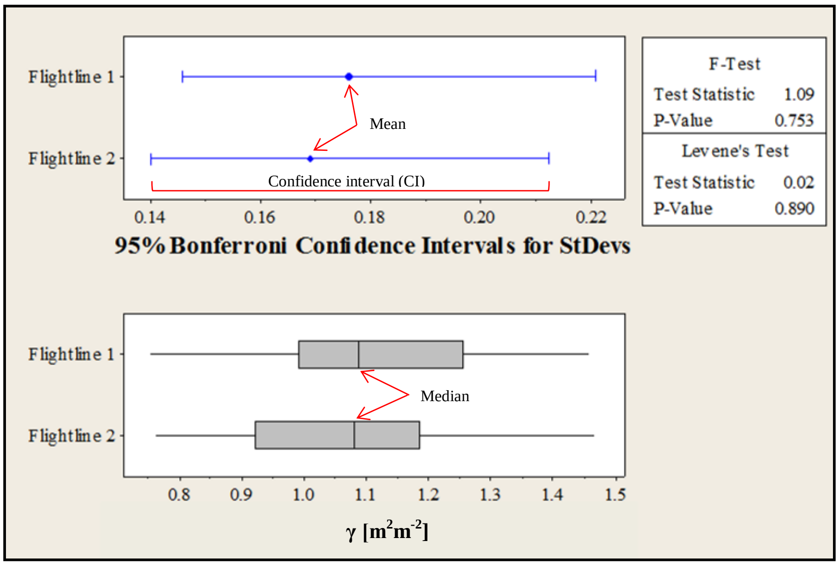

(a) Results from applying the developed radiometric calibration routine.

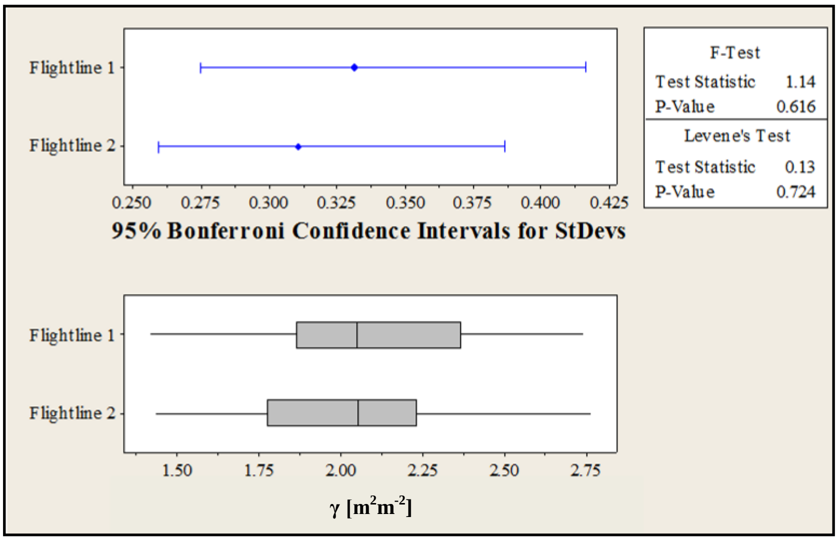

(b) Results from applying Alexander et al. (2010) routine.

Figure 4.19. Variance of backscatter coefficient signals over a selected road target from overlapping flightlines in the Bournemouth dataset.

Table 4.9 illustrates the T-test statistical reports for both approaches. It shows that the estimate for the differences between the means is lying within the confidence interval (CI) in both approaches. Consequently, it can be concluded that the datasets in both approaches are not significantly different. This is also clear from the P-value results which proved that no significant differences can be observed through both approaches. That means, both approaches deliver a significant agreement between signals from overlapping flightlines after calibration. However, the developed approach delivers a higher P-value than the one delivered from the Alexander et al. (2010) approach. Moreover, the T-values which interpret completely opposite the P-value interpretation (this will be discussed further in next sections) also meet with these findings. Although γ_α proved to be the best parameter to assess the developed routine, these finding confirms the potential of using γ rather than σ to estimate the calibration constant for radiometric calibration purposes.

The developed routine	Difference = mean (Flightline 1) - mean (Flightline 2) Estimate for difference: 0.0476 95% CI for difference: (-0.0148, 0.1099) T-Test of difference: T-Value = 1.35, P-Value = 0.299
Alexander et al. (2010) routine	Difference = mean (Flightline 1) - mean (Flightline 2) Estimate for difference: 0.0823 95% CI for difference: (-0.0315, 0.1961) T-Test of difference: T-Value = 1.43, P-Value = 0.155

Table 4.9. Two-sample T-test reports of backscatter coefficient signals delivered from overlapping flightlines through both approaches.

4.3.5 Assessing the Calibrated Backscatter Signals

The calibrated backscatter signals delivered from overlapping flightlines over a variety of land cover types with different surface trends and properties were analysed and compared for both investigated datasets. In order to assess which configuration is able to best eliminate flightline discrepancies, the four aforementioned backscatter parameters were considered. A selected interest area from the Bournemouth study site and several homogeneous targets (in terms of feature composition and material) from both datasets were tested and validated using statistical and visual analysis. The validation process aims to compare the backscatter signals from overlapping flightlines to demonstrate the performance of the backscatter signals after calibration. Thirty-two targets were tested for the Bournemouth dataset, including planar and natural discontinuous trends. However due to lower point density, only twenty targets were investigated for the Bristol dataset. These include roads, house roofs, artificial ground, cars, natural and undulating terrain, bare ground, grassed ground, hedge, scrub, high trees and canopies.

For each examined target and each selected interest area, the signals from overlapping flightlines were firstly investigated individually to check whether they follow the normal distributed curve. It should be noted that the target refers to one land cover feature, however the interest area refers to multi features within a certain region. This is essential as the majority of the standard statistical tests are reliant on the normal distribution assumption. To check the normality of the examined signals in each particular target, one of two approaches was implemented. The first approach was to plot a histogram and compute skewness and kurtosis values, in order to check sample data distribution and whether there is a skewness behaviour or not. The second approach was by applying a normality statistical test available from any statistical software such as Minitab, which delivers the same information by means of P-value. By adopting either of the previous approaches, the normality distribution of the comparative datasets can be analysed.

Based on the normality check results, the decision is made in whether to utilise the F-test or Levene’s test when testing variances. Thereafter, a 2-sample T-test is applied to check whether the comparative signals have equal means or not. This is based on the P-value or alternatively T-value analysis (in the case where the P-values are found to be equal). The T-value can also be used to analyse the probability of a significant difference between two datasets by delivering a T-index value to be compared with a tabulated critical T-value which is available from T-distribution tables found in most statistical resources. The critical T-value is usually detected in the T-distribution table based on the confidence interval level selected to implement the analysis test. To better understand the hypothesis and interpretation of the T-value, refer to Montgomery (2005). Finally, to identify the parameter that provides the greatest potential for improvements amongst the four investigated backscatter parameters, a Pareto chart is produced for each distinct target. The Pareto chart is a series of frequency bars whose heights indicate the impact of a certain problem. It utilised in this study to reflect the discrepancies between flightlines based on T-value analysis.

To demonstrate the implemented calibration workflow, a small interest area (≈ 100 m x 60 m) which comprises various surface features was selected and analysed from the Bournemouth study site. Gradient black and white-coded maps of original echo amplitude signals and the four derived backscatter parameters delivered for overlapping flightlines is presented in Figure 4.20.

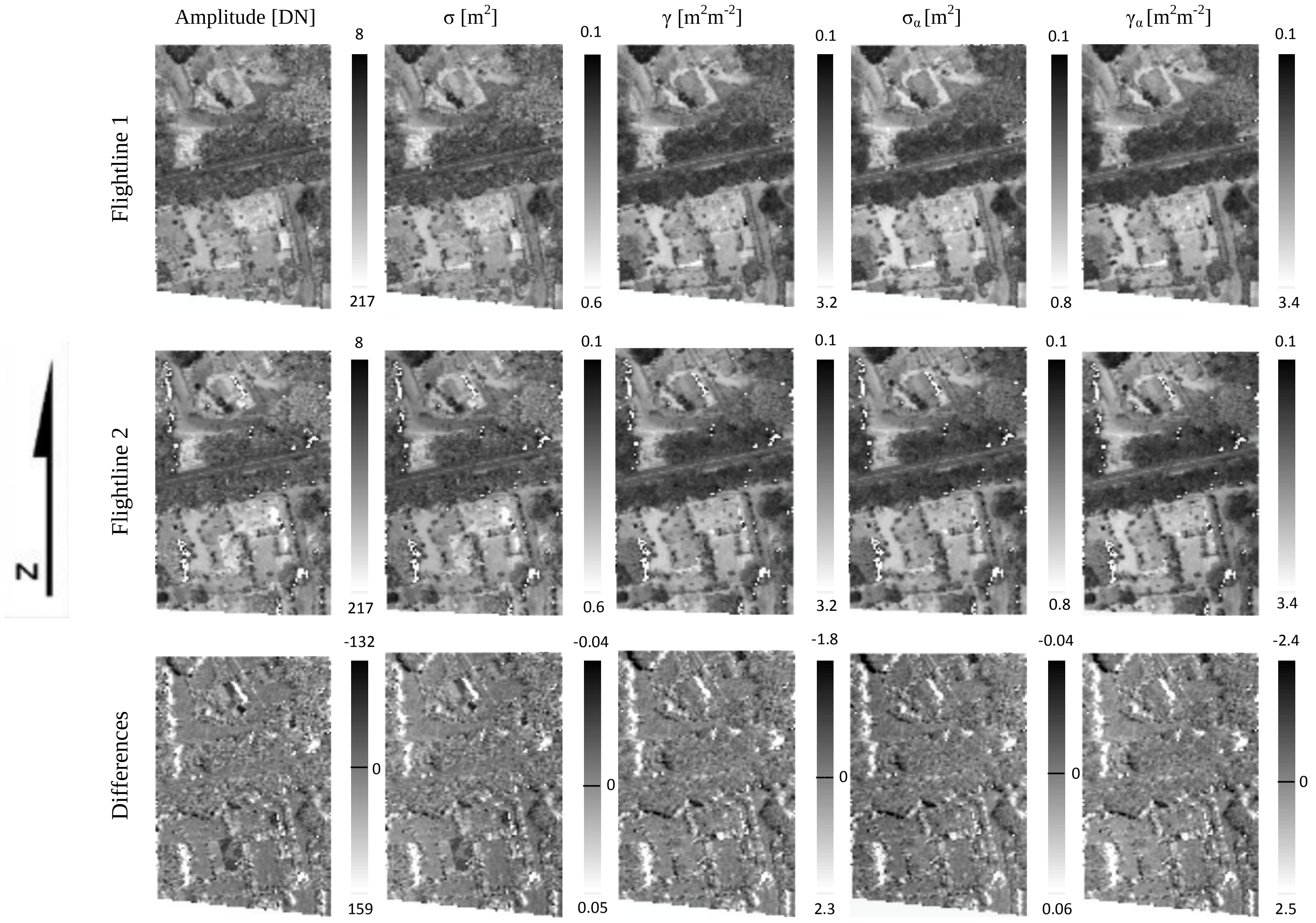

Figure 4.20. Difference maps for two overlapping flightlines of an interest area in the Bournemouth study site, showing the original echo amplitude signals and the four backscatter parameters (σ, γ, σ_α, γ_α).

The results show that γ_α delivers the smallest differences between overlapping flightline signals in comparison with other parameters. This is evidenced over house roofs, roads and grass regions. Consequently, in order to examine the performance of the calibration routine, colour-coded difference maps for overlapping flightline signals were produced as shown in Figure 4.21. These include the original amplitude signals and their corresponding calibrated signals delivered from the γ_α parameter. The reduction in the signal differences is clearly visualised over roofs, roads and grass regions in Figure 4.21, demonstrating the minimisation of differences between the backscatter signals before and after calibration. It is also evident that a relative improvement in the signal differences has been detected over vegetated regions in this case, which requires further investigations.

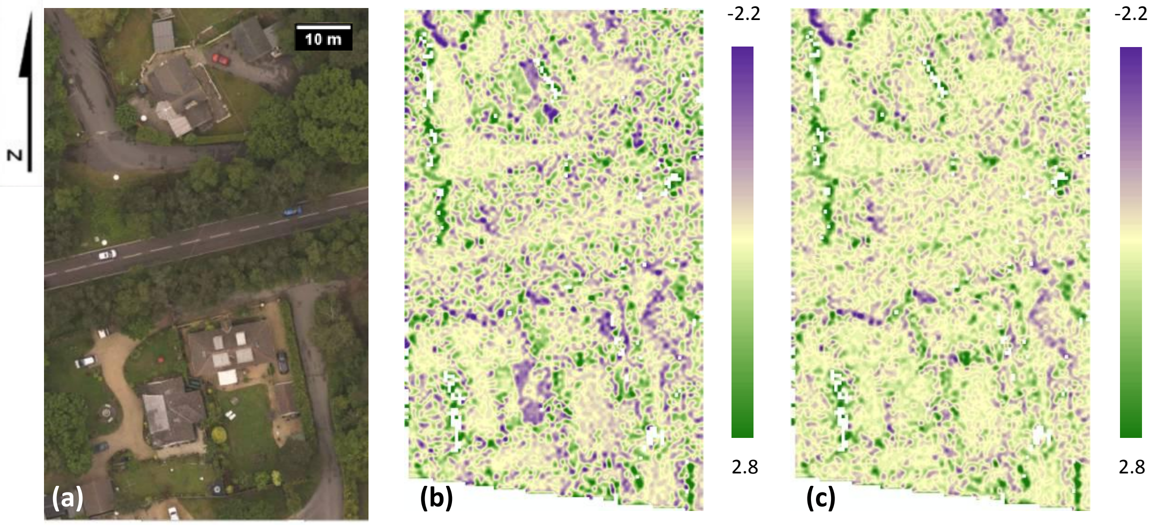

Figure 4.21. Difference maps from two overlapping flightlines for an interest area in the Bournemouth study site: **(a)** orthophoto of the interest area; **(b)** original echo amplitude difference map; **(c)** γ_α difference map.

To summarise these outcomes over the selected interest area, a Pareto chart of all backscatter parameters is shown in Figure 4.22. The chart describes the discrepancies between flightlines delivered from the four backscatter parameters based on the T-values following the T-test. It shows that the γ_α parameter delivers the best match through the lowest T-value (highest P-values), while σ shows the poorest performance of all the parameters. This is because the backscatter coefficient parameter normalised with respect to incidence angle, can better account for the differences in signals acquired from trajectories of different position and orientation. However, these results represent overall signal behaviour over the selected interest area which is composed of multiple target materials and geometries. Therefore, the next part of this section focuses on results from individual, homogeneous targets.

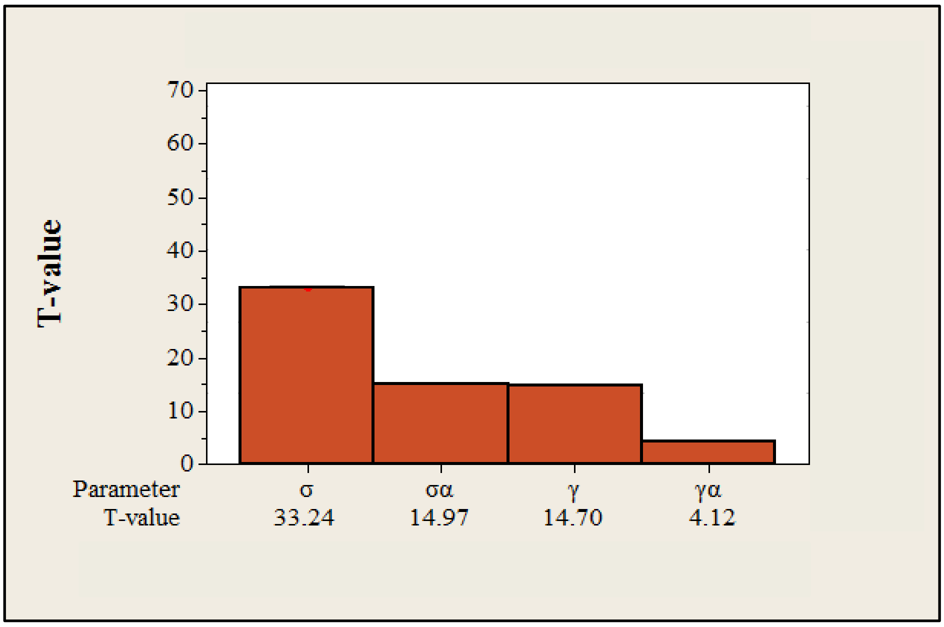

Figure 4.22. Pareto chart of the backscatter parameters over an interest area in the Bournemouth study site.

To demonstrate the visual discrepancies between the flightlines for the backscattered signals before and after calibration, two homogeneous targets from both datasets were examined. Figure 4.23 illustrates the sample targets from the Bournemouth and Bristol datasets respectively. Figures 4.24 and Figure 4.25 show the corresponding backscatter signals from overlapping flightlines for the two mentioned targets for both datasets respectively, represented by the histograms and the normal distribution curves.

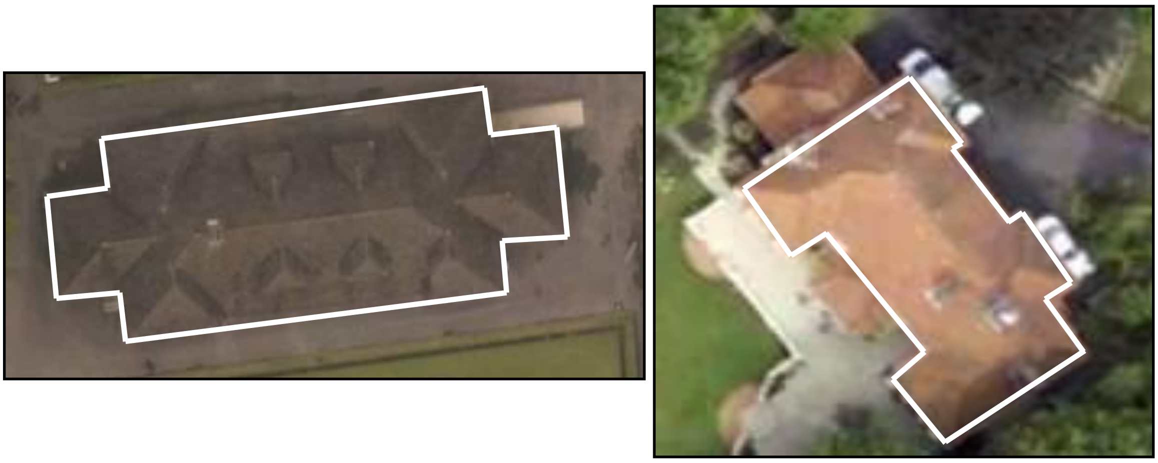

Figure 4.23. Orthophotos highlighting roof targets from Bournemouth (left) and Bristol (right) study sites.

It can be realised from both Figure 4.24 and Figure 4.25 that the backscatter coefficient parameter γ delivers more homogeneous signals and a better match between the flightlines than σ for both targets. However, the incidence angle normalised version γ_α shows the best performance amongst the four backscatter parameters by eliminating the differences between the standard deviation and mean values for both flightlines through the inclusion of robust incidence angle estimation.

The results delivered from all examined targets in both datasets indicate marked improvements after calibration. However, the γ_α parameter delivers the optimal match between flightlines except over vegetation, where the σ parameter shows better performance. This was evidenced by the small standard deviation differences as compared with the original echo amplitude differences delivered from all backscatter parameters, and as shown in Table 4.10 and Table 4.11. However, the differences in the ratio R of the variation coefficients V_C is more representative as it considers both standard deviation and the mean values of each particular target. Therefore, the outcomes were demonstrated over all tested targets and presented in Table 4.10 and 4.11 for the Bournemouth and Bristol datasets respectively. The analysis is based on computing the differences in the ratio R of the variation coefficients V_C between overlapping flightlines for the four backscatter parameters, as follows:

$$Diff(R) = R_{flight1} - R_{flight2}$$ **Eqn. 4-1**

$$R_1 = \frac{V_{C(\sigma)}}{V_{C(Amplitude)}},\ R_2 = \frac{V_{C(\gamma)}}{V_{C(Amplitude)}},\ R_3 = \frac{V_{C(\sigma\alpha)}}{V_{C(Amplitude)}},\ \text{and}\ \ R_4 = \frac{V_{C(\gamma\alpha)}}{V_{C(Amplitude)}}$$ **Eqn. 4-2**

$$V_C = \frac{std}{Mean}$$ **Eqn. 4-3**

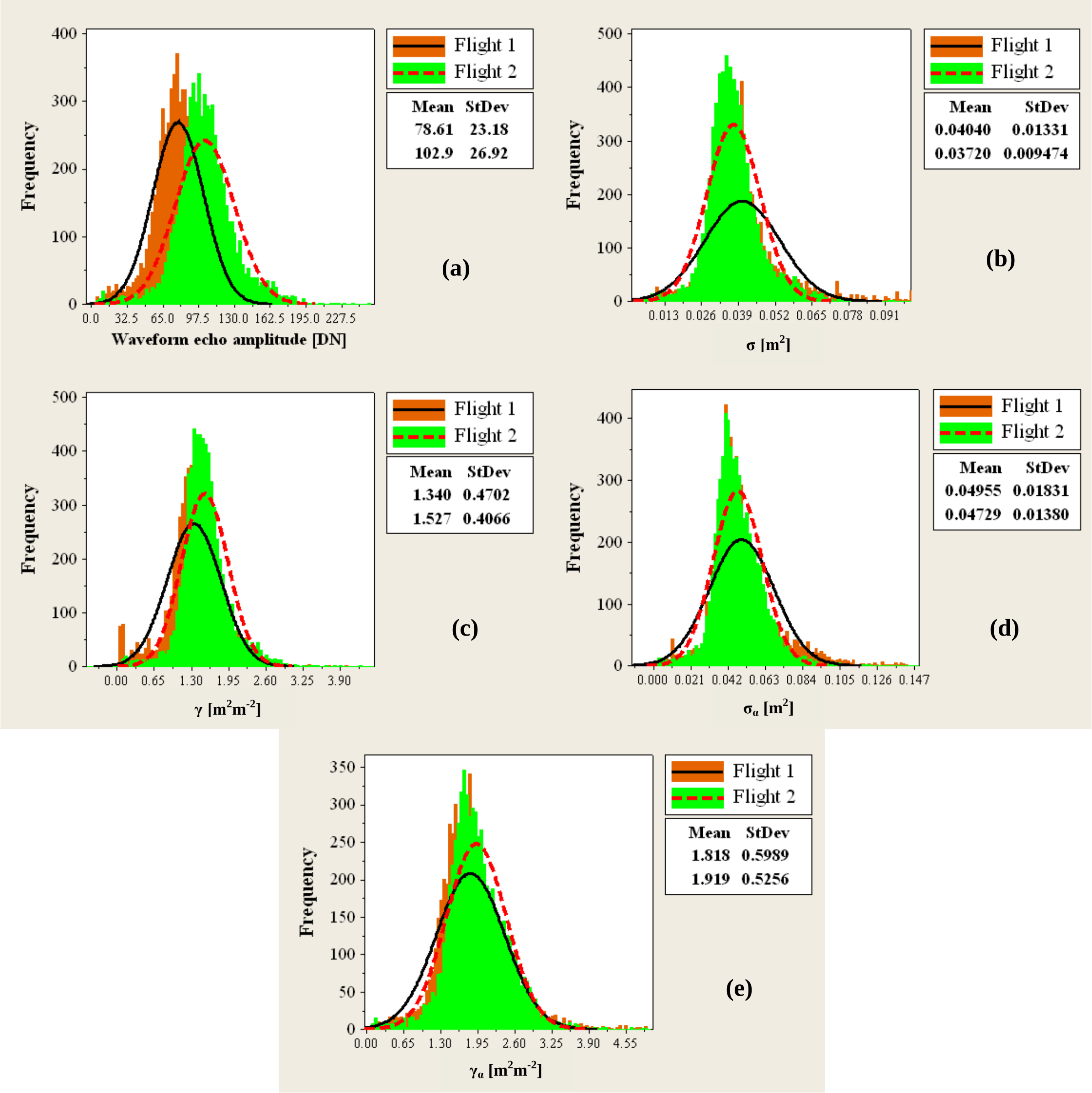

Figure 4.24. The backscatter signals from two overlapping flightlines of a roof target in the Bournemouth study site: **(a)** the original amplitude signals **(b-e)** the four backscatter parameters (σ, γ, σ_α, γ_α) respectively.

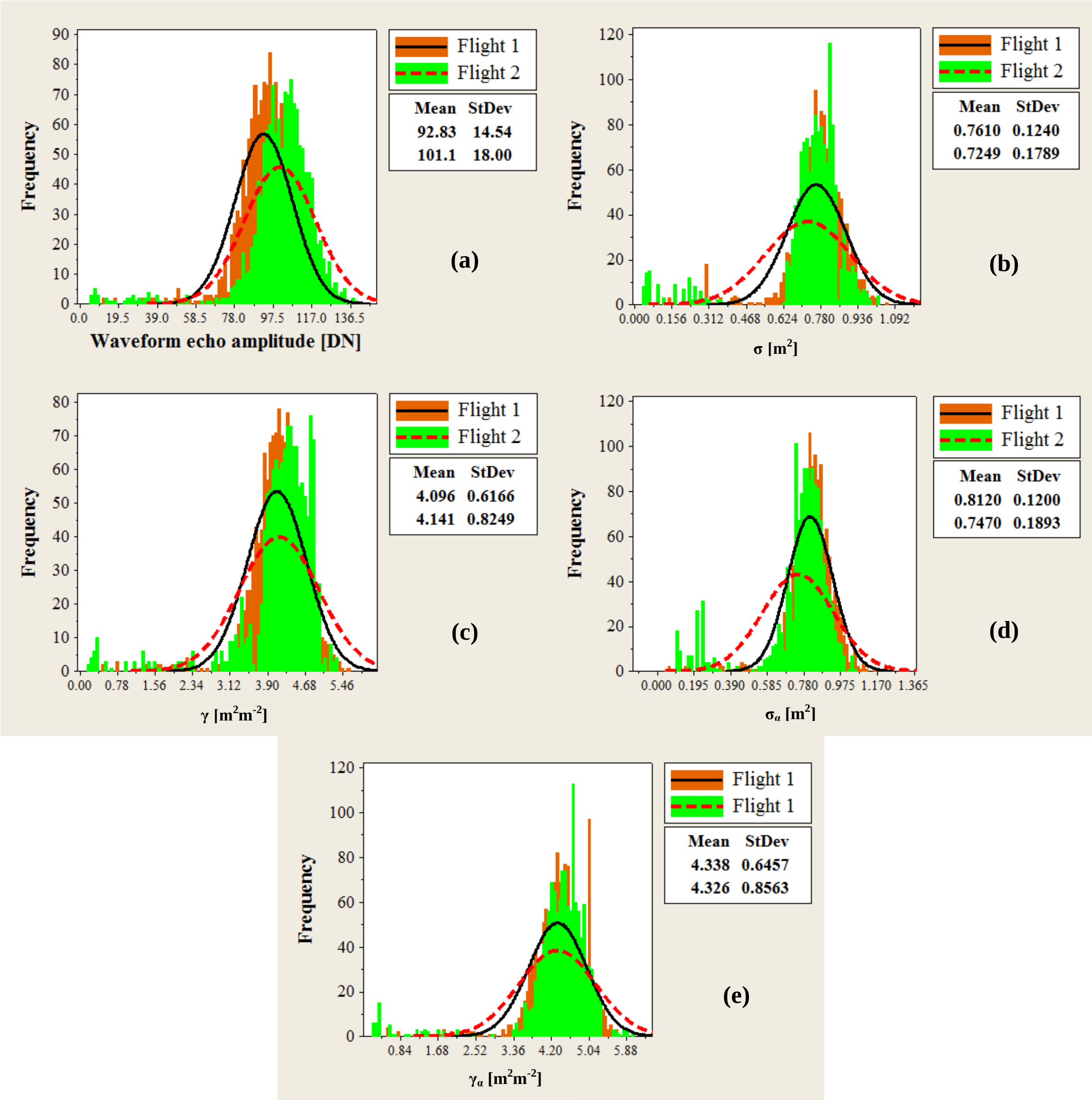

Figure 4.25. The backscatter signals from two overlapping flightlines of a roof target in the Bristol study site: **(a)** the original amplitude signals **(b-e)** the four backscatter parameters (σ, γ, σ_α, γ_α) respectively.

	Targets	**No. of points**		**%ϭ diff (Amplitude)**	**%ϭ diff (σ)**	**%ϭ diff (γ)**	**%ϭ diff (σ_a)**	**%ϭ diff (γ_a)**	**Diff (R1)**	**Diff (R2)**	**Diff (R3)**	**Diff (R4)**
		Flightline 1	**Flightline 2**									
1	Asphalt road	2944	2785	17.819	7.818	3.725	1.793	1.076	0.017	0.004	0.004	0.004
2	Slant house roof1	1663	1576	15.784	14.067	10.438	8.769	3.699	0.192	0.017	0.192	0.014
3	Slant house roof2	1287	1324	11.118	7.698	7.139	6.330	4.193	0.020	0.009	0.021	0.001
4	Complex house roof1	1818	1730	19.922	16.687	11.538	3.070	2.939	0.357	0.007	0.353	0.006
5	Complex house roof2	1498	1544	12.518	10.232	8.338	7.603	0.040	0.112	0.056	0.480	0.016
6	Complex house roof3	585	611	24.883	19.616	13.229	9.292	3.733	0.091	0.045	0.053	0.043
7	Complex house roof4	583	494	12.061	11.378	4.139	3.497	1.477	0.062	0.002	0.062	0.002
8	Tennis play ground	1126	1035	3.666	2.332	3.454	3.761	1.025	0.016	0.008	0.019	0.008
9	Artificial ground1	202	139	11.582	7.330	3.042	8.052	3.000	0.017	0.011	0.016	0.010
10	Artificial ground2	471	385	7.631	2.533	1.273	2.729	1.218	0.028	0.008	0.011	0.008
11	Bridge	4420	4547	17.616	15.053	5.252	12.389	3.557	0.017	0.017	0.102	0.003
12	Car1	192	119	6.489	5.576	11.666	2.940	2.751	0.400	0.013	0.900	0.013
13	Car2	44	66	11.558	17.294	18.647	16.409	19.415	0.018	0.019	0.014	0.023
14	Car3	54	54	7.992	11.737	0.932	10.176	0.744	0.571	0.572	0.500	0.499
15	Natural terrain1	2592	2650	31.710	29.178	20.826	26.588	4.070	0.604	0.314	0.556	0.208
16	Natural terrain2	2882	2904	56.315	33.091	27.233	15.121	7.121	0.729	0.987	0.860	0.549
17	Natural terrain3	2985	2721	31.626	34.985	29.585	20.113	13.756	0.453	0.441	0.456	0.349
18	Natural terrain4	1574	1524	4.738	4.345	3.183	3.750	2.207	0.930	0.019	0.926	0.016
19	Natural terrain5	1219	1237	10.918	12.485	7.063	11.485	6.186	0.016	0.021	0.015	0.005
20	Natural terrain6	2962	2911	17.881	17.372	15.217	12.526	7.211	0.321	0.062	0.157	0.059
21	Natural terrain7	1395	1430	20.952	14.899	8.768	8.759	3.706	0.033	0.034	0.297	0.030
22	Bare ground	2447	2409	12.237	8.178	5.722	4.161	2.322	0.023	0.017	0.017	0.010
23	Bare slope ground	1987	1789	11.356	10.608	7.673	2.667	2.634	0.054	0.054	0.047	0.034
24	Sloped terrain	1261	1300	1.906	1.337	1.784	1.547	0.137	0.028	0.028	0.019	0.015
25	Undulate terrain	1570	1518	49.566	33.825	26.472	27.022	9.493	0.105	0.012	0.087	0.005
26	Cricket play ground	1517	1481	9.220	8.439	2.440	8.429	2.210	0.013	0.000	0.013	0.000
27	Low grass1	13496	13447	29.419	24.483	17.739	20.852	13.885	0.008	0.014	0.004	0.004
28	Low grass2	895	960	28.463	25.209	22.171	21.393	21.28	0.049	0.055	0.050	0.048
29	Hedge	535	533	31.448	25.834	25.446	17.077	16.920	0.060	0.069	0.063	0.059
30	Scrub	178	168	12.037	5.164	7.879	69.417	44.059	0.053	0.054	0.167	1.161
31	High tree	1391	1361	1.364	0.557	0.768	16.042	20.143	0.009	0.012	0.072	0.088
32	Canopy	12202	12248	14.657	8.491	9.855	38.903	38.898	0.011	0.028	0.556	0.573

Table 4.10. Results of the standard deviation difference in percentage and the ratio R of the variation coefficients V_C delivered from all tested targets in the Bournemouth dataset. Highlighted red numbers are discussed in details in Section 4.3.5.

	Targets	No. of points		%Ϭ diff (Amplitude)	%Ϭ diff (σ)	%Ϭ diff (γ)	%Ϭ diff (σ_a)	%Ϭ diff (γ_a)	Diff (R1)	Diff (R2)	Diff (R3)	Diff (R4)
		Flightline 1	Flightline 2									
1	Asphalt road	1321	1352	0.047	0.040	0.034	0.037	0.029	0.038	0.029	0.031	0.018
2	House roof1	812	790	6.62	0.055	0.300	0.052	0.210	0.027	0.022	0.026	0.009
3	House roof2	1719	2060	1.873	0.087	0.041	0.067	0.019	0.061	0.051	0.015	0.007
4	House roof3	538	533	0.68	0.0934	0.0662	0.077	0.0175	0.013	0.011	0.009	0.002
5	Complex roof1	2100	2084	0.82	0.059	0.033	0.034	0.009	0.029	0.024	0.025	0.022
6	Complex roof2	1206	1179	3.456	0.389	0.111	0.370	0.106	0.048	0.032	0.021	0.015
7	Complex roof3	1376	1379	6.12	0.304	0.054	0.281	0.007	0.022	0.016	0.021	0.012
8	Artificial ground2	725	729	1.14	0.045	0.034	0.036	0.034	0.029	0.011	0.025	0.000
9	Artificial ground1	913	972	3.85	0.093	0.067	0.078	0.023	0.010	0.010	0.010	0.010
10	Highway bridge	1501	1472	5.131	0.162	0.043	0.093	0.014	0.119	0.078	0.117	0.069
11	Natural terrain1	594	522	1.28	0.019	0.100	0.010	0.005	0.033	0.031	0.029	0.027
12	Natural terrain2	828	726	0.861	0.135	0.041	0.084	0.032	0.049	0.039	0.039	0.017
13	Natural terrain3	605	527	2.726	0.077	0.013	0.067	0.010	0.026	0.023	0.028	0.011
14	Bare ground	331	388	0.26	0.110	0.035	0.083	0.022	0.029	0.022	0.021	0.012
15	Bare slope	1022	1007	0.083	0.025	0.006	0.014	0.003	0.002	0.006	0.001	0.001
16	Low grass1	1551	1559	0.669	0.543	0.171	0.342	0.134	0.266	0.235	0.243	0.143
17	Low grass2	1613	1729	2.842	0.185	0.035	0.159	0.030	0.065	0.064	0.005	0.005
18	Low tree	2225	2169	0.32	0.013	0.037	0.214	0.038	0.016	0.045	0.089	0.091
19	High tree	3515	3355	1.722	0.016	0.077	0.019	0.092	0.019	0.027	0.125	0.122
20	Canopy	5543	5503	1.559	0.006	0.017	0.013	0.008	0.005	0.047	0.029	0.036

Table 4.11. Results of the standard deviation difference in percentage and the ratio *R* of the variation coefficients V_C delivered from all tested targets in the Bristol dataset.

The γ_α parameter shows optimal agreement by delivering the smallest difference *R* value represented by *Diff (R4)* over all targets in both datasets except in the case of vegetation, where σ is shown to deliver a better agreement over these targets. However, one particular case was detected which did not meet with these outcomes. The Car2 target in the Bournemouth dataset was found to deliver the smallest *R* value for σ_α. In this particular case, the standard deviation difference between flightlines was found to deteriorate after calibration in comparison with the original amplitude signals. It was also noticed that the backscatter cross-section performs better than the backscatter coefficient over this target. As a result, the incidence angle normalised version of the backscatter cross-section shows better performance than the corresponding normalised version of the backscatter coefficient. This may be caused by the fact that the sample size for this particular target is relatively small, and therefore, the comparison with the corresponding signals from overlapping flightlines may be biased by the inclusion of the FWF points. A similar deteriorating behaviour in the discrepancies of the overlapping signals after calibration was also detected over Car3. However in this case, R_4 was found to be the smallest which meets with the overall outcomes. Another odd behaviour was detected over the Tennis playground target, where σ delivers a smaller standard deviation difference than γ. However, after considering the incidence angle effect, γ_α shows the best agreement results between overlapping flightline signals, which leads to small R_4 value. Although the Bristol dataset contains a lower point density than Bournemouth, no odd behaviour was reported with any of the examined targets.

4.4 ASSESSING THE DEVELOPED SEGMENTATION ROUTINE

4.4.1 Selecting the Optimal Backscatter Parameter

The radiometric calibration analysis can deliver four backscatter parameters for individual echoes. However, no general assumption can be applied to all surface feature types regarding the optimal parameter to use in the developed segmentation approach. Therefore it is necessary to discriminate between land cover classes based on a reliable criterion in order to select the optimal parameter for individual classes.

Previous studies into FWF-ALS data have found, pulse width to be a reliable parameter to group points into rough and smooth surfaces. Simulation results presented by Lin (2009) for the same datasets as investigated here, showed that a pulse width value of 2.69 ns can be used to effectively group points into these two classes. However in reality, and especially over natural land coverage, it is likely that there will be rough surfaces which do not necessarily represent vegetation.

To better understand the relationship between pulse width and roughness, pulse width was investigated over different land cover types at the two test sites. Nine and seven land cover categories were investigated and analysed from the Bournemouth and the Bristol datasets respectively (Table 4.12). The examined categories included multiple targets from different land cover types with variant levels of roughness. These targets were identified with the aid of orthophotography from multiple flightlines and different regions in both study sites. The values highlighted in red and green in Table 4.12 represent categories with a mean pulse width > 2.69 ns. Values in green represent rough surfaces which are not vegetation. Therefore another criterion must be used to exclude non-vegetation from the rough class. The number of returns delivered from vegetation was greater than those delivered from non-vegetation. Therefore, a condition was proposed to use the number of returns as a criterion to separate vegetation echoes from non-vegetation in the rough class.

Following these analyses, a condition was set to select the optimal backscatter parameter for individual classes, as illustrated in Table 4.13. This condition was used to select the optimal backscatter parameter for individual echoes based on the surface roughness. It is important to mention that the smooth class does not only include perfectly smooth surfaces such as man-made features. It also includes all regular surfaces, even hedges and mown grass, as these surfaces exhibit a well-defined geometry in terms of incidence angle. Thereafter, the decision was made following the diagram in Figure 4.26.

Dataset	**Feature type**	**No. of points**	**Height above ground (m)**	**Mean of the pulse width (ns)**	**Std. of the pulse width (ns)**
Bournemouth	House roof	3198	3.0-6.0	2.557	0.015
	Mowed grass	3348	0-0.1	2.555	0.079
	Asphalt road	385	0	2.626	0.028
	Bare natural sloping	648	0	2.701	0.055
	Undulating terrain	2722	0	2.769	0.066
	Hedge	533	0.5-2.5	2.599	0.053
	Scrub	568	1.0-1.2	2.754	0.242
	Small tree	3361	1.5-2.0	3.864	0.588
	Canopy	6202	12.0-17.0	3.004	0.652
Bristol	House roof	1735	6.0-10.0	2.508	0.104
	Mowed grass	1422	0-0.2	2.561	0.321
	Asphalt road	1313	0	2.526	0.033
	Bare natural sloping	915	0	2.771	0.384
	High grass	4551	0.4-0.7	2.698	0.362
	Scrub	1540	1.0-2.0	2.977	0.634
	Canopy	2376	15.0-20.0	3.119	0.780

Table 4.12. Pulse width analysis for the Bournemouth and Bristol datasets.

Class	Condition	Backscatter parameter
Smooth	Pulse width <= 2.69	γ_α
Rough but not vegetation	Pulse width > 2.69 AND no. of returns <= 2	γ_α
Vegetation	Pulse width > 2.69 AND no. of returns > 2	σ

Table 4.13. Backscatter parameters selection for subsequent segmentation.

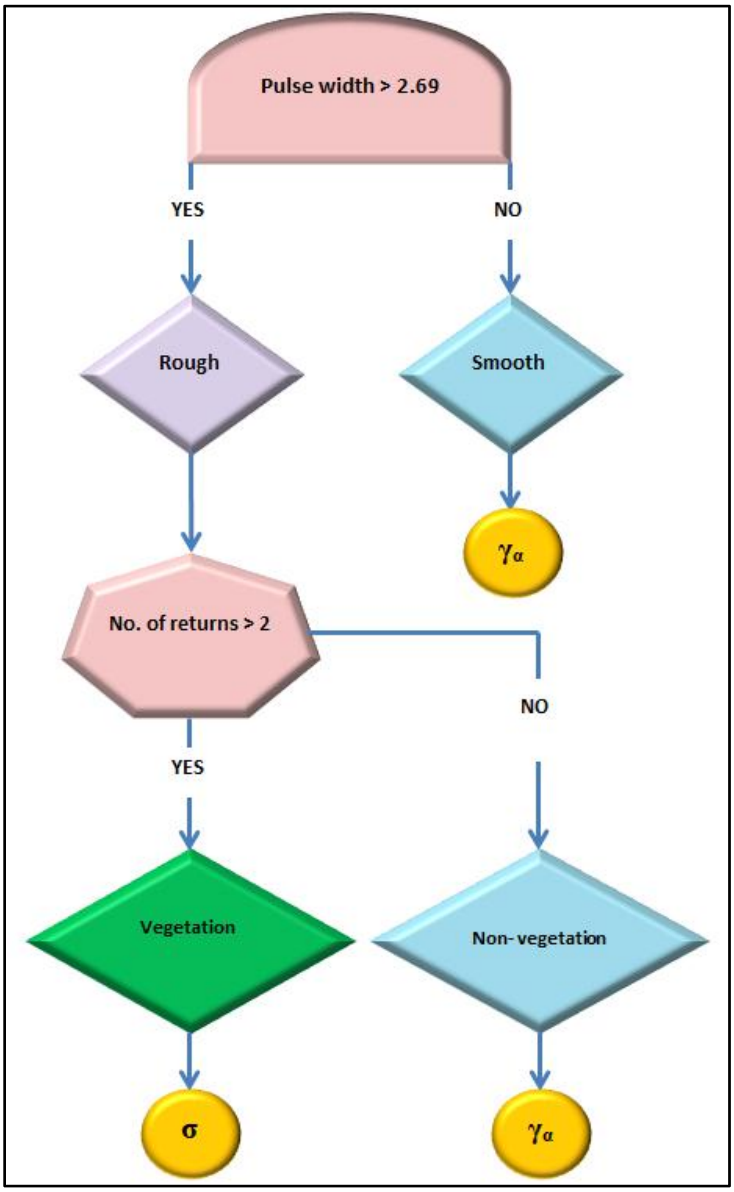

Figure 4.26. Backscatter parameter decision diagram.

4.4.2 Testing the Developed Routine

The developed routine was tested over selected targets from several land cover types for both datasets. These targets were selected using orthophoto coverage and they include surfaces with planar and non-planar trends such as man-made and natural features. Consequently, an interest area from the Bournemouth dataset was selected to visualise the performance of the implemented method over an extended region with various land cover features. The reason for choosing the majority of the selected targets and the interest area to demonstrate the results to be from the Bournemouth dataset is due to its high point density as compared with Bristol. As a result, this provides better visualisation of the detection of minor details and delivers more comprehensive outcomes. Later, the results were compared with results delivered from applying the same segmentation workflow without integrating FWF physical information. Thereafter, outcomes from both approaches are analysed and discussed.

Figure 4.27 shows the segmentation results for a house roof target from the Bournemouth study site. The results demonstrate how the method can successfully discriminate between different roof facets and group point clouds into meaningful segments which define the geometry of the selected target. It is also evident from Figure 4.27 that the method can successfully detect a chimney on the roof surface and group the points from this feature into a separate segment from the background. Although the method still shows some shortcomings at the very sharp edges where the points fail to be included to either side of the surface, this was shown to be overcome in cases when adjacent sides belong to different homogeneous materials by means of different backscatter values.

In addition, the method shows promising results over grass regions where two types of mown grass were successfully discriminated from each other. This can be demonstrated in Figure 4.28 over a selected target region in the Bournemouth study site. The results demonstrate the method’s performance in distinguishing between two types of well cut grass regions where both have similar geometric characteristics, but different backscatter values, thus enabling their differentiation.

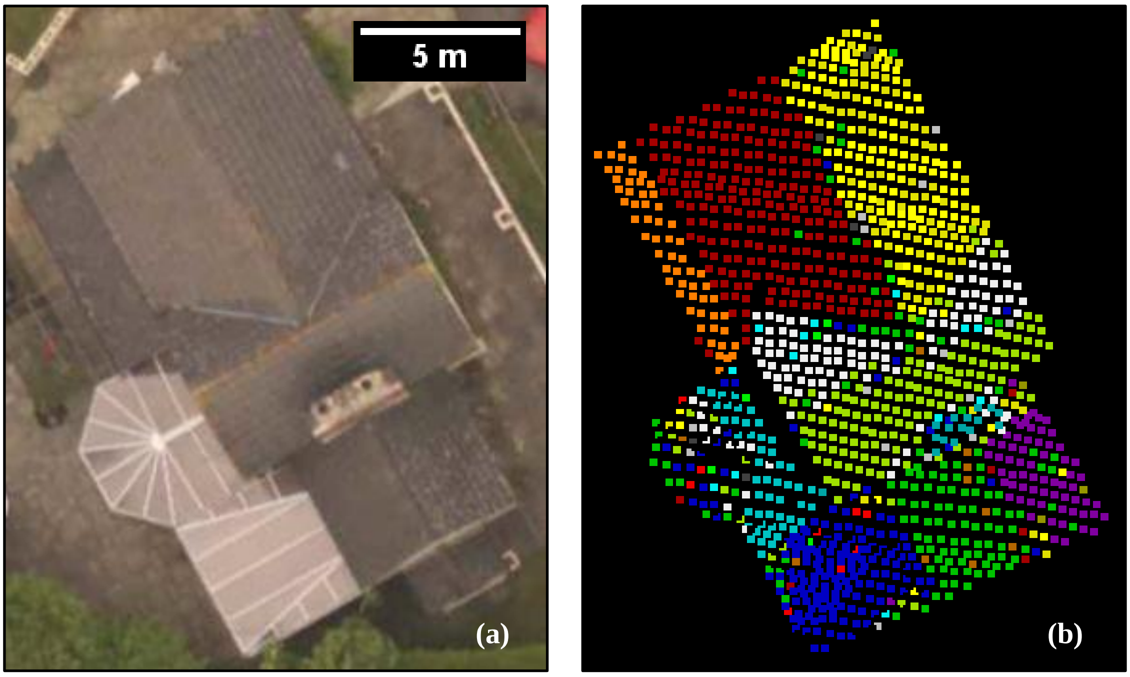

Figure 4.27. The segmentation results of house roof target from the Bournemouth study site: **(a)** orthophoto **(b)** segmented point clouds.

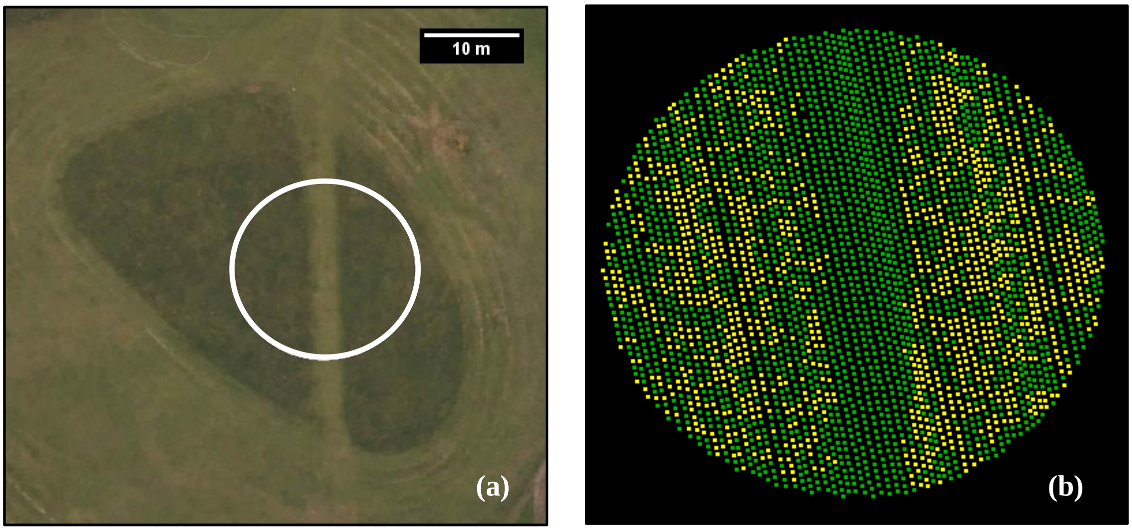

Figure 4.28. The segmentation results of a mown grass target from the Bournemouth study site: **(a)** orthophoto **(b)** segmented point cloud.

Another example is presented in Figure 4.29, illustrating a natural terrain target from the Bristol study site which comprises a mound of earth with clumps of vegetation and grass. This demonstrates the performance of the developed method over non-planar surfaces such as natural land coverage which are likely to be partly covered by vegetation. The results show successful detection of the small mound and differentiate this from the semi-flat surrounding ground. Furthermore, the method can distinguish between both sides of the mound and also detect the vegetation patches in the upper left corner of the figure.

Further, Figure 4.30 shows interesting results for a highway bridge target from the Bournemouth study site, which includes various different materials such as asphalt, metal, and grass. As the target represents a highway, it can be realised from the segmented point cloud results in Figure 4.30-b that a car was captured during the scan, but which was not captured in the orthophoto in Figure 4.30-a. The segmentation routine shows successful detection of the bridge barriers on both sides as well as the central reservation between the two carriageways on the ground. Although the method fails to discriminate between the bridge and the highway beneath (a well-known shortcoming in the majority of available segmentation approaches), the method shows promising results in detecting some of the road markings on the highway. Figure 4.30 also shows the detection of the grassy regions beneath the bridge by delivering a separate segment from the surrounding asphalt region.

In order to generalise the outcomes over a large scale study, an interest area was selected, as shown in Figure 4.31. The figure shows various land cover features over a selected urban area of 65 m x 65 m in the Bournemouth study site, as visualised from the orthophoto in Figure 4.31-a. Figure 4.31-b shows the Digital Surface Model (DSM) of the selected area rendered by height differences for better understanding of the FWF echo coverage. The segmentation results are presented in Figure 4.32 where some interesting behaviour is highlighted and analysed. Note that, due to limited options available to colour segments in Figure 4.32, same colours of different segments does not mean they are of same material/geometry. For example, the purple ground segments and purple roof facets are obviously different.

The most interesting outcome from the developed method is the capability to discriminate grass from artificial ground such as asphalt. This can be visualised clearly from the purple segment on the left bottom part of the interest area. This segment was delivered after successful separation from the green grass segment that covers most of the rest of the ground surface of the area. These outcomes can be further visualised in the highlighted inset regions of 1, 2, and 5. In region 1, it can be seen from the orthophoto imagery in Figure 4.31-a that this area is represented by a grass lawn, and Figure 4.32 (1) shows the successful segmentation of the majority of the grass echoes in this region. The method can also distinguish some of the artificial ground echoes from the surrounding grass segment, as shown in region 2. In region 5, the method detects some of the asphalt echoes of the ground, but fails to detect the surrounding area, by mistakenly grouping echoes lying in the south-east corner of the interest area as part of the grass segment.

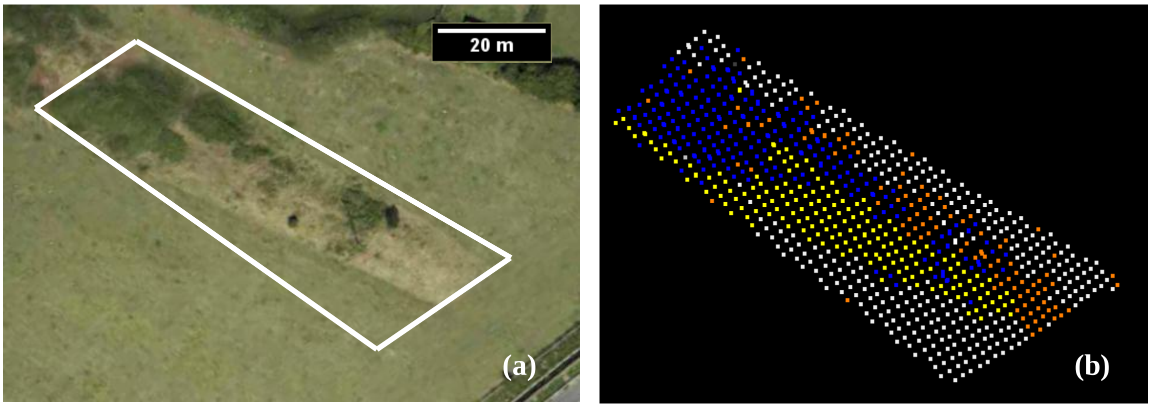

Figure 4.29. The segmentation results for a natural terrain target from the Bristol study site: **(a)** orthophoto **(b)** segmented point cloud.

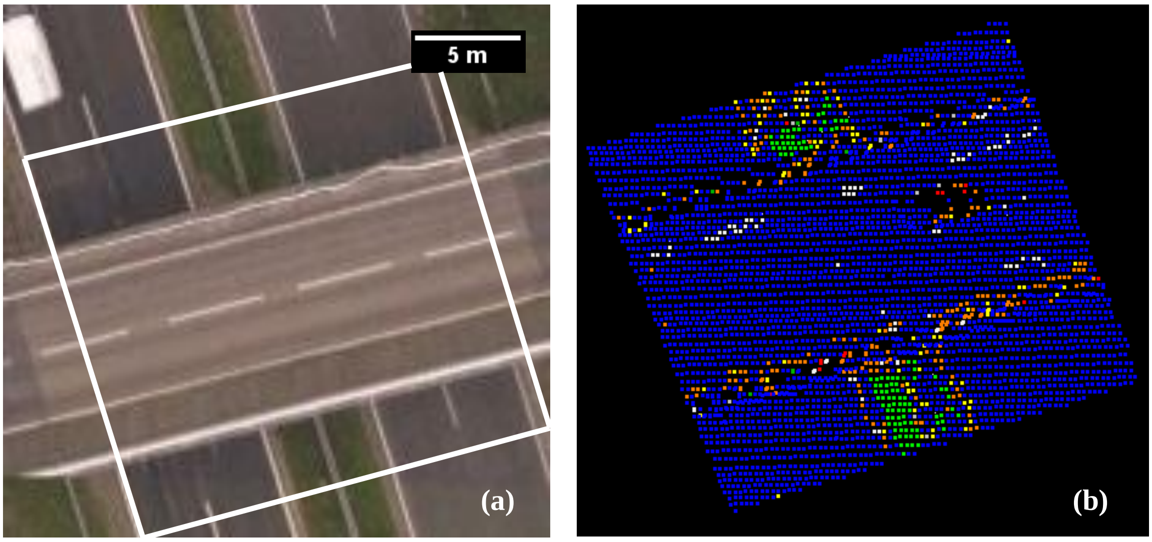

Figure 4.30. The segmentation results of a highway bridge target from the Bournemouth study site: **(a)** orthophoto **(b)** segmented point cloud.

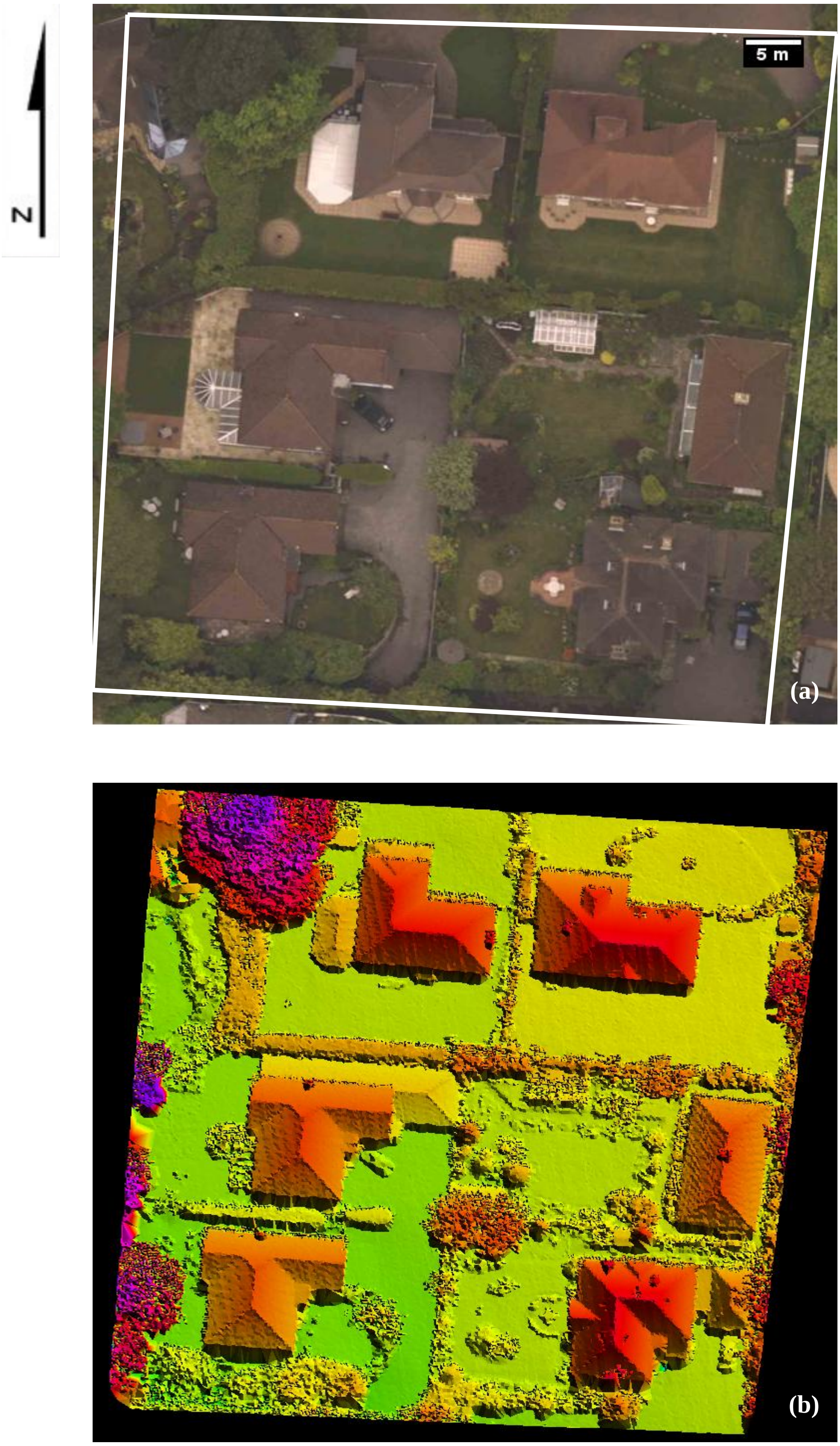

Figure 4.31. An interest area from Bournemouth study site: **(a)** orthophoto **(b)** Digital Surface Model.

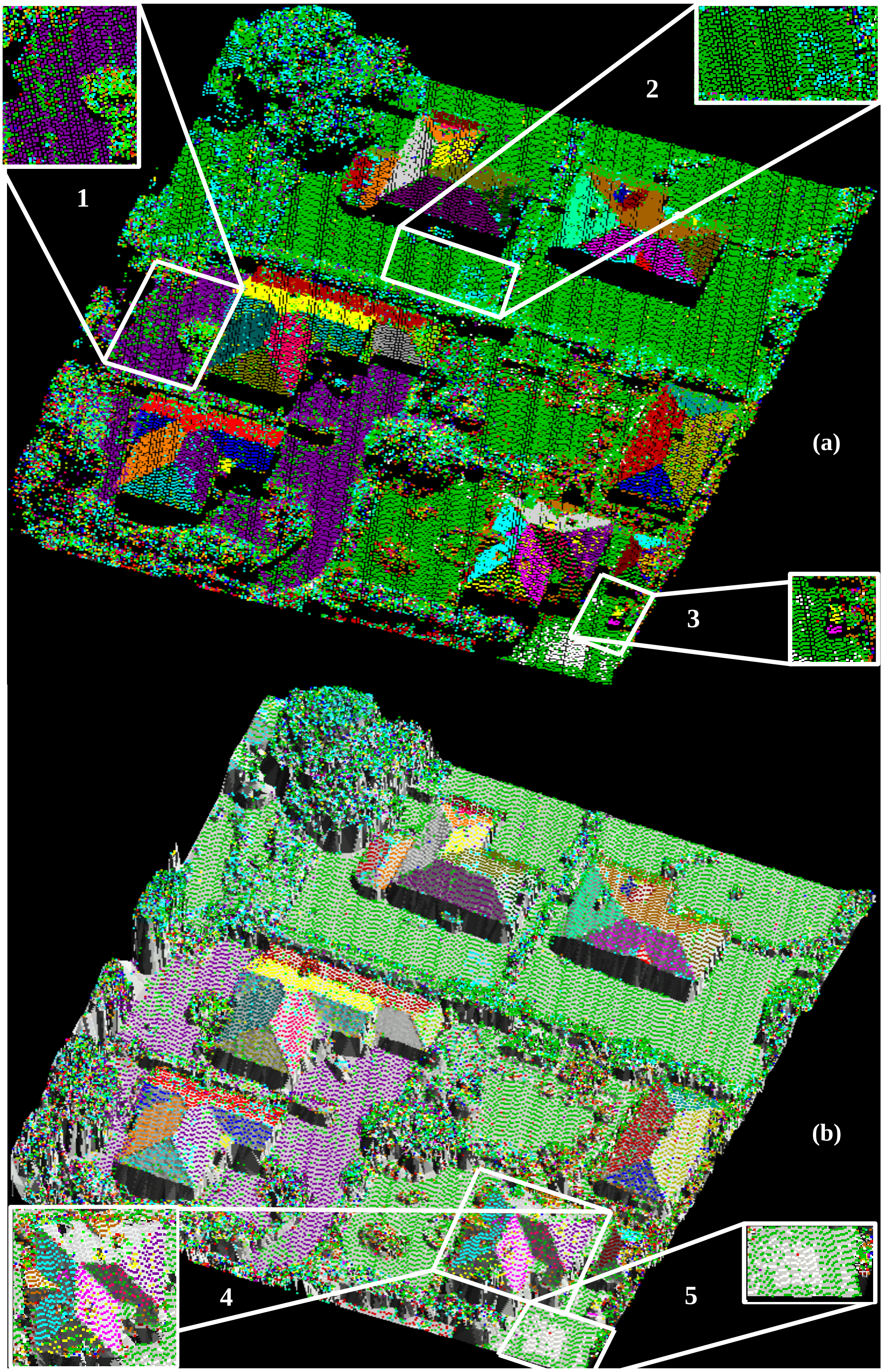

Figure 4.32. The segmentation results for the interest area in the Bournemouth study site: **(a)** 3D perspective view of the segmented point clouds **(b)** 3D perspective view of the segmented point clouds with DSM in the background.

The method was also found to successfully detect cars from the surrounding background and discriminate between different planes of these minor features such as the car’s body and roof, as illustrated in region 3. Furthermore, the successful detection of chimneys and dormer windows on the house roofs has been demonstrated across the interest area. This performance is evident in region 4. It also can be seen from Figure 4.32 that the method can successfully discriminate hedges from trees and grass.

In order to analyse the potential of FWF additional information, the method was applied without integrating FWF physical observables (either in echo amplitude normalisation or in the segmentation process) for the same interest area and otherwise following the same approach. The results are demonstrated in Figure 4.33. It can be seen that, without integrating FWF additional information, the method fails to discriminate grass from artificial ground as expected. It also fails to deliver meaningful segments of car targets and shows shortcomings in segmenting some roof facets which have similar geometric characteristics but belong to different surfaces, as highlighted at the top of the figure. Moreover, this segmentation approach shows poor results over hedges as compared with the results delivered from Figure 4.32. Furthermore, the approach shows poor performance over some roof surfaces where vegetation was found to cover some facets of the roof. In this case, meaningless segments were delivered, such as the example highlighted at the bottom of the figure.

In comparison with the integration of FWF information, it can also be noticed that using FWF additional information can deliver more homogeneous segments than those delivered without using this information over some house roofs facets. This behaviour can be considered as a positive outcome of the developed method, which overcomes the sensitivity of the RSN method to discontinuities. It was also found that using FWF information can better describe the minor details over house roofs than without integrating this information.

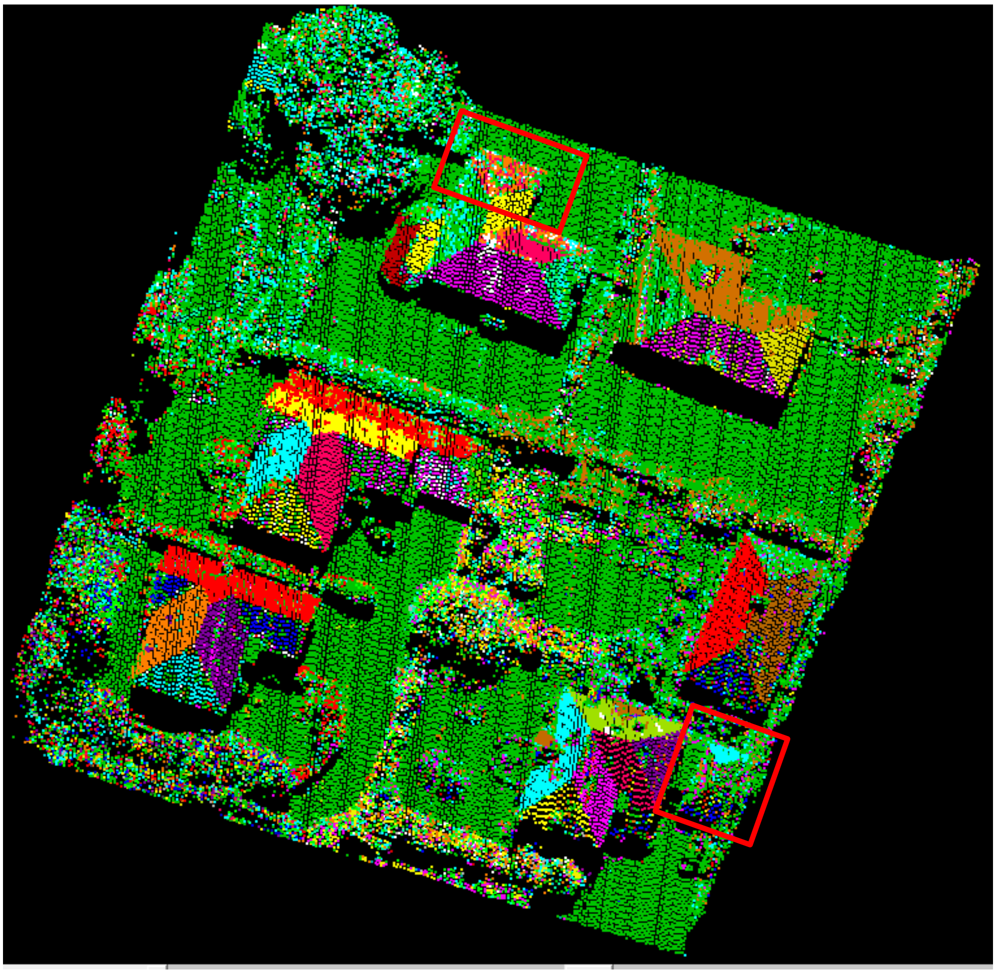

Figure 4.33. The segmentation results for the interest area in the Bournemouth study site without integration of FWF physical information.

4.4.3 Validating the Developed Segmentation Routine

The segmentation routine was validated through comparison to a manual segmentation process in order to assess the accuracy and the performance of the implemented approach. The same interest area from the high density (Bournemouth) dataset used in the previous section was utilised in the validation process. For accuracy assessment purposes, an error matrix (or confusion matrix as usually termed in the remote sensing community, (Campbell, 1996)) was produced. This was performed after excluding all vegetation segments (except mown grass), as it is hard to assess performance and accuracy over such irregular features.

Firstly, the interest area was segmented manually into 193 different segments using the orthophoto as a visual reference. The ground pixel size of the orthophotops was 5 cm x 5 cm. These segments included house roof facets, minor details over the roofs such as dormer windows and chimneys, cars, artificial ground, and mown grass segments, in addition to different kinds of vegetation. Figure 4.34 illustrates the results of the manual segmentation.

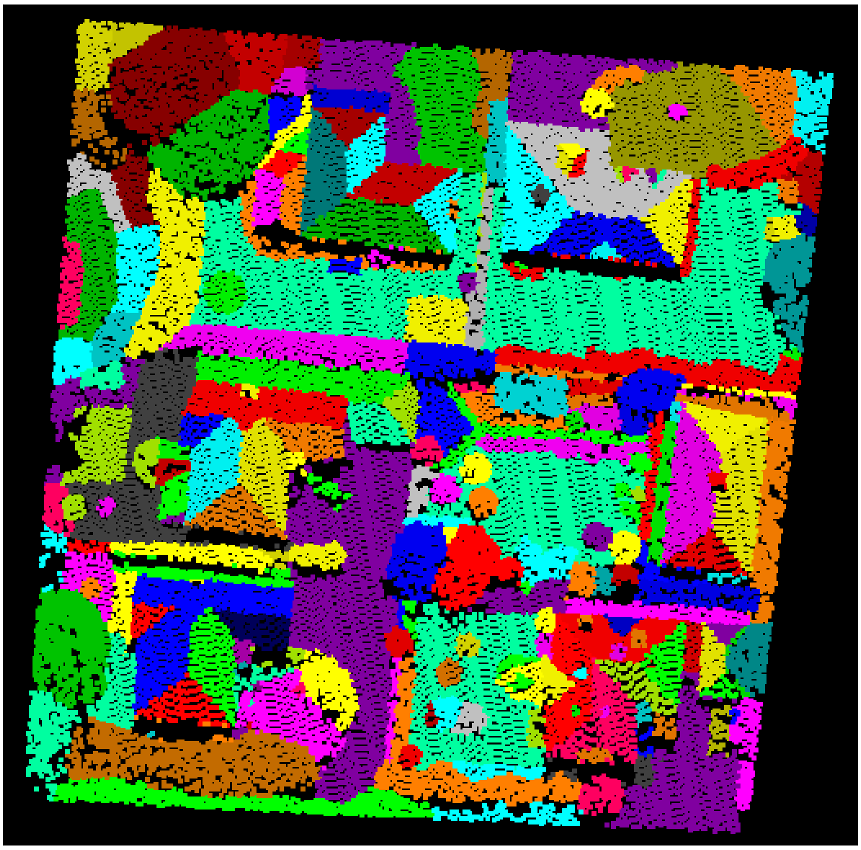

Figure 4.34. The results of the manual segmentation of the selected interest area for the Bournemouth study site.

It is evident from Figure 4.34 that numerous different details have been included based on the orthophoto. However, the majority of these details represent vegetation. In order to visualise the performance of the introduced routine in comparison with the manual results, house roof segments were only considered and presented in Figure 4.35.

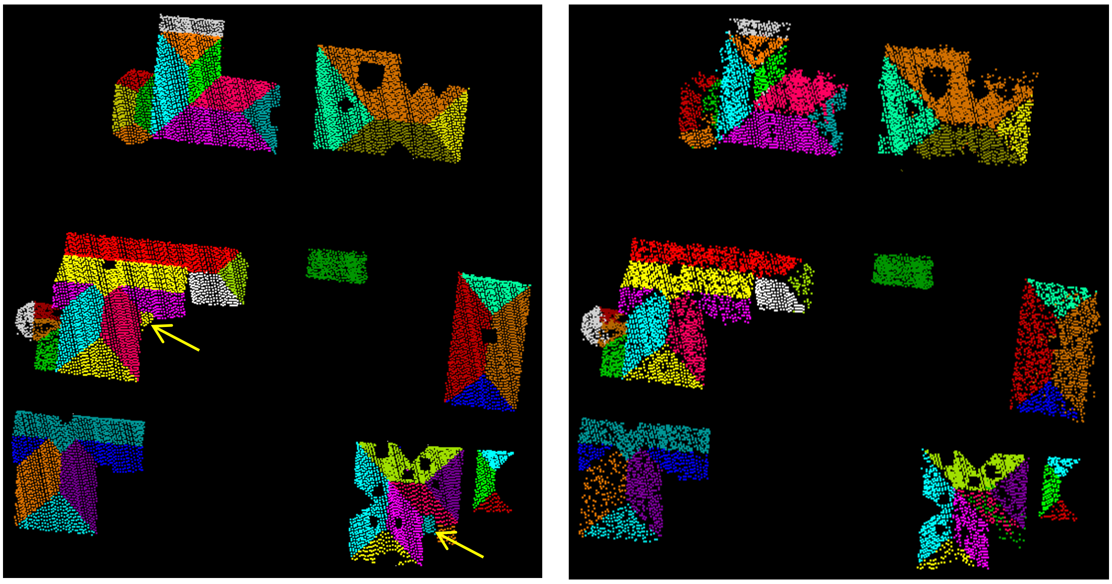

(a) **(b)**

Figure 4.35. The validation results for the house roof segments for the selected interest area in the Bournemouth study site: **(a)** manual segmentation **(b)** automatic segmentation.

It can be seen from Figure 4.35 that the overall performance of the automatic routine is promising, as all of the segments were correctly segmented except a couple of minor segments in the lower-right and left-middle of the area (highlighted), which seem to be missing from this layer. Apart from this, the automatic method effectively defines the shape of individual segments by correctly distinguishing the different surfaces and geometries. However, visual validation analysis is not sufficient to assess the performance of the developed method. Therefore, accuracy assessment analysis was undertaken and implemented through error matrix analysis.

The Error matrix is a means of comparing two datasets in a tabular form (Campbell, 1996; Lillesand et al., 2004). One of these datasets should represent the reference (truth) dataset while the other represents the data derived from the automated user technique (tested). The error matrix is usually used to assess classification accuracy in terms of user accuracy and producer accuracy as a percentage, through Eqn. 4-4 and 4-5 respectively, (Lillesand et al., 2004). User accuracy represents error of commission as estimated based on the tested dataset while the producer's accuracy represents the error of omission in the reference dataset.

$$User's\ accuracy = \frac{T \cap R}{T} \times 100$$ **Eqn. 4-4**

$$Producer's\ accuracy = \frac{T \cap R}{R} \times 100$$ **Eqn. 4-5**

Where T represents the number of points delivered from the tested routine, and R represents the number of points delivered from the reference routine.

Firstly, the segments were classified into five main categories and symbolised as stated in Table 4.14 to facilitate category representation in the error matrix. Later, the summation of points of all segments was delivered for individual categories and presented in the error matrix as the total number of points, as illustrated in Table 4.15. Thereafter, user and producer accuracies were estimated for individual categories following Eqn. 4-4 and 4-5 respectively, as illustrated in the error matrix.

Categories	No. of segments	Symbol
House roof facets	43	H
Chimneys and minor roof features	26	CH
Cars	2	C
Artificial ground	8	AR
Mown grass	8	CL

Table 4.14. Error matrix categories and their corresponding symbols.

	Automatic segmentation						
Manual segmentation	H	CH	C	AR	CL	Total	Producer's accuracy %
H	11367	69	0	1473	1890	14799	77
CH	87	693	0	0	23	803	86
C	0	0	101	43	0	144	70
AR	343	0	19	4880	1962	7204	68
CL	364	0	0	126	12099	12589	96
Total	12161	762	120	6522	15974	35539	
User's accuracy %	93	91	84	75	76		

Table 4.15. Error matrix of the selected interest area in the Bournemouth study site, excluding vegetation, and showing FWF echo counts in addition to producer and user accuracies.

The user's accuracy shows very promising results over all the categories. However, slightly poorer performance of 75% and 76% is delivered from artificial ground and mown grass respectively. These outcomes were expected following the visual segmentation results in Figure 4.32 which demonstrate miss-discriminations between artificial ground and clipped grass in region 5 and the surrounded area. This is also evident from the low producer's accuracy for the artificial ground category. However, high producer's accuracy was delivered from the mown grass. For a general outcome, overall and mean accuracies were estimated using the error matrix results and following Eqn. 4-6 and 4-7 respectively, (Lillesand et al., 2004).

$$Overall\ accuracy = \frac{\sum T \cap R}{\sum R}$$

Eqn. 4-6

$$Mean\ accuracy = \frac{\sum producer\prime s\ accuracy}{no.of\ categories}$$

Eqn. 4-7

The overall accuracy was 82% while the mean accuracy was 79% which can be considered to be extremely promising.

In order to compare these outcomes with the approach without integrating FWF physical information, the same validation analysis was performed and a new error matrix was delivered (Table 4.16).

	Automatic segmentation without FWF						
Manual segmentation	H	CH	C	AR	CL	Total	Producer's accuracy %
H	10452	162	0	54	4131	14799	71
CH	56	611	0	0	136	803	76
C	0	0	58	18	68	144	40
AR	0	0	0	1787	5417	7204	25
CL	809	200	11	580	10989	12589	87
Total	11317	973	69	2439	20741	35539	
User's accuracy %	92	63	84	73	53		

Table 4.16. Error matrix of the selected interest area in the Bournemouth study site, excluding vegetation, and showing FWF echo counts without considering FWF physical information in addition to producer and user accuracies.

The reduction in the user's accuracy over the mown grass category was obvious from Table 4.16 in a comparison with the results delivered from integrating the FWF additional information in Table 4.15. However, the poor producer accuracy of 25% was obtained over artificial ground which defines the mis-segmentation results delivered from this particular category as illustrated in Figure 4.33. The segmentation accuracies (user and producer) of chimneys and minor roof features were also noticed in Table 4.16 to be less than the corresponding accuracies delivered from Table 4.15. On the other hand, the producer's accuracy from the cars category was reported to be very low. No logical explanation for this particular behaviour of the approach for cars could be found, however, this outcome meets with the results delivered from Figure 4.33. The overall and the mean accuracies of the segmentation results over the interest area without integration FWF additional information were 67% and 60% respectively. These outcomes show the deterioration in the results without FWF physical information and proved the potential of integrating this additional information in the segmentation techniques. However, these outcomes could not be achieved without a comprehensive radiometric calibration of the FWF physical information.

4.5 SUMMARY

In Chapter Four, results delivered from the methodology introduced in Chapter Three are presented and analysed. The chapter presented the results of the main three sections of the methodology by testing and validating these techniques using visual and statistical analysis. The aim was to deliver a quantitative evidence of the successful implementation of the developed methodology, and demonstrate the values of fully utilising FWF information. The results were tested over multiple surface features of different characteristics and for two datasets of different point densities through visual and statistical analysis.

The outcomes of this chapter can be summarized as follows:

- The results delivered from testing and validating the new RSN method demonstrate that weaknesses in the available surface normal estimation approaches can be overcome. Consequently, the normalised amplitude signals show a significant reduction in the signal differences between overlapping flightlines through the RSN method. The main outcomes can be listed as follows:
    1. The RSN method is capable of detecting small disturbing objects on slanted roofs and delivering an accurate estimation of the normal for relatively minor features.
    2. The RSN method successfully managed to differentiate walls from roofs and clearly represents the wall structure, which is promising for urban feature extraction.
    3. The RSN method is able to effectively define discontinuities by following the trend the challenging natural surfaces and faithfully reflecting minor rough detail.
    4. The RSN method shows a marked reduction in the difference of the echo amplitude signals between overlapping flightlines after normalisation.
    5. The RSN method shows better performance for dense datasets (e.g. > 10 points/m^2). However this is based on feature of interest and the application of the study.

- The results delivered from the developed radiometric calibration routine show the effective role of the incidence angle parameter in reducing backscatter signal discrepancies between overlapping flightlines after calibration. The main outcomes can be listed as follows:

1. It was proven that using reference target with known reflectivity value delivered from practical measurements can lead to a better match between calibrated backscatter signals from overlapping flightlines than using published literature values. However, it is recommended to perform the reflectivity measurements of the reference target at the time of data capture in order to deliver the same conditions of the day of scan.
2. Results show the positive potential of using γ rather than σ to estimate the calibration constant for radiometric calibration purposes.
3. It was proven that the γ_α parameter provides the greatest potential amongst the four investigated backscatter parameters (σ, γ, σ_α) by delivering the optimal match between flightlines except over vegetation where the σ parameter shows better performance.

- The results delivered from testing the developed segmentation technique emphasise the potential of integrating FWF calibrated physical information to develop segmentation approaches which fully utilise FWF information. The main outcomes can be summarised as follows:
    1. It was found that echo width and the number of returns can be successfully utilised to select the optimal backscatter parameter for individual echoes to be integrated later in the developed segmentation routine.
    2. It was proven that the developed method can successfully discriminate between features having the same geometric characteristics but different backscatter values such as artificial ground and clipped grass.
    3. It was demonstrated that the developed approach can deliver successful discrimination of minor details over houses roofs from the surrounding roof echoes such as chimneys, and dormer windows, and can also better define car's facets than relying on geometric information alone.
    4. The developed segmentation routine was found to offer an overall accuracy of 82% based on comparison with a manual validation process. This is considered an encouraging basis for future utilisation of FWF information in segmentation applications.

CHAPTER

5

DISCUSSION

5.1 INTRODUCTION

A methodology to segment unstructured 3D point clouds from FWF-ALS data into meaningful clusters, which reliably represent 3D objects and simulate land cover features, was introduced in Chapter 3. The approach is based on incorporating the physical observables from FWF alongside the geometric information to enhance 3D object segmentation routines. The method was tested and validated through implementation on real surface targets by visual and statistical analysis using two datasets with different characteristics as introduced in Chapter 4. This chapter will evaluate the implemented routines and discuss the main findings delivered from the practical implementation of the proposed methodology. It will also highlight robustness issues to enable rigorous evaluation of segmentation approaches, and associated techniques.

Firstly, the appropriateness of the adopted data management and processing methodology is discussed in Section 5.2. This includes the adequacy of the RGD approach to post-process the raw FWF-ALS data used in this research. This section also reviews the significant potential of the high-throughput computing scenario to handle intensive processing and management of large lidar datasets. In Section 5.3, detailed discussion of the reliability of the physical data normalisation approach is addressed. This considers a number of issues associated with the novel RSN method, including accuracy and effectiveness in relation to the methodology, and the datasets utilised. In Section 5.4, the performance of the developed radiometric calibration routine is discussed and further analysed. This comprises quality assessment of the adopted calibration constant and the derived calibrated backscatter energy values. Finally, in Section 5.5, the developed segmentation algorithm is assessed in the context of performance and accuracy, and in comparison to existing segmentation scenarios.

5.2 FWF DATA MANAGEMENT AND PROCESSING

The reason for using the RGD method to post-process FWF-ALS data in this research lies in its reliability as a pulse detection method to deliver higher range accuracy than other available routines. Furthermore, the RGD method was utilised because of its capability to resolve challenging signals and detect targets from complex overlapping waveforms. This leads to enhanced representation of land cover features by translating the complete received energy into rigorous spatial and physical information. This algorithm has already been demonstrated to deliver a greater number of valid echoes from individual waveforms than those delivered from the standard approaches, leading to better descriptions of surface features. Thus, more accurate 3D data for diverse applications can be delivered, including terrain generation, 3D modelling, forest mapping, etc. As a result, post-processing with RGD ensures increasing the density of the overall datasets, which provides potential in defining neighbourhoods for individual points. This performance can potentially increase the accuracy of the adopted RSN method and minimise the chances of discarding fine surface details, which cannot be delivered if only a limited number of echoes are detected. Therefore, the RGD method was adopted here to extract accurate geo-referenced 3D point cloud alongside physical observables for individual echoes to facilitate this goal.

As the proper processing strategy to deliver optimal outputs, high-throughput computing was adopted to run the RGD method. The potential of this type of processing can be identified as the capability to run independent parallel jobs on different physical computers and later merge their output to deliver one combined solution. Therefore, it saves time and cost needed to run successive jobs on single computer with limited memory size, which can slow processing down considerably. This is basically relying on the efficiency of accessing independent memories and using a network for communication (Section 2.4). Whereas the processing time is an important factor here to deliver FWF point cloud, the Condor workflow was adopted.

However, with Condor based student clusters, such as the case in Newcastle University, large “cycle stealing” can occur, as the computers are not dedicated for high-throughput computing only. In order to reduce network usage and the wastage of computation time that occurs in cases of eviction by student login, the new technique of returning data to the user while the code is still running on the remote computer was developed, as explained in Section 3.3. The routine was developed in cooperation with the Digital Institute in Newcastle University to tackle problems in managing large datasets through the Condor system, which had less than six years history in the University network.

This technique was modified to fulfil the needs for a model that keeps on processing until all jobs are completed, thus no data is lost due to computer eviction. As check pointing can provide reliable data storage for a period of time (refer to Section 3.3), the developed pull mode helped the user to re-request a new job upon eviction without wasting time to re-data transfer. As a result, this pull model allowed the running of a large number of jobs without the need for shared file space. This provides an advantage of using the free time on worker nodes more dynamically, such as in the case of non-dedicated Condor environments, which has the potential to run large datasets. Furthermore, the developed routine addresses and analyses any log run errors that might occur, which helps the user to diagnose the problem for a potential manipulation while the code is still running remotely. The project shows significant and powerful potential to speed up the processing records as highlighted in Section 3.3, which can potentially increase with customised settings and larger network usage.

5.3 FWF DATA NORMALISATION USING RSN METHOD

The RSN method proposes a new strategy, which is applicable to a wide variety of land cover types and dataset point densities. The aim of the RSN method is to normalise the FWF physical observables from the incidence angle effect acquired due to different flying direction and position of multiple flightlines. Correcting the backscatter signal from this major effect facilitates signal calibration towards full integration of FWF information. Consequently, this method is not restricted to FWF as it could be adopted to compensate incidence angle effects in any laser scanning physical signals for a range of downstream radiometric calibration and point cloud segmentation applications. Compensating the backscatter signals of individual echoes from this effect will eliminate signal discrepancies in adjacent overlapping flightlines. Therefore, performance assessment of the RSN method was undertaken through checking normalised signal discrepancies from overlapping flightlines over individual targets and selected areas. The validation process was based on comparing the differences in the STD values between overlapping flightlines before and after normalisation. The normalised signals from the RSN method were compared with the original amplitude signals and the results from applying the standard spherical approach to assess variations.

5.3.1 Neighbourhood Definition

In order to fulfil the needs for different applications, it is essential to process the collected point cloud to extract useful information such as surface normal. The first step for potential processing is to define the neighbourhood system for individual points in an appropriate way because inappropriate neighbourhood definition can lead to erroneous surface detection that ends with wrong 3D object representation. Point density, which gives an indication of the point spacing, is one of the key dataset characteristics for successful neighbourhood implementation. The overwhelming majority of existing neighbourhood definitions considers point clouds with uniform point density. However, this is unlikely to occur over all land cover features because of the various scanning specifications and target characteristics. Further, these neighbourhood approaches, which are used to define the 3D volume for normal vector estimation in ALS data, only consider the 2D distribution of the point cloud. These methods are designed to work with 2.5D points and discard the characteristics of the surface enclosing individual points.

The neighbourhood definition of the developed RSN method is based on selecting the reliable minimum number of points to define the surface for individual points. All available approaches are based on fitting a plane to all included neighbourhood points. However, the RSN method finds the exact plane associated with a specific point for planar surfaces and the best approximate surface over non-planar surfaces by establishing small planes from a minimum number of neighbourhoods. In this case, the defined spherical system is overcoming the challenge of considering an arbitrary set of coplanar points those representing various surfaces to be identified by the same space parameters. This has shown potential to represent land cover features with various surface trends and as demonstrated in Section 4.2.

5.3.2 Quality Analysis of the Normal Vector Estimates

The available normal vector estimation methods are based on minimising the distances between neighbourhood points and the postulated plane by iterating the procedure until no significant change to plane parameters is acquired. This solution can deliver uncertain results over non-planar surfaces because small surface details are discarded. Therefore, depending on the surface characteristics, the delivered normal from the standard spherical method is not always reliable and should not adopt over different land cover types. Whilst the normal delivered from existing methods may be reliable for some of the points used to define the system, it is not necessarily to be certain and reliable for the point of interest itself. Therefore, the RSN method was developed to deliver robust normal vector estimations for individual point cloud over different land cover types.

The core difference of the RSN approach lies in the fact that a rather large 3D spherical metric definition is adopted with the existing approaches; it is then reduced until some planarity criterion is met. Thus, many points could be included and fitted to the generated surface, which may not necessarily represent the surface properties. Reducing the radial distance to the minimum with these approaches to assure robustness was shown to detect a lower number of points than the minimum required to apply the moment invariant theory (less than 3 points) over some features. This is mainly due to varying point density and distribution over different land cover types.

In contrast with the RSN method, the approach starts at point of interest and selects only the nearest three neighbours which delivers a sufficient good plane. In other words, the RSN method is better considering the orientation of individual points rather than delivering an approximation solution. This was achieved by checking all possibilities in the nominated neighbourhood points in order to meet the definition threshold and select the optimal solution for individual points following the workflow explained in Section 3.4.1. The solution is obtained through the robust planarity checking that delivers reliable normal estimates for different targets with various surface trends. This is preferable to the unreliable normal delivered from fitting a plane to a group of points with different orientations, which is commonly acquired over natural land coverage and surfaces with rough trends. This is the main difference between RSN and other approaches as these techniques are likely to discard topographic details of rough surfaces and minor features over planar surfaces. This may be acquired because of the non-homogeneity and the complex distribution of these points. Later, this translates to a wrong normalised echo amplitude value and erroneous results for different lidar applications including the segmentation of point cloud.

The novelty in the RSN method is based on the notion of minimum neighbourhood definition validated by robust planarity checking, which is necessary to assure robustness because of reliance on point density and accuracy. Further, the covariance matrix in the RSN method, which delivers the normal for individual points, relies on both the geometric and the additional physical information from FWF. This overcomes the non-homogeneity in the points enclosed within the volumetric neighbourhood system defined for individual points. As a result, this helps to deliver a more accurate normal value over planar surfaces and the best approximate normal over non-planar surfaces. The method was tested over a maximum point density of 15 pt/m^2 in the Bournemouth dataset. However, it is expected to deliver better results with even higher point densities. This is because denser point cloud data can deliver better object representation, which results in more accurate normal vectors.

The RSN method can deliver a highly precise estimation over planar surfaces and the best approximation over non-planar surfaces following robustness checking. This delivers a marked reduction in the echo amplitude signal discrepancies between overlapping flightlines over all tested targets after normalisation. This is because the RSN method is adaptive and defines a constant and minimal number of neighbourhood points, ensuring relatively accurate results over data of variable density. Consequently, results are highly sensitive to local point density and scan pattern, which can vary spatially across a dataset, and which cannot be accommodated for through use of a fixed spherical radius. In the case of the Bournemouth dataset, this may amount to more than 35 points being included within the defined 3D spherical volume, and thus considered in the computation of the normal vector by the standard spherical method. In contrast, the RSN method maintains a relatively high accuracy as it defines a fixed and limited number of neighbourhood points for each individual point. The RSN method results are robust and reliable for determining ALS point orientation estimates over a wide range of natural and man-made targets. Furthermore, this approach demonstrates the potential to integrate additional FWF observables in order to improve existing segmentation approaches.

5.3.3 Overall Performance assessment

The RSN method shows very reliable performance in corner regions, including corners between roofs and walls and other examples of corners between planar surfaces. In these instances, the normal estimates for a point near a corner on one plane are not degraded by the influence of points on an adjacent plane, which is oriented differently. Although the method still has weaknesses in estimating the correct normal for corner points where the adjacent surfaces are of differing material types (e.g. where a concrete wall meets a grassed ground surface), further improvements were delivered through the inclusion of backscatter parameters. The method has demonstrated the capability to robustly define planar surfaces and represent details of minor features. However, some shortcomings in the results were delivered with the Bristol dataset because of the lower point density.

Performance assessment was adopted for individual targets in order to analyse the effect of incidence angle on objects with similar characteristics. Later, the analysis was extended to include selected regions with various surface characteristics. The standard deviation difference was selected as a validation criterion because this can deliver an accurate representation of the discrepancies in performance between overlapping flightlines after normalisation. The normalised signals have shown significant improvements in comparison with the original echo amplitude signals. Further, the outcomes from the RSN routine have shown potential and reliability as compared with those produced through the standard spherical method, especially over natural land cover where discontinuities prevail. This is because more reliable normal vectors are delivered for individual points, which leads to a better surface description and improvements in the normalised signals. In other words, the incidence angle error was reliably normalised over natural land cover with a rough surface. Although results cannot be trusted over vegetation, promising outcomes are delivered over scrub vegetation. Moreover, the method delivers very promising results over low vegetation (e.g. grass), as discussed further in Section 5.5.

All results delivered in Section 4.2 prove the significant improvements in the normalised echo amplitude signals using the RSN method. Although differences between flightlines still exist due to data noise and systematic errors in the ALS system, further improvements can be achieved when all variables affecting the backscatter signal are considered in the solution.

5.4 CALIBRATION OF THE FWF PHYSICAL OBSERVABLES

5.4.1 Backscatter Signal of the Reference Target

In order to estimate the calibration constant for the entire dataset, the absolute reflectivity of the reference target was measured to deliver its backscatter signal for optimal radiometric calibration results. Because of the reasons explained in Section 3.5.2, the reflectivity measurements could not be taken at time of flight. To assure, as close as possible, the conditions of the day of scan on the backscatter signal such as weather conditions, angle of incidence, illumination, and wet and dirt of the target, all these variables were considered on the points enclosed by the reference target. This was explained in detail in Section 3.5 for the Bournemouth and the Bristol datasets. However, in the case of Bristol, natural reference targets comprising selected asphalt road sections were used to deliver the calibration constant. Although practical reflectivity measures were delivered for the artificial targets in the case of Bournemouth, a published literature reflectivity value was utilised for the natural reference targets in the case of Bristol. This was considered as one of the shortcomings in the radiometric calibration results in the Bristol dataset, in addition to the lower point density.

As explained in Section 2.5.2, the incidence angle effect has a great influence on the backscatter signal. Therefore, it was essential to consider this effect when delivering the backscatter signals of the reference target in both datasets. In the case of the Bournemouth dataset, this can be justified, as the targets cannot be guaranteed to be perfectly flat because they were deployed over different ground types such as natural surfaces. Further examples are shown in Figure 5.1.

Figure 5.1. Reference target deployment in the Bournemouth study site.

As for the Bristol study sites, the case was different as flat asphalt road sections have been selected carefully as reference, following the distribution shown in Figure 3.16. However, the incidence angle was considered in the individual backscatter echoes of the reference target to assure robustness. The incidence angle computations of the reference target echoes show variation of up to 10° in the Bristol dataset. This confirms the importance of considering the angle of incidence effect even over flat surfaces. Further, it demonstrates the robustness of the RSN method to detect minor slope variations by delivering the fine details of the surface, which were probably acquired from bumps and pavement maintenance.

5.4.2 Validation of the Calibration Constant

In order to check the potential of using the PVC artificial targets as a reference in the Bournemouth dataset, the calibration constant from the PVC target was compared with the constant delivered from a natural target. This was achieved by comparing results of the backscatter parameters from both approaches over a slanted roof target as introduced in Section 4.3.3. The validation was based on checking discrepancies between overlapping flightlines delivered from both approaches and represented by the STD differences in percentage. Both approaches were similar in accounting for the variables influencing the backscatter signal and the values used were identical except in the reflectivity value from the different reference targets. The PVC reflectivity value was delivered from a practical measure as stated in Section 3.5.2. However, a literature value of 0.25 was adopted for the natural asphalt road target. The delivered results showed significant dependency on the reflectivity value by delivering less STD differences with the PVC reference target and thus better agreement between signals from overlapping flightlines in all backscatter parameters. This means that the calibration constant delivered from the artificial PVC target is more robust to calibrate the signals than the constant delivered from the natural target. This behaviour is likely due to the more reliable reflectivity value of the artificial target, which was delivered from a practical measure rather than relying on a standard literature value. Thus, a good reflectivity measure is important for delivering a robust calibration constant. Further, it was also shown that the best agreement in results between flightlines was delivered from the γ_α parameter, which highlights the potential of the incidence angle effect in the radiometric calibration.

The developed radiometric calibration routine in this research is based on the γ rather than the σ backscatter parameter of the reference target to deliver the calibration constant as stated in Section 3.5.3. This is because γ is more stable than σ due to the different system and target characteristics and as stated in Section 2.5.1. Although the system used in this research was the same for both datasets (i.e. Riegl LMS-Q560), the differences acquired from various target characteristics exerted greatest influence. Therefore, γ was the parameter of choice to deliver the calibration constant in the developed radiometric calibration in this research.

In order to assess the selection of γ to deliver the calibration constant against the standard σ parameter, a comparison was presented in Section 4.3.4 to an existing approach introduced by (Alexander et al., 2010). This comparison study was applicable for the Bournemouth dataset only as Alexander et al. (2010) used the same dataset and provide the calibration constant to facilitate the comparison procedure. In the Alexander et al. (2010) approach, the incidence angle effect was neglected and a literature reflectivity value was adopted to deliver σ for the reference target. In order to avoid the effect of the angle of incidence here, a flat road section was selected to validate the results. In theory and following the geometry of the selected road target, the backscatter signals from overlapping flightlines should be approximately the same. This was proven in a practical sense through the γ results of the developed routine, which show a significant reduction in the differences between flightlines. However, a significant reduction in the σ results was delivered. No practical justification could be found for these shortcomings, however it emphasised the potential effect of the target characteristics on the σ value. Although the atmospheric effect was also considered in the developed routine, the bad weather conditions on the day of the survey might potentially have affected the results. In contrast, the γ_α results show perfectly matched signals from overlapping flightlines as demonstrated in Section 4.3.4. Although the incidence angle was not of concern in this comparison test as the selected asphalt road target was selected to be as flat as possible and picked to have nearly same conditions (e.g. range) from both flightlines, the incidence angle shows potential through the γ_α results. This emphasises the conclusion from the previous section to importantly consider the angle of incidence effect even over flat surfaces especially when a robust method is utilised to deliver this variable.

With regard to testing the potential of the calibration constant of the developed calibration routine, the γ asphalt road target results was compared statically with the γ results from the Alexander et al. (2010) approach as explained in Section 4.3.4. The STD results showed improvements over the original signals, however, the differences between flightlines still outperformed the results delivered from following the developed calibration routine. The shortcomings in the Alexander et al. (2010) approach can be explained due to firstly the unreliable reflectivity value used to deliver the σ of the reference target. The second probable reason for these outcomes is discarding the change in the reference target characteristics such as the incidence angle when using σ rather than γ to deliver the calibration constant. The comparison also shows that the homogeneous flatness of the reference target should not be trusted even if the echoes are selected from near-nadir. These effects can lead to an unreliable calibration constant, which can deliver significantly incorrect calibrated backscatter values, especially over complex and natural land cover. Therefore, it is important to account for all variables, which affect the received backscatter signal upon calibration.

5.4.3 Reliability of the Backscatter Parameters

To deliver a representative assessment study, the reliability of the developed calibration routine was tested over various land cover types with different target characteristics. This was explained in detail in Section 4.3.5. The assessments include man-mad and natural targets, homogeneous and non-homogeneous, smooth and rough surfaces. The analysis comprises two main phases, statistical and visual, to deliver a comprehensive outcome.

The results of the reliability assessment of the backscatter parameters show a significant potential of the normalised backscatter coefficient with respect to the incidence angle (γ_α). This was demonstrated over almost all of the tested targets and area of studies in both datasets except in the case of vegetation where σ shows better performance. These outcomes are delivered because the γ_α parameter considers the variations in the target characteristics and accounts for the important effect of angle of incidence to provide the calibrated backscatter signal. This could not be achieved over vegetation because of the uncertain estimations of the incidence angle such as over trees where the size of the target (leaves) are smaller than the laser footprint. However, in case of lower accuracy requirements where it may be appropriate to discount the incidence angle, the backscatter coefficient (γ) provides better performance than the backscatter cross-section (σ) over all selected targets except vegetation. Although the overall outcomes show significant improvements in eliminating the discrepancies between overlapping flightlines after calibration, better results were delivered over the Bournemouth dataset. This can be explained by the more robust incidence angle estimations, which are delivered from the higher point density dataset.

5.5 SEGMENTATION ALGORITHM OF THE FWF-ALS DATA

Integrating additional attributes to the geometric-based segmentation algorithms such as FWF physical observables, can increase reliability of the segmentation results (Höfle et al., 2007; Mucke et al., 2010). This is because these additional attributes can deliver extra information those cannot be provided from the merely geometric information. Integrating laser backscatter signal alongside the standard geometric information has shown potential to better discriminate between different land cover types and enhance segmentation scenarios more than integrating the echo width and amplitude alone

(Mucke, 2008). Motivated by these findings, the developed segmentation routine in this research is based on integrating the backscatter parameters from FWF to improve the identification of surface features. The method is a data-driven algorithm that is feature-based rather than object-based. This is because the method not only considers the spatial relationship between points but also considers information from additional attributes such as the calibrated backscatter signals.

5.5.1 Potential of the Developed Algorithm

The potential of the developed routine is presented in Section 3.6. This utilises the original unstructured 3D point cloud, the normal vector weighted by the calibrated FWF backscatter signal, and applied a seeded surface growing algorithm to grow the segmentation strategy following robust thresholds. The raw geospatial information is utilised as an input in the developed algorithm because pre-classified, filtered, thinned, and interpolated data has the potential to contribute additional error sources to the final results. Thus, using any alternative assumption rather than raw data can put many non-reasonable hurdles to hinder the research meeting its objectives.

The normal vector was selected to be the segmentation criterion, firstly because it is a well-trusted constraint to use as a similarity measure and secondly because of the robustness of the RSN method which has been shown to deliver reliable normal estimates in comparison with the standard algorithms. However, this time the normal vector was augmented by the calibrated backscatter signal, which should lead to better discrimination between objects having the same geometric characteristics but different physical properties. This is a common problem in standard segmentation routines where it is difficult to discriminate between two surfaces with similar geospatial information but from different materials or roughness characteristics using the geometric information alone. Further, the available combined routines, which integrate FWF additional observables such as echo width and amplitude individually (e.g. Reitberger et al. (2009b)) still have shortcomings, as these parameters did not combine all variables affecting the received backscatter signal including all target characteristics.

5.5.2 Selecting Optimal Backscatter Parameters for Segmentation

Before incorporating the calibrated backscatter signal in the segmentation algorithm, it is important to select the optimal backscatter parameter to use in order to represent this signal for individual laser echoes. This is because these parameters have demonstrated different performance over different target types and these targets are composed of groups of neighbourhood points. As these points have a non-homogeneous distribution following the land cover types and the scan characteristics, it is therefore essential to select the proper backscatter parameter for individual points to use in the normal vector definition.

Four backscatter parameters (σ, γ, σ_α, γ_α) are delivered for individual points. The analysis in Section 4.3 has shown that γ_α parameter can deliver the best calibration results amongst other parameters over different target types. The only exception was over vegetation where σ shows the best performance. To differentiate vegetation from other land cover types, the echo width parameter was utilised to detect roughness. This is because the echo width has demonstrated potential to define surface roughness (Section 2.6.5). Echo width simulations were undertaken over multiple land cover categories from both datasets, as explained in Section 4.4.1, to separate vegetation from non-vegetation echoes. The simulation was applied using a roughness threshold based on echo width. The results showed successful separation between rough and smooth echoes. However, not all of the rough echoes necessarily representing vegetation such as in the case of natural land coverage. Because the number of returns is a good indicator to detect vegetation, in this research, this was therefore adopted as a complementary condition to differentiate vegetation from other echoes.

Following this analysis, a condition was adopted to select the optimal backscatter parameter for individual echoes. With this condition, γ_α was utilised as a weighting function to augment the normal vector in the segmentation algorithm for all echoes except vegetation where σ was used instead. In this case, two adjacent surfaces with the same geometric characteristics but made from different materials can be differentiated from each other successfully using their backscatter values. Because the normal vector in both cases will be different as both are differentiated by their individual calibrated backscatter signal.

5.5.3 Performance Assessment

To demonstrate the performance of the developed segmentation algorithm, the routine was tested over various types of land cover targets, firstly with the integration of FWF additional observables and then secondly without it. This scenario was adopted to highlight the potential of weighting the normal by its calibrated backscatter signal against utilising pure geometric information as detailed in Section 4.4.2

The routine with the integration of FWF additional observables was tested firstly. It has shown a successful detection of the multiple planar facets of a house roof target from the Bournemouth dataset. This is because the normal vectors are accurately estimated due to the homogeneous geometry and backscatter signal for the overall echoes. The high point density of the dataset provides a visual demonstration of the successful performance of the algorithm to detect minor details, which was represented by the chimney on the roof. This has shown the successful performance of the RSN method to define these minor details and differentiate these echoes from the background by delivering independent normal vector values and representing this particular feature. Although some points on the sharp edges between two facets still prove difficult to assign correctly to either plane, this issue can be overcome when the adjacent facets are from different materials and thus exhibit different backscatter values.

This latter case was demonstrated through the variation in the backscatter values, which leads to successful differentiation between two types of mown grass. It has shown that the two grass types have the same geometric information because they have been cut in a regular manner which helps to deliver a well-defined geometry in terms of incidence angle. Despite the fact of the similarity in the geospatial information, the variations in the backscatter signal facilitate grouping points of the selected grass region into two individual segments. Although the segmentation is not perfectly performed, the results are promising for this kind of challenging target type.

The developed routine was also tested over non-planar land coverage such as natural earth mound using the lower point density Bristol dataset. The routine has shown a successful description of the natural topography where the sides of the mound has been successfully defined and differentiated from the surrounding semi-flat topographic ground. These are promising outcomes because with the small plane detection using the RSN method it was possible to accurately define the tilted sides of the mound, which are less than 4 m in width in the south-east corner in Figure 4.29, even with the lower point density of the Bristol dataset. In contrast, with the standard fitting algorithms, the sides of the mound might not be well-defined or may even be missed for detection as clear segments from the surrounding ground. The potential of the calibrated backscatter signal in the developed routine has been demonstrated through the clear detection of the grass regions visualised on the north-west corner and close to the middle of the mound. This has facilitated the successful description of the natural land coverage by delivering separate segments from the background for better terrain feature segmentation results.

Similar outcomes were delivered from an urban scene where a highway bridge was successfully segmented with complex object details in the Bournemouth dataset as explained in Section 4.4.2. The bridge barrier was successfully identified from the background and the metal highway barrier beyond the bridge was detected and separated from the surrounding grass regions. Although the surface facets of the car, which was detected on the highway bridge, were not defined correctly, some of the road markings have been clearly visualised and segmented as a separate segment from the surrounding black asphalt background. This latter finding is indeed promising for detailed and accurate urban mapping applications. However, the problem acquired with the definition of the car facets can be explained due to the high speed of the cars, which might prevent delivery of enough point cloud coverage over this particular car target.

Although the method fails to discriminate between the bridge and the highway beneath, this shortcoming can be addressed in future work by incorporating height difference and STD of Z values for each segment. Although the overall performance of this target was not perfect, it can be highlighted as a potential progress in segmentation. Because it demonstrated a successful detection of minor feature details by relying on cooperation between geometric and physical information.

Aiming to deliver a representative study, the developed routine was applied over a selected urban area from the high point density Bournemouth dataset. This area was selected because it comprises various types of surface targets to demonstrate segmentation performance in urban areas. However, the Bournemouth dataset was selected to demonstrate performance because of the high point density which provides further details which cannot be delivered with the Bristol dataset. The overall planar surfaces have been segmented successfully, as visualised through house roofs facets and dormer windows. However, some points have not been classified correctly over these planar surfaces. This might be because of the sensitivity of the RSN method to discontinuity and sometimes because of the non-perfect homogeneity of the backscatter signal over these surfaces. However, the minor surface details such as chimneys and windows have successfully detected and differentiated from the surrounding background in separate independent segments for individual features. This outcome was also delivered from segmenting the cars available in the scene by differentiating the roof from the body.

However, the potential of integrating the calibrated backscatter signal in the developed segmentation routine was demonstrated through differentiating between natural and artificial ground such as asphalt and mown grass. Because the grass regions in this selected area were perfectly cut to deliver flat surfaces similar to the asphalt pavement, the geometric properties for both surfaces were nearly the same. However, the differences in the calibrated backscatter signals represented by the γ_α parameter in this case, have delivered this separation between these two features. Because the normal vector value was augmented differently in both cases, this has led to different segments. Further, promising results have been delivered as well in differentiating between hedges and vegetation. In this case, in addition to the variation in the geometric information, the calibrated backscatter parameters are also different which leads to this differentiation.

In contrast, the results for the segmentation where FWF physical observables are not integrated show clear shortcomings in the overall performance. This is clearly visualised over features with similar geospatial information such as grass and asphalt where the routine fails to differentiate between both mentioned features. Although the developed routine was utilised here and represented by the RSN method but without integrating any additional physical information from FWF, the segmentation results over planar surfaces is not in the same level of performance as the results delivered from integrating FWF additional observables. This has been partially overcome with the integration of FWF additional observables. Adding to this, the sensitivity of the RSN method to discontinuities has shown to be overcome with the backscatter signal integration. Further shortcomings relate to the delivery of meaningful segments for hedges as an independent class from other vegetation types, which reflect the failure of the merely geometric information to define target properties such as roughness.

It worth mentioning that the results delivered from the developed segmentation algorithm are generally sensitive to three main parameters defined by the normal vector residuals (ϕ_i) for individual points, residual threshold (ϕ_{th}), and the angle threshold difference (δ). Normal vector residuals are delivered from the RSN method for independent points, thus checking planarity is a particular important aspect to deliver small ϕ values towards optimal seed points selection. On the other hand, noise presence in the dataset is defining the residual threshold value (ϕ_{th}) which can easily estimated and assessed by following the RSN checking routine to obtain the threshold value defined by (ϕ), which delivered based on data density and accuracy, refer to Section 3.4.1. Finally, the angle threshold difference (δ) is defining the accepted angle difference between the normal of the seed region and the normal of the neighbourhood points, which should be defined accurately depending on the variability in the surface orientation, in dependence with the application and features of interest.

5.5.4 Validation of Results

The results delivered from the analysis so far have shown significant potential over various land cover types. However, the performance accuracy needs to be analysed and validated against reference results to generalise the overall accuracy. To accomplish this, the results delivered from the developed algorithm over the selected urban area were validated against a manual process, as explained in Section 4.4.3. The manual segmentation was based on visual reference from the orthophotos to group the available features into 193 different segments. Because vegetation can deliver irregular outcomes, the validation process has excluded these features from the process except the mown grass because it is cut in a regular manner.

To allow visualisation of the performance of the developed algorithm versus the manual process, outcomes from both routines were presented over house roof segments. This group of segments was selected to investigate the accuracy performance over regular planar surfaces and to check the potential of the backscatter signal integration on the developed routine with planar surfaces. The results show successful segmentation results in detecting planes and defining edges and differentiating minor features from the roof facets correctly. Although a couple of minor surfaces are not segmented correctly, all other facets were correctly segmented and defined.

To investigate the accuracy level of the segmentation, an error matrix was generated. Because the error matrix can deal with the process numerically per echo, it was adopted to simulate the accuracy validation in this study. However, the outcomes are not perfectly representative of reality because it depends on the referenced dataset. The reference dataset is correlated to the visual human performance, which may vary from user to another. However, the error matrix can deliver a true representation of the accuracy performance because it demonstrates the relationship between the error of commission and the error of omission in respect of user accuracy and producer accuracy (Section 4.4.3).

Because it is impossible to evaluate segments individually, the segments are instead grouped into individual categories/classes to facilitate error matrix implementation. The overall performance has met with the visual outcomes as it shows a very promising outcome by delivering high overall accuracy of 82% through the developed routine. The overall accuracy from the routine without the integration of FWF additional information was 67%. The shortcoming with the routine without FWF physical observables was clearly demonstrated over artificial ground and mown grass. This clearly indicates the potential of the physical observables to support geometric information to differentiate between different features of similar characteristics. Further limitations were highlighted from all other categories but with relative overall limits for a routine without FWF backscatter integration. In contrast, the results from the developed routine have highlighted the successful implementation of the algorithm over the individual categories by delivering promising accuracy outcomes as explained in Section 4.4.3.

5.6 SUMMARY

Chapter Five has discussed the results delivered from applying the developed 3D object segmentation routine with FWF-ALS data. The chapter discussed reliability assessment and the potential to overcome the weaknesses in currently available algorithms. This was presented through the validation process to demonstrate the potential of fully exploiting FWF information to improve segmentation scenarios.

The discussion of the FWF post processing and data management shows the potential of the RGD method to post-process FWF data to deliver more rigorous estimations from the waveform signal and provide the user with additional valid echoes. The benefits of this have been proven in the developed normalisation approach, enabling increased reliability of the incidence angle estimations. Further, the RGD adoption has shown reliability through the implementation of the Condor pull model, using high-throughput computing and producing savings in terms of time and cost exerted to process massive datasets. The routine contributes in reducing network usage and wasted computation time by providing a successful processing environment for non-detected Condor networks.

The RSN method results proved the potential of the developed algorithm over various land cover types by delivering robust estimations for point cloud orientation. This was demonstrated through utilising the minimum number of neighbourhood points to deliver the normal and taking data accuracy and density into consideration. However, better performance was detected over targets from higher point density data. The performance assessments demonstrated the feasibility of the RSN routine over challenging and complex surface types such as natural land cover in addition to simple, planar surface types. This has led to successful identification of surface details, which translates to powerful elimination of the differences in echo amplitude signals between flightlines.

The results from the radiometric calibration routine have shown feasibility to calibrate the backscatter signal of FWF data. The emitted energy investigation should be undertaken for each dataset on a per flightline basis to determine whether one calibration constant should be adopted for all flightlines or per flightline, before initiating the calibration process. Consequently, the reflectivity of the reference target should be treated seriously through a practical process and all variables affecting the backscatter signal should be taken into consideration, including the angle of incidence effect. Further, the γ has shown potential in comparison with the σ parameter over all features except irregular vegetation. However, the γ_α was identified as the optimum calibration parameter for all surface types excluding vegetation.

Finally, the developed segmentation algorithm has demonstrated the potential of utilising FWF information to deliver improved results through a better identification of land cover features. This has been shown through the integration of the calibrated backscatter parameters to differentiate between different features with similar geospatial information. However, these improvements cannot be delivered without a proper selection of the suitable backscatter parameters to integrate in the developed routine. The developed algorithm has shown successful implementation, achieving 82% versus 67% accuracy using the same routine with, and then without the integration of the FWF physical observables.

CHAPTER

6

CONCLUDING REMARKS

6.1 CONCLUSIONS

This thesis has set out the development, implementation and testing of a methodology to improve the automatic segmentation of ALS point clouds through exploitation of FWF information. Following the investigation and analysis carried out during the research programme, several concluding remarks can derived, as summarised in the following sections.

6.1.1 Revisiting the Research Objectives

In this research, the potential of fully integrate FWF-ALS information to enhance automatic segmentation algorithms was adopted as a research aim. Progress towards achieving this aim was undertaken following six established research objectives, as follows:

- *Objective One*: to investigate the potential of the additional information from FWF to improve existing 3D object segmentation techniques through reviewing available segmentation algorithms and addressing the weaknesses in these standard methods. This objective was addressed in Chapter 2 through a comprehensive critique of existing literature, reporting on FWF-ALS data processing for 3D object segmentation applications. This included a comprehensive review and discussion of the available calibration approaches for delivering an improved backscatter signal for segmentation applications. The limitations in the standard segmentation algorithms, which rely merely on the geometric information from ALS data, were highlighted. Potential for fusion of the additional observables from FWF with geometric information was also discussed by reviewing available segmentation routines in this respect.

- *Objective Two*: to develop an automatic and effective routine to manage and process FWF-ALS datasets in a manner which requires less human effort and reduces time needed to process large laser scanning datasets efficiently. This objective was tackled in Chapter 3, which reports on the development of a processing strategy for FWF data based on the RGD pulse detection method. The solution adopted a grid computing Condor-based approach, which showed significant potential to reduce the time and effort needed to process large datasets such as FWF-ALS.

- *Objective Three*: to calibrate the FWF backscatter signal from all error sources that have affected the signal during its travel between the target and the sensor to provide the backscatter energy estimate. This objective was achieved, as described in Chapter 3, through accomplishing two essential stages. The first stage was by compensating the laser backscatter energy for the incidence angle effect in multiple flightlines by the development of a signal normalisation approach. This approach is based on a novel technique to estimate the orientation of the individual point cloud robustly using the RSN method. The methodology accounts for Earth surface target orientation through robust normal vector estimation of individual ALS points. The second stage was achieved by accounting for all variables affecting the backscatter signal, including the angle of incidence, through the adoption of a comprehensive calibration routine. The presented routine aims to deliver a more appropriate physical signal for further applications.

- *Objective Four*: to assess the developed calibration technique to ensure reliability for integration in the developed segmentation algorithm. This objective was achieved and is reported in Chapter 4. An assessment was firstly carried out for the echo amplitude normalisation approach, by checking the performance of the RSN method (Section 4.2). Thereafter, the calibrated backscatter energy was assessed following the developed radiometric calibration routine, as detailed in Section 4.3. The results were validated over various feature types, including natural and man-made targets, using visual and statistical analysis to assess reliability prior to adopting the approach for segmentation. Discussion of the delivered results was provided in Chapter 5.

- *Objective Five*: to develop an automatic segmentation routine that fully integrates the calibrated FWF additional information alongside the standard geometric information to deliver accurate and detailed segmentation outputs. The approach for this was set out in Chapter 3, where a hybrid algorithm was developed aiming to fully utilise FWF information to overcome the weaknesses in the existing geometric-based approaches. The motivation was to prove that integrating FWF physical observables can potentially improve segmentation scenarios by distinguishing between different surface features with similar geometric information.

- *Objective Six*: to assess and validate the developed segmentation method on real datasets under various conditions. This objective was achieved in Chapter 4 and discussed in Chapter 5. To demonstrate the potential of the FWF additional observables, results are presented comparing the segmentation performance with the use of FWF additional information to results delivered without incorporation of FWF information following the same routine. An interest area from the high point density dataset was utilised for validation purposes through comparison to a manual segmentation process, as presented in Section 4.4.3. The developed segmentation algorithm was found to be highly effective, delivering an overall accuracy of greater than 80%.

Through the accomplishment of the above objectives, the research aim has been achieved and the potential of the FWF additional observables for improving segmentation has been evidenced.

6.1.2 Main Research Findings

By following the research programme, several research outcomes have emerged, with the main highlights as follows:

1. The developed Condor model is a significant and a powerful technique to speed up the processing of FWF data. It can potentially reduce network usage and eliminate wasted computation effort. This can therefore save time and cost needed to process massive datasets. This technique has shown potential using the RGD pulse detection method which can overcome complex waveforms and detect weak pulses, therefore enabling the detection of more targets. Thus, this routine is recommended for uptake when distributed computing resources are available.

2. The spherical neighbourhood definition is a reliable assumption to adopt for point cloud orientation estimation over different land cover surfaces, including planar surfaces. However, this assumption should be implemented following the *k*-nearest neighbours algorithm rather than relying on a fixed-distance set of neighbours, where uniform point density is assumed. It is essential to consider data density and accuracy to deliver robust normalisation results for individual points. This can be achieved through considering the least number of neighbourhood points to estimate the orientation, which is also effective for accommodating fine surface details, especially in dense datasets. However, robust planarity checking is essential for robust normal derivation and rigorous normalisation results. A robust estimation of point cloud orientation is achievable through the developed RSN method.

3. The RSN routine has shown strong performance over challenging and complex surface types, in addition to simple and planar surface types. Therefore, a successful segmentation of surface details can be delivered following this novel method, which translates to a powerful means of eliminating the differences in echo amplitude signals between flightlines.

4. The incidence angle has an influential role on the variations in the backscatter signals due to different target characteristics. This has shown effectiveness on the area of the land cover target which illuminated by the laser beam. Therefore considering the normalised backscatter cross-section according to the illumination area (γ) in order to deliver the backscatter energy is highly recommended when applying radiometric calibration. This is particularly so when estimating the calibration constant for the entire campaign of a certain lidar dataset.

5. The importance of the incidence angle effect has been shown through the adoption of the normalised backscatter coefficient with respect to angle of incidence (γ_α). This parameter has greatest potential to effectively minimise the discrepancies between signals from overlapping flightlines over any land cover targets excluding irregular vegetation. In cases of irregular vegetation where a target maybe smaller than the footprint size, such as tree leaves, it is challenging to guarantee robust incidence angle estimation and therefore the backscatter cross-section (σ) is recommended instead. However, in cases of regular vegetation surfaces, such as hedges and mown grass, the γ_α has proved effective in eliminating discrepancies between backscatter signals from overlapping flightlines, as these surfaces exhibit a well-defined geometry in terms of incidence angle.

6. Integrating the physical observables from FWF alongside the geometric information provides a powerful approach to improving segmentation scenarios and thus developing feature identification and extraction methods. The developed segmentation algorithm has been demonstrated in this context through successful discrimination between different features with similar geometric characteristics as shown in Section 4.4.2.

6.1.3 Research Contributions

An automatic segmentation algorithm, which fully exploits FWF information, was developed in this research. Through this research, a number of contributions can be highlighted:

- Incorporation of the physical information from FWF provides a strong approach for better identifying features alongside the standard geometric information, and thus improving segmentation and classification techniques.

- Throughput computing within distributive environments is the optimal solution to process large lidar datasets towards fully automatic workflow with efficient saving of time and effort.

- The RSN method is a rigorous approach for delivering the optimal estimation of the surface normal for various types of land cover features with planar and non-planar surfaces and thus can be used as a generic approach for multiple applications.

- Calibrating the backscatter signals from FWF is essential before initial use to increase the benefits of the collected information for further analysis.

- In the case of absolute calibration, it is recommended to use a reference target with a known reflectivity value to deliver the calibration constant. However, the value should be derived from practical reflectivity measurements and delivered at the time of data capture in order to reflect the same conditions as the day of the survey.

- It was practically demonstrated that echo width and the number of return echoes can be successfully utilised to select the optimal backscatter parameter for individual echoes for future integration in segmentation routines.

- The developed segmentation method, which is implemented through the normal vector augmented by the calibrated backscatter signal, can deliver successful discrimination between features having the same geometric characteristics but different backscatter values such as artificial ground and clipped grass.

6.2 SUGGESTIONS FOR FUTURE WORK AND OUTLOOK

The main research areas for improvements and future development can be summarised in the following:

- The geometric calibration of the FWF-ALS data was outside the scope of this research. However, for optimal and accurate results it is required to calibrate both the geometric and the physical FWF information before integration for advanced applications (e.g. feature extraction).

- Limitations were encountered in delivering reliable incidence angle estimations over features which were smaller than the laser footprint (e.g. tree leaves). As a result, extreme normalised amplitude values could be delivered which act as outliers in a comparison with other normalised signals. Therefore, it is recommended to treat such targets separately upon calibration, or otherwise exclude them during analysis.

- In terms of radiometric calibration, reference targets with known backscatter value were not available to deliver the calibration constant in the Bristol dataset. Therefore, it is recommended that suitable reference targets should be distributed in the field at the time of survey, and considered to be of similar importance to standard geometric control targets.

- For further comparison purposes, it is recommended to segment overlapping flightlines individually and compare results, visually and statistically, to investigate the potential of the radiometric calibration on the developed segmentation algorithm from multiple trajectories.

- Segmentation limitations were encountered in discriminating between objects having similar normal values but differences in height, such as a bridge with a road beneath. Therefore, it is recommended to use the height difference as an additional segmentation criterion to the normal vector to overcome this limitation.

- It would be interesting to integrate the spectral information from another remote sensing data source such as photogrammetry or radar imagery to apply the developed routine and investigate potential with the FWF additional information in this context.

- It is also recommended for future work to use the γ_α parameter to develop existing classification techniques and improve DTMs. This can be achieved by integrating this additional parameter alongside the standard geometric information to improve surface modelling algorithms and DTM generation in challenging natural areas and over complex surface types. This parameter could also be valuable in reducing ambiguity between building points and nearby vegetation in urban sites for segmentation and classification applications, and in detecting breaklines for accurate DTMs.

REFERENCES

Abed, F. M. and McGough, S. (2010), 'Processing data intensive Matlab jobs through Condor', In: *Proceedings of All Hands Meeting 2010*. Cardiff, Wales, UK:On CD-ROM.

Abed, F. M., Mills, J. P. and Miller, P. E. (2010), 'Radiometric calibration of full-waveform ALS data based on local incidence angle in natural terrain', In: *Proceedings of RSPSoc and Irish Earth Observation Symposium*. Cork, Ireland, pp. 250-257:On CD-ROM.

Abed, F. M., Mills, J. P. and Miller, P. E. (2011), 'Calibration of full-waveform ALS data based on robust incidence angle estimation', *International Archives of Photogrammetry, Remote Sensing and Spatial Information Sciences,* 38 (5/W12), 6 p.

Abed, F. M., Mills, J. P. and Miller, P. E. (2012), 'Echo amplitude normalisation of full-waveform airborne laser scanning data based on robust incidence angle estimation', *IEEE Transactions on Geoscience and Remote Sensing*, 50 (7), 9 p.

Abdelhafiz, A. (2009), *Integrating digital photogrammetry and terrestrial laser scanning*. PhD thesis. University of Braunschweig - Institute of Technology, Germany.

Ackermann, F. (1999), 'Airborne laser scanning- present status and future expectations', *ISPRS Journal of Photogrammetry and Remote Sensing*, 54 (2-3), pp. 64-67.

Aguilar, F. J. and Mills, J. P. (2008), 'Accuracy assessment of lidar-derived digital elevation models', *The Photogrammetric Record*, 23 (122), pp. 148-169.

Ahokas, E., Kaasalainen, S., Hyyppa, J. and Suomalainen, J. (2006), 'Calibration of the Optech ALTM 3100 laser scanner intensity data using brightness targets', *International Archives of Photogrammetry, Remote Sensing and Spatial Information Sciences*, 36 (A1), 6 p.

Akca, D. (2007), *Least Squares 3D Surface Matching*. PhD thesis. ETH Zurich, Germany, 78 p.

Alexander, C., Tansey, K., Kaduk, J., Holland, D. and Tate, N. J. (2010), 'Backscatter coefficient as an attribute for the classification of full-waveform airborne laser scanning data in urban areas', *ISPRS Journal of Photogrammetry and Remote Sensing*, 65 (5), pp. 423-432.

Anttila, K., Kaasalainen, S., Krooks, A., Haartinen, H., Kukko, A., Manninen, T., Lahtinen, P. and Siljamo, N. (2011), 'Radiometric calibration of TLS intensity:

Application to snow cover change detection', *International Archives of Photogrammetry, Remote Sensing and Spatial Information Sciences*, 38 (5/W12), 6 p.

Appia, V., Ganapathy, B., Abufadel, A., Yezzi, A. and Faber, T. (2010), 'A regions of confidence based approach to enhance segmentation with shape priors', In: *Proceedings of SPIE "Computational imaging VIII*". San Jose, USA, 12 p.

ASD (2009), View Spec Pro program. Available at: http://support.asdi.com/Products/Products.aspx (Accessed: 12 Oct 2009).

Asmat, A., Milton, E. J. and Atkinson, P. M. (2008), 'Atmospheric correction of multiple flightline hyperspectral data (CASI-2)', In: *Proceedings of the Remote Sensing and Photogrammetry Society annual conference "Measuring change in the earth system"*. Exeter, UK, 4 p.

Atkinson, K. B. (1996), *Close range photogrammetry and machine vision Caithness*, Scotland: Whittles Publishing.

Awwad, T. M., Zhu, Q., Du, Z. and Zhang, Y. (2010), 'An improved segmentation approach for planar surfaces from unstructured 3D point clouds', *The Photogrammetric Record*, 25 (129), pp. 5-23.

Axelsson, A. (2010), 'Rapid topographic and bathymetric reconnaissance using airborne lidar', In: *Proceedings of SPIE "Electro-Optical Remote Sensing, Photonic Technologies, and Applications IV"*. Toulouse, France, 10 p.

Baltsavias, E. P. (2004), 'Object extraction and revision by image analysis using existing geodata and knowledge: current status and steps towards operational systems', *ISPRS Journal of Photogrammetry and Remote Sensing*, 58 (3-4), pp. 129-151

Barnea, S. and Filin, S. (2008), 'Segmentation of terrestrial laser scanning data by integrating range and image content', *International Archives of Photogrammetry, Remote Sensing and Spatial Information Sciences*, 37 (B5), pp. 745-750.

Blythe, J., Deelman, E., Gil, Y. and Kesselman, C. (2003), 'Transport grid computing: a knowledge-based approach', In: *Proceedings of The fifth Innovative Applications of Artificial Intelligence conference (IAAI-03)*. Acapulco, Mexico, 8 p.

Bornaz, L., Rinaudo, F. and Roggero, M. (2003), 'Object segmentation in cultural heritage', Available at: http://cipa.icomos.org/text%20files/antalya/131.pdf (Accessed: 14 May 2010).

Boulaassal, H., Landes, T., Grussenmeyer, P. and Tarsha-Kurdi, F. (2007), 'Automatic segmentation of building facades using terrestrial laser data', *International Archives of Photogrammetry, Remote Sensing and Spatial Information Sciences*, 36 (3/W52), 6 p.

Bretar, F., Chauve, A., Bailly, J.-S., Mallet, C. and Jacome, A. (2009), 'Terrain surfaces and 3-D landcover classification from small footprint full-waveform lidar data: application to badlands', *Hydrology and Earth System Sciences*, 13 (8), pp. 1531-1545.

Briese, C. and Lehner, H. (2009), ' Radiometric calibration of full-waveform small-footprint airborne laser scanner data' In: *Proceedings of Digital Terrain Models from Full-waveform Laser Scanning Workshop*, Vienna University of Technology. Vienna, Austria, 26 p.

Briese, C., Höfle, B., Lehner, H., Wagner, W., Pfennigbauer, M. and Ullrich, A. (2008), 'Calibration of full-waveform airborne laser scanning data for object classification', In: *Proceedings of SPIE 2008*, 6950, DOI: 10.1117/12.781086, pp. 69501-69508.

Briese, C., Pfeifer, N. and P., D. (2002), 'Applications of the robust interpolation for DTM determination', *International Archives of photogrammetry, Remote sensing and Spatial information sciences*, 34 (3A), pp. 55-61.

Campbell, J. B. (1996), *Introduction to remote sensing*. London, UK: Taylor and Francis.

Castillo, E. and Zhao, H. (2009), 'Point cloud segmentation via constrained nonlinear least squares surface normal estimates', Technical Report CAM09-104, Available at: ftp://ftp.math.ucla.edu/pub/camreport/cam09-104.pdf (Accessed: 02 Sep 2010).

Chauve, A., Bretar, F., Durrieu, S., Pierrot-Deseilligny, M. and Puech, W. (2009), 'FullAnalyze: A research tool for handling, processing and analysing Full-waveform Lidar data', In: *Proceedings of Geoscience and Remote Sensing Symposium, 2009 IEEE International, IGARSS 200,*, Cape Town, South Africa, pp. 841-844.

Chauve, A., Mallet, C., Bretar, F., Durrieu, S., Deseilligny, M. and Puech, W. (2007), 'Processing full-waveform lidar data: Modelling raw signals', *International Archives of Photogrammetry, Remote Sensing and Spatial Information Sciences*, 36 (3/W52), pp. 102-107.

Chehata, N., Guo, L. and Mallet, C. (2009), 'Contribution of airborne full-waveform lidar and image data for urban scene classification', In: *Proceedings of IEEE 2009 International Conference on Image Processing*. Cairo, Egypt, pp. 1713-1716.

Chelle, M. (2006), 'Could plant leaves be treated as Lambertian surfaces in dense crop canopies to estimate light absorption', *Ecological Modelling*, 198 (2), pp. 219-228.

Chen, F. M., Jin, X. Y., Liu, Y. J., Yang, H. X. and Li, Z. M. (2007), 'Engineering algorithm of the Atmospheric Attenuation in the Infrared Wireless Communication', In: *Proceedings of Wireless Communications, Networking and Mobile Computing, 2007 (WiCOM2007)*. Shanghai, China, pp. 984-987.

Condor (1988), Condor Team. Available at: http://www.cs.wisc.edu/condor/ (Accessed: 15 Oct 2009).

Coren, F. and Sterzai, P. (2006), 'Radiometric correction in laser scanning', *International Journal of Remote Sensing*, 27 (15), pp. 3097-3104.

Dai, Y. S., Xie, M. and Poh, K. L. (2002), 'Reliability analysis of grid computing systems', In: *Proceedings of the 2002 Pacific Rim International Symposium on Dependable Computing*. Tsukuba-City, Ibarski, Japan, pp. 97-104.

Dean, J. and Ghemawat, S. (2008), 'Map Reducer: simplified data processing on large clusters', *Communications of the ACM*, 51 (1), pp. 107-113.

Demantke, J., Mallet, C., David, N. and Vallet, B. (2011), 'Dimensionality based scale selection in 3D lidar point clouds', *International Archives of Photogrammetry, Remote Sensing and Spatial Information Sciences*, 38 (5/W12), 6 p.

Doneus, M. and Briese, C. (2006), 'Digital terrain modelling for archaeological interpretation within forested areas using full-waveform lasers canning', In: *Proceedings of The 7th International Symposium on Virtual Reality, Archaeology and Cultural Heritage (VAST2006)*. Nicosia, Cyprus, pp. 155-162.

Doneus, M., Briese, C., Fera, M. and Janner, M. (2008), 'Archaeological prospection of forested areas using full-waveform airborne laser scanning', *Journal of Archaeological Science*, 35 (4), pp. 882-893.

Dong, F. and Akl, S. G. (2006), 'Scheduling algorithms for grid computing: State of the art and open problems', School of computing, Queen's University, Ontario, Canada, 55p.

Dorninger, P. and Nothegger, C. (2007), '3D segmentation of unstructured point clouds for building modelling', *International Archives of Photogrammetry, Remote Sensing and Spatial Information Sciences*, 36 (3/W49A), pp. 191-196.

Dorninger, P. and Pfeifer, N. (2008), 'A comprehensive automated 3D approach for building extraction, reconstruction, and regularization from airborne laser scanning point clouds', *Sensors*, 8 (11), pp. 7323-7343.

Duan, Y., Li, X., Maerz, N. and Otoo, J. (2011), 'Automatic 3D facet orientations estimation from lidar imaging', In: *Proceedings of 2011 NSF Engineering Research and Innovtion Conference*. Atlanta, Georgia, USA, 5 p.

Ducic, V., Hollaus, M., Ullrich, A., Wagner, W. and Melzer, T. (2006), '3D vegetation and classification using full-waveform laser scanning', In: *Proceedings of 3D Remote Sensing in Forestry*. Vienna, Austria, pp. 211-217.

El-Halawany, S., Moussa, A., Lichti, D. and El-Sheimy, N. (2011), 'Detection of road curb from mobile terrestrial laser scanner point cloud', *International Archives of Photogrammetry, Remote Sensing and Spatial Information Sciences*, 38 (5/W12), 6 p.

Elwasif, W., Plank, J. and Wolski, R. (2001), 'Data staging effects in wide area task framing applications', In: *Proceedings of IEEE ISCC and the Grid Brisbane,* Australia, 9 p.

Filin, S. (2002), 'Surface clustering from airborne laser scanning data', *International Archives of Photogrammetry, Remote Sensing and Spatial Information Sciences*, 32 (3/W13), pp. 119-124.

Filin, S. (2005), 'Elimination of systematic errors from airborne laser scanning data', In: *Proceedings of IEEE International Geoscience and Remote Sensing Symposium, 2005 (IGARSS 2005)*. Seoul South-Korea, pp. 517-520.

Filin, S. and Pfeifer, N. (2005), 'Neighborhood systems for airborne laser data', *Photogrammetric Engineering & Remote Sensing*, 71 (6), pp. 743-755.

Filin, S. and Pfeifer, N. (2006), 'Segmentation of airborne laser scanning data using a slope adaptive neighbourhood', *ISPRS Journal of Photogrammetry and Remote Sensing*, 60 (2), pp. 71-80.

Fraleigh, J. B. and Beauregard, R. A. (1995), *Linear Algebra*. Columbia, USA: Addison-Wesley.

Friedman, J. H., Bentley, J. L. and Finkel, R. (1977), 'An algorithm for finding best matches in logarithmic expected time', *ACM Transactions on Mathematical Software (TOMS)*, 3 (3), pp. 209-226.

Fukunaga, K. and Hostetler, L. D. (1975), 'The estimation of the gradient of a density function with applications in pattern recognition', *IEEE Transactions on Information Theory*, IT-21 (1), pp. 32-40.

FullAnalyze (2009), Open source lidar software. Available at: http://code.google.com/p/fullanalyze/ (Accessed: 16 Dec 2009).

Gross, H. and Thoennessen, U. (2006), 'Extraction of lines from laser point clouds', *International Archives of Photogrammetry, Remote Sensing and Spatial Information Sciences*, 36 (3), pp. 86-91.

Gross, H., Jutzi, B. and Thoennessen, U. (2007), 'Segmentation of tree regions using data of a full-waveform laser', *International Archives of Photogrammetry, Remote Sensing and Spatial Information Sciences*, 36 (3/W49A), pp. 57-62.

Gross, H., Jutzi, B. and Thoennessen, U. (2008), 'Intensity normalization by incidence angle and range of full-waveform lidar data', *International Archives of Photogrammetry, Remote Sensing and Spatial Information Sciences*, 37 (B4), pp. 405-411.

Guan, X. and Wu, H. (2010), 'Leveraging the power of multi-core platforms for large-scale geospatial data processing: Exemplified by generating DEM from massive lidar point clouds', *Computers and Geosciences*, 36 (10), pp. 1276-1282.

Guo, L., Chehata, N., C., M. and Boukir, S. (2011), 'Relevance of airborne lidar and multispectral image data for urban scene classification using Random Forests', *ISPRS Journal of Photogrammetry and Remote Sensing*, 66 (1), pp. 56-66.

Habib, A. and Rens, J. V. (2008), Quality assurance and quality control of lidar systems and derived data. University of Calgary, Calgery, Alberta, Canada, 15 p.

Habib, A. F., Ghanma, M. S., Kim, C. J. and Mitishita, E. (2004b), 'Alternative approaches for utilizing lidar data as a source of control information for photogrammetric models', *International Archives of Photogrammetry, Remote Sensing and Spatial Information Sciences*, 35 (B1), pp. 193-198.

Habib, A. F., Kersting, A. P., Ruifang, Z., Al-Durgham, M., Kim, C. and Lee, D. C. (2008), 'Lidar strip adjustment using conjugate linear features in overlapping strips', *International Archives of Photogrammetry, Remote Sensing and Spatial Information Sciences*, 37 (B1), pp. 385-390.

Habib, A. F., Kersting, A. P., Shaker, A. and Yan, W. Y. (2011), 'Geometric calibration and radiometric correction of lidar data and their impact on the quality of derived products', *Sensors*, 11 (9), pp. 9069-9097.

Habib, A., Ghanma, M. and Mitishita, E. (2004a), 'Co-registration of photogrammetry and lidar data: methodology and case study', *Journal of the Brazilian Society of Cartography, Geodesy, Photogrammetry and Remote Sensing*, 56 (1), pp. 47-54.

Habib, A., Kersting, A. P., Bang, K. I. and Lee, D.-C. (2010), 'Alternative methodologies for the internal quality control of parallel lidar strips', *IEEE Transactions on Geoscience and Remote Sensing*, 48 (1), pp. 221-236.

Han, S.-H., Lee, J.-H. and Yu, K.-Y. (2007), 'An approach for segmentation of airborne laser point clouds utilising scan-line characteristics', *ETRI*, 29 (5), pp. 641-648.

Hastie, T. and Tibshirani, R. (1996), 'Discriminant adaptive nearest neighbour classification', *IEEE Transactions on Pattern Analysis and Machine Intelligence*, 18 (6), pp. 607-616.

Heinzel, J. and Koch, B. (2010), 'Exploring full-waveform lidar parameters for tree species classification', *International Journal of Applied Earth Observation and Geoinformation*, 13 (1), pp. 152-160.

Höfle, B. (2007), *Detection and utilization of the information potential of airborne laser scanning point cloud and intensity data by developing a management and analysis system*. PhD thesis. University of Innsbruck. 129 p.

Höfle, B. and Hollaus, M. (2010), 'Urban vegetation detection using high density Full-waveform airborne lidar data - Combination of object-based image and point cloud analysis', *International Archives of Photogrammetry, Remote Sensing and Spatial Information Sciences*, 38 (7B), pp. 281-286.

Höfle, B., Hollaus, M. and Hagenauer, J. (2012), 'Urban vegetation detection using radiometrically calibrated small-footprint full-waveform airborne lidar data', *ISPRS Journal of Photogrammetry & Remote Sensing*, 67 (1), pp. 134-147.

Höfle, B., Vetter, M., Pfeifer, N., Mandlburger, G. and Stötter, J. (2009), 'Water surface mapping from airborne laser scanning using signal intensity and elevation data', *Earth Surface Processes and Landforms*, 34 (12), pp. 1635-1649.

Höfle, B. and Pfeifer, N. (2007), 'Correction of laser scanning intensity data: Data and model-driven approaches', *ISPRS Journal of Photogrammetry and Remote Sensing*, 62 (6), pp. 415-433.

Höfle, B., Geist, T., Rutzinger, M. and Pfeifer, N. (2007), 'Glacier surface segmentation using airborne laser scanning point cloud and intensity data', *International Archives of Photogrammetry, Remote Sensing and Spatial Information Sciences*, 36 (3/W52), pp. 195-200.

Höfle, B., Hollaus, M., lehner, H., Pfeifer, N. and Wagner, W. (2008), 'Area-based parameterization of forest structure using full-waveform airborne laser scanning data', In: *Hill, R., Suárez, J. & Rosette, J. (Eds.), Proceedings of SilviLaser 2008*. Edinburgh, UK, pp. 227-235.

Hofmann, A. D. (2004), 'Analysis of Tin-structure parameter spaces in airborne laser scanner data for 3-D building model generation', *International Archives of Photogrammetry, Remote Sensing and Spatial Information Sciences*, 34 (B3), pp. 302-307.

Hofmann, A. D., Maas, H.-G. and Streilein, A. (2002), 'Knowledge-based building detection based on laser scanner data and topographic map information', *International Archives of Photogrammetry, Remote Sensing and Spatial Information Sciences*, 34 (3A), pp. 169-174.

Hollaus, M. and Höfle, B. (2010), 'Terrain roughness parameters from Full-waveform airborne lidar data', *International Archives of Photogrammetry, Remote Sensing and Spatial Information Sciences*, 38 (7B), pp. 287-292.

Hopkinson, C. (2007), 'The influence of flying altitude, beam divergence, and pulse repetition frequency on laser pulse return intensity and canopy frequency distribution', *Canadian Journal of Remote Sensing*, 33 (4), pp. 312-324.

Hoppe, H., DeRose, T., Duchamp, T., John, M. and Stuetzle, W. (1992), 'Surface reconstruction from unorganized points', *Computer Graphics (SIGGRAPH '92)*, 26 (2), pp. 71-78.

Hough, P. V. C. (1962), 'Method and means for recognising complex patterns', United States Patent Office 3,069,654, 6 p.

Hu, M.-K. (1962), 'Visual pattern recognition by moment invariants', *IRE Transactions on Information Theory*, 8 (2), pp. 179-187.

Jelalian, A. V. (1992), *Laser radar systems*. Boston, United Kingdom: Artech House.

Jiang, X. Y. and Bunke, H. (1994), 'Fast segmentation of range images into planar regions by scan line grouping', *Machine Vision and Applications*, 7 (2), pp. 115-122.

Jochem, A., Höfle, B., Wichmann, V., Rutzinger, M. and Zipf, A. (2012), 'Area-wide roof plane segmentation in airborne Lidar point clouds', *Computers, Environment and Urban Systems*, 36 (1), pp. 54–64.

Jutzi, B. and Gross, H. (2010), 'Investigations on surface reflection models for intensity normalisation in airborne laser scanning (ALS) data', *Photogrammetric Engineering and Remote sensing*, 76 (9), pp. 1051-1060.

Jutzi, B. and Stilla, U. (2005a), 'Measuring and processing the waveform of laser pulses', In: *Gruen, A., Kahmen, H. (Eds.), Optical 3-D Measurement Techniques VII*. pp. 194-203.

Jutzi, B. and Stilla, U. (2005b), 'Waveform processing of laser pulses for reconstruction of surfaces in urban areas', *International Archives of Photogrammetry, Remote Sensing and Spatial Information Sciences*, 36 (8/W27), 6 p.

Jutzi, B. and Stilla, U. (2006), 'Range determination with waveform recording laser systems using a Wiener Filter', *ISPRS Journal of Photogrammetry and Remote sensing*, 61 (2), pp. 95–107.

Jutzi, B., Eberle, B. and Stilla, U. (2002), 'Estimation and measurement of backscattered signals from pulsed laser radar', In: *Serpico, S.B. (Eds.), Image and Signal Processing for Remote Sensing VIII, SPIE Proceedings*. pp. 256-267.

Jutzi, B., Gross, H. and (2009), 'Normalization of lidar intensity data based on range and surface incidence angle', *International Archives of Photogrammetry, Remote Sensing and Spatial Information Sciences*, 38 (3/W8), 6 p.

Jutzi, B., Neulist, J. and Stilla, U. (2005), 'Sub-pixel edge localization based on laser waveform analysis', *International Archives of Photogrammetry, Remote Sensing and Spatial Information Sciences*, 36 (3/W19), pp. 109-114.

Kaasalainen, S., Ahokas, E., Hyyppa, J. and Suomalainen, J. (2005), 'Study of surface brightness from backscatter laser intensity: calibration of laser data', *IEEE Geoscience and Remote Sensing Letters*, 2 (3), pp. 255-259.

Kaasalainen, S., Hyyppa, H., Kukko, A., Litkey, P., Ahokas, E., Hyyppa, J., Lehner, H., Jaakkola, A., Suomalainen, J., Akujarvi, A., Kaasalainen, M. and Pyysalo, U. (2009a), 'Radiometric calibration of lidar intensity with commercially available reference targets', *IEEE Transactions on Geoscience and Remote Sensing*, 47 (2), pp. 588-598.

Kaasalainen, S., Hyyppa, J., Litkey, P., Hyyppa, H., Ahokas, E., Kukko, A. and Kaartinen, H. (2007), 'Radiometric calibration of ALS intensity', In: *Proceedings of ISPRS Workshop on Laser Scanning 2007 and SilviLaser 2007*. Espoo, Finland, pp. 201-205.

Kaasalainen, S., Jaakkola, A., Kaasalainen, M., Krooks, A. and Kukko, A. (2011a), 'Analysis of incidence angle and distance effects on terrestrial laser scanner intensity: Search for correction methods', *Remote Sensing*, 3 (1), pp. 2207-2221.

Kaasalainen, S., Krooks, A., Kukko, A. and Kaartinen, H. (2009b), 'Radiometric calibration of terrestrial laser scanners with external reference targets', *Remote Sensing*, 1 (1), pp. 144-158.

Kaasalainen, S., Kukko, A., Lindroos, T., Litkey, P., Kaartinen, H., Hyyppa, J. and Ahokas, E. (2008), 'Brightness measurements and calibration with airborne and terrestrial laser scanners', *IEEE Transactions on Geoscience and Remote Sensing*, 46 (2), pp. 528-534.

Kaasalainen, S., Pyysalo, U., Krooks, A., Vain, A., Kukko, A., Hyyppa, J. and Kaasalainen, M. (2011), 'Absolute radiometric calibration of ALS intensity data: effects on accuracy and target classification', *Sensors*, 11 (1), pp. 10586-10602.

Kaasalainen, S., Vain, A., Krooks, A. and Kukko, A. (2009c), 'Topographic and distance effects in laser scanner intensity corrections', *International Archives of Photogrammetry, Remote Sensing and Spatial Information Sciences*, 38 (3/W8), pp. 219-223.

Kager, H. (2004), 'Discrepancies between overlapping laser scanner strips - simultaneous fitting of aerial laser scanner strips', *International Archives of Photogrammetry, Remote Sensing and Spatial Information Sciences*, 34 (B/1), pp. 555-560.

Kawashima, K., Kanai, S. and Date, H. (2001), 'Automatic recognition of piping system from large-scale terrestrial laser scan data', *International Archives of Photogrammetry, Remote Sensing and Spatial Information Sciences*, 38 (5/W12), 6 p.

Kim, C., Habib, A. F. and Mrstik, P. (2007), 'New approach for planar patch segmentation using airborne laser data', In: *Proceedings of The ASPRS 2007 Annual Conference*. Tampa, Florida, USA, May 7-11, 2007. 11 p.

Kim, I. I., McArthur, B. and Eric, K. (2000), 'Comparison of laser beam propagation at 785nm and 1550nm in fog and haze for optical wireless communications', In: *Proceedings of SPIE-Optical wireless communications III*. pp. 26-37.

Korpela, I., Ole Orka, H., Hyyppa, J., Heikkinen, V. and Tokola, T. (2010), 'Range and AGC normalization in airborne discrete-return LiDAR intensity data for forest canopies', *ISPRS Journal of Photogrammetry and Remote Sensing*, 65 (4), pp. 369-379.

Kraus, K. and Pfeifer, N. (1998), 'Determination of terrain models in wooded areas with airborne laser scanner data', *ISPRS Journal of Photogrammetry and Remote Sensing*, 53 (4), pp. 193-203.

Kukko, A., Kaasalainen, S. and Litkey, P. (2008), 'Effect of incidence angle on laser scanner intensity and surface data', *Applied Optics*, 47 (7), pp. 986-992.

Lafarge, F., Descombes, X., Zerubia, J. and Pierrot-Deseilligny, M. (2008), 'Automatic building extraction from DEMs using an object approach and application to the 3D-city modelling', *ISPRS Journal of Photogrammetry and Remote Sensing*, 63 (3), pp. 365-381.

Lari, Z., Habib, A. and Kwak, E. (2011), 'An adaptive approach for segmentation of 3D laser cloud', *International Archives of Photogrammetry, Remote Sensing and Spatial Information Sciences*, 38 (5/W12), 6 p.

Lee, I. and Schenk, T. (2001), '3D perceptual organisation of laser altimetry data', *International Archives of Photogrammetry, Remote Sensing and Spatial Information Sciences*, 34 (3/W4), pp. 57-65.

Lee, I. and Schenk, T. (2002), 'Perceptual organisation of 3D surface points', *International Archives of Photogrammetry, Remote Sensing and Spatial Information Sciences*, 34 (3A), pp. 193-198.

Lee, J., Yu, K., Kim, Y. and Habib, A. F. (2007), 'Adjustment of discrepancies between lidar data strips using linear features', *IEEE Geoscience and Remote Sensing Letters*, 4 (3), pp. 275-279.

Lee, J.-B., Yu, K.-Y., Kim, Y.-I. and Habib, A. F. (2005), 'Segmentation and extraction of linear features for detecting discrepancies between lidar data strips', In: *Proceedings of The International Geoscience and Remote Sensing Symposium 2005*. pp. 4954- 4957.

Lehner, H. and Briese, C. (2010), 'Radiometric calibration of Full-Waveform airborne laser scanning data based on natural surfaces', *International Archives of Photogrammetry, Remote Sensing and Spatial Information Sciences*, 38 (7B), pp. 360-365.

Lehner, H., Kager, H., Roncat , A. and Zlinszky, A. (2011), 'Consideration of laser pulse fluctuations and automatic gain control in radiometric calibration of airborne laser scanning data', In: *Proceedings of The 6th ISPRS Student Consortium and Working Group VI/5 Summer School*. Fayetteville, NC, USA, ISPRS WG VI/5: On CD-ROM.

Lillesand, T. M., Kiefer, R. W. and Chipman, J. W. (2004), *Remote sensing and image interpretation*. USA: John Wiley and Sons.

Lin, Y.-C. (2009), *Digital terrain modelling from small-footprint, full-waveform airborne laser scanning data*. PhD thesis. Newcastle University, 205 p.

Lin, Y.-C. and Mills, J. P. (2009), 'Factors influencing pulse width of small-footprint, full-waveform airborne laser scanning data', *Photogrammetric Engineering & Remote Sensing*, 75 (11), pp. 49-59.

Lin, Y.-C. and Mills, J. P. (2009b), 'Integration of full-waveform information into the airborne laser scanning data filtering process', *International Archives of*

Photogrammetry, Remote Sensing and Spatial Information Sciences, 38 (3/W8), pp. 224-229.

Lin, Y.-C., Mills, J. and Smith-Voysey, S. (2008), 'Detection of weak and overlapping pulses from waveform airborne laser scanning data', In: *Hill, R., Suárez, J. & Rosette, J. (Eds.), Proceedings of SilviLaser 2008*, Edinburgh, United Kingdom, 10 p.

Lin, Y.-C., Mills, J. P. and Smith-Voysey, S. (2010), 'Rigorous pulse detection from full-waveform airborne laser scanning data', *International Journal of Remote Sensing*, 31 (5), pp. 1303-1324.

Lindholm, T. and Yellin, F. (1999), *Java virtual machine specification*. 2nd Ed. Boston, MA, USA Addison-Wesley Longman.

Litzkow, M., Livny, M. and Mutka, M. (1988), 'Condor - A hunter of idle workstations', In: *Proceedings of The 8th International Conference on Distributed Computing Systems*. San Jose, California, USA, IEEE-CS, pp. 104-111.

Liu, Y., Li, Z., Hayward, R., Walker, R. and Jin, H. (2009), 'Classification of airborne lidar intensity data using statistical analysis and Hough Transform with application to power line corridors', In: *In proceedings of Digital Image Computing: Techniques and Application*. Melbourne, Australia, pp. 462-467.

Lutz, E., Geist, T. and Stotter, J. (2003), 'Investigations of airborne laser scanning signal intensity on glacial surfaces-utilizing comperhensive laser geometry modeling and orthophoto surface modelling (A case study: Savartisheibreen, Norway)', *International Archives of Photogrammetry, Remote Sensing and Spatial Information Sciences*, 34 (3/W13): On CD-ROM.

Luzum, B., Starek, M. and Slatton, K. C. (2004), 'Normalizing ALSM Intensities', Geosensing Engineering and Mapping (GEM)/ Civil and Coastal Engineering Department, (2004_07_001), Florida, USA, 8 p.

Maas, H.-G. (2002), 'Methods for measuring height and planimetry discrepancies in airborne laser scanner data', *Photogrammetric Engineering & Remote Sensing*, 68 (1), pp. 933–940.

Maas, H.-G. and Vosselman, G. (1999), 'Two algorithms for extraction building models from raw laser altimetry data', *ISPRS Journal of Photogrammetry and Remote Sensing*, 54 (2-3), pp. 153-163.

MacArthur, A. (2007a), Field guid for the ASD FieldSpec Pro - white reference mode. Available at: http://fsf.nerc.ac.uk/resources/guides/pdf_guides/asd_guide_v2_wr.pdf (Accessed: 15 Oct 2009).

MacArthur, A. (2007b), Field guid for the ASD FieldSpec Pro - raw DN mode. Available at: http://fsf.nerc.ac.uk/resources/guides/pdf_guides/asd_guide_v2_dn.pdf (Accessed: 15 Oct 2009).

Mallet, C. and Bretar, F. (2009), 'Full-waveform topographic lidar: State-of-the-art', *ISPRS Journal of Photogrammetry and Remote Sensing*, 64 (1), 16 p.

Mallet, C., Bretar, F., Roux, M., Soergel, U. and Heipke, C. (2011), 'Relevance assessment of full-waveform lidar data for urban area classification', *ISPRS Journal of Photogrammetry and Remote Sensing*, 66 (6), pp. S71-S84.

Mallet, C., Lafarge, F., Roux, M., Soergel, U., Bretar, F. and Heipke, C. (2010), 'A marked point process for modeling lidar waveforms', *IEEE Transaction on Image Processing*, 19 (12), pp. 3204-3221.

Mallet, C., Soergel, U. and Bretar, F. (2008), 'Analysis of full-waveform lidar data for classification of urban areas', *International Archives of Photogrammetry, Remote Sensing and Spatial Information Sciences*, 37 (B3A), pp. 85-91.

Mandlburger, G. (2011), ' Airborne lidar data processing: practical exercises', In: *Proceedings of the 6th ISPRS Student Consortium and Working Group VI/5 Summer Schoo*l. Fayetteville, NC, USA.

Mandlburger, G., Briese, C. and Pfeifer, N. (2007), 'Progress in lidar sensor technology-chance and challenge for DTM generation and data administration', In: *Proceedings of The 51st Photogrammetric Week*. Stuttgart, Germany, pp. 159-169.

Mandlburger, G., Otepka, J., Karel, W., Wagner, W. and Pfeifer, N. (2009), 'Orientation and processing of airborne laser scanning data (OPALS) - concept and first results of a comprehensive ALS software', *International Archives of Photogrammetry, Remote Sensing and Spatial Information Sciences*, 38 (3/W8), pp. 55-60.

Mandlburger, G., Pfeifer, N., Ressl, C., Briese, C., Roncat , A., Lehner, H. and Mucke, W. (2010), 'Algorithms and tools for airborne lidar data processing from a scientific perspective', In: *Proceedings of The European Lidar Mapping Forum (ELMF) 2010*. Hague/ Netherlands: On CD-ROM.

Mangin, J.-F., Poupon, F., Riviere, D. and Cachia, A. (2003), '3D moment invariant based morphometry', Lecture Notes in Computer Science, 2879 (2), pp. 505-512.

McGough, S. (2011), 'Parallel computing, myths and truths', Available at: https://researchtools.ncl.ac.uk/portal/site/!gateway/page/!gateway-100 (Accessed: 24 Nov 2011).

McGough, S., Robinson, P., Gerrard, C., Haldane, P., Hamlander, S., Sharples, D., Swan, D. and Wheater, S. (2010), 'Intelligent power management over large clusters ', In: *Proceedings of Green Computing and Communications (Green Com 2010)*. Hangzhou, China, 8 p. :On CD-ROM.

Meek, D. S. and Walton, D. J. (2000), 'On surface normal and Gaussian curvature approximations given data sampled from a smooth surface', *Computer Aided Geometric Design*, 17 (6), pp. 521-543.

Melzer, T. (2007), 'Non-parametric segmentation of ALS point clouds using mean shift', *Journal of Applied Geodesy*, 1 (3), pp. 159-170.

Middleton, W. E. K. (1952), *Vision through the atmosphere*. Toronto, Canada: University of Toronto Press.

Miller, P. (2007), *A robust surface matching technique for coastal geohazard monitoring*. PhD thesis. Newcastle University. 311 p.

Mladen, I. G. (1996), 'Comparison of Parzen density and frequency histogram as estimators of probability density functions ', *Pflügers Archive European Journal of Physiology* 433 (1-2), pp. 174-179.

Montgomery, D. C. (2005), *Design and analysis of experiments*. Chichester, UK: Willy-BlackWell.

Mücke, W. (2008), *Analysis of full-waveform airborne laser scanning data for the improvement of DTM generation*. Master thesis. Vienna University of Technology, 67 p.

Mücke, W., Briese, C. and Hollaus, M. (2010a), 'Terrain echo probability assignment based on Full-Waveform airborne laser scanning observables', *International Archives of Photogrammetry, Remote Sensing and Spatial Information Sciences*, 38 (7A), pp. 157-162.

Mücke, W., Hollaus, M. and Briese, C. (2010b), 'Segmentation-based determination of terrain points from full-waveform airborne laser scanning data', In: *Proceedings of The EGU 2010*. Vienna, Austria, Geophysical Research Abstracts.

Neidhart, H. and Sester, M. (2008), 'Extraction of building ground plans from lidar data', *International Archives of Photogrammetry, Remote Sensing and Spatial Information Sciences*, 37 (B2), pp. 405-410.

NERC (2009), NERC Field Spectroscopy Facility. Available at: http://fsf.nerc.ac.uk/ (Accessed: 10 Oct 2009).

Neuenschwander, A., Magruder, L., Londo, A. and Tweddale, S. (2009), 'Fundamental relationships inherent to lidar waveforms for classification', In: *Proceedings of SPIE 2009*. Orlando, Florida, USA, pp. 73230A_1-73230A_8.

Niemeyer, J., Wagner, J. D., Mallet, C., Rottensteiner, F. and Sörgel, U. (2011), 'Conditional random fields for urban scene classification with full-waveform lidar data', *Lecture Notes in Computer Science*, 6952 (1), pp. 233-244.

Nizar, A. A., Filin, S. and Doytsher, Y. (2006), 'Reconstruction of building from airborne laser scanning data', In: *Proceedings of ASPRS Annual Conference 2006*. Reno, Nevada, USA, 10 p.

Noel, V., Roy, G., Bissonnette, L., Chepfer, H. and Flamant, P. (2002), 'Analysis of lidar measurements of ice clouds at multiple incidence angles', *Geophysical Research Letters*, 29 (9), 4 p.

Nordin, L. (2006), *Analysis of waveform data from airborne laser scanner systems*. Master thesis. Lulea University of Technology, 40 p.

OPALS (2009), Orientation and processing of airborne laser scanning data. Available at: http://www.ipf.tuwien.ac.at/opals/opals_docu/index.html (Accessed: 18 Sep 2009).

Ou Yang, D. and Feng, H.-Y. (2005), 'On the normal vector estimation for point cloud data from smooth surfaces', *Computer-Aided Design*, 37 (10), pp. 1071-1079.

Petrie, G. (2009), 'Current developments in airborne laser scanning technologies', In: *Proceedings of the IX International Scientific and Technical Conference "From Imagery to map: Digital Photogrammetric Technologies"*. Attica, Greece, 41 p.

Pfeifer, N. (2009), 'Georeferencing of ALS data', In: *Digital Terrain Models from Full-waveform Laser Scanning Workshop*, Vienna University of Technology. Vienna, Austria, 60 p.

Pfeifer, N. (2011), 'Lidar: theory, point cloud, DTM', In: *Proceedings of the 6th ISPRS Student Consortium and Working Group VI/5 Summer School*. Fayetteville, NC, USA, 218 p.

Pfeifer, N. and Briese, C. (2007), 'Laser scanning- Principals and applications', In: *Proceedings of The 3rd International Exhibition & Scientific Congress on Geodesy, Mapping, Geology, Geophisics, Cadaster GEO-SIBERIA 2007*. Novosibirsk, Russia, 20 p.

Pfeifer, N., Dorninger, P., Haring, A. and Fan, H. (2007), 'Investigation terrestrial laser scanning intensity data: quality and functional relations', In: *International conference on optical 3-D measurement techniques*. Zurich, Switzerland, pp. 328-337.

Pfeifer, N., Elberink, S. O. and Filin, S. (2005), 'Automatic tie elements detection for laser scanner strip adjustment', *International Archives of Photogrammetry, Remote Sensing and Spatial Information Sciences*, 36 (3/W19), pp. 174-179.

Pfeifer, N., Höfle, B., Briese, C., Rutzinger, M. and Haring, A. (2008), 'Analysis of the backscattered energy in terrestrial laser scanning data', *International Archives of Photogrammetry, Remote Sensing and Spatial Information Sciences*, 37 (1), 6 p.

Phong, B. T. (1975), 'Illumination for computer generated pictures', *Communications of ACM*, 18 (6), pp. 311-317.

Pu, S. (2008), 'Automatic building modelling from terrestrial laser scanning', In: *Oosterom, P. v., Zlatanova, S., Penninga, F. and Fendel, E. M.(eds) Advances in 3D geoinformation system*. Springer, pp. 147-160.

Pu, S. and Vosselman, G. (2006), 'Automatic extraction of building features from terrestrial laser scanning', *International Archives of Photogrammetry, Remote Sensing and Spatial Information Sciences*, 36 (5), 5 p.

Qin, Y., Li, B., Niu, Z., Huang, W. and Wang, C. Y. (2010), 'Stepwise decomposition and relative radiometric normalization for small footprint lidar waveform', *Science China Earth Sciences Journal*, 54 (4), pp. 625-630.

Rabbani, T. (2006), *Automatic reconstruction of industrial installations using point clouds and images*. PhD thesis. Delft University of Technology, 154 p.

Rabbani, T. and Heuvel, F. v. d. (2005), 'Efficient hough transform for automatic detection of cylinders in point clouds', *International Archives of Photogrammetry, Remote Sensing and Spatial Information Sciences*, 36 (3/W19), pp. 60-65.

Rabbani, T., Van Den Heuevel, F. and Vosselman, G. (2006), 'Segmentation of point clouds using smoothness constraint', *International Archives of Photogrammetry, Remote Sensing and Spatial Information Sciences*, 36 (5), pp. 248-253.

Raman, R., Livny, M. and Solomon, M. (1998), 'Matchmaking: Distributed resource management for high throughput computing', In: *Proceedings of The 7th IEEE International symposium on high performance distributed computing*. Chicago, USA, 7p.

Reeves, A. P., Prokop, R. J., Andrews, S. E. and Kuhl, F. P. (1988), 'Three-dimensional shape analysis using moments and fourier descriptors', *IEEE Transactions on Pattern Analysis and Machine Intelligence*, 10 (6), pp. 937-943.

Reitberger J., Schnorr, C., Krzystek, P. and Stilla, U. (2009), '3D segmentation of single trees exploiting full waveform lidar data', *ISPRS Journal of Photogrammetry and Remote Sensing*, 64 (6), pp. 561-574.

Reitberger, J., Krzystek, P. and Stilla, U. (2008), 'Analysis of full waveform LIDAR data for the classification of deciduous and coniferous trees', *International Journal of Remote Sensing*, 29 (5), pp. 1407-1431.

Reitberger, J., Krzystek, P. and Stilla, U. (2009a), 'Benefit of airborne full waveform lidar for 3D segmentation and classification of single trees', In: *Proceedings of The ASPRS 2009*, Baltimore, Maryland, USA, 9 p.

Remondino, F. and El-Hakim, S. (2006), 'Image-based 3D modelling: a review', *The Photogrammetric Record*, 21 (115), pp. 269-291.

Ressl, C., Kager, H. and Mandlburger, G. (2008), 'Quality checking of ALS projects using statistics of strip differences', *International Archives of Photogrammetry, Remote Sensing and Spatial Information Sciences*, 37 (B3b), pp. 253-260.

Rieger, P., Ullrich, A. and Reichert, R. (2006), 'Laser scanners with echo digitization for full waveform analysis', In: *Proceedings of The workshop on 3D remote sensing in forestry*. Vienna, Austria, pp. 204-211.

Riegl. (2008), 'RiAnalyze 560 for Full Waveform Analysis user Manual', Available at: http://www.riegl.com/index.php?id=231 (Accessed: 4 March 2009).

Riegl. (2009), 'LMS-Q560', Airborne Laser Scanner for full-waveform analysis, Available at: http://www.riegl.com/uploads/tx_pxpriegldownloads/10_DataSheet_Q560_20-09-2010_01.pdf (Accessed: 20 Sep 2010).

Roggero, M. (2002), 'Object segmentation with region and principal component analysis', *International Archives of Photogrammetry, Remote Sensing and Spatial Information Sciences*, 34 (3A), pp. 289-294.

Roncat , A., Lehner, H. and Briese, C. (2011), 'Laser pulse variations and their influence on radiometric calibration of full-waveform laser scanner data', *International Archives of Photogrammetry, Remote Sensing and Spatial Information Sciences*, 38 (5/W12), 6 p.

Ronnholm, P., Honkavaara, E., Erving, A., Nuikka, M., Haggren, H., Kaasalainen, S., Hyyppa, H. and Hyyppa, J. (2008), 'Registration of airborne laser scanning point clouds with aerial images through terrestrial image blocks', *International Archives of Photogrammetry, Remote Sensing and Spatial Information Sciences*, 37 (B1), pp. 473-480.

Ruiz-Cortes, V. A. (2002), 'Experimental light-scattering measurements from large-scale composite randomly rough surfaces', *Journal of Optical Society of America*, 19 (10), pp. 2043-2052.

Rutzinger, M., Hofle, B. and Pfeifer, N. (2008a), 'Object detection in airborne laser scanning data- an integrative approach on object-based image and point cloud analysis', In: *Blaschke, T., Lang, S. and Hay, G. j.(eds) Object-based image analysis (Spatial concepts of knowledge-driven remote sensing applications)*. Springer, pp. 645-662.

Rutzinger, M., Höfle, B., Hollaus, M. and Pfeifer, N. (2008b), 'Object-based point cloud analysis of full-waveform airborne laser scanning data for urban vegetation classification', *Sensors*, 8 (1), pp. 4505-4528.

Sampath, A. and Shan, J. (2008), 'Building roof segmentation and reconstruction from lidar point clouds using clustering techniques', *International Archives of Photogrammetry, Remote Sensing and Spatial Information Sciences*, 37 (B3a), pp. 279-284.

Schaer , P., Skaloud , J., Landtwing , S. and Legat , K. (2007), 'Accuracy estimation for laser point cloud including scanning geometry', In: *Proceedings of The 5th International Symposium on Mobile Mapping Technology (MMT2007)*. Padua, Italy, 7 p.

Schiewe, J. (2002), 'Segmentation of high-resolution remotely sensed data-concepts, Applications and problems', In: *Joint ISPRS Commission IV Symposium: Geospatial Theory, Processing and Applications*. Ottawa, Canada, 6 p.

Schnabel, R., Wahl, R. and Klein, R. (2007), 'Efficient RANSAC for point-cloud shape detection', *Computer Graphics Forum*, 26 (2), pp. 214-226.

Shaker, A., Yan, W. Y. and El-Ashmawy, N. (2011), 'The effects of laser reflection angle on radiometric correction of the airborne lidar intensity data', *International Archives of Photogrammetry, Remote Sensing and Spatial Information Sciences*, 38 (5/W12), 6 p.

Shan, J. and Toth, C. K. (2009), *Topographic laser ranging and scanning - principles and processing*. FL, USA: Taylor & Francis.

Shen, J., Liu, J., Zhao, R. and Lin, X. (2011), 'A Kd-tree-based outlier detection method for airborne lidar point clouds', In: *Proceedings of the 2011 International Symposium on Image and Data Fusion (ISIDF)*. Tengchong, Yunnan, China, 4 p.

Shi, J. and Malik, J. (2000), 'Normalised cuts and image segmentation', *IEEE Transactions on Pattern Analysis and Machine Intelligence*, 22 (8), pp. 888-905.

Siqueira, P., Hensley, S., Chapman, B. and Ahmed, R. (2008), 'Combining LIDAR and INSAR observations over the Harvard and Duke forests for making wide area maps of vegetation height', In: *Proceedings of the Geoscience and Remote Sensing Symposium, 2008. IGARSS 2008*. Boston, USA, pp. 538-541.

Sithole, G. (2005), *Segmentation and classification of airborne laser scanning data*. PhD thesis. Delft University of Technology, 185 p.

Sithole, G. and Vosselman, G. (2003), 'Automatic structure detection in a point-cloud of an urban landscape', In: *Proceedings of The 2nd GRASS/ISPRS joint workshop on remote sensing and data fusion over urban areas*. Berlin, Germany, pp. 67-71.

Sithole, G. and Vosselman, G. (2005), 'Filtering of airborne laser scanner data based on segmented point clouds', *International Archives of Photogrammetry, Remote Sensing and Spatial Information Sciences*, 36 (3/W19), pp. 66-71.

Skaloud , J. and Lichti, D. (2006), 'Rigorous approach to bore-sight self-calibration in airborne laser scanning', *ISPRS Journal of Photogrammetry and Remote Sensing*, 61 (6), pp. 47-59.

Skaloud , J. and Schaer , P. (2007), 'Towards automated lidar boresight self-calibration', In: *Proceedings of the 5th International Symposium on Mobile Mapping Technology*, Padova, Italy, 6 p.

Song, J.-H., Soo-Hee, H., Kiyun, Y. and Kim, Y.-I. (2002), 'Assessing the possibility of land-cover classification using lidar intensity data', *International Archives of Photogrammetry, Remote Sensing and Spatial Information Sciences*, 34 (3B), pp. 259-262.

Steinvall, O. (2000), 'Effects of target shape and reflection on laser radar cross sections', *Applied Optics*, 39 (24), pp. 4381-4391.

Swinehart, D. F. (1962), 'The Beer-Lambert Law', *Journal of chemical education*, 39 (7), pp. 333-335.

Teague, M. R. (1980), 'Image analysis via the general theory of moments', *Optical Society of America*, 70 (8), pp. 920-930.

Terrasolid. (2008), 'TerraScan User's Guid ', Available at: http://www.terrasolid.fi/en/users_guide/terrascan_users_guide (Accessed: 03 Feb 2009).

Thain, D., Tannenbaum, T. and Livny, M. (2005), 'Distributed computing in practice: The Condor experience', *Concurrency and computation: practice and experience*, 17 (2-4), pp. 323-356.

Torr, P. and Zisserman, A. (1998), 'Robust computation and parameterisation of multiple view relations', In: *Proceedings of The Sixth International Conference on Computer Vision (ICCV'98)*. Bombay, India, 6 p.

Tovari, D. (2006), *Segmentation based classification of airborne laser scanner data*. PhD thesis. Karlsruhe Institute of Technology. 132 p.

Tovari, D. and Pfeifer, N. (2005), 'Segmentation based robust interpolation- a new approach to laser data filtering', *International Archives of Photogrammetry, Remote Sensing and Spatial Information Sciences*, 36 (3/W19), pp. 79-84.

Ullrich, A. (2009), 'Principle of full- and online waveform analysis in airborne, mobile and terrestrial laser scanning', In: *Digital Terrain Models from Full-waveform Laser Scanning Workshop*, Vienna University of Technology. Vienna, Austria, 45 p.

Ullrich, A., Studnicka, N., Hollaus, M., Briese, C., Wagner, W., Doneus, M. and Mucke, W. (2008), 'Improvements in DTM generation by using full-waveform airborne laser scanning data', Available at: http://publik.tuwien.ac.at/files/pub-geo_2121.pdf (Accessed: 26 Jan 2009).

Vain, A., Kaasalainen, S., Pyysalo, U., Krooks, A. and Litkey, P. (2009), 'Use of naturally available reference targets to calibrate airborne laser scanning intensity data', *Sensors*, 9 (4), pp. 2780-2796.

Vain, A., Yu, X., Kaasalainen, S. and Hyyppa, J. (2010), 'Correcting airborne laser scanning intensity data for automatic gain control effect', *IEEE Geoscience and Remote Sensing Letters*, 7 (3), pp. 511-514.

Vanco, M. (2002), *A direct approach for the segmentation of unrecognized points and recognition of simple algebraic surfaces*. PhD thesis. University of technology Chemnitz, 94 p.

Vosselman, G. (1999), 'Building reconstruction using planar faces in very high density height data', *International Archives of Photogrammetry, Remote Sensing and Spatial Information Sciences*, 32 (3/2W5), pp. 87-92.

Vosselman, G. (2004), 'Strip offset estimation using linear features', In: Proceedings of The 3rd International Workshop on Mapping Geo-Surficial Processes using Laser Altimetry. Columbus, Ohio, USA, 9 p.

Vosselman, G. and Dijkman, S. (2001), '3D building model reconstruction from point clouds and ground plans', *International Archives of Photogrammetry, Remote Sensing and Spatial Information Sciences*, 34 (3/W4), pp. 37-43.

Vosselman, G. and Maas, H.-G. (2010), *Airborne and terrestrial laser scanning*. Scotland, UK: Whittles Publishing

Vosselman, G., Gorte, B. G. H., Sithole, G. and Rabbani, T. (2004), 'Recognising structure in laser scanner point clouds', *International Archives of Photogrammetry, Remote Sensing and Spatial Information Sciences*, 46 (8/W2), pp. 33-38.

Wagner, W. (2005), 'Physical principles of airborne laser scanning'. Institute of Photogrammetry and Remote Sensing, Vienna University of Technology, 40 p.

Wagner, W. (2009), 'Measurements principle and physical fundamentals', In: *Digital Terrain Models from Full-waveform Laser Scanning Worksho*p, Vienna University of Technology. Vienna, Austria, 38 p.

Wagner, W. (2010), 'Radiometric calibration of small-footprint full-waveform airborne laser scanner measurements: Basic physical concepts', *ISPRS Journal of Photogrammetry and Remote Sensing*, 65 (6), pp. 505-513.

Wagner, W., Hollaus, M., Briese, C. and Ducic, V. (2008a), '3D vegetation mapping using small-footprint full-waveform airborne laser scanners', *International Archives of Photogrammetry, Remote Sensing and Spatial Information Sciences*, 29 (5), pp. 1433-1452.

Wagner, W., Hyyppa, J., Ullrich, A., Lehner, H., Briese, C. and Kaasalainen, S. (2008), 'Radiometric calibration of full-waveform small-footprint airborne laser scanners', *International Archives of Photogrammetry, Remote Sensing and Spatial Information Sciences*, 37 (B1), pp. 163-168.

Wagner, W., Roncat , A., Melzer, T. and Ullrich, A. (2007), 'Waveform analysis techniques in airborne laser scanning', *International Archives of Photogrammetry, Remote Sensing and Spatial Information Sciences*, 36 (3/W52), pp. 413-418.

Wagner, W., Ullrich, A., Ducic, V., Melzer, T. and Studnicka, N. (2006), 'Gaussian decomposition and calibration of a novel small-footprint full-waveform digitising airborne laser scanner', *ISPRS Journal of Photogrammetry and Remote Sensing*, 60 (2), pp. 100–112.

Wagner, W., Ullrich, A., Melzer, T., Briese, C. and Kraus, K. (2004), 'From single-pulse to full-waveform airborne laser scanners: potential and practical challenges', *International Archives of Photogrammetry, Remote Sensing and Spatial Information Sciences*, 35 (B3), pp. 201–206.

Wang, C.-K. and Lu, Y.-Y. (2009), 'Potential of ILRIS3D intensity data for planar surfaces segmentation', *Sensors*, 9 (7), pp. 5771-5782.

Wang, J. and Shan, J. (2009), 'Segmentation of lidar point clouds for building extraction', In: *Proceedings of The ASPRS 2009*. Baltimore, Maryland, US, 13 p.

Wang, O. (2006), *Using aerial lidar data to segment and model building*. Master thesis. California University. 57 p.

Wang, Y., Zhang, J., Roncat , A., Kunzer, C. and Wagner, W. (2009), 'Regularizing method for the determination of the backscatter cross section in lidar data', *Optical Society of America*, 26 (5), pp. 1071-1079.

Wehr, A. and Lohr, U. (1999), 'Airborne laser scanning—an introduction and overview', *ISPRS Journal of Photogrammetry and Remote Sensing*, 54 (2-3), pp. 68–82.

Weingarten, J. W., Gruener, G. and Siegwart, R. (2004), 'Probabilistic plane fitting 3D and an application to robotic mapping', In: *Proceedings of The 2004 IEEE International Conference on Robotics and Automation (ICRA2004)*. New Orleans, LA, USA, pp. 927-932.

West, K. F., Webb, B. N., Lersch, J. R. and Pothier, S. (2004), 'Context-driven automated target detection in 3-D data', In: *Sadjadi, F.A. (Eds.), Proceedings of SPIE-Automatic Target Recognition XIV*. pp. 133-143.

Xudong, L., Youchuana, W. and Wei, W. (2008), 'A flow to generate DEM and segmentation building in urban areas fr om lidar data', *International Archives of Photogrammetry, Remote Sensing and Spatial Information Sciences*, 37 (B3b), pp. 149-152.

Yan, W. Y., Shaker, A., Habib, A. and Kersting, A. P. (2011), 'Improving classification accuracy of airborne lidar intensity data by geometric calibration and radiometric calibration', *ISPRS Journal of Photogrammetry and Remote Sensing*, 67 (1), pp. 35-44.

Yokoyama, H., Date, H., Kanai, S. and Takeda, H. (2011), 'Pole-like objects recognition from mobile laser scanning data using smoothing and principal component analysis', *International Archives of Photogrammetry, Remote Sensing and Spatial Information Sciences*, 38 (5/W12), 6 p.

Yoon, J.-S., Shin, J.-I. and Lee, K.-S. (2008), 'Land cover characteristics of airborne lidar intensity data: A case study', *IEEE Geoscience and Remote Sensing Letters*, 5 (4), pp. 801-805.

Zhan, Q., Liang, Y. and Xiao, Y. (2008), 'Colour-based segmentation of point clouds', *International Archives of Photogrammetry, Remote Sensing and Spatial Information Sciences*, 38 (3/W8), 6 p.

Zhao, W., Cheng, L., Tong, L., Liu, Y. and Li, M. (2011), 'Robust segmentation of building points from airborne lidar data and imagery', In: *Proceedings of The19th International Conference on Geoinformatics (Geoinformatics 2011)*, 5 p.

Zizhen, R., Zhou, G., Minyi , C., Tonggang, Z. and Qiyong, Z. (2008), 'A novel method for extracting building from LIDAR Data-Fc-S method', *International Archives of Photogrammetry, Remote Sensing and Spatial Information Sciences*, 37 (B1), pp. 283-288.

Zou, W. and Ye, X. (2007), 'Multi-resolution hierarchical point cloud segmentation', In: *Proceedings of the 2nd International Multi-Symposiums on Computer and Computational Sciences 2007*. Iowa City, Iowa, USA, pp. 137-143.

Zublin, M., Fischer, L. and Eisenbeiss, H. (2008), 'Combining photogrammetry and laser scanning for DEM generation iun steep high-mountain areas', *International Archives of Photogrammetry, Remote Sensing and Spatial Information Sciences*, 37 (B6b), pp. 38-44.